



Computational Design of Two-Dimensional Materials for Energy Conversion

Yiqing Chen

Department of Mining and Materials Engineering

McGill University, Montreal, QC, Canada

December 2022

A thesis submitted to McGill University in partial fulfillment of the requirements for the degree
of Doctor of Philosophy

© Yiqing Chen, 2022

Abstract

The discovery of graphene in 2004 has ignited a surge of interest in various two-dimensional (2D) materials, such as transition metal dichalcogenides (TMDCs), 2D group III-nitrides (2D III-nitrides), and black phosphorus (BP). Thanks to their unique structures, 2D materials exhibit distinct properties including high conductivity, large specific surface area and high catalytic activity, being ideal candidates for a variety of applications. Recently, 2D materials have demonstrated great promise in energy-related applications. Particularly, 2D materials like 2D TMDCs have been extensively studied as effective electrocatalysts and photocatalysts for hydrogen evolution reaction (HER). However, many 2D materials show limited HER performance due to the low density of catalytic sites in their structures. To overcome this limitation, various strategies have been developed to engineer the 2D material structures so as to improve HER performance. Among different engineering strategies, phase boundary and alloying can provide attractive options as they are able to enhance the density of active sites while retaining the structural integrity of 2D materials. However, systematic research on engineering 2D materials via phase boundaries and alloying for catalytic applications remains rather limited, with the mechanisms underlying enhanced catalytic performance elusive. Such lack of mechanistic understanding is a critical obstacle hindering rational design of the properties of 2D materials in a predictable manner.

In this regard, the present thesis systematically studied the two important engineering strategies of 2D materials, i.e., via phase boundaries and alloying, and their roles in improving the HER performance. The focus is placed mainly on 2D TMDCs as the representative 2D material group, but with other 2D materials, i.e., 2D III-nitride alloys, also considered for generality. Density functional theory (DFT) calculations were employed as the computational tool to examine

the catalytic properties of phase boundaries and alloys, and band center theory was adopted to clarify the important mechanism underlying the enhanced catalytic activities. These efforts were further augmented by machine learning and cluster expansion method to accelerate the exploration of the vast alloy composition space, and physical and chemical property spectrums.

The thesis is in the manuscript-based format, containing three inherently connected articles, including 2D MoTe₂ phase boundaries for catalyzing HER (Chapter 4), 2D cation-mixed TMDC alloys for HER electrocatalysts (Chapter 5), and monolayer Ga_(1-x)Al_xN alloys for electronics and photocatalysis (Chapter 6). These studies provide mechanistic insights into property tailoring of 2D materials via introducing phase boundaries and alloying, and more generally, guide the rational design and exploration of new 2D materials-based catalytic systems.

Résumé

La découverte du graphène en 2004 a suscité un regain d'intérêt pour divers matériaux bidimensionnels (2D), tels que les dichalcogénures de métaux de transition (TMDC), les nitrures 2D du groupe III (nitrures 2D III) et le phosphore noir (BP). Grâce à leurs structures uniques, les matériaux 2D présentent des propriétés distinctes, notamment une conductivité élevée, une grande surface spécifique et une activité catalytique élevée, étant des candidats idéaux pour une variété d'applications. Récemment, les matériaux 2D se sont révélés très prometteurs dans les applications liées à l'énergie. En particulier, les matériaux 2D tels que les TMDC 2D ont été largement étudiés en tant qu'électrocatalyseurs et photocatalyseurs efficaces pour la réaction de dégagement d'hydrogène (HER). Cependant, de nombreux matériaux 2D présentent des performances HER limitées en raison de la faible densité de sites catalytiques dans leurs structures. Pour surmonter cette limitation, diverses stratégies ont été développées pour concevoir les structures matérielles 2D afin d'améliorer les performances de HER. Parmi les différentes stratégies d'ingénierie, la limite de phase et l'alliage peuvent fournir des options intéressantes car ils sont capables d'améliorer la densité des sites actifs tout en conservant l'intégrité structurelle des matériaux 2D. Cependant, la recherche systématique sur l'ingénierie des matériaux 2D via les frontières de phase et l'alliage pour les applications catalytiques reste plutôt limitée, les mécanismes sous-jacents aux performances catalytiques améliorées étant insaisissables. Un tel manque de compréhension mécaniste est un obstacle critique qui entrave la conception rationnelle des propriétés des matériaux 2D de manière prévisible.

À cet égard, la présente thèse a systématiquement étudié les deux stratégies d'ingénierie importantes des matériaux 2D, c'est-à-dire via les frontières de phase et l'alliage, et leurs rôles dans l'amélioration des performances HER. L'accent est mis principalement sur les TMDC 2D en tant

que groupe de matériaux 2D représentatif, mais avec d'autres matériaux 2D, c'est-à-dire les alliages 2D III-nitride, également considérés pour la généralité. Les calculs de la théorie fonctionnelle de la densité (DFT) ont été utilisés comme outil de calcul pour examiner les propriétés catalytiques des limites de phase et des alliages, et la théorie du centre de bande a été adoptée pour clarifier le mécanisme important sous-jacent aux activités catalytiques améliorées. Ces efforts ont été renforcés par l'apprentissage automatique et la méthode d'expansion des clusters pour accélérer l'exploration du vaste espace de composition des alliages et des spectres de propriétés physiques et chimiques.

La thèse est au format manuscrit, contenant trois articles intrinsèquement liés, y compris les limites de phase 2D MoTe_2 pour catalyser HER (Chapitre 4), les alliages TMDC à mélange cationique 2D pour les électrocatalyseurs HER (Chapitre 5) et les alliages monocouches $\text{Ga}_{(1-x)}\text{Al}_x\text{N}$ pour l'électronique et photocatalyse (Chapitre 6). Ces études fournissent des informations mécanistes sur l'adaptation des propriétés des matériaux 2D via l'introduction de limites de phase et d'alliages, et plus généralement, guident la conception et l'exploration rationnelles de nouveaux systèmes catalytiques à base de matériaux 2D.

Acknowledgements

Foremost, I would like to express my deepest appreciation to my supervisor, Professor Jun Song, for his professional guidance, continuous support and patience. He not only guided me to think outside the box with his innovative ideas and deep insights, but also offered me invaluable space and freedom in choosing research projects of my interest. I consider myself very fortunate for being part of his research group and being able to work with an encouraging and easy-going professor like him.

I would like to extend my sincere thanks to many of my group members, particularly Dr. Pengfei Ou and Dr. Fanchao Meng for their kind assistance during the initial stage of my research. Many thanks to all my friends, especially Chuhong Wang, Tiantian Yin and Xun Du, who always offer support and wonderful ideas along the journey of my Ph.D.

I would also like to thank Natural Science and Engineering Research Council (NSERC) and McGill Engineering Doctoral Award (MEDA) for the financial support and Compute Canada and Calcul Québec for providing computing resources.

Last but not least, words cannot express my gratitude to my caring and supportive family. I owe so many thanks to my mother Yunping Zhou for her love, strength, and wisdom that keep me motivated and confident, my father Guoqiao Chen for his unconditional support, and my twin sister Yidan Chen for giving me inspiration in life and the courage to keep moving forward. Without such a team behind me, this thesis would not have been possible.

Preface and Contributions of Authors

This doctorate thesis is in manuscript-based format and consists of three published or to-be-submitted manuscripts. The authorship and contributions of authors are listed below (* represents the corresponding author):

1. **Basal plane activation in monolayer MoTe₂ for the hydrogen evolution reaction via phase boundaries**, *Journal of Materials Chemistry A*, 2020, 8, 19522-19532.

By: Yiqing Chen, Pengfei Ou, Xiaohan Bie, and Jun Song*

2. **Basal plane activation of two-dimensional transition metal dichalcogenides via alloying for hydrogen evolution reaction: first-principles calculations and machine learning prediction**, to be submitted.

By: Yiqing Chen, Pengfei Ou, Ying Zhao, and Jun Song*

3. **Two-dimensional III-nitride alloys: Electronic and chemical properties of monolayer Ga_(1-x)Al_xN**, to be submitted.

By: Yiqing Chen, Pengfei Ou, Ying Zhao, and Jun Song*

Author contributions: For all listed manuscripts, Yiqing Chen and Jun Song conceived the ideas and design the simulations; Yiqing Chen conducted all simulations, analyzed all data, and wrote all the manuscripts. Jun Song reviewed and edited all the manuscripts. For manuscript 1, Pengfei Ou assisted in conceiving the idea and analyzing the data, and Xiaohan Bie offered information on the model construction. For manuscripts 2 and 3, Pengfei Ou and Ying Zhao helped analyze the results and offered discussions.

Table of Contents

| | |
|--|--------------|
| Abstract..... | i |
| Résumé..... | iii |
| Acknowledgements | v |
| Preface and Contributions of Authors..... | vi |
| Table of Contents | vii |
| List of Figures..... | xi |
| List of Tables | xviii |
| List of Abbreviations | xix |
| Chapter 1 : Introduction | 1 |
| 1.1 References | 4 |
| Chapter 2 : Literature Review..... | 7 |
| 2.1 2D materials | 7 |
| 2.1.1 2D TMDCs | 8 |
| 2.1.2 2D III-nitrides | 11 |
| 2.2 Computational modeling in catalysis | 14 |
| 2.2.1 Sabatier principle..... | 14 |
| 2.2.2 Computational hydrogen electrode..... | 16 |
| 2.2.3 Limitations of the CHE method..... | 17 |
| 2.3 HER performance of 2D materials..... | 18 |
| 2.4 Improving catalytic activities of 2D materials | 21 |
| 2.4.1 Defect engineering..... | 22 |
| 2.4.2 Alloying | 29 |
| 2.4.3 Substrate engineering | 32 |
| 2.5 Summary | 33 |
| 2.6 References | 34 |
| Chapter 3 : Methodology..... | 43 |
| 3.1 Introduction | 43 |
| 3.2 First-principles methods..... | 44 |
| 3.3 Density functional theory | 47 |
| 3.4 Cluster expansion method | 50 |

| | |
|--|------------|
| 3.5 Machine learning..... | 52 |
| 3.6 References..... | 55 |
| Chapter 4 : Basal Plane Activation in Monolayer MoTe₂ for Hydrogen Evolution Reaction via Phase Boundaries..... | 58 |
| 4.1 Abstract..... | 59 |
| 4.2 Introduction..... | 59 |
| 4.3 Methods and models..... | 62 |
| 4.4 Results and discussion..... | 66 |
| 4.4.1 Formation energies of MoTe ₂ phase boundaries..... | 66 |
| 4.4.2 Hydrogen adsorption at MoTe ₂ phase boundaries..... | 68 |
| 4.4.3 Relation of hydrogen adsorption to electronic properties..... | 74 |
| 4.5 Conclusion..... | 80 |
| 4.6 Acknowledgements..... | 81 |
| 4.7 Supporting information..... | 82 |
| 4.7.1 Benchmark studies on nanoribbon models..... | 82 |
| 4.7.2 The effect of exchange-correlation functional on the electronic structure calculations..... | 83 |
| 4.7.3 Details of formation energy calculations of zigzag phase boundaries..... | 83 |
| 4.7.4 Local bond variation at the phase boundary..... | 85 |
| 4.7.5 Thermal stability of phase boundaries at room temperature..... | 86 |
| 4.7.6 Hydrogen adsorption at HL sites..... | 87 |
| 4.7.7 Adsorption sites of pristine 2H and 1T' MoTe ₂ | 89 |
| 4.7.8 Free energy diagrams for the hydrogen evolution at the phase boundaries..... | 89 |
| 4.7.9 HER performance of few-layer MoTe ₂ nanosheets..... | 90 |
| 4.7.10 HER performance of other TMDC phase boundaries..... | 91 |
| 4.7.11 DOS of different Te sites in phase boundaries..... | 92 |
| 4.7.12 The Fermi-abundance model for Mo sites..... | 94 |
| 4.7.13 Charge distribution at various adsorption sites along phase boundaries..... | 95 |
| 4.7.14 DOS plots of various Mo sites..... | 97 |
| 4.7.15 Projected DOS for d orbitals of Mo ₂ atoms..... | 98 |
| 4.8 References..... | 98 |
| Chapter 5 : Basal Plane Activation of Two-Dimensional Transition Metal Dichalcogenides via Alloying for Hydrogen Evolution Reaction: First-Principles Calculations and Machine Learning Prediction..... | 103 |

| | |
|--|------------|
| 5.1 Abstract | 104 |
| 5.2 Introduction | 104 |
| 5.3 Results | 107 |
| 5.3.1 Machine learning (ML) workflow | 107 |
| 5.3.2 Predictions of electrocatalytic activity of TMDC alloys | 112 |
| 5.3.3 The origin of alloying in enhancing HER activity | 117 |
| 5.4 Conclusions | 122 |
| 5.5 Methods | 123 |
| 5.5.1 Enumeration of hydrogen adsorption configurations | 123 |
| 5.5.2 Density-functional theory (DFT) calculations | 123 |
| 5.5.3 Construction of machine learning (ML) model | 126 |
| 5.6 Acknowledgements | 127 |
| 5.7 Supporting Information | 127 |
| 5.7.1 Data distribution | 127 |
| 5.7.2 Performance of ML model | 129 |
| 5.7.3 Gibbs free energies of hydrogen adsorption on pristine MX ₂ | 130 |
| 5.7.4 Feature vector assignment | 131 |
| 5.7.5 Electrocatalytic Activity of 72 TMDC Alloys | 132 |
| 5.7.6 HER activity mapping for MSe ₂ | 138 |
| 5.7.7. HER activity mapping for MS ₂ at different concentrations | 139 |
| 5.7.8 p-band center ϵ_p vs. concentration x of TMDC alloys | 139 |
| 5.7.9 Example adsorption configurations | 140 |
| 5.8 References | 140 |
| Chapter 6 : Two-Dimensional III-Nitride Alloys: Electronic and Chemical Properties of Monolayer Ga_(1-x)Al_xN | 146 |
| 6.1 Abstract | 147 |
| 6.2 Introduction | 147 |
| 6.3 Computational methods | 150 |
| 6.3.1 Cluster expansion | 150 |
| 6.3.2 Special quasi-random structure (SQS) method | 151 |
| 6.3.3 Free energy of random alloys | 151 |
| 6.3.4 DFT calculations | 152 |
| 6.4 Results and discussion | 152 |

| | |
|--|------------|
| 6.4.1 Configurations and stabilities of Ga _(1-x) Al _x N alloys | 152 |
| 6.4.2 Electronic properties | 156 |
| 6.4.3 Effect of strain | 157 |
| 6.4.4 Potential applications in photocatalysis..... | 158 |
| 6.5 Conclusion..... | 160 |
| 6.6 Acknowledgements | 161 |
| 6.7 Supporting Information | 162 |
| 6.7.1 Optimized geometries of various Ga _(1-x) Al _x N alloys | 162 |
| 6.7.2 Phonon calculations of 2D GaN, AlN and Ga _{0.5} Al _{0.5} N | 162 |
| 6.7.4. Band gap variation using 2x2 Ga _(1-x) Al _x N ordered alloys | 163 |
| 6.8 References | 164 |
| Chapter 7 : General Discussion | 167 |
| 7.1 Strategies for activating the basal plane of 2D TMDCs for HER..... | 167 |
| 7.1.1 Phase boundary activated HER on 2D TMDCs | 168 |
| 7.1.2 Alloying activated HER on 2D TMDCs..... | 171 |
| 7.1.3 Phase boundaries in alloys for catalyzing HER..... | 174 |
| 7.2 Broadening alloying strategy to other 2D materials..... | 175 |
| 7.4 Descriptors for electronic structures of 2D catalysts | 176 |
| 7.5 References | 178 |
| Chapter 8 : Conclusions | 180 |
| 8.1 Final conclusions..... | 180 |
| 8.2 Contribution to the original knowledge | 182 |
| 8.3 Future work | 183 |

List of Figures

- Fig. 1.1** Overview of the objectives of this thesis..... 4
- Fig. 2.1** Top and side views of atomic configurations of various TMDC phases: (a) 2H, (b) 1T, (c) 1T', and (d) 1T'' phases. Transition metal and chalcogen atoms are indicated in purple and yellow, respectively. Adapted with permission from ref. [17]. Copyright 2015 AIP Publishing. 9
- Fig. 2.2** (a) Schematic of single-layer MoS₂ transistor. (b) Source-drain current (I_{ds}) versus top gate voltage (V_{tg}) of the MoS₂ monolayer transistor recorded for a bias voltage ranging from 10 mV to 500 mV. The inset shows I_{ds} - V_{tg} for back gate voltage $V_{bg} = -10, -5, 0, 5$ and 10 V. Results obtained from experiments. Adapted with permission from ref. [25]. Copyright 2011 Springer Nature. (c) Optical image of single-layer MoS₂ phototransistor. (d) Photoswitching characteristics of single-layer MoS₂ phototransistor at different optical power (P_{light}) and drain voltage (V_{ds}). Results obtained from experiments. Adapted with permission from ref. [26]. Copyright 2012 American Chemical Society. (e) Schematic of the MoS₂/graphene solar cell. M1 and M2 indicate low and high workfunction metals, respectively. Adapted with permission from ref. [27]. Copyright 2013 American Chemical Society. 11
- Fig. 2.3** Atomic structures of 2D XN. (a) Planar and buckled hexagonal structures. Adapted with permission from ref. [44]. Copyright 2019 American Chemical Society. (b) Haeckelite structure (T-XN) [42]. (c) porous structure (H-XN). Adapted with permission from ref. [43]. Copyright 2017 Elsevier. 13
- Fig. 2.4** (a) The false-colored SEM image of a 2D GaN field effect transistor. (b) Gate-dependent I_{ds} - V_{ds} characteristic curves from experiments. Adapted with permission from ref. [48]. Copyright 2018 American Chemical Society. (c) Top and side views of the GaN/Mg(OH)₂ vdW heterostructure, where Ga, N, Mg, O, and H atoms are shown in green, grey, orange, red, and pink, respectively. (d) Photocatalytic mechanism for GaN/Mg(OH)₂ vdW heterostructure. Adapted with permission from ref. [49]. Copyright 2019 AIP Publishing. 14
- Fig. 2.5** (a) Schematic representation of the Sabatier principle. Adapted with permission from ref. [59]. Copyright 2015 Elsevier. (b) Schematic representation of the thermodynamic free-energy profile of a catalytic reaction with one reaction intermediate. Adapted with permission from ref. [60]. Copyright 2021 Ooka, Huang and Exner. 16
- Fig. 2.6** (a) Schematics and DFT-calculated ΔG_H values of 2D TMDCs basal planes and edges. Adapted with permission from ref. [72]. Copyright 2014 Royal Society of Chemistry. (b) DFT-calculated ΔG_H values of the basal plane of 1T' TMDC monolayers. Adapted with permission from ref. [73]. Copyright 2015 Royal Society of Chemistry. (c) HER polarization curves of 2H-MoS₂ basal plane and edge sites from experiments. (d) HER polarization curves of 1T'-MoS₂ basal plane and edge sites from experiments. (e) HER polarization curves of 2H- and 1T' MoS₂ basal plane from experiments. Adapted with permission from ref. [74]. Copyright 2017 John Wiley and Sons. (f) Band edge positions of 2D TMDCs, CdS and TiO₂ relative to the vacuum level. Dash

lines indicate the redox potentials, including the potentials of water splitting at pH = 0 and the potential of CO₂ reduction at pH = 7. Adapted with permission from ref. [77]. Copyright 2015 Elsevier. 21

Fig. 2.7 (a) Schematic of 2H-MoS₂ with S-vacancies, where Mo and S atoms are indicated in blue and yellow. The red region around the S-vacancy indicates Kohn-Sham orbitals corresponding to the new bands just below the Fermi level. (b) Band structure of 2H-MoS₂ with 25% S-vacancies. The new bands introduced by S-vacancies are indicated in red. (c) Calculated Gibbs free energies of HER for the S-vacancy range of 0-25%. Adapted with permission from ref. [82]. Copyright 2015 Springer Nature. (d)-(f) Hydrogen adsorption configurations at V_S, V_{MoS₃} and MoS₂ site, where S, Mo, and H atoms in defect regions are shown in yellow, purple and cyan, respectively. Adapted with permission from ref. [83]. Copyright 2016 American Chemical Society. 24

Fig. 2.8 (a) The hydrogen adsorption sites and corresponding ΔG_H values of various monolayer MoS₂ grain boundaries, including 5|7a, 5|7b, 4|8a, 4|8b, 4|8c, 4|4, 8|10a and 8|10b. Adapted with permission from ref. [91]. Copyright 2018 Springer Nature. (b),(c) Relationship between DFT-calculated H adsorption energies and (b) d- or (c) p-band center of MoS₂ defects. Adapted with permission from ref. [83]. Copyright 2016 American Chemical Society. 27

Fig. 2.9 Optimized structures of (a) ZZ_{Mo-S}, (b) ZZ_{Mo-Mo}, (c) ZZ_{S-S}, (d) ZZ_{S-Mo} and (e) AC 2H/1T' MoS₂ phase boundaries, where Mo and S atoms in the 2H phase are shown in cyan and yellow, and Mo and S atoms in the 1T' phase are shown in cyan and purple. The dashed circles with red or black colors indicate the optimal adsorption site for hydrogen on the top or bottom S layers. (f) Calculated Gibbs free energies for hydrogen adsorption ΔG_H on different sites of ZZ and AC phase boundaries compared with pristine 2H-MoS₂. (g) The volcano plot that indicates the relationship between the exchange current density i_0 and the Gibbs free energy ΔG_H . Adapted with permission from ref. [110]. Copyright 2019 American Chemical Society. 29

Fig. 2.10 (a) Schematic (left) and high-magnification STEM-HAADF image (right) of the W_xMo_{1-x}S₂/graphene heterostructure. (b) The activation energy barrier versus alloy concentration for Volmer reaction mechanism obtained from simulations. (c) The activation energy barrier versus alloy concentration for Heyrovsky reaction mechanism obtained from simulations. Adapted with permission from ref. [127]. Copyright 2017 American Chemical Society. 32

Fig. 3.1 Schematic of the alloy AB in a two-dimensional lattice space. Each site in the alloy can be represented by either (a) an atom type, or (b) an occupation variable (+1 for atom A and -1 for atom B). 52

Fig. 3.2 Applications of machine learning methods in materials science [50]. 54

Fig. 4.1 The top and side views of pristine (a) 2H and (b) 1T' MoTe₂, where Mo atoms are shown in purple and Te atoms are shown in brown, with the black arrows indicating the AC and ZZ directions of MoTe₂ lattice. Two types of 2H edges (i.e., α and β) and 1T' edges (i.e., C and T) are indicated on the side views. (c) The relaxed configurations of the twelve 2H/1T' phase boundaries examined, named following the convention suggested by Zhao et al. [43]. (d) The top

and side views of a representative ZZ phase boundary, $ZZMo - \alpha - C| -$ embedded in a nanoribbon model with 2H and 1T' edges at each side, and an AC phase boundary $AC| +$ embedded in a periodic sheet model. 65

Fig. 4.2 Formation energies of the phase boundaries as functions of the chemical potential of Te, μTe 68

Fig. 4.3 (a), (c) Adsorption sites of $ZZMo - \alpha - C| -$ and $ZZMo - \beta - T| +$ phase boundaries respectively. Adsorption sites are labeled by as Hollow (HL), Mo, and Te categories, respectively. (b), (d) ΔGH values of $ZZMo - \alpha - C| -$ and $ZZMo - \beta - T| +$ phase boundaries, compared with the respective adsorption energies on pristine $MoTe_2$ at the representative hydrogen coverage of 50%. For Mo2 or Mo5 site, there exist two corresponding sites, in either pristine 2H or 1T' $MoTe_2$ lattice, and we only presented the pristine lattice site of lower ΔG_H here for comparison. (e) Volcano plot between the theoretical exchange current density i_0 and Gibbs free energy ΔGH . (f) ΔGH as a function of hydrogen coverage for three sites, HL1, Mo2 and Te1. 73

Fig. 4.4 (a) DOS of two representative Te atoms for H adsorption sites. The symbol “+” labels the position of Fermi-abundance center (DF). (b) Relationship between DF values and ΔGH for Te atoms. 79

Fig. 4.5 Charge distribution contour plots for hydrogen adsorption sites (a) Te1, (b) Mo1 and (c) HL1 sites at the $MoTe_2$ phase boundary. The yellow and cyan surfaces correspond to gain and loss of charge respectively, with isosurface of $0.003e/\text{\AA}^3$. (d) DOS plots for Te and Mo atoms respectively (top panel) before hydrogen adsorption, (second panel) after hydrogen adsorption on Te1 site, (third panel) after hydrogen adsorption at the Mo1 site, and (bottom panel) after hydrogen adsorption at the HL1 site. 79

Fig. 4.6 Projected DOS (pDOS) plots for the d orbitals of the Mo1 atom along the $MoTe_2$ phase boundary, (top panel) before adsorption, after adsorption on Mo1 site, and after adsorption on HL1 site. Black arrow indicates the reinforcing states of d_{xy} and $d_{x^2 - y^2}$ orbitals near the Fermi level. 80

Fig. 4.7 Benchmark studies of the possible effect, induced by edge-edge and edge-boundary interactions, on the formation energy E_f of the phase boundary $ZZMo - \beta - T| +$ and the Gibbs free energy of adsorption ΔGH as functions of the number (n) of unit cells in each phase. E_f was calculated under Te-rich condition ($\mu Te = -3.14 eV$), and the hydrogen coverage in benchmark studies was set as 1. 82

Fig. 4.8 Total density of states (DOS) of pristine 2H $MoTe_2$ and pristine 1T' $MoTe_2$, obtained from calculations using GGA-PBE [48] (red) and HSE06 [50] (blue) functionals. 83

Fig. 4.9 (a), (b) Simulation cells of 2H $MoTe_2$ nanoribbon and 1T' $MoTe_2$ nanoribbon respectively. (c) Top views of quantum dot n , using $n = 5$ and $n = 11$ as representatives. (d) Linear fitting of fn (see Eq. (4.13)) as a function of n 85

- Fig. 4.10** (a) Top and side views of pristine 2H and 1T' MoTe₂, where the black arrow indicates the Mo-Te bond length of pristine 2H MoTe₂, while blue, green, orange and yellow arrows indicate various Mo-Te bonds length of pristine 1T' MoTe₂. (b) Top and side views of representative ZZ phase boundaries. For each phase boundary configuration, black and blue arrows indicate the longest and shortest Mo-Te bonds at the phase boundary, respectively..... 86
- Fig. 4.11** (a) The potential energy (blue curve, left vertical axis) and temperature (red curve, right vertical axis) of MoTe₂ boundaries with simulation time. (b) Snapshots of configurations of $ZZMo - \alpha - C| -$ and $ZZMo - \beta - T| +$ boundaries at room temperature (300K). 87
- Fig. 4.12** (a), (b), (c) The hydrogen adsorption configurations for HL1, HL2 and the pristine MoTe₂. 88
- Fig. 4.13** Adsorption sites of pristine 2H and 1T' MoTe₂. Adsorption sites are categorized into hollow (HL), Mo, and Te sites respectively, and labelled accordingly. 89
- Fig. 4.14** Free energy diagram of the HER following (a) the Volmer-Heyrovsky pathway and (b) the Volmer-Tafel pathway at HL1, Mo2, and Te1 sites along the MoTe₂ phase boundaries..... 90
- Fig. 4.15** (a) Side view of a double-layered MoTe₂ nanosheet containing phase boundaries in each layer, where Mo atoms are colored purple and Te atoms are colored brown. The three adsorption sites, selected as representatives and labeled as HL1, Mo2, and Te1, are indicated in the figure. (b) ΔG_H values at those sites in single-layered and double-layered MoTe₂. 91
- Fig. 4.16** (a) Representative adsorption sites in the TMDC phase boundary, labeled as HL1, M1 (metal site), and X1 (chalcogen site) respectively, as well as (b) their corresponding counterparts in the pristine TMDC basal plane, labeled as pris HL1, pris M1 (metal site), and pris X1 (chalcogen site) respectively. (c) ΔG_H values of X1, HL, M1 sites at MoSe₂, WTe₂, MoTe₂ phase boundaries, and at their corresponding counterparts in pristine TMDC basal planes. 92
- Fig. 4.17** Corresponding DOS plots of different Te sites (locations and configurations of those sites, please see Fig. 4.3(a) and (c)). The symbol “+” labels the position of Fermi-abundance center (*DF*). 93
- Fig. 4.18** Calculated (a) *DF* and (b) d-band center of various Mo sites versus the corresponding ΔGH values. 94
- Fig. 4.19** Charge distribution at various Te sites in MoTe₂ phase boundaries. 95
- Fig. 4.20** Charge distribution at Mo and HL sites in MoTe₂ phase boundaries. 96
- Fig. 4.21** DOS of Mo sites in phase boundaries in comparison with the Mo site in pristine MoTe₂ sites (locations and configurations of those sites, please see Fig. 4.3(a), (c) and Fig. 4.10). 97
- Fig. 4.22** Projected DOS (pDOS) plot for the d orbitals of the Mo2 atom along the MoTe₂ phase boundary, (top panel) before adsorption, after adsorption on Mo2 site, and after adsorption on HL1

site. Black arrow indicates the reinforcing states of dxy and $dx^2 - y^2$ orbitals near the Fermi level..... 98

Fig. 5.1 (a) Template adsorption configuration of hydrogen on a 2D TMDC sheet, where transition metal ($M=Cr, Mo, W, V, Nb, Ta, Ti, Zr$ or Hf) and chalcogen atoms ($X = S, Se$) are indicated by cyan and yellow spheres, while the hydrogen atom is shown in white. (b) Workflow for predicting ΔG_H and stability via machine learning. 111

Fig. 5.2 (a) The normalized distribution of the DFT-calculated ΔG_H for hydrogen adsorption on MS_2 and MSe_2 respectively. Dashed lines indicate the 0.1 eV range around the optimal ΔG_H value of 0 eV. (b) Prediction performance of the training set and the test set for ΔG_H prediction. (c) The fraction of the DFT-calculated stable and unstable alloys for MS_2 and MSe_2 respectively. (d) Prediction performance of the training set and the test set for stability prediction. 112

Fig. 5.3 (a)-(h) Machine learning predictions for ΔG_H of 8 representative TMDC ternary alloys at different concentrations. Black dash lines indicate the optimal ΔG_H to achieve best HER performance. 116

Fig. 5.4 HER activity heatmaps for MS_2 alloys showing (a) the fraction of adsorption sites of ΔG_H within the optimal range of (-0.1,0.1) eV for each alloy, and (b) the fraction of adsorption sites that are both stable and have optimal ΔG_H for each MS_2 alloy. The number indicates the fraction value an alloy exhibits, which is also reflected by the color. 117

Fig. 5.5 (a) Relationship between ϵ_p values and ΔG_H for MS_2 and MSe_2 . (b) ϵ_p of the adsorption sites in $Mo_{(1-x)}V_xS_2$ and $W_{(1-x)}V_xSe_2$ alloys with the best (lowest) ΔG_H as a function of the composition (i.e., atomic fraction of V)..... 121

Fig. 5.6 (a) The evolution of composition-weighted average of ϵ_p at the VD, CEX, and SR steps. (b) Representative hydrogen adsorption configurations on $W_{0.22}V_{0.78}S_2$ and $W_{0.78}V_{0.22}S_2$ alloys, with related charge density difference maps of metal atoms at the vicinity of the adsorption site. Atoms are colored according to the follows: V (red), W (grey), S (yellow), and hydrogen (pink). The black cross symbol in charge density difference maps indicate the center of the metal atom (W or V)..... 121

Fig. 5.7 Lowest ΔG_H values for hydrogen adsorption on $W_{(1-x)}V_xS_2$ as the composition (x) varies. The insets illustrate sample adsorption configurations yielding the lowest ΔG_H . V, W, S and hydrogen atoms are shown in red, grey, yellow, and pink respectively. 122

Fig. 5.8 (a) The normalized distribution of the DFT-calculated ΔG_H for the training and testing set, respectively. (b) The distribution of alloy types for the training and testing set for ΔG_H prediction. 128

Fig. 5.9 (a) The distribution of stability of alloys for the training and testing set. (b) The distribution of alloy types for the training and testing set for stability prediction. 128

| | |
|--|-----|
| Fig. 5.10 Error metrics vs. size of training set or testing set for the prediction of (a) ΔG_H and (b) stability of 2D TMDC alloys. | 130 |
| Fig. 5.11 Illustration of feature vector assignment. Alloy structures are reduced to numerical representations. | 131 |
| Fig. 5.12 Machine learning predicted ΔG_H values of TMDC ternary alloys at different concentrations. Black dash lines indicate the optimal ΔG_H desirable for HER..... | 132 |
| Fig. 5.13 Machine learning predicted ΔG_H values of TMDC ternary alloys at different concentrations. Black dash lines indicate the optimal ΔG_H desirable for HER..... | 133 |
| Fig. 5.14 Machine learning predicted ΔG_H values of TMDC ternary alloys at different concentrations. Black dash lines indicate the optimal ΔG_H desirable for HER..... | 134 |
| Fig. 5.15 Machine learning predicted ΔG_H values of TMDC ternary alloys at different concentrations. Black dash lines indicate the optimal ΔG_H desirable for HER..... | 135 |
| Fig. 5.16 Machine learning predicted ΔG_H values of TMDC ternary alloys at different concentrations. Black dash lines indicate the optimal ΔG_H desirable for HER..... | 136 |
| Fig. 5.17 Machine learning predicted ΔG_H values of TMDC ternary alloys at different concentrations. Black dash lines indicate the optimal ΔG_H desirable for HER..... | 137 |
| Fig. 5.18 HER activity heatmaps for MSe ₂ alloys showing (a) the fraction of adsorption sites of ΔG_H within the optimal range of (-0.1,0.1) eV for each alloy, and (b) the fraction of adsorption sites that are stable and have optimal ΔG_H for each MSe ₂ alloy. The number indicates the fraction value an alloy exhibits, which is also reflected by the color. | 138 |
| Fig. 5.19 HER activity heatmap for MS ₂ alloys showing the fraction of adsorption sites that are stable and have optimal ΔG_H for each alloy at different concentrations. The number indicates the fraction value an alloy exhibits, which is also reflected by the color. | 139 |
| Fig. 5.20 p-band center ϵ_p vs. concentration x plots for all adsorption sites in (a) Mo _(1-x) V _x S ₂ and (b) W _(1-x) V _x Se ₂ . Green solid points here highlight the adsorption sites with the best (lowest) ΔG_H at each concentration..... | 140 |
| Fig. 5.21 Example hydrogen adsorption configurations on six representative TMDC alloys, where S atoms, Se atoms and H atoms are colored yellow, green, and pink respectively. | 140 |
| Fig. 6.1 The top and side views of monolayer III nitrides, where Ga, Al and N atoms are shown in green, blue and grey, respectively..... | 154 |
| Fig. 6.2 (a) DFT calculated and cluster expansion fitted results for the formation enthalpies ΔH of Ga _(1-x) Al _x N at different concentration. The ΔH values of ground structures are shown in black solid line, and ΔH values of random alloys generated using special quasi-random structure (SQS) method are shown in blue dash line. (b) effective cluster interaction (ECI) J_α for cluster figures, | |

i.e., pairs and triplets, as a function of cluster diameter. (c) Atomic configurations of SQS structures at different concentration, where Ga, Al and N atoms are shown in green, blue and grey. 155

Fig. 6.3 Free energies of mixing for $\text{Ga}_{(1-x)}\text{Al}_x\text{N}$ random alloys vs. concentration x under different temperatures..... 155

Fig. 6.4 (a) Band gap E of $\text{Ga}_{(1-x)}\text{Al}_x\text{N}$ random alloys as a function of concentration x . (b) The VBM and CBM positions of $\text{Ga}_{(1-x)}\text{Al}_x\text{N}$ random alloys as a function of concentration x 157

Fig. 6.5 (a) Band gap values of GaN, AlN and $\text{Ga}_{(1-x)}\text{Al}_x\text{N}$ random alloy as a function of strain. (b) The VBM and CBM positions of GaN, AlN and $\text{Ga}_{(1-x)}\text{Al}_x\text{N}$ random alloy as a function of strain. Black dash lines indicate the position of potentials of oxidation ($\text{O}_2/\text{H}_2\text{O}$) and reduction (H^+/H_2) at pH 0 for water splitting. 158

Fig. 6.6 (a) Atomic configurations of hydrogen adsorption on GaN, AlN and $\text{Ga}_{0.5}\text{Al}_{0.5}\text{N}$, where Ga, Al, N and H atoms are shown in green, blue, grey and pink. (b) Calculated ΔG_{H} for $\text{Ga}_{0.5}\text{Al}_{0.5}\text{N}$ random alloy under tensile strain. 160

Fig. 6.7 Top views of optimized geometries of five representative $\text{Ga}_{(1-x)}\text{Al}_x\text{N}$ alloys generated by ATAT code. Ga, Al and N atoms are shown in green, blue and grey, respectively. 162

Fig. 6.8 Phonon dispersion curves for 2D GaN, AlN and 2×2 $\text{Ga}_{0.5}\text{Al}_{0.5}\text{N}$, respectively. Corresponding atomic structures are shown in each plot. 163

Fig. 6.9 Lattice constant a of $\text{Ga}_{(1-x)}\text{Al}_x\text{N}$ random alloys as a function of concentration x 163

Fig. 6.10 (a) Band gap E of 2×2 $\text{Ga}_{(1-x)}\text{Al}_x\text{N}$ ordered alloys as a function of concentration x . (b) The top views of 2×2 $\text{Ga}_{(1-x)}\text{Al}_x\text{N}$ ordered alloys used for band gap calculations. 164

Fig. 7.1 (a) Top and side views of the hollow sites at the phase boundaries of 2D TMDCs, where transition metals ($\text{M} = \text{Mo}, \text{W}, \text{Cr}, \text{and V}$) and chalcogens ($\text{X} = \text{S}, \text{Se}, \text{and Te}$) are shown in purple and green. (b) ΔG_{H} of the hollow sites of various 2D TMDC phase boundaries. 170

Fig. 7.2 DFT calculated and cluster expansion fitted results for the formation enthalpies ΔH of (a) $2\text{H Mo}_{(1-x)}\text{W}_x\text{Te}_2$, (b) $2\text{H WSe}_{2(1-x)}\text{Te}_{2x}$, (c) $1\text{T}' \text{Mo}_{(1-x)}\text{W}_x\text{Te}_2$, and (d) $1\text{T}' \text{WSe}_{2(1-x)}\text{Te}_{2x}$ at different concentration. The ΔH values of ground structures are shown in blue solid line, and ΔH values of random alloys generated using special quasi-random structure (SQS) method are shown in black dash line. 174

Fig. 7.3 Schematic of phase boundaries in 2D $\text{Mo}_{(1-x)}\text{W}_x\text{Te}_2$ alloys, where Mo, W and Te atoms are shown in purple, grey and brown. The black dash line indicates the phase boundary line. . 174

Fig. 7.4 Calculated (a) p-band center, (b) modified p-band center and (c) Fermi-abundance (D_{F}) values of various Te sites with respect to ΔG_{H} values..... 177

List of Tables

| | |
|--|-----|
| Table 4.1 ΔG_H values for different hollow sites..... | 88 |
| Table 5.1 Gibbs free energies of hydrogen adsorption on pristine MX_2 | 130 |

List of Abbreviations

| | |
|--------------|--|
| 2D | Two-dimensional |
| 3D | Three-dimensional |
| CE | Cluster expansion |
| DFT | Density functional theory |
| HER | Hydrogen evolution reaction |
| ML | Machine learning |
| TMDC | Transition metal dichalcogenide |
| ΔG_H | Gibbs free energy of hydrogen adsorption |

Chapter 1 : Introduction

Renewable energy conversion plays an important role in the clean energy economy. The energy converted from the environment, such as wind, heat, and sunlight can be utilized for the electrolysis of water to produce hydrogen [1], which is one of the cleanest fuels showing great potential in replacing fossil fuels [2, 3]. To facilitate the water splitting process, the development of earth-abundant materials for catalyzing hydrogen evolution reaction (HER) is of great importance [4, 5]. Among various candidate materials in different dimensionalities, two-dimensional (2D) materials with fascinating properties have received sustainable attention. [6-8].

2D materials are defined as atomically thin crystalline solids. Since the isolation of graphene in 2004 [9], the family of 2D materials keeps growing every year and features thousands of 2D materials [10], including transition metal dichalcogenides (TMDCs), hexagonal boron nitride (h-BN), 2D group III-nitrides (2D III-nitrides), black phosphorus (BP) and etc. [11-17]. These 2D materials possess novel properties distinct from their bulk counterparts due to quantum confinement [18]. Particularly, their intrinsically large specific surface area makes them good candidates for catalysis [19]. One important class of 2D materials, 2D TMDCs (e.g., MoS₂, WSe₂ and MoTe₂) are receiving increasing attention over the years and have been synthesized via several methods, including mechanical exfoliation, chemical exfoliation, and chemical vapor deposition [20-22]. They possess effective catalytic sites in the edges and exhibit band edge positions ideal for photocatalytic HER [19, 23, 24]. Additionally, the electronic and catalytic properties of 2D TMDCs vary with different phases and different combinations of transition metals and chalcogens, which allow the tuning of their HER performance [25-27]. Recently, another new group of 2D materials, 2D III-nitrides was synthesized via graphene encapsulation [28]. First-principles calculations show that 2D III-nitrides (e.g., 2D GaN and AlN) possess excellent electronic

properties, suitable band edge positions, and good adsorption abilities that could probably promote water splitting [16, 29-32].

Despite those advantages favoring HER, the catalytic performance of 2D materials is still lower than that of Pt-based catalysts [33]. The low HER activity mainly originates from the low density of active sites due to the inertness of the basal plane of 2D materials. To address this limitation, several strategies for activating the basal plane have been proposed, including defect engineering, phase engineering, strain engineering, doping, alloying and etc. [34-38]. Among various strategies, introducing phase boundaries and alloying have shown great potential, but research work in these two fields is rather scarce. Consequently, knowledge regarding the role of phase boundaries and alloys in 2D materials for catalyzing HER remains largely absent.

The main theme of this thesis is to computationally explore phase boundaries and alloys in 2D materials, and to understand their role in catalyzing HER, with emphasis focused on two important classes of 2D materials, i.e., 2D TMDCs and 2D III-nitrides (Fig. 1.1). The specific objectives of the thesis are as follows:

1. Examine the structural stabilities and HER performance of phase boundaries in 2D MoTe₂.
2. Elucidate the mechanisms underlying enhanced hydrogen adsorption at phase boundaries of 2D MoTe₂.
3. Develop a machine learning workflow to accurately predict the HER activities and thermodynamic stabilities of ternary 2D TMDC alloys.
4. Clarify the important mechanism underlying the alloying-induced basal plane activation for HER.
5. Investigate the structural, electronic, and chemical properties of 2D Ga_(1-x)Al_xN alloys and their potential applications in water splitting.

The results obtained from the above objectives are discussed in Chapters 4-6 in detail. To be specific:

1. Chapter 4 studied 2H/1T' phase boundaries in monolayer MoTe₂ for catalyzing HER using first-principles calculations. The structural stabilities of possible phase boundary configurations were examined, and potential catalytic centers at the phase boundaries were identified. Enhanced HER activities in MoTe₂ by introducing phase boundaries were demonstrated, and the underlying HER mechanisms were understood, strongly dependent on the local hydrogen adsorption geometry and electronic structures.
2. Chapter 5 investigated 2D cation-mixed TMDC alloys for activating the basal plane for HER using first-principles calculations in conjunction with machine learning models. Successful basal plane activation via alloying was observed in various 2D TMDCs. High throughput screenings were performed on HER activities and thermodynamic stabilities of 2D TMDC alloys. Alloying effects in enhancing the HER performance in the basal plane were clarified via band center theory and local charge distribution.
3. Chapter 6 studied the properties of monolayer Ga_(1-x)Al_xN alloys employing first-principles calculations and cluster expansion method. The thermodynamic stability and atomic arrangements of 2D Ga_(1-x)Al_xN alloys were revealed. The electronic properties and chemical properties of alloys were found to be tunable by varying chemical compositions and strain, making them good candidates as photocatalysts for water splitting.

Strategies for Basal plane activation of 2D materials for HER

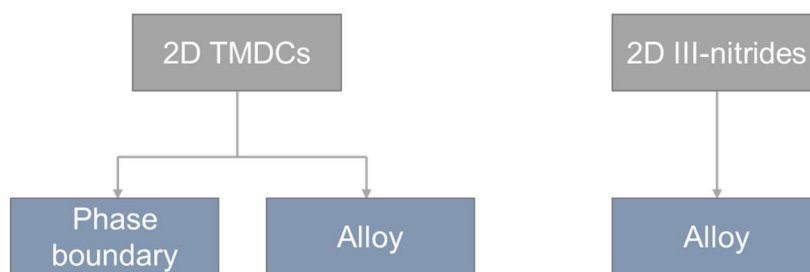


Fig. 1.1 Overview of the objectives of this thesis.

1.1 References

- [1] S. Chu, A. Majumdar, Opportunities and challenges for a sustainable energy future, *Nature* 488(7411) (2012) 294-303.
- [2] M.S. Dresselhaus, I.L. Thomas, Alternative energy technologies, *Nature* 414(6861) (2001) 332-337.
- [3] X. Ren, H. Fan, C. Wang, J. Ma, H. Li, M. Zhang, S. Lei, W. Wang, Wind energy harvester based on coaxial rotatory freestanding triboelectric nanogenerators for self-powered water splitting, *Nano Energy* 50 (2018) 562-570.
- [4] Z.W. Seh, J. Kibsgaard, C.F. Dickens, I. Chorkendorff, J.K. Nørskov, T.F. Jaramillo, Combining theory and experiment in electrocatalysis: Insights into materials design, *Science* 355(6321) (2017) eaad4998.
- [5] Y. Jiao, Y. Zheng, M. Jaroniec, S.Z. Qiao, Design of electrocatalysts for oxygen- and hydrogen-involving energy conversion reactions, *Chem Soc Rev* 44(8) (2015) 2060-86.
- [6] Y. Chen, K. Yang, B. Jiang, J. Li, M. Zeng, L. Fu, Emerging two-dimensional nanomaterials for electrochemical hydrogen evolution, *Journal of Materials Chemistry A* 5(18) (2017) 8187-8208.
- [7] S. Jayabal, G. Saranya, J. Wu, Y. Liu, D. Geng, X. Meng, Understanding the high-electrocatalytic performance of two-dimensional MoS₂ nanosheets and their composite materials, *Journal of Materials Chemistry A* 5(47) (2017) 24540-24563.
- [8] X. Chia, M. Pumera, Layered transition metal dichalcogenide electrochemistry: journey across the periodic table, *Chem Soc Rev* 47(15) (2018) 5602-5613.
- [9] K.S. Novoselov, A.K. Geim, S.V. Morozov, D. Jiang, Y. Zhang, S.V. Dubonos, I.V. Grigorieva, A.A. Firsov, Electric Field Effect in Atomically Thin Carbon Films, *Science* 306(5696) (2004) 666-669.
- [10] M. Gjerding, A. Taghizadeh, A. Rasmussen, S. Ali, F. Bertoldo, T. Deilmann, U. Holguin, N. Knøsgaard, M. Kruse, S. Manti, Recent progress of the computational 2D materials database (C2DB), *arXiv preprint arXiv:2102.03029* (2021).
- [11] A. Splendiani, L. Sun, Y. Zhang, T. Li, J. Kim, C.-Y. Chim, G. Galli, F. Wang, Emerging Photoluminescence in Monolayer MoS₂, *Nano Letters* 10(4) (2010) 1271-1275.

- [12] S. Tongay, J. Zhou, C. Ataca, K. Lo, T.S. Matthews, J. Li, J.C. Grossman, J. Wu, Thermally Driven Crossover from Indirect toward Direct Bandgap in 2D Semiconductors: MoSe₂ versus MoS₂, *Nano Letters* 12(11) (2012) 5576-5580.
- [13] L. Song, L. Ci, H. Lu, P.B. Sorokin, C. Jin, J. Ni, A.G. Kvashnin, D.G. Kvashnin, J. Lou, B.I. Yakobson, P.M. Ajayan, Large Scale Growth and Characterization of Atomic Hexagonal Boron Nitride Layers, *Nano Letters* 10(8) (2010) 3209-3215.
- [14] P. Vogt, P. De Padova, C. Quaresima, J. Avila, E. Frantzeskakis, M.C. Asensio, A. Resta, B. Ealet, G. Le Lay, Silicene: Compelling Experimental Evidence for Graphenelike Two-Dimensional Silicon, *Physical Review Letters* 108(15) (2012) 155501.
- [15] L. Li, Y. Yu, G.J. Ye, Q. Ge, X. Ou, H. Wu, D. Feng, X.H. Chen, Y. Zhang, Black phosphorus field-effect transistors, *Nature Nanotechnology* 9 (2014) 372.
- [16] Z. Huang, T.-Y. Lü, H.-Q. Wang, S.-W. Yang, J.-C. Zheng, Electronic and thermoelectric properties of the group-III nitrides (BN, AlN and GaN) atomic sheets under biaxial strains, *Computational Materials Science* 130 (2017) 232-241.
- [17] D. Kecik, A. Onen, M. Konuk, E. Gürbüz, F. Ersan, S. Cahangirov, E. Aktürk, E. Durgun, S. Ciraci, Fundamentals, progress, and future directions of nitride-based semiconductors and their composites in two-dimensional limit: A first-principles perspective to recent synthesis, *Applied Physics Reviews* 5(1) (2018).
- [18] J. Hu, Z. Guo, P.E. McWilliams, J.E. Darges, D.L. Druffel, A.M. Moran, S.C. Warren, Band Gap Engineering in a 2D Material for Solar-to-Chemical Energy Conversion, *Nano Letters* 16(1) (2016) 74-79.
- [19] B. Peng, P.K. Ang, K.P. Loh, Two-dimensional dichalcogenides for light-harvesting applications, *Nano Today* 10(2) (2015) 128-137.
- [20] V. Nicolosi, M. Chhowalla, M.G. Kanatzidis, M.S. Strano, J.N. Coleman, Liquid Exfoliation of Layered Materials, *Science* 340(6139) (2013).
- [21] X. Zhang, Z. Jin, L. Wang, J.A. Hachtel, E. Villarreal, Z. Wang, T. Ha, Y. Nakanishi, C.S. Tiwary, J. Lai, L. Dong, J. Yang, R. Vajtai, E. Ringe, J.C. Idrobo, B.I. Yakobson, J. Lou, V. Gambin, R. Koltun, P.M. Ajayan, Low Contact Barrier in 2H/1T' MoTe₂ In-Plane Heterostructure Synthesized by Chemical Vapor Deposition, *ACS Appl Mater Interfaces* 11(13) (2019) 12777-12785.
- [22] X. Hong, J. Kim, S.-F. Shi, Y. Zhang, C. Jin, Y. Sun, S. Tongay, J. Wu, Y. Zhang, F. Wang, Ultrafast charge transfer in atomically thin MoS₂/WS₂ heterostructures, *Nature Nanotechnology* 9(9) (2014) 682-686.
- [23] J. Bonde, P.G. Moses, T.F. Jaramillo, J.K. Nørskov, I. Chorkendorff, Hydrogen evolution on nano-particulate transition metal sulfides, *Faraday Discussions* 140(0) (2009) 219-231.
- [24] C. Tsai, K. Chan, F. Abild-Pedersen, J.K. Nørskov, Active edge sites in MoSe₂ and WSe₂ catalysts for the hydrogen evolution reaction: a density functional study, *Phys Chem Chem Phys* 16(26) (2014) 13156-64.
- [25] G. Eda, H. Yamaguchi, D. Voiry, T. Fujita, M. Chen, M. Chhowalla, Photoluminescence from Chemically Exfoliated MoS₂, *Nano Letters* 11(12) (2011) 5111-5116.
- [26] Y.C. Lin, D.O. Dumcenco, Y.S. Huang, K. Suenaga, Atomic mechanism of the semiconducting-to-metallic phase transition in single-layered MoS₂, *Nat Nanotechnol* 9(5) (2014) 391-6.
- [27] S. Kretschmer, H.P. Komsa, P. Boggild, A.V. Krashennnikov, Structural Transformations in Two-Dimensional Transition-Metal Dichalcogenide MoS₂ under an Electron Beam: Insights from First-Principles Calculations, *J Phys Chem Lett* 8(13) (2017) 3061-3067.

- [28] Z.Y. Al Balushi, K. Wang, R.K. Ghosh, R.A. Vilá, S.M. Eichfeld, J.D. Caldwell, X. Qin, Y.-C. Lin, P.A. DeSario, G. Stone, S. Subramanian, D.F. Paul, R.M. Wallace, S. Datta, Joan M. Redwing, J.A. Robinson, Two-dimensional gallium nitride realized via graphene encapsulation, *Nature Materials* 15(11) (2016) 1166-1171.
- [29] K. Ren, J. Yu, W. Tang, A two-dimensional vertical van der Waals heterostructure based on g-GaN and Mg(OH)₂ used as a promising photocatalyst for water splitting: A first-principles calculation, *Journal of Applied Physics* 126(6) (2019) 065701.
- [30] M. Kanli, A. Onen, A. Mogulkoc, E. Durgun, Characterization of two-dimensional Ga_{1-x}Al_xN ordered alloys with varying chemical composition, *Computational Materials Science* 167 (2019) 13-18.
- [31] H. Shu, X. Niu, X. Ding, Y. Wang, Effects of strain and surface modification on stability, electronic and optical properties of GaN monolayer, *Applied Surface Science* 479 (2019) 475-481.
- [32] Q. Chen, H. Hu, X. Chen, J. Wang, Tailoring band gap in GaN sheet by chemical modification and electric field: Ab initio calculations, *Applied Physics Letters* 98(5) (2011) 053102.
- [33] Z. Wang, M.T. Tang, A. Cao, K. Chan, J.K. Nørskov, Insights into the Hydrogen Evolution Reaction on 2D Transition-Metal Dichalcogenides, *The Journal of Physical Chemistry C* 126(11) (2022) 5151-5158.
- [34] H. Li, C. Tsai, A.L. Koh, L. Cai, A.W. Contryman, A.H. Fragapane, J. Zhao, H.S. Han, H.C. Manoharan, F. Abild-Pedersen, J.K. Nørskov, X. Zheng, Activating and optimizing MoS₂ basal planes for hydrogen evolution through the formation of strained sulphur vacancies, *Nature Materials* 15(1) (2016) 48-53.
- [35] X. Wang, L. Meng, B. Li, Y. Gong, Heteroatoms/molecules to tune the properties of 2D materials, *Materials Today* 47 (2021) 108-130.
- [36] D.B. Putungan, S.H. Lin, J.L. Kuo, A first-principles examination of conducting monolayer 1T'-MX₂ (M = Mo, W; X = S, Se, Te): promising catalysts for hydrogen evolution reaction and its enhancement by strain, *Phys Chem Chem Phys* 17(33) (2015) 21702-8.
- [37] J. Zhang, J. Wu, H. Guo, W. Chen, J. Yuan, U. Martinez, G. Gupta, A. Mohite, P.M. Ajayan, J. Lou, Unveiling Active Sites for the Hydrogen Evolution Reaction on Monolayer MoS₂, *Adv Mater* 29(42) (2017).
- [38] Q. Gong, L. Cheng, C. Liu, M. Zhang, Q. Feng, H. Ye, M. Zeng, L. Xie, Z. Liu, Y. Li, Ultrathin MoS₂(1-x)Se_{2x} Alloy Nanoflakes For Electrocatalytic Hydrogen Evolution Reaction, *ACS Catalysis* 5(4) (2015) 2213-2219.

Chapter 2 : Literature Review

This chapter provides an overview of recent research progress in 2D materials relevant to the work presented in the thesis. The literature review concentrates on two groups of 2D materials, i.e., 2D transition metal dichalcogenides (2D TMDCs) and 2D group III-nitrides (2D III-nitrides), and their applications in one fundamentally significant chemical reaction, hydrogen evolution reaction (HER). The contents of this chapter are arranged as follows: first, a brief introduction to 2D materials is presented, focusing on 2D TMDCs and 2D III-nitrides. This is followed by a brief overview of computational methods used in catalysis. Then, the catalytic properties of 2D materials as HER catalysts are summarized. Finally, common strategies for enhancing the HER activities of 2D materials, i.e., defect engineering and alloying are discussed.

2.1 2D materials

The 2D material revolution began with the discovery of graphene in 2004 [1]. This single layer of graphite possesses extraordinary properties such as large specific surface area, high electronic quality, superior thermal conductivity and outstanding mechanical properties [2-5], showing great potential in electronics, sensors and energy storage [6]. The graphene rush has also accelerated the discovery of numerous new 2D materials, including 2D TMDCs, black phosphorus (BP), transition metal carbides and nitrides (MXenes), 2D III-nitrides, 2D metal-organic frameworks (MOFs), etc. [7-9]. These emerging 2D materials show diverse electronic behaviors and chemical properties, largely compensating for the applications of graphene in various fields [10]. In the following subsection 2.1.1 and 2.1.2, two typical groups of 2D materials, namely 2D TMDCs and 2D III-nitrides, will be introduced as they are the main subjects of research focus in this thesis.

2.1.1 2D TMDCs

TMDCs have the chemical formula MX_2 , where M is a transition metal atom (such as Mo, W and Nb) and X is one of the chalcogens (S, Se and Te). The most famous member of TMDCs, MoS_2 , is a silvery black solid widely used as solid lubricants due to its low friction and long wear life [11]. Two-thirds of TMDC crystals have layered structures similar to graphite [12]. A typical TMDC structure comprises strongly bonded two-dimensional X-M-X layers that are loosely held together by weak van der Waals forces [12, 13]. As a result, a single layer of TMDCs can be obtained by removing one layer from their bulk counterparts. In fact, 2D TMDCs are found to be stable, and controllable and uniform TMDC layers have been synthesized via several methods, including mechanical exfoliation, chemical exfoliation, and chemical vapor deposition [14-16].

2D TMDCs can exhibit different phases. Fig. 2.1 describes the atomic configurations of four typical phases of 2D MX_2 , i.e., trigonal prismatic (2H), octahedral (1T) and distorted (1T' and 1T'') phases [17]. As shown in Fig. 2.1 (a), the 2H phase has a hexagonal symmetry (D_{3h}) with sulfur atoms in the monolayer vertically aligned along the z-direction. The 1T phase with tetragonal symmetry (D_{3d}) can be seen as a structural transformation from the 2H phase where one atomic layer of X atoms is shifted (Fig. 2.1 (b)). Further distortions in the metal atoms of the 1T structure result in the displacement of chalcogen atoms along the z-direction to form the 1T' and 1T'' phases (Fig. 2.1 (c)-(d)). The dominant phases of each 2D TMDCs are determined by the filling of d orbitals. For example, most group VI TMDCs (e.g., MoS_2 and WSe_2) have 2H phases, while group X TMDCs (e.g., PtS_2) usually have 1T phases. 2D TMDCs with different phases can lead to different applications. For instance, 2H TMDCs with semiconducting nature are attractive to electronic and optoelectronic devices, while 1T TMDCs with the active basal plane and high conductivity are ideal for electrochemical catalysts [18-20]. Phase transition has provided a viable

route to tune the properties of 2D TMDCs, and the precise phase control of 2D TMDCs has become a hot topic in research [21].

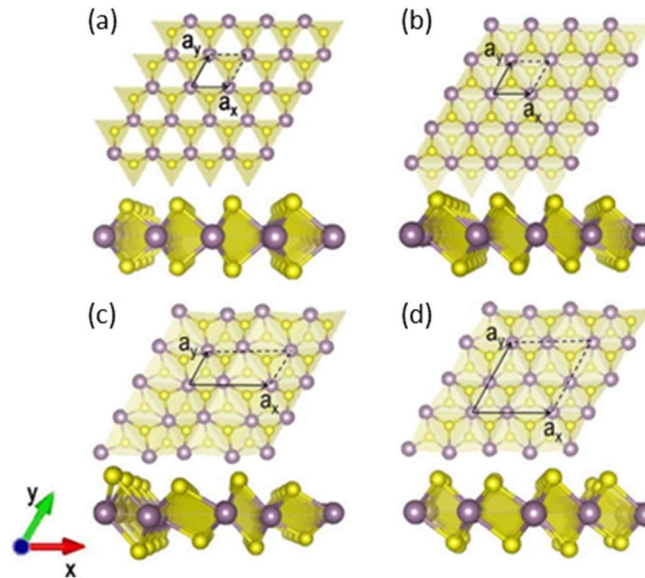


Fig. 2.1 Top and side views of atomic configurations of various TMDC phases: (a) 2H, (b) 1T, (c) 1T', and (d) 1T'' phases. Transition metal and chalcogen atoms are indicated in purple and yellow, respectively. Adapted with permission from ref. [17]. Copyright 2015 AIP Publishing.

Asides from the phase engineering, the electronic and chemical properties of 2D TMDCs can also be tuned by choosing different combinations of the M and X elements. Generally, the electronic properties of 2D TMDCs are mostly determined by the filling of d orbitals of their transition metals [22]. The fully filled d orbitals result in semiconducting behavior, while the metallic nature is attributed to the partially filled d orbitals [21]. It is worth mentioning that for 2D TMDC semiconductors, their band gap values are also affected by chalcogen atom types. The band gap of 2D TMDCs usually decrease with the increase of the atomic number of chalcogen.

One challenging issue for building high-performance graphene-based electronics is that pristine graphene is a semimetal without a band gap [23]. The advent of 2D TMDCs can successfully overcome such limitations. 2D TMDCs can achieve tunable band gaps ranging from

the visible to the infrared [24]. Particularly, group VI TMDCs show band gaps in the range of 1-2 eV, being suitable for switching nanodevices. In 2011, Single-layer MoS₂ transistors were fabricated by Radisavljevic et al. using a hafnium oxide gate dielectric (Fig. 2.2 (a)) [25]. They demonstrated the mobility of MoS₂ of at least 200 cm²·V⁻¹·s⁻¹ at room temperature, and transistors were able to control charge density in a local manner with room-temperature current on/off ratios exceeding 10⁸ (Fig. 2.2 (b)).

While bulk TMDCs are indirect band gap semiconductors, 2D TMDCs exhibit direct band gaps, which are promising for optoelectronics applications. In 2012, Yin et al. first synthesized single-layer MoS₂ phototransistor with good switching behavior and high stability (Fig. 2.2 (c)) [26]. The photoresponsivity from this device reaches 7.5 mA/W under illumination with an optical power of 80 μW and a gate voltage of 50 V (Fig. 2.2 (d)). Moreover, the unique optical properties of 2D TMDCs hold promise for applications in light harvesting. Bernardi et al. proposed bilayer solar cells using MoS₂/graphene bilayer or stacked TMDC monolayers (Fig. 2.2 (e)) [27]. Their calculations showed that these devices can attain power conversion efficiencies of up to ~1%, and a power density of up to 2.5 MW/kg.

The adsorption properties of a catalyst's surface are strongly correlated to its electronic structures. Thus, the tunability of the electronic properties of 2D TMDCs can also extend to the chemical properties. In fact, 2D TMDCs have been widely explored as catalysts for various chemical reactions, such as hydrogen evolution reaction and carbon dioxide reduction, showing much promise for photochemical and electrochemical applications [28]. This topic will be explicitly discussed in section 2.3.

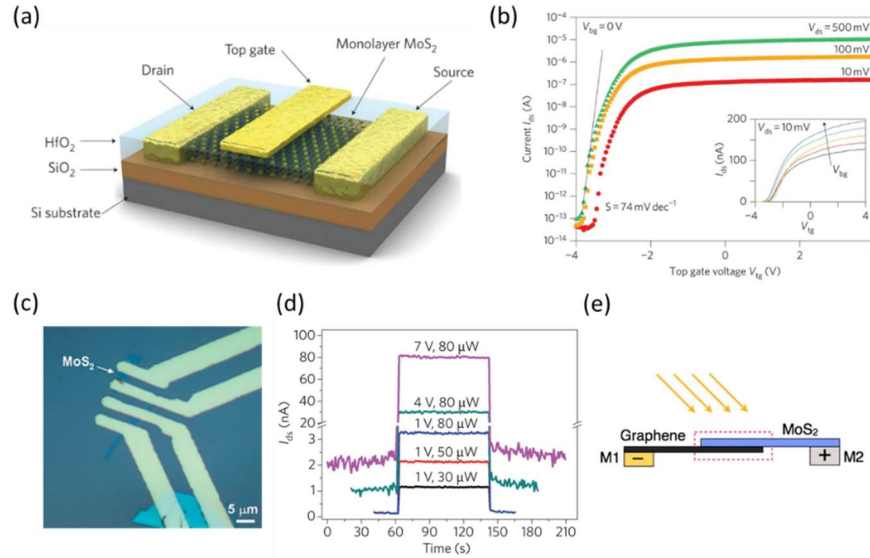


Fig. 2.2 (a) Schematic of single-layer MoS₂ transistor. (b) Source-drain current (I_{ds}) versus top gate voltage (V_{tg}) of the MoS₂ monolayer transistor recorded for a bias voltage ranging from 10 mV to 500 mV. The inset shows I_{ds} - V_{tg} for back gate voltage $V_{bg} = -10, -5, 0, 5$ and 10 V. Results obtained from experiments. Adapted with permission from ref. [25]. Copyright 2011 Springer Nature. (c) Optical image of single-layer MoS₂ phototransistor. (d) Photoswitching characteristics of single-layer MoS₂ phototransistor at different optical power (P_{light}) and drain voltage (V_{ds}). Results obtained from experiments. Adapted with permission from ref. [26]. Copyright 2012 American Chemical Society. (e) Schematic of the MoS₂/graphene solar cell. M1 and M2 indicate low and high workfunction metals, respectively. Adapted with permission from ref. [27]. Copyright 2013 American Chemical Society.

2.1.2 2D III-nitrides

Three-dimensional (3D) group III-nitrides, including AlN, GaN and InN and their alloys, are excellent wide band gap semiconductors. They possess tunable band gaps covering the whole solar spectrum from ultraviolet to infrared [29, 30], affording their excellent properties for applications in electronics, optoelectronics and photocatalysis [30-35]. Recently, their 2D allotropes have been successfully synthesized via graphene encapsulation [36], which has brought a new group of 2D materials, 2D III-nitrides into the focus of research interest.

The common formula of 2D III-nitrides is XN, where X = Al, Ga, or In. Although 3D III-nitrides do not have layered structures similar to graphite, a graphene-like hexagonal structure has

been predicted to exist in 2D III-nitrides and is the basic structure that has been extensively studied [37, 38]. As shown in Fig. 2.3 (a), in 2D hexagonal XN, all atoms remain in the same plane. N atoms in the 2D hexagonal XN are sp^2 -hybridized, and the nonbonding p_z orbitals introduce unsaturated dangling bonds on the surface, resulting in an active surface ideal for chemical reactions but also with less stability. Several theoretical studies have been performed to understand the stability of 2D hexagonal XN. For example, previous studies confirmed the stability of 2D hexagonal GaN and AlN by *ab initio* phonon calculations [39, 40]. In addition, 2D hexagonal XNs were demonstrated to be stable under thermal excitations by *ab initio* finite temperature molecular dynamics (MD) calculations performed under 1000 K [41]. Moreover, the stability of 2D hexagonal XN can be enhanced by hydrogen passivation to form a buckled structure (Fig. 2.3 (a)), which exhibits different electronic properties compared to the planar one [36]. Besides from the 2D hexagonal structures, other potential structures have been proposed by theoretical studies. Camacho-Mojica and López-Urías proposed a planar GaN structure containing square and octagonal rings, called haeckelites 8-4 or T-GaN [42]. Zhang et al. predicted a GaN porous structure possessing a large specific surface area, which is called H-GaN [43]. The atomic structures of T-GaN and H-GaN are presented in Fig. 2.3 (b)-(c). The formation energies of H-GaN and T-GaN were calculated by density functional theory (DFT) calculations, with values of 0.061 and 0.055 eV, respectively, slightly higher than that of 2D hexagonal GaN (0.042 eV) [43]. These results indicate that the 2D hexagonal structure is the most stable form of 2D III-nitrides.

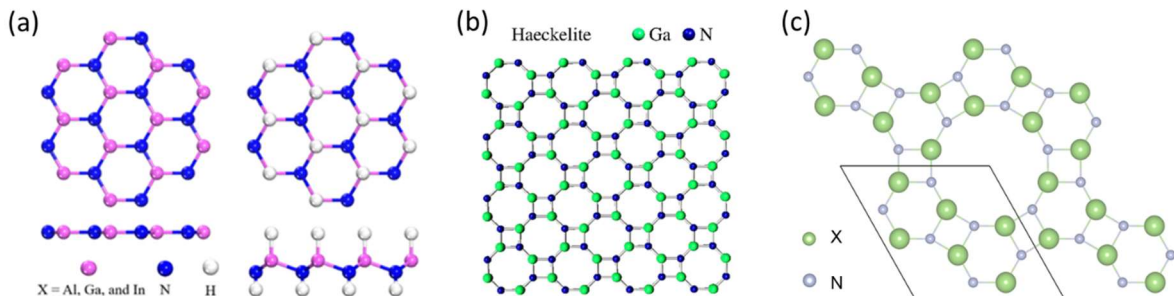


Fig. 2.3 Atomic structures of 2D XN. (a) Planar and buckled hexagonal structures. Adapted with permission from ref. [44]. Copyright 2019 American Chemical Society. (b) Haeckelite structure (T-XN) [42]. (c) porous structure (H-XN). Adapted with permission from ref. [43]. Copyright 2017 Elsevier.

2D III-nitrides have demonstrated desirable electronic and chemical properties. In particular, the band gap of 2D III-nitrides can be tailored by various methods, e.g., alloying, strain, and surface modification [37, 45-47], showing great potential for electronic or optoelectronic devices. Chen et al. constructed a field effect transistor device with 2D GaN as the dielectric layer and graphene sheets as contact layers (Fig. 2.4 (a)-(b)) [48]. The electron mobility of the 2D GaN achieved $160 \text{ cm}^2 \cdot \text{V}^{-1} \cdot \text{s}^{-1}$ with an on/off ratio of around 10^6 . Besides, the large area of active surface and suitable band gaps make 2D III-nitrides very promising for photocatalysis. Ren et. al proposed a vertical van der Waals heterostructure based on 2D hexagonal GaN and $\text{Mg}(\text{OH})_2$ as a photocatalyst for water splitting (Fig. 2.4 (c)-(d)) [49]. DFT calculations predicted that this structure has suitable band edge positions and adsorption abilities that promote water splitting. However, despite those great prior efforts, the applications of 2D III-nitrides in those fields are still in their infancy. One challenge that remains in this area is the low stability of 2D III-nitrides, which makes the synthesis process difficult [50].

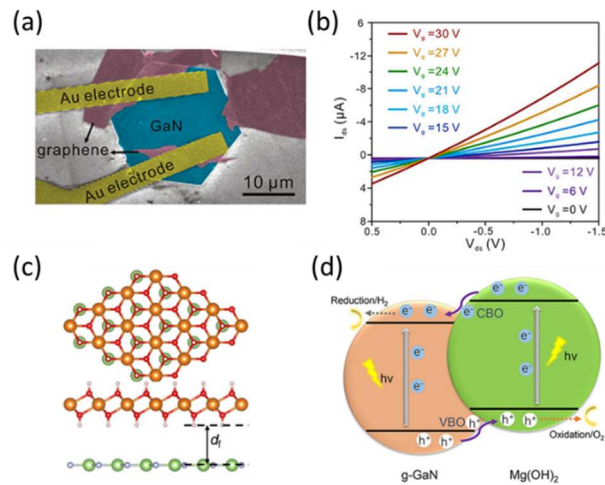


Fig. 2.4 (a) The false-colored SEM image of a 2D GaN field effect transistor. (b) Gate-dependent $I_{ds}-V_{ds}$ characteristic curves from experiments. Adapted with permission from ref. [48]. Copyright 2018 American Chemical Society. (c) Top and side views of the GaN/Mg(OH)₂ vdW heterostructure, where Ga, N, Mg, O, and H atoms are shown in green, grey, orange, red, and pink, respectively. (d) Photocatalytic mechanism for GaN/Mg(OH)₂ vdW heterostructure. Adapted with permission from ref. [49]. Copyright 2019 AIP Publishing.

2.2 Computational modeling in catalysis

Computational modeling has become increasingly critical in catalyst design thanks to the rapid growth of computing power. The utility of first-principles calculations in understanding the atomic-level reaction energetics is widely acknowledged. However, establishing a direct correlation between the macroscopic functionality and atomic-scale properties of the catalyst presents a formidable challenge. Although multiscale modeling approach that integrates electronic structure calculations and kinetic models could potentially bridge these gaps, their practical implementation necessitates high computational costs [51]. This limits their feasibility in computational catalyst design, particularly for the high-throughput screening of new catalysts. One viable method to address this challenge is to find reasonable and simple descriptors of the catalytic activity to help us identify potential catalysts and understand their activity trends [52]. This subsection provides a brief overview of the research endeavors towards developing appropriate descriptors for reactivity trends, with a specific emphasis on the hydrogen evolution reaction.

2.2.1 Sabatier principle

It is important to develop a design principle that establishes a connection between the catalytic surface property and the catalytic activity. In this regard, in 1913, Paul Sabatier first proposed a conceptual framework based on empirical observations, suggesting that an ideal catalyst must bind the adsorbates at an intermediate strength, neither too weakly nor too strongly

[53, 54]. This framework resulted in the widely renowned 'volcano plot', which depicts the relationship between activity (rate) and bond strength, as illustrated in Figure 2.5 (a). However, the concept of 'bond strength' is not clearly defined in Sabatier principle and necessitates descriptors that can best characterize the catalytic reaction. In the case of hydrogen evolution reaction, in 1957, Parsons established a similar 'volcano-type' relation between the exchange current for electrolytic HER and the Gibbs free energy of atomic hydrogen adsorption ΔG_H , proposing that ΔG_H should ideally have a value around 0 [55]. Subsequent studies combining experiments and theories further confirmed the significance of ΔG_H as a suitable descriptor for HER for a broad range of materials [52, 56].

Gibbs free energy, denoted G , is a thermodynamic potential that describes the energy available to a system to do non-volume work at constant temperature and pressure. G is minimized at chemical equilibrium and the change in G can be used to determine the spontaneity and direction of a reaction. In two-step reactions like HER, the reaction proceeds from reactant to product with only one reaction intermediate. The Gibbs free energy of intermediate formation (ΔG_{RI}) at equilibrium is thus a crucial factor in determining the activity of the reaction and is often considered as a 'descriptor' for this purpose [57]. As shown in Fig. 2.5 (b), ideal catalysts should have thermoneutral bonding to the intermediate ($\Delta G_{RI} = 0$). If the catalyst binds the intermediate too weakly ($\Delta G_{RI} > 0$)/strongly ($\Delta G_{RI} < 0$), the first/second step of the reaction is thermodynamically unfavorable, resulting in a thermodynamic overpotential to the reaction [58]. In the case of HER, the intermediate state is the chemisorption of hydrogen atoms at the surface, and this makes Gibbs free energy of hydrogen adsorption ΔG_H an effective descriptor for the reaction rate.

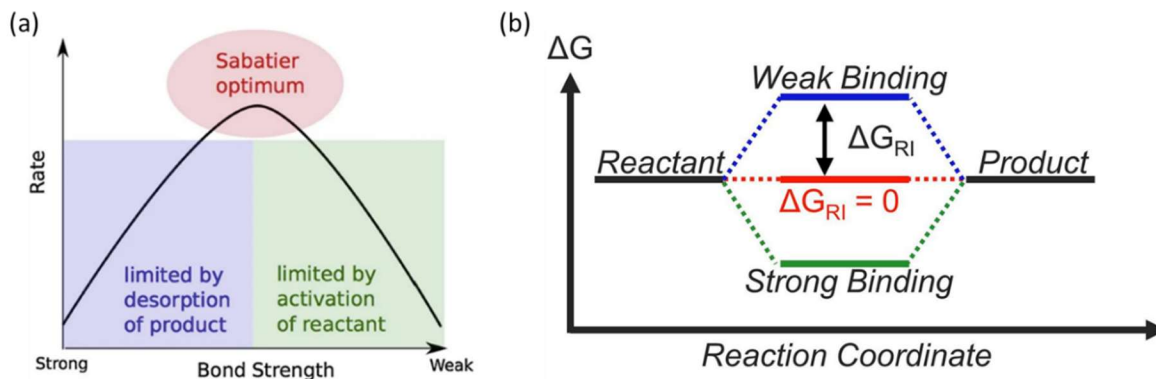


Fig. 2.5 (a) Schematic representation of the Sabatier principle. Adapted with permission from ref. [59]. Copyright 2015 Elsevier. (b) Schematic representation of the thermodynamic free-energy profile of a catalytic reaction with one reaction intermediate. Adapted with permission from ref. [60]. Copyright 2021 Ooka, Huang and Exner.

2.2.2 Computational hydrogen electrode

The free-energy profile of an electrochemical reaction at a catalyst surface can be obtained from computational methods. Typically, the Gibbs free energies of adsorbates are calculated using density functional theory (DFT), which takes into account the energy (E), zero-point energy correction (ZPE), and entropy (S). However, accurately treating the chemical potentials of electrons and protons is challenging in DFT calculations. Moreover, it is crucial to ensure that the calculated energies are aligned with the known quantities so that comparison with experimental data is possible. To address these issues, Nørskov and his colleagues developed the computational hydrogen electrode (CHE) method, which defines a coupled chemical potential of protons and electrons for simplification [58]. Standard hydrogen electrode (SHE) is first set as a reference:



The chemical potential of an electron-proton pair can then be expressed with half of the Gibbs free energy of a hydrogen molecule ($U = 0$) [58]:

$$\mu_{H^+} + \mu_{e^-} = \frac{1}{2}G_{H_2} \quad (2.2)$$

where μ_{H^+} and μ_{e^-} are the chemical potentials of protons in solution and electrons at the Fermi level at the reference electrode. With the above equation, the Gibbs free energy change in a proton-electron transferred step at any electrochemical condition can be calculated as:

$$\begin{aligned} \Delta G_{CHE}(n, U) &= \Delta E - T\Delta S + \Delta ZPE - n(\mu_{H^+} + \mu_{e^-}) \\ &= \Delta E - T\Delta S + \Delta ZPE - n\left(\frac{1}{2}G_{H_2} + eU_{RHE}\right) \\ &= \Delta E - T\Delta S + \Delta ZPE - n\left(\frac{1}{2}G_{H_2} + eU_{SHE} - 0.059pH\right) \end{aligned} \quad (2.3)$$

where n is the number of proton-electron transferred.

The CHE method has enabled both detailed investigations of reaction mechanisms and high-throughput computational screening for new catalysts [58, 61, 62]. This straightforward approach is currently the most widely used method for evaluating electrocatalytic activity *in silico* and has effectively rationalized numerous experimental trends [56, 59].

2.2.3 Limitations of the CHE method

The computational hydrogen electrode (CHE) scheme considers only potential-free neutral systems. Consequently, the effects of applied electrode potential and pH are added to the free energy as posterior corrections. Since the influence of the applied electrode potential and pH on the catalyst surface are not explicitly included in CHE, this may lead to inaccurate or erroneous results in alkaline environments [63, 64]. Recently, a new generalized computational hydrogen electrode (GCHE) has been developed to partially address these issues in electrochemical environments. It considers overall electrochemical potential as a function of applied electrostatic potential and chemical potential of protons and electrons [65-67].

Also, CHE-based calculations frequently neglected the solvation effect, which could possibly impact the stability of the charged intermediates and even change the reaction pathways [64]. The reason for this omission is due to the high computational cost of explicitly simulating solvents and treating charge in the system, as well as the difficulty in controlling the solid-liquid interface in computer simulations. Implicit solvation models can address the complexity of explicit solvation models but require careful parametrization to the specific system [51, 64]. Nonetheless, further investigations are needed to improve the accuracy of modeling the solvents.

2.3 HER performance of 2D materials

Water splitting is regarded as one of the most economical and eco-friendly approaches for hydrogen production, which is essential for the global goal towards clean energy economy and sustainability [68]. Hydrogen evolution reaction (HER) is the cathodic reaction in water splitting that yields hydrogen. An efficient catalyst is always required to facilitate the conversion from protons to hydrogen. Currently, platinum (Pt) and Pt-based materials are the most efficient catalysts for HER, but the high cost and scarcity hinder their possibility of large-scale utilization [69, 70]. The need for clean and economical energy has driven efforts to develop affordable and earth-abundant catalysts for HER. Among various materials in different dimensionalities, 2D materials, e.g., 2D TMDCs, are promising as alternatives to Pt-based catalysts since many of them contain only earth-abundant elements and are relatively active toward HER.

2D materials are promising HER catalysts with many distinct properties. Firstly, many 2D materials possess effective catalytic sites for the HER. Group VI TMDC monolayers (e.g., 2H-MoS₂ and 2H-WSe₂) has been explored as excellent HER electrocatalysts with active sites located in the edges [71, 72]. DFT calculations show that the Gibbs free energies of hydrogen adsorption

ΔG_H of those edge sites are close to the thermoneutral value near zero, indicating optimal HER activities (Fig. 2.6 (a)). Putungan et al. examined the ΔG_H in the basal plane of various 2D TMDCs by first-principles calculations [73]. The results show that the basal plane of 1T'-MoS₂ is relatively active for HER with a low ΔG_H value (Fig. 2.6 (b)). The active sites in 2D TMDCs have also been validated by experiments. Zhang et. al investigated the HER activities on the edge and the basal plane of 2H-MoS₂ and 1T'-MoS₂ using a local probe method [74]. As shown in the HER polarization curve in Fig. 2.6 (c), the HER performance of 2H-MoS₂ mainly comes from the edge sites while the contribution from the basal plane is negligible. Similar phenomenon can be observed in 1T'-MoS₂ (Fig. 2.6 (d)), except that the basal plane of 1T'-MoS₂ is more active compared to that of 2H-MoS₂ (Fig. 2.6 (e)). The catalytic performances of MoS₂ in terms of turnover frequencies (TOFs) are calculated as 3.8 and 1.6 s⁻¹ for 1T' and 2H edges, comparable to that of platinum ($\approx 1-10$ s⁻¹). Moreover, many 2D materials have suitable electronic structures for photocatalytic HER. To drive the photocatalytic water splitting, the valence band maximum (VBM) should be more negative than the oxygen reduction potential and the conduction band minimum (CBM) should be more positive than the hydrogen reduction potential. Fig. 2.6 (f) summarizes the band edge positions of 2D TMDCs. As demonstrated, many 2D TMDCs have favorable band edge positions for photocatalytic applications. 2D III-nitrides also exhibit suitable band edge positions for water splitting combining with high carrier mobility, making them ideal for photocatalysis [75]. Besides from the active sites and electronic structures, 2D materials show advantages in favor of HER as they possess ultra-large specific surface area. Thanks to the low dimensionality, the atoms in the basal plane and edges of 2D materials are maximally exposed to chemical reactions. Thus, 2D materials can provide more active sites for HER compared to their 3D counterparts. Thirdly, the properties of 2D materials can be easily tuned by stacking them together or growing them on

other substrates [7]. 2D materials can serve as building blocks for heterostructures, with different 2D materials held together by van der Waals forces. Such heterostructures consisting of several layers allow numerous combinations of 2D materials and can therefore generate materials with desirable properties for HER. Finally, 2D materials are suitable models for researchers to understand the active site-catalytic activity relationship [76]. To understand the catalytic mechanisms and guide the catalyst design, it is crucial to minimize the difference between idealized models and real catalysts. 2D materials are ideal systems to achieve this goal, as they have relatively simple structures and high fractions of active sites.

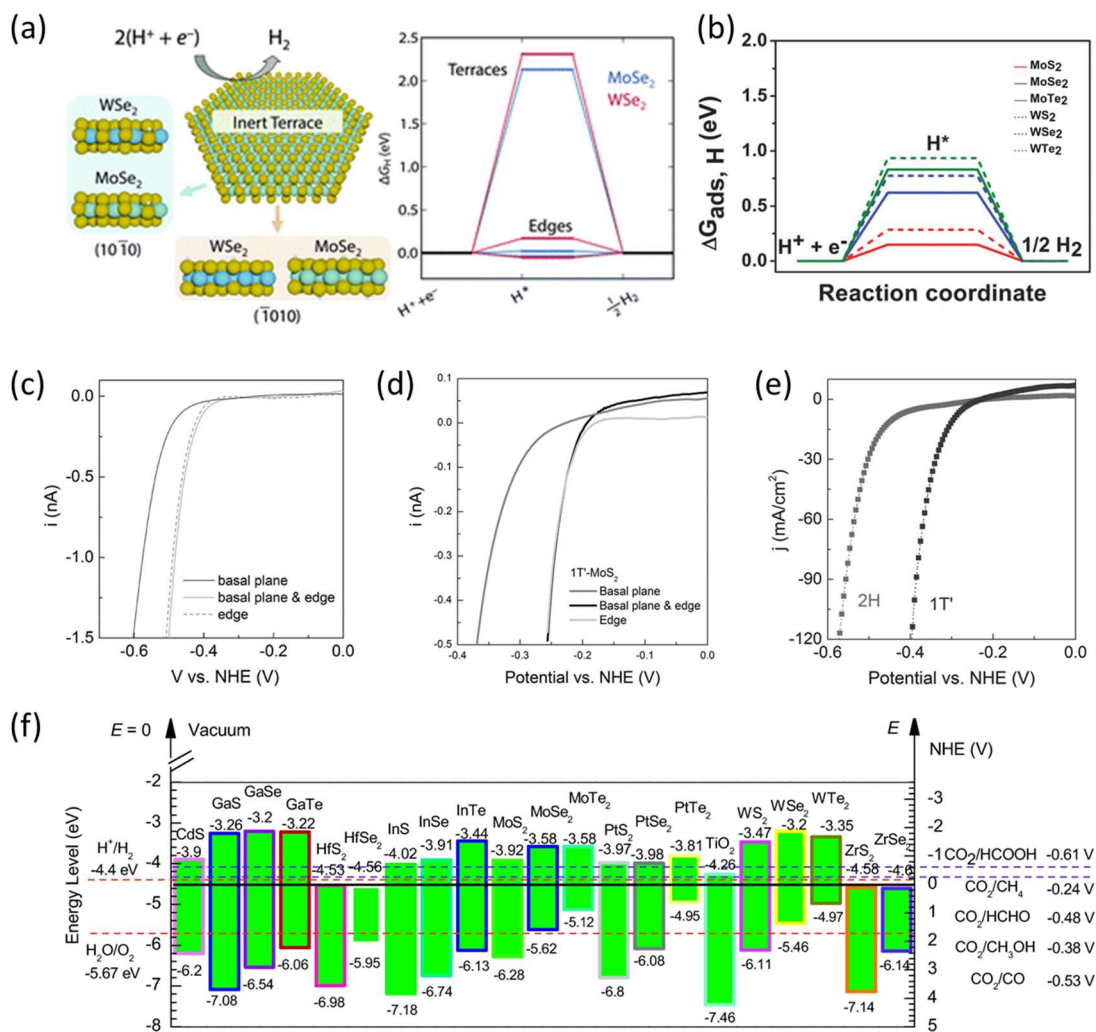


Fig. 2.6 (a) Schematics and DFT-calculated ΔG_H values of 2D TMDCs basal planes and edges. Adapted with permission from ref. [72]. Copyright 2014 Royal Society of Chemistry. (b) DFT-calculated ΔG_H values of the basal plane of 1T' TMDC monolayers. Adapted with permission from ref. [73]. Copyright 2015 Royal Society of Chemistry. (c) HER polarization curves of 2H-MoS₂ basal plane and edge sites from experiments. (d) HER polarization curves of 1T'-MoS₂ basal plane and edge sites from experiments. (e) HER polarization curves of 2H- and 1T' MoS₂ basal plane from experiments. Adapted with permission from ref. [74]. Copyright 2017 John Wiley and Sons. (f) Band edge positions of 2D TMDCs, CdS and TiO₂ relative to the vacuum level. Dash lines indicate the redox potentials, including the potentials of water splitting at pH = 0 and the potential of CO₂ reduction at pH = 7. Adapted with permission from ref. [77]. Copyright 2015 Elsevier.

In spite of those advantages favoring HER, the HER performance of 2D materials is still limited. Recent experiments show that the HER activity of 2D TMDCs is about 3 orders of magnitude lower than that of transition metals [78]. One of the main reasons related to such limitation is that most TMDC monolayers are only active for HER at edge sites, rendering large areas of the surface catalytically useless [28, 79]. Besides, benchmark studies show that the surface of free-standing 2D III-nitrides is also inert toward HER in terms of ΔG_H . To address this limitation, strategies for activating the basal plane of 2D materials are required. In addition, the low HER activity of 2D materials is also caused by unsatisfactory conductivity [80]. It is of great importance to improve the electrical conductivity of 2D materials so as to improve the overall HER performance.

2.4 Improving catalytic activities of 2D materials

The explosive popularity of 2D materials in electronics and catalytic applications does not merely attribute to the intrinsic material properties of 2D materials, but also relies on the tunability of their electronic and chemical properties. Generally, the catalytic ability of 2D materials can be improved by increasing active sites in their structures. For 2D TMDCs, the edge sites are active for HER, while the basal planes are rather inert. The HER performance of 2D TMDCs can be

improved by increasing the number of edge sites. For example, abundant edges were created by growing dendritic monolayer MoS₂ flakes on SrTiO₃, rendering excellent HER performance reflected by a Tafel slope of 73 mV/decade, outperforming regular MoS₂ flakes with the same area [81]. Besides, phase transition has been made to improve the HER activities of 2D TMDCs. 1T- and 1T'-MoS₂ have catalytically active sites in the basal plane, exhibiting better HER performance than their 2H counterparts [73, 74]. However, 1T and 1T' phases of MoS₂ are metastable, which limits their large-scale applications. Besides from creating more edge sites and phase engineering, an alternative strategy for improving the HER performance of 2D TMDCs is basal plane activation, including defect engineering, alloying, substrate engineering and strain engineering, etc. Compared to edge engineering, basal plane activation can provide a high density of active sites while retaining structural stability, providing promising routes to develop new catalysts with excellent performance and high stability. It is worth noting that the literature on 2D III-nitrides for catalytic applications is limited. Therefore, in this section, emphasis will be focused on 2D TMDCs, and two methodologies for activating the basal plane of 2D materials, i.e., defect engineering and alloying, will be discussed. Besides, substrate engineering will also be briefly discussed for the inevitable effects of substrates on the overall HER performance of 2D materials.

2.4.1 Defect engineering

Introducing defects, e.g., point defects, grain boundaries and phase boundaries, into the basal plane of 2D TMDCs has been demonstrated as an effective method to enhance HER performance. The additions of defects modify the electronic structure of 2D TMDCs to get closer to the Fermi level, thus optimizing the hydrogen binding strengths and rendering good HER activities.

The fabrication of 2D materials inevitably introduces imperfections in the structures. Point defects are the first type of defects investigated in 2D TMDCs, and recently defect-rich MoS₂ monolayers have been successfully synthesized via plasma modification [82]. Li et. al first reported basal plane activation in 2H-MoS₂ by introducing sulfur vacancies (Fig. 2.7 (a)) [82]. Theoretical results show that the introduction of S-vacancies modifies the electronic structure of 2H-MoS₂. As indicated by the band structure for 2H-MoS₂ with S-vacancy concentration of 25% (Fig. 2.7 (b)), new states occur in the gap near the Fermi level, which contribute to the enhanced hydrogen binding on the vacancy sites. The addition of S-vacancies decreases the ΔG_H of 2H-MoS₂, which can further be manipulated by adjusting the S-vacancy density. As shown in Fig. 2.7 (c), optimal ΔG_H can be achieved when the S-vacancy concentration is between 12.50 and 15.62%. These theoretical predictions were then validated by experiments, with 2H-MoS₂ with S-vacancies exhibiting higher turnover frequency than that of the pristine MoS₂. Inspired by those findings, Ouyang et al. systematically investigated the capabilities of various point defects in 2H-MoS₂ for basal plane activation [83]. Using DFT calculations, they confirmed that three types of point defects, i.e., monosulfur vacancy (V_S), vacancy complex of Mo and three sulfurs (V_{MoS_3}) and antisite defect with a Mo atom substituting an S₂ atom (MoS_2) (Fig. 2.7 (d)-(f)), can greatly improve the HER activity of 2H-MoS₂. Moreover, V_S and MoS_2 point defects show excellent HER performance in terms of Heyrovsky and Tafel reactions. The exploration of point defects for HER has also extended to other 2D TMDC system. Shu et al. conducted first-principles calculations to investigate the structural stability and HER activity on a series of MoSe₂ point defects [84]. Their results demonstrate that point defects in MoSe₂ are thermodynamically stable, and they exhibit superior HER activity than that of the corresponding structures in MoS₂. The point defects in MoSe₂ and their HER activities have been explored experimentally by Truong et al. [85]. The

successful formation of various vacancies in the exfoliated MoSe₂ nanosheets was confirmed by high angle annular dark field (HAADF) imaging. Those defects are found to favor the catalytic H₂ evolution, with the electrode showing an overpotential of 300 mV at a current of 10 mA/cm². Similarly, Gao et al. introduced dual Mo and Se vacancies in 2H MoSe₂ nanosheets [86]. Experimentally, the working electrode made of these nanosheets possesses an overpotential of 126 mV at a current density of 100 mA/cm² with long-term stability. Despite the above advances, the applications of point defects in 2D TMDCs are bottlenecked by point defect induced structural instability. In the case of 2H-MoS₂, the formation energies of the most stable point defect, i.e., S-vacancy, are still relatively high with values of around 1.6 eV in Mo-rich and 3.5 eV in S-rich conditions [87]. From a HER point of view, those vacancies create dangling bonds in the plane of 2D TMDCs, which can poison the vacancies and thus results in structural instability.

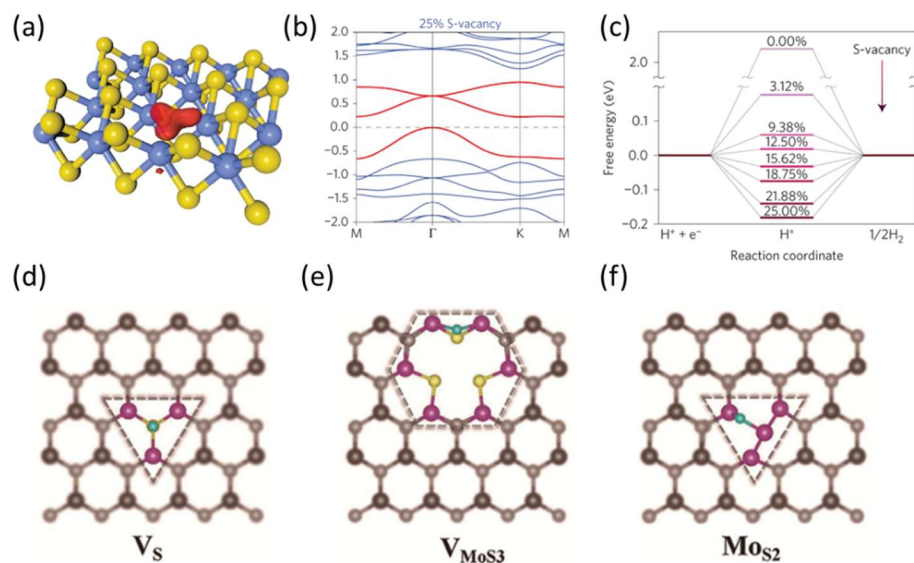


Fig. 2.7 (a) Schematic of 2H-MoS₂ with S-vacancies, where Mo and S atoms are indicated in blue and yellow. The red region around the S-vacancy indicates Kohn-Sham orbitals corresponding to the new bands just below the Fermi level. (b) Band structure of 2H-MoS₂ with 25% S-vacancies. The new bands introduced by S-vacancies are indicated in red. (c) Calculated Gibbs free energies of HER for the S-vacancy range of 0-25%. Adapted with permission from ref. [82]. Copyright 2015 Springer Nature. (d)-(f) Hydrogen adsorption configurations at V_S, V_{MoS3} and MoS₂ site, where S, Mo, and H atoms in defect regions are shown in yellow, purple and cyan, respectively. Adapted with permission from ref. [83]. Copyright 2016 American Chemical Society.

Except for point defects, grain boundaries also play an important role in activating the basal plane of 2D materials. Large-scale 2D TMDCs are usually synthesized using chemical vapor deposition (CVD) growth, a method that often forms polycrystalline with many grain boundaries [88]. Recent studies validated the formation of grain boundaries in MoS₂ experimentally, with the morphologies of various grain boundaries directly observed using transmission electron microscopy [88-90]. It was found that grain boundaries in MoS₂ mainly consist of 4-, 5-, 7-, 8- and 10-membered rings [91]. Grain boundaries have also been observed in the basal plane of other 2D TMDCs, such as WS₂ and MoSe₂ [92-94]. Similar to that of point defects, the presence of grain boundaries in 2D TMDCs affects the electronic properties [95], which in turn alters the chemical properties. Dong and Wang systematically investigated the catalytic behavior of eight types of grain boundaries in 2D MoS₂ based on DFT calculations [91]. The hydrogen adsorption configurations on those boundaries along with the corresponding calculated ΔG_H are shown in Fig. 2.8 (a). While ΔG_H of hydrogen adsorbed on pristine MoS₂ monolayer is 1.93 eV, ΔG_H of hydrogen adsorption on all MoS₂ grain boundaries exhibit much lower values, indicative of enhanced hydrogen adsorption ability at the boundary regions. In particular, grain boundaries consisting of 4|8- and 8|10-membered rings have ΔG_H values close to zero, showing great potential toward HER. Similar theoretical work on activating basal plane for HER using grain boundaries has been conducted by Ouyang et. al [83]. DFT calculations show that grain boundaries in MoS₂ monolayer possess catalytic active sites, exhibiting outstanding HER activities in Heyrovsky and Tafel reactions. Besides, the mechanism of enhanced HER activities by introducing point defects and grain boundaries was then revealed using a modified band-center model. As illustrated in Fig. 2.8 (b)-(c), the adsorption energies of hydrogen at defect sites show a linear trend in relation to the absolute values of the d-band center or p-band center. This indicates that the reduced hydrogen

adsorption energies of grain boundaries are attributed to the modification of electronic structures which are well described by the band centers. The role of grain boundaries in 2D MoS₂ for HER have also been revealed by experiments. Zhu et al. reported the realization of grain boundaries in the basal plane of 2D MoS₂ to enhance the HER performance [96]. The results show that samples with grain boundaries have better catalytic performances than samples free of grain boundaries. An overpotential of ~ 325 mV at current density of 10 A cm⁻² and a Tafel slope of ~ 95 mV dec⁻¹ were achieved by samples with grain boundaries. The effect of boundary density to the HER performance was also investigated. It was found that samples with higher densities of grain boundaries offer better HER performance as confirmed by polarization curves and Tafel plots.

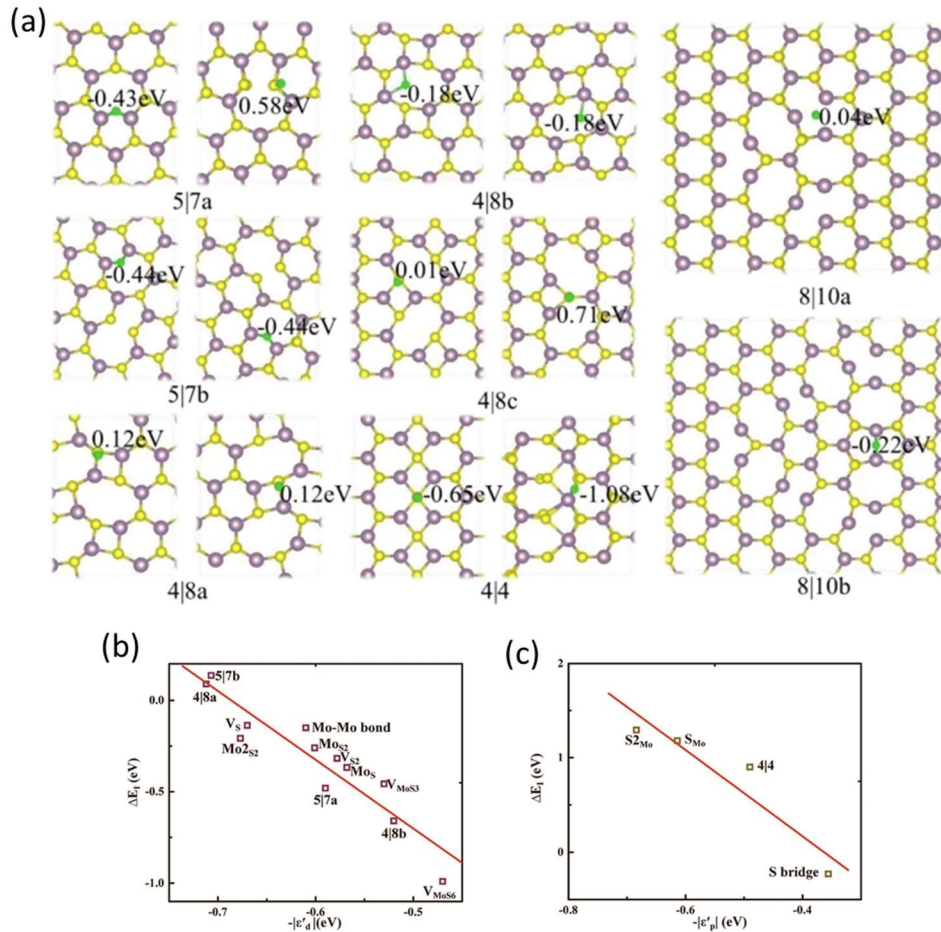


Fig. 2.8 (a) The hydrogen adsorption sites and corresponding ΔG_H values of various monolayer MoS₂ grain boundaries, including 5|7a, 5|7b, 4|8a, 4|8b, 4|8c, 4|4, 8|10a and 8|10b. Adapted with permission from ref. [91]. Copyright 2018 Springer Nature. (b),(c) Relationship between DFT-calculated H adsorption energies and (b) d- or (c) p-band center of MoS₂ defects. Adapted with permission from ref. [83]. Copyright 2016 American Chemical Society.

Asides from point defects and grain boundaries, the coexistence of different phases in 2D TMDCs leads to the formation of another important group of defects, i.e., phase boundary. Phase boundaries in 2D TMDCs can be controllably induced by several methods, including chemical exfoliation, thermal treatment, particle irradiation and strain engineering [97-104], and dozens of phase boundary configurations have been identified in 2D TMDCs based on experimental observations and first-principles calculations [20, 105-108]. Current studies of phase boundaries in 2D TMDCs toward catalytic applications mostly focus on the 2H-1T or 2H-1T' phase boundaries of 2D MoS₂. Wang et al. synthesized ultrastable in-plane 1T-2H MoS₂ heterostructures via annealing of 2H bulk MoS₂ under Ar and phosphorous mixture gas [109]. The 1T-2H MoS₂ heterostructures show excellent HER performance with a Tafel slope of 65 mV/dec. The enhanced HER performance was attributed to not only the highly active sites provided by the 1T phase but also the significantly improved electrical conductivity. Zhu et. al fabricated 2H-1T phase boundaries in MoS₂ monolayers by Ar-plasma bombardments [96]. They found that phase boundaries themselves can serve as active sites in HER. The density of 2H-1T phase boundaries can be manipulated by treatment durations. The sample including high densities of grain boundaries and phase boundaries shows a low overpotential of 136 mV and a Tafel slope of 73 mV/dec. The role of phase boundaries in 2D MoS₂ and their reaction energetics were then investigated by theoretical work performed by Zhao et al. [110]. As shown in Fig. 2.9 (a)-(e), five kinds of 2H/1T' phase boundaries were considered and the ΔG_H of adsorption sites at these boundaries were calculated. The results show that adsorption sites at zigzag boundaries exhibit

ΔG_H values close to zero, indicating high HER performance comparable to that of Pt in terms of theoretical exchange current density (Fig. 2.9 (f)-(g)). However, unlike point defects and grain boundaries which have been extensively studied, the HER mechanism of phase boundaries in 2D TMDCs are less understood. Meanwhile, other 2D TMDCs, e.g., MoTe₂ and WTe₂, are rarely explored in this field. It is worth noting that among various 2D TMDCs, 2D MoTe₂ is the best candidate material for achieving 2H/1T' interfaces since the energy differences of 2H and 1T' phase is small [111, 112]. The phase boundaries of 2D MoTe₂ are relatively easy to synthesize and have already been realized by CVD and heteroepitaxy [106, 108]. Additionally, experimental study shows that the metallic 1T'-MoTe₂ can exhibit high catalytic performance for HER [113]. Therefore, it is expected that phase boundaries of 2D MoTe₂ should have great potential towards HER. Our theoretical work predicted an increase in HER activity at the phase boundaries of 2D MoTe₂, which was later confirmed by experimental findings from Lee et al. with a turnover frequency of 317 s⁻¹ [114, 115].

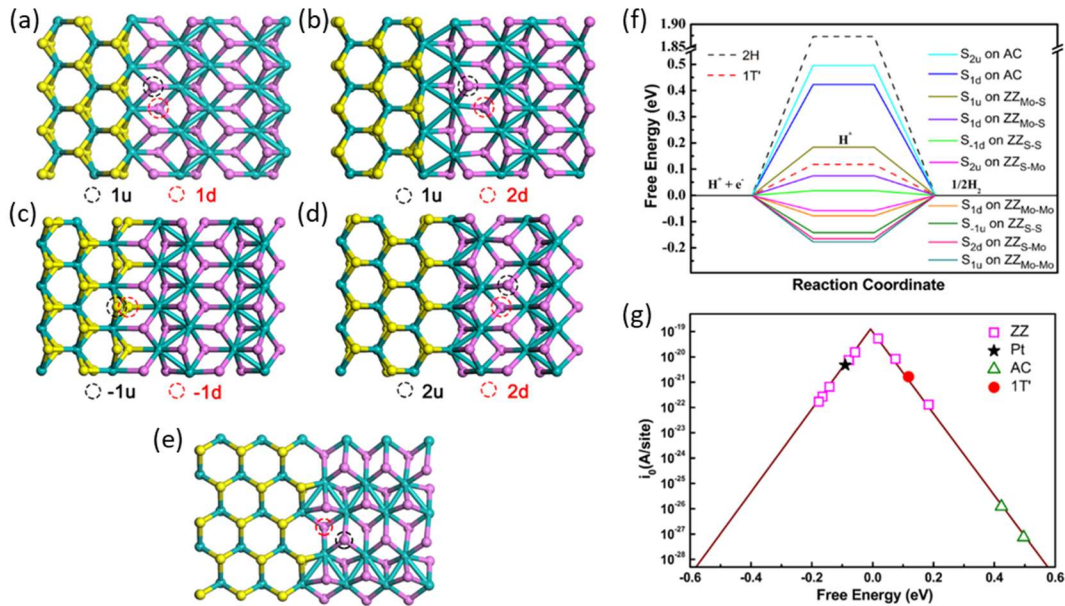


Fig. 2.9 Optimized structures of (a) ZZ_{Mo-S} , (b) ZZ_{Mo-Mo} , (c) ZZ_{S-S} , (d) ZZ_{S-Mo} and (e) AC 2H/1T' MoS_2 phase boundaries, where Mo and S atoms in the 2H phase are shown in cyan and yellow, and Mo and S atoms in the 1T' phase are shown in cyan and purple. The dashed circles with red or black colors indicate the optimal adsorption site for hydrogen on the top or bottom S layers. (f) Calculated Gibbs free energies for hydrogen adsorption ΔG_H on different sites of ZZ and AC phase boundaries compared with pristine 2H- MoS_2 . (g) The volcano plot that indicates the relationship between the exchange current density i_0 and the Gibbs free energy ΔG_H . Adapted with permission from ref. [110]. Copyright 2019 American Chemical Society.

2.4.2 Alloying

Alloying is one fundamentally important method to tune the physical and chemical properties of 2D materials. In particular, it has been extensively studied for band gap tuning in 2D TMDCs. For example, by changing the S/Se ratio, the band gaps of monolayer $MoS_{2(1-x)}Se_{2x}$ film can be tuned continuously between the values of 2D MoS_2 (1.87 eV) and $MoSe_2$ (1.55 eV) [116]. Since the chemical properties of 2D TMDCs are strongly correlated to the electronic structures, it is reasonable to expect that the catalytic performance of 2D TMDCs can also be continuously modified by varying their chemical composition.

Ternary 2D TMDCs alloys are created by mixing either transition metals or chalcogens. Generally, alloying within the same transition metal group is more favorable in terms of stability due to the small lattice mismatches and the same chalcogen coordination configurations. By contrast, alloying between different transition metal groups is relatively difficult. Recently, the thermodynamic stabilities of various 2D cation-mixed TMDC alloys have been confirmed using first-principles calculations [117]. Besides, several efforts have been made to fabricate various 2D TMDC alloys, including $MoS_{2(1-x)}Se_{2x}$, $Mo_{1-x}W_xS_2$, $Mo_{1-x}W_xSe_2$, $WS_{2(1-x)}Se_{2x}$, $Co_xMo_{1-x}S_2$, $Mo_{1-x}W_xTe_2$ and $WSe_{2(1-x)}Te_{2x}$ [118-124].

Many kinds of 2D TMDC alloys have been constructed to improve the HER activity. Gong et al. reported the fabrication of monolayer and few-layer $MoS_{2(1-x)}Se_{2x}$ alloy nanoflakes for

catalyzing HER [125]. They found that the monolayer $\text{MoS}_{2(1-x)}\text{Se}_{2x}$ has shown a better HER performance in comparison to either MoS_2 or MoSe_2 . The overpotentials of $\text{MoS}_{2(1-x)}\text{Se}_{2x}$ nanoflakes are in the range of 80-100 mV, which varies with the tunable chemical compositions with the activity peaking at $x=0.5$. $\text{MoS}_{2(1-x)}\text{Se}_{2x}$ nanoflakes also show high durability with negligible activity loss after 10000 potential cycles. It is suggested that the enhanced HER performance originates from the activation of edge sites. While hydrogen adsorption is slightly too strong on MoSe_2 edges and slightly too weak on MoS_2 edges, alloying MoS_2 with MoSe_2 can adjust the Se/S ratios to achieve optimal adsorption on the edges. It is also evidenced by X-ray photoelectron spectroscopy (XPS) that alloying modulates the d band electronic structures of transition metals and consequently the HER activity. The HER performance of $\text{MoS}_{2(1-x)}\text{Se}_{2x}$ alloys can be further improved by increasing the electronic conductivity. Nakayasu et al. synthesized edges-rich $\text{MoS}_{2(1-x)}\text{Se}_{2x}$ alloys complexing with graphene using supercritical fluid (SCF) techniques [126]. The synthesized $\text{MoS}_{0.9}\text{Se}_{1.1}$ /graphene shows improved conductivity and high electrocatalytic HER performance with a low overpotential. Similarly, $\text{WS}_{2(1-x)}\text{Se}_{2x}$ monolayer also exhibited high electrochemical catalytic activity and long-term electrocatalytic stability for the hydrogen evolution reaction. Fu et al. first reported the synthesis of monolayer $\text{WS}_{2(1-x)}\text{Se}_{2x}$ for tunable band gaps and HER [121]. Benefit from the remarkable electronic structures, $\text{WS}_{2(1-x)}\text{Se}_{2x}$ alloy possesses high HER catalytic activity with a very low onset overpotential of around 80 mV and a Tafel slope of 85 mV/dec, outperforming that of both WS_2 and WSe_2 . The impressive HER performance of $\text{WS}_{2(1-x)}\text{Se}_{2x}$ alloy was believed to come from the chemically activated basal plane in addition to the edges. Due to the different radii of S and Se atoms, mixing Se into WS_2 crystals could induce lattice distortion into the structures, resulting in the basal plane activation that facilitates the HER process.

In addition to chalcogen alloys, alloying by mixing metals has also been investigated for electrocatalysis. Lei et al. synthesized large-area $W_xMo_{1-x}S_2$ /graphene heterostructures by wet chemical routes for catalyzing HER (Fig. 2.10 (a)) [127]. The heterostructures show outstanding HER performance with a low onset potential of 96 mV and a Tafel slope of 38.7 mV/dec at current density of 10 mA/cm, superior to the pristine TMDC system. Besides, $W_xMo_{1-x}S_2$ /graphene heterostructures remain electrocatalytic stable with negligible activity loss even after 1000 cycles. The HER mechanisms of alloying were further investigated by DFT calculations. As shown in Fig. 2.10 (b)-(c), the enhanced HER performance of $W_xMo_{1-x}S_2$ alloys comes from the lower energy barriers of both Volmer and Heyrovsky reaction steps, and the energy barrier achieves the lowest value for $W_{0.4}Mo_{0.6}S_2$ alloy. It was also found that the catalytic activities in the basal plane of $W_xMo_{1-x}S_2$ alloys are higher than that of MoS_2 and WS_2 . Therefore, the inert basal plane of 2D TMDCs was activated via alloying and thus enhance the HER performance.

Alloying is particularly attractive for activating the basal plane of 2D TMDCs as it can provide high density of active sites on the surface while retaining structural integrity [96]. However, despite the abovementioned efforts, basal plane activation of 2D TMDC alloys for HER has not been systematically studied. Previous experimental studies that reported 2D TMDC alloys for catalyzing HER can hardly confirm the contribution of basal plane due to the coexistence of both the basal plane and the active edges in the TMDC systems [121, 125-127]. Besides, the absence of theoretical studies on basal plane activation 2D TMDC alloys hinders the understanding of this aspect. Additionally, due to the vast compositional space provided by 2D TMDC alloys, it is necessary to computationally screen 2D TMDC alloys for highly active electrocatalysts for the HER so as to guide the rational design of 2D TMDC alloys in experiments.

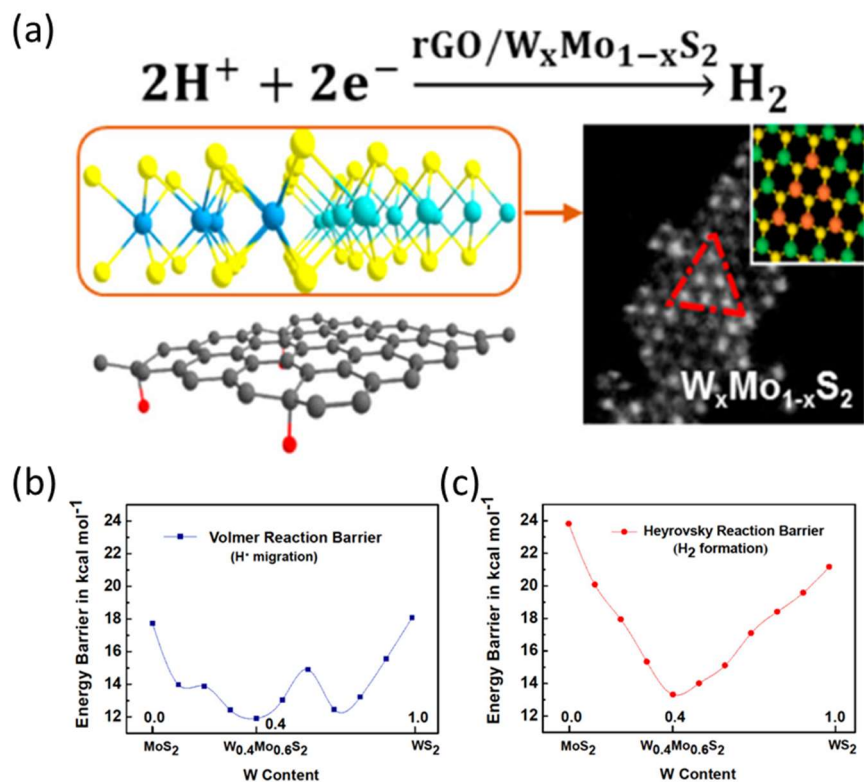


Fig. 2.10 (a) Schematic (left) and high-magnification STEM-HAADF image (right) of the $\text{W}_x\text{Mo}_{1-x}\text{S}_2/\text{graphene}$ heterostructure. (b) The activation energy barrier versus alloy concentration for Volmer reaction mechanism obtained from simulations. (c) The activation energy barrier versus alloy concentration for Heyrovsky reaction mechanism obtained from simulations. Adapted with permission from ref. [127]. Copyright 2017 American Chemical Society.

2.4.3 Substrate engineering

Synthesizing 2D materials through bottom-up techniques like chemical vapor deposition typically requires a supporting substrate. The ideal 2D catalyst system for HER should consist of a 2D material with active sites at the edges and the basal plane, along with a substrate that is chemically stable and conductive [128]. Previous studies have demonstrated that the morphology and structure of 2D TMDCs are significantly influenced by the growth substrates, leading to impacts on both catalytic activity and electrical conductivity [128, 129].

In addition, substrates can induce strain in 2D materials, thereby modulating their electronic and chemical properties. Tensile strains, which alter the lattice and electronic structures in 2D TMDCs, can reduce the band gap and effective carrier mass, leading to the enhancement in the electrical properties and carrier mobility [130, 131]. Furthermore, strain has been shown to enhance the HER activity of 2D TMDCs by activating their basal plane. Specifically, by inducing strain in monolayer MoS₂ through S-vacancies, the variation in electronic structures can alter the ΔG_{H} of the adsorption site, resulting in a near-zero value and thus improving its HER activity [82, 132].

Notably, the performance of catalytic devices relying on 2D materials is substantially influenced by the electrical contacts connected to the external circuits. Unlike 3D materials, the pristine surfaces of 2D materials typically do not form covalent bonds with metal contacts [133]. Consequently, the van der Waals (vdW) gap at the interface introduces a tunneling barrier between the metal and 2D materials prior to the Schottky barrier, which could significantly increase the contact resistance and lower the overall catalytic performance [134]. To overcome this, various new contact types have been developed, including edge contacts, hybrid contacts, and seamless contacts [133]. For instance, Ti has been found to form covalent bonds with the basal plane of MoS₂, leading to the elimination of the vdW gap [135].

2.5 Summary

This chapter discusses the recent progress in the computational design of 2D materials for HER, focusing on developing strategies, i.e., defect engineering and alloying, for activating the basal plane of 2D TMDCs and 2D III-nitrides. These two promising strategies have not yet been

systematically investigated and their mechanisms remain elusive, which will be addressed in this thesis, and discussed in detail in the following three chapters.

Notably, this thesis focuses on the HER activity of the 2D catalysts from the thermodynamic perspective at the atomic level, however, as illustrated in Subsection 2.2, this investigation can serve as a starting point for the design of superior electrocatalytic and photocatalytic devices. The strong correlation between adsorption properties and the overall reaction rate suggests that an improvement in HER activity can enable a more efficient hydrogen production process, leading to the development of more effective catalytic devices. However, it is important to note that factors such as stability and conductivity also play critical roles in achieving effective energy conversion. Therefore, when incorporating defects, substrates, and solvents into computational models, it is essential to carefully consider their potential impact on these factors.

2.6 References

- [1] K.S. Novoselov, D. Jiang, F. Schedin, T.J. Booth, V.V. Khotkevich, S.V. Morozov, A.K. Geim, Two-dimensional atomic crystals, *Proceedings of the National Academy of Sciences of the United States of America* 102(30) (2005) 10451-10453.
- [2] S.V. Morozov, K.S. Novoselov, M.I. Katsnelson, F. Schedin, D.C. Elias, J.A. Jaszczak, A.K. Geim, Giant intrinsic carrier mobilities in graphene and its bilayer, *Phys Rev Lett* 100(1) (2008) 016602.
- [3] A. Peigney, C. Laurent, E. Flahaut, R.R. Bacsa, A. Rousset, Specific surface area of carbon nanotubes and bundles of carbon nanotubes, *Carbon* 39(4) (2001) 507-514.
- [4] C. Lee, X. Wei, J.W. Kysar, J. Hone, Measurement of the Elastic Properties and Intrinsic Strength of Monolayer Graphene, *Science* 321(5887) (2008) 385-388.
- [5] K.S. Novoselov, A.K. Geim, S.V. Morozov, D. Jiang, Y. Zhang, S.V. Dubonos, I.V. Grigorieva, A.A. Firsov, Electric Field Effect in Atomically Thin Carbon Films, *Science* 306(5696) (2004) 666-669.
- [6] Y. Zhu, S. Murali, W. Cai, X. Li, J.W. Suk, J.R. Potts, R.S. Ruoff, Graphene and graphene oxide: synthesis, properties, and applications, *Adv Mater* 22(35) (2010) 3906-24.
- [7] K.S. Novoselov, A. Mishchenko, A. Carvalho, A.H. Castro Neto, 2D materials and van der Waals heterostructures, *Science* 353(6298) (2016) aac9439.
- [8] J.-C. Lei, X. Zhang, Z. Zhou, Recent advances in MXene: Preparation, properties, and applications, *Frontiers of Physics* 10(3) (2015) 276-286.

- [9] M. Zhao, Y. Wang, Q. Ma, Y. Huang, X. Zhang, J. Ping, Z. Zhang, Q. Lu, Y. Yu, H. Xu, Ultrathin 2D metal–organic framework nanosheets, *Advanced Materials* 27(45) (2015) 7372-7378.
- [10] G.G. Naumis, 5 - Electronic properties of two-dimensional materials, in: E.-H. Yang, D. Datta, J. Ding, G. Hader (Eds.), *Synthesis, Modeling, and Characterization of 2D Materials, and Their Heterostructures*, Elsevier 2020, pp. 77-109.
- [11] T.W. Scharf, S.V. Prasad, Solid lubricants: a review, *Journal of Materials Science* 48(2) (2013) 511-531.
- [12] J.A. Wilson, A.D. Yoffe, The transition metal dichalcogenides discussion and interpretation of the observed optical, electrical and structural properties, *Advances in Physics* 18(73) (1969) 193-335.
- [13] L.F. Mattheiss, Band Structures of Transition-Metal-Dichalcogenide Layer Compounds, *Physical Review B* 8(8) (1973) 3719-3740.
- [14] V. Nicolosi, M. Chhowalla, M.G. Kanatzidis, M.S. Strano, J.N. Coleman, Liquid Exfoliation of Layered Materials, *Science* 340(6139) (2013).
- [15] X. Zhang, Z. Jin, L. Wang, J.A. Hachtel, E. Villarreal, Z. Wang, T. Ha, Y. Nakanishi, C.S. Tiwary, J. Lai, L. Dong, J. Yang, R. Vajtai, E. Ringe, J.C. Idrobo, B.I. Yakobson, J. Lou, V. Gambin, R. Koltun, P.M. Ajayan, Low Contact Barrier in 2H/1T' MoTe₂ In-Plane Heterostructure Synthesized by Chemical Vapor Deposition, *ACS Appl Mater Interfaces* 11(13) (2019) 12777-12785.
- [16] X. Hong, J. Kim, S.-F. Shi, Y. Zhang, C. Jin, Y. Sun, S. Tongay, J. Wu, Y. Zhang, F. Wang, Ultrafast charge transfer in atomically thin MoS₂/WS₂ heterostructures, *Nature Nanotechnology* 9(9) (2014) 682-686.
- [17] B. Ouyang, G. Lan, Y. Guo, Z. Mi, J. Song, Phase engineering of monolayer transition-metal dichalcogenide through coupled electron doping and lattice deformation, *Applied Physics Letters* 107(19) (2015) 191903.
- [18] D. Voiry, M. Salehi, R. Silva, T. Fujita, M. Chen, T. Asefa, V.B. Shenoy, G. Eda, M. Chhowalla, Conducting MoS₂ nanosheets as catalysts for hydrogen evolution reaction, *Nano Lett* 13(12) (2013) 6222-7.
- [19] S. Liu, J. Li, B. Shi, X. Zhang, Y. Pan, M. Ye, R. Quhe, Y. Wang, H. Zhang, J. Yan, L. Xu, Y. Guo, F. Pan, J. Lu, Gate-tunable interfacial properties of in-plane ML MX₂ 1T'–2H heterojunctions, *Journal of Materials Chemistry C* 6(21) (2018) 5651-5661.
- [20] A. Li, J. Pan, X. Dai, F. Ouyang, Electrical contacts of coplanar 2H/1T' MoTe₂ monolayer, *Journal of Applied Physics* 125(7) (2019).
- [21] D. Voiry, A. Mohite, M. Chhowalla, Phase engineering of transition metal dichalcogenides, *Chemical Society Reviews* 44(9) (2015) 2702-2712.
- [22] S. Kretschmer, H.P. Komsa, P. Boggild, A.V. Krasheninnikov, Structural Transformations in Two-Dimensional Transition-Metal Dichalcogenide MoS₂ under an Electron Beam: Insights from First-Principles Calculations, *J Phys Chem Lett* 8(13) (2017) 3061-3067.
- [23] Y. Zhang, T.-T. Tang, C. Girit, Z. Hao, M.C. Martin, A. Zettl, M.F. Crommie, Y.R. Shen, F. Wang, Direct observation of a widely tunable bandgap in bilayer graphene, *Nature* 459 (2009) 820.
- [24] F. Xia, H. Wang, D. Xiao, M. Dubey, A. Ramasubramaniam, Two-dimensional material nanophotonics, *Nature Photonics* 8(12) (2014) 899-907.
- [25] B. Radisavljevic, A. Radenovic, J. Brivio, V. Giacometti, A. Kis, Single-layer MoS₂ transistors, *Nature Nanotechnology* 6 (2011) 147.
- [26] Z. Yin, H. Li, H. Li, L. Jiang, Y. Shi, Y. Sun, G. Lu, Q. Zhang, X. Chen, H. Zhang, Single-Layer MoS₂ Phototransistors, *ACS Nano* 6(1) (2012) 74-80.

- [27] M. Bernardi, M. Palummo, J.C. Grossman, Extraordinary Sunlight Absorption and One Nanometer Thick Photovoltaics Using Two-Dimensional Monolayer Materials, *Nano Letters* 13(8) (2013) 3664-3670.
- [28] Y. Chen, K. Yang, B. Jiang, J. Li, M. Zeng, L. Fu, Emerging two-dimensional nanomaterials for electrochemical hydrogen evolution, *Journal of Materials Chemistry A* 5(18) (2017) 8187-8208.
- [29] S. Mokkaṡati, C. Jagadish, III-V compound SC for optoelectronic devices, *Materials Today* 12(4) (2009) 22-32.
- [30] Z.C. Feng, III-nitride devices and nanoengineering, World Scientific 2008.
- [31] S. Nakamura, T. Mukai, M. Senoh, Candela-class high-brightness InGaN/AlGaN double-heterostructure blue-light-emitting diodes, *Applied Physics Letters* 64(13) (1994) 1687-1689.
- [32] A.V. Akimov, J.T. Muckerman, O.V. Prezhdo, Nonadiabatic Dynamics of Positive Charge during Photocatalytic Water Splitting on GaN(10-10) Surface: Charge Localization Governs Splitting Efficiency, *Journal of the American Chemical Society* 135(23) (2013) 8682-8691.
- [33] R.T. Rashid, Y. Chen, X. Liu, F.A. Chowdhury, M. Liu, J. Song, Z. Mi, B. Zhou, Tunable green syngas generation from CO₂ and H₂O with sunlight as the only energy input, *Proceedings of the National Academy of Sciences* 119(26) (2022) e2121174119.
- [34] M.G. Kibria, Z. Mi, Artificial photosynthesis using metal/nonmetal-nitride semiconductors: current status, prospects, and challenges, *Journal of Materials Chemistry A* 4(8) (2016) 2801-2820.
- [35] D. Wang, A. Pierre, M.G. Kibria, K. Cui, X. Han, K.H. Bevan, H. Guo, S. Paradis, A.-R. Hakima, Z. Mi, Wafer-Level Photocatalytic Water Splitting on GaN Nanowire Arrays Grown by Molecular Beam Epitaxy, *Nano Letters* 11(6) (2011) 2353-2357.
- [36] Z.Y. Al Balushi, K. Wang, R.K. Ghosh, R.A. Vilá, S.M. Eichfeld, J.D. Caldwell, X. Qin, Y.-C. Lin, P.A. DeSario, G. Stone, S. Subramanian, D.F. Paul, R.M. Wallace, S. Datta, Joan M. Redwing, J.A. Robinson, Two-dimensional gallium nitride realized via graphene encapsulation, *Nature Materials* 15(11) (2016) 1166-1171.
- [37] Z. Huang, T.-Y. Lü, H.-Q. Wang, S.-W. Yang, J.-C. Zheng, Electronic and thermoelectric properties of the group-III nitrides (BN, AlN and GaN) atomic sheets under biaxial strains, *Computational Materials Science* 130 (2017) 232-241.
- [38] D. Kecik, A. Onen, M. Konuk, E. Gürbüz, F. Ersan, S. Cahangirov, E. Aktürk, E. Durgun, S. Ciraci, Fundamentals, progress, and future directions of nitride-based semiconductors and their composites in two-dimensional limit: A first-principles perspective to recent synthesis, *Applied Physics Reviews* 5(1) (2018).
- [39] A. Onen, D. Kecik, E. Durgun, S. Ciraci, GaN: From three- to two-dimensional single-layer crystal and its multilayer van der Waals solids, *Physical Review B* 93(8) (2016) 085431.
- [40] C. Bacaksiz, H. Sahin, H.D. Ozaydin, S. Horzum, R.T. Senger, F.M. Peeters, Hexagonal AlN: Dimensional-crossover-driven band-gap transition, *Physical Review B* 91(8) (2015) 085430.
- [41] E. Gürbüz, S. Cahangirov, E. Durgun, S. Ciraci, Single layers and multilayers of GaN and AlN in square-octagon structure: Stability, electronic properties, and functionalization, *Physical Review B* 96(20) (2017) 205427.
- [42] D.C. Camacho-Mojica, F. López-Urías, GaN Haeckelite Single-Layered Nanostructures: Monolayer and Nanotubes, *Scientific Reports* 5(1) (2015) 17902.
- [43] H. Zhang, F.-S. Meng, Y.-B. Wu, Two single-layer porous gallium nitride nanosheets: A first-principles study, *Solid State Communications* 250 (2017) 18-22.
- [44] Y. Guo, H. Zhu, Q. Wang, Piezoelectric Effects in Surface-Engineered Two-Dimensional Group III Nitrides, *ACS Applied Materials & Interfaces* 11(1) (2019) 1033-1039.

- [45] M. Kanli, A. Onen, A. Mogulkoc, E. Durgun, Characterization of two-dimensional Ga_{1-x}Al_xN ordered alloys with varying chemical composition, *Computational Materials Science* 167 (2019) 13-18.
- [46] H. Shu, X. Niu, X. Ding, Y. Wang, Effects of strain and surface modification on stability, electronic and optical properties of GaN monolayer, *Applied Surface Science* 479 (2019) 475-481.
- [47] Q. Chen, H. Hu, X. Chen, J. Wang, Tailoring band gap in GaN sheet by chemical modification and electric field: Ab initio calculations, *Applied Physics Letters* 98(5) (2011) 053102.
- [48] Y. Chen, K. Liu, J. Liu, T. Lv, B. Wei, T. Zhang, M. Zeng, Z. Wang, L. Fu, Growth of 2D GaN Single Crystals on Liquid Metals, *Journal of the American Chemical Society* 140(48) (2018) 16392-16395.
- [49] K. Ren, J. Yu, W. Tang, A two-dimensional vertical van der Waals heterostructure based on g-GaN and Mg (OH) 2 used as a promising photocatalyst for water splitting: A first-principles calculation, *Journal of Applied Physics* 126(6) (2019) 065701.
- [50] H.L. Zhuang, A.K. Singh, R.G. Hennig, Computational discovery of single-layer III-V materials, *Physical Review B* 87(16) (2013) 165415.
- [51] B.W.J. Chen, L. Xu, M. Mavrikakis, Computational Methods in Heterogeneous Catalysis, *Chemical Reviews* 121(2) (2021) 1007-1048.
- [52] J. Greeley, J.K. Nørskov, L.A. Kibler, A.M. El-Aziz, D.M. Kolb, Hydrogen Evolution Over Bimetallic Systems: Understanding the Trends, *ChemPhysChem* 7(5) (2006) 1032-1035.
- [53] P. Sabatier, *La catalyse en chimie organique*, Librairie Polytechnique, (1913).
- [54] M. Che, Nobel Prize in chemistry 1912 to Sabatier: Organic chemistry or catalysis?, *Catalysis Today* 218-219 (2013) 162-171.
- [55] R. Parsons, The rate of electrolytic hydrogen evolution and the heat of adsorption of hydrogen, *Transactions of the Faraday Society* 54(0) (1958) 1053-1063.
- [56] J.K. Nørskov, T. Bligaard, A. Logadottir, J.R. Kitchin, J.G. Chen, S. Pandelov, U. Stimming, Trends in the Exchange Current for Hydrogen Evolution, *Journal of The Electrochemical Society* 152(3) (2005) J23-J26.
- [57] M.T.M. Koper, Analysis of electrocatalytic reaction schemes: distinction between rate-determining and potential-determining steps, *Journal of Solid State Electrochemistry* 17(2) (2013) 339-344.
- [58] J.K. Nørskov, J. Rossmeisl, A. Logadottir, L. Lindqvist, J.R. Kitchin, T. Bligaard, H. Jónsson, Origin of the Overpotential for Oxygen Reduction at a Fuel-Cell Cathode, *The Journal of Physical Chemistry B* 108(46) (2004) 17886-17892.
- [59] A.J. Medford, A. Vojvodic, J.S. Hummelshøj, J. Voss, F. Abild-Pedersen, F. Studt, T. Bligaard, A. Nilsson, J.K. Nørskov, From the Sabatier principle to a predictive theory of transition-metal heterogeneous catalysis, *Journal of Catalysis* 328 (2015) 36-42.
- [60] H. Ooka, J. Huang, K.S. Exner, The Sabatier Principle in Electrocatalysis: Basics, Limitations, and Extensions, *Frontiers in Energy Research* 9 (2021).
- [61] K. Tran, Z.W. Ulissi, Active learning across intermetallics to guide discovery of electrocatalysts for CO₂ reduction and H₂ evolution, *Nature Catalysis* 1(9) (2018) 696-703.
- [62] J. Greeley, T.F. Jaramillo, J. Bonde, I.B. Chorkendorff, J.K. Nørskov, Computational high-throughput screening of electrocatalytic materials for hydrogen evolution, *Nat Mater* 5(11) (2006) 909-13.
- [63] J. Rossmeisl, K. Chan, R. Ahmed, V. Tripković, M.E. Björketun, pH in atomic scale simulations of electrochemical interfaces, *Physical Chemistry Chemical Physics* 15(25) (2013) 10321-10325.

- [64] H. Oberhofer, Electrocatalysis Beyond the Computational Hydrogen Electrode, in: W. Andreoni, S. Yip (Eds.), Handbook of Materials Modeling: Applications: Current and Emerging Materials, Springer International Publishing, Cham, 2020, pp. 1505-1537.
- [65] M. Nielsen, M.E. Björketun, M.H. Hansen, J. Rossmeisl, Towards first principles modeling of electrochemical electrode–electrolyte interfaces, *Surface Science* 631 (2015) 2-7.
- [66] M.H. Hansen, J. Rossmeisl, pH in Grand Canonical Statistics of an Electrochemical Interface, *The Journal of Physical Chemistry C* 120(51) (2016) 29135-29143.
- [67] M.H. Hansen, A. Nilsson, J. Rossmeisl, Modelling pH and potential in dynamic structures of the water/Pt(111) interface on the atomic scale, *Physical Chemistry Chemical Physics* 19(34) (2017) 23505-23514.
- [68] Z.W. Seh, J. Kibsgaard, C.F. Dickens, I. Chorkendorff, J.K. Nørskov, T.F. Jaramillo, Combining theory and experiment in electrocatalysis: Insights into materials design, *Science* 355(6321) (2017) eaad4998.
- [69] S. Trasatti, Work function, electronegativity, and electrochemical behaviour of metals: III. Electrolytic hydrogen evolution in acid solutions, *Journal of Electroanalytical Chemistry and Interfacial Electrochemistry* 39(1) (1972) 163-184.
- [70] N. Cheng, S. Stambula, D. Wang, M.N. Banis, J. Liu, A. Riese, B. Xiao, R. Li, T.K. Sham, L.M. Liu, G.A. Botton, X. Sun, Platinum single-atom and cluster catalysis of the hydrogen evolution reaction, *Nat Commun* 7 (2016) 13638.
- [71] J. Bonde, P.G. Moses, T.F. Jaramillo, J.K. Nørskov, I. Chorkendorff, Hydrogen evolution on nano-particulate transition metal sulfides, *Faraday Discussions* 140(0) (2009) 219-231.
- [72] C. Tsai, K. Chan, F. Abild-Pedersen, J.K. Nørskov, Active edge sites in MoSe₂ and WSe₂ catalysts for the hydrogen evolution reaction: a density functional study, *Phys Chem Chem Phys* 16(26) (2014) 13156-64.
- [73] D.B. Putungan, S.H. Lin, J.L. Kuo, A first-principles examination of conducting monolayer 1T'-MX₂ (M = Mo, W; X = S, Se, Te): promising catalysts for hydrogen evolution reaction and its enhancement by strain, *Phys Chem Chem Phys* 17(33) (2015) 21702-8.
- [74] J. Zhang, J. Wu, H. Guo, W. Chen, J. Yuan, U. Martinez, G. Gupta, A. Mohite, P.M. Ajayan, J. Lou, Unveiling Active Sites for the Hydrogen Evolution Reaction on Monolayer MoS₂, *Adv Mater* 29(42) (2017).
- [75] K. Ren, Y. Luo, S. Wang, J.-P. Chou, J. Yu, W. Tang, M. Sun, A van der Waals Heterostructure Based on Graphene-like Gallium Nitride and Boron Selenide: A High-Efficiency Photocatalyst for Water Splitting, *ACS Omega* 4(26) (2019) 21689-21697.
- [76] Y. Sun, S. Gao, F. Lei, Y. Xie, Atomically-thin two-dimensional sheets for understanding active sites in catalysis, *Chemical Society Reviews* 44(3) (2015) 623-636.
- [77] B. Peng, P.K. Ang, K.P. Loh, Two-dimensional dichalcogenides for light-harvesting applications, *Nano Today* 10(2) (2015) 128-137.
- [78] Z. Wang, M.T. Tang, A. Cao, K. Chan, J.K. Nørskov, Insights into the Hydrogen Evolution Reaction on 2D Transition-Metal Dichalcogenides, *The Journal of Physical Chemistry C* 126(11) (2022) 5151-5158.
- [79] C.R. Zhu, D. Gao, J. Ding, D. Chao, J. Wang, TMD-based highly efficient electrocatalysts developed by combined computational and experimental approaches, *Chem Soc Rev* 47(12) (2018) 4332-4356.
- [80] Y. Cao, Roadmap and Direction toward High-Performance MoS₂ Hydrogen Evolution Catalysts, *ACS Nano* 15(7) (2021) 11014-11039.

- [81] Y. Zhang, Q. Ji, G.-F. Han, J. Ju, J. Shi, D. Ma, J. Sun, Y. Zhang, M. Li, X.-Y. Lang, Y. Zhang, Z. Liu, Dendritic, Transferable, Strictly Monolayer MoS₂ Flakes Synthesized on SrTiO₃ Single Crystals for Efficient Electrocatalytic Applications, *ACS Nano* 8(8) (2014) 8617-8624.
- [82] H. Li, C. Tsai, A.L. Koh, L. Cai, A.W. Contryman, A.H. Fragapane, J. Zhao, H.S. Han, H.C. Manoharan, F. Abild-Pedersen, J.K. Nørskov, X. Zheng, Activating and optimizing MoS₂ basal planes for hydrogen evolution through the formation of strained sulphur vacancies, *Nature Materials* 15(1) (2016) 48-53.
- [83] Y. Ouyang, C. Ling, Q. Chen, Z. Wang, L. Shi, J. Wang, Activating Inert Basal Planes of MoS₂ for Hydrogen Evolution Reaction through the Formation of Different Intrinsic Defects, *Chemistry of Materials* 28(12) (2016) 4390-4396.
- [84] H. Shu, D. Zhou, F. Li, D. Cao, X. Chen, Defect Engineering in MoSe₂ for the Hydrogen Evolution Reaction: From Point Defects to Edges, *ACS Appl Mater Interfaces* 9(49) (2017) 42688-42698.
- [85] Q.D. Truong, Y. Nakayasu, Q.T. Nguyen, D.N. Nguyen, C.T. Nguyen, M.K. Devaraju, D. Rangappa, K. Nayuki, Y. Sasaki, P.D. Tran, T. Tomai, I. Honma, Defect-rich exfoliated MoSe₂ nanosheets by supercritical fluid process as an attractive catalyst for hydrogen evolution in water, *Applied Surface Science* 505 (2020) 144537.
- [86] D. Gao, B. Xia, Y. Wang, W. Xiao, P. Xi, D. Xue, J. Ding, Dual-Native Vacancy Activated Basal Plane and Conductivity of MoSe₂ with High-Efficiency Hydrogen Evolution Reaction, *Small* 14(14) (2018) 1704150.
- [87] X. Sun, Z. Wang, Y.Q. Fu, Defect-Mediated Lithium Adsorption and Diffusion on Monolayer Molybdenum Disulfide, *Scientific Reports* 5(1) (2015) 18712.
- [88] Y.-H. Lee, X.-Q. Zhang, W. Zhang, M.-T. Chang, C.-T. Lin, K.-D. Chang, Y.-C. Yu, J.T.-W. Wang, C.-S. Chang, L.-J. Li, T.-W. Lin, Synthesis of Large-Area MoS₂ Atomic Layers with Chemical Vapor Deposition, *Advanced Materials* 24(17) (2012) 2320-2325.
- [89] S. Najmaei, Z. Liu, W. Zhou, X. Zou, G. Shi, S. Lei, B.I. Yakobson, J.-C. Idrobo, P.M. Ajayan, J. Lou, Vapour phase growth and grain boundary structure of molybdenum disulphide atomic layers, *Nature Materials* 12(8) (2013) 754-759.
- [90] S. Najmaei, J. Yuan, J. Zhang, P. Ajayan, J. Lou, Synthesis and Defect Investigation of Two-Dimensional Molybdenum Disulfide Atomic Layers, *Accounts of Chemical Research* 48(1) (2015) 31-40.
- [91] S. Dong, Z. Wang, Grain Boundaries Trigger Basal Plane Catalytic Activity for the Hydrogen Evolution Reaction in Monolayer MoS₂, *Electrocatalysis* 9(6) (2018) 744-751.
- [92] Y. Ma, S. Kolekar, H. Coy Diaz, J. Aprozanz, I. Miccoli, C. Tegenkamp, M. Batzill, Metallic Twin Grain Boundaries Embedded in MoSe₂ Monolayers Grown by Molecular Beam Epitaxy, *ACS Nano* 11(5) (2017) 5130-5139.
- [93] Y. Zhang, Y. Zhang, Q. Ji, J. Ju, H. Yuan, J. Shi, T. Gao, D. Ma, M. Liu, Y. Chen, X. Song, H.Y. Hwang, Y. Cui, Z. Liu, Controlled Growth of High-Quality Monolayer WS₂ Layers on Sapphire and Imaging Its Grain Boundary, *ACS Nano* 7(10) (2013) 8963-8971.
- [94] C. Lan, D. Li, Z. Zhou, S. Yip, H. Zhang, L. Shu, R. Wei, R. Dong, J.C. Ho, Direct Visualization of Grain Boundaries in 2D Monolayer WS₂ via Induced Growth of CdS Nanoparticle Chains, *Small Methods* 3(2) (2019) 1800245.
- [95] Z. Wang, Q. Su, G.Q. Yin, J. Shi, H. Deng, J. Guan, M.P. Wu, Y.L. Zhou, H.L. Lou, Y.Q. Fu, Structure and electronic properties of transition metal dichalcogenide MX₂ (M = Mo, W, Nb; X = S, Se) monolayers with grain boundaries, *Materials Chemistry and Physics* 147(3) (2014) 1068-1073.

- [96] J. Zhu, Z.C. Wang, H. Dai, Q. Wang, R. Yang, H. Yu, M. Liao, J. Zhang, W. Chen, Z. Wei, N. Li, L. Du, D. Shi, W. Wang, L. Zhang, Y. Jiang, G. Zhang, Boundary activated hydrogen evolution reaction on monolayer MoS₂, *Nat Commun* 10(1) (2019) 1348.
- [97] S. Kim, J.H. Kim, D. Kim, G. Hwang, J. Baik, H. Yang, S. Cho, Post-patterning of an electronic homojunction in atomically thin monoclinic MoTe₂, *2D Materials* 4(2) (2017) 024004.
- [98] Y. Yu, G.-H. Nam, Q. He, X.-J. Wu, K. Zhang, Z. Yang, J. Chen, Q. Ma, M. Zhao, Z. Liu, High phase-purity 1T'-MoS₂-and 1T'-MoSe₂-layered crystals, *Nature chemistry* 10(6) (2018) 638-643.
- [99] L. Li, Z. Qin, L. Ries, S. Hong, T. Michel, J. Yang, C. Salameh, M. Bechelany, P. Miele, D. Kaplan, M. Chhowalla, D. Voiry, Role of Sulfur Vacancies and Undercoordinated Mo Regions in MoS₂ Nanosheets toward the Evolution of Hydrogen, *ACS Nano* 13(6) (2019) 6824-6834.
- [100] P. Valerius, S. Kretschmer, B.V. Senkovskiy, S. Wu, J. Hall, A. Herman, N. Ehlen, M. Ghorbani-Asl, A. Grueneis, A.V. Krashennnikov, Reversible crystalline-to-amorphous phase transformation in monolayer MoS₂ under grazing ion irradiation, *2D Materials* 7(2) (2020) 025005.
- [101] R. Zhao, Y. Wang, D. Deng, X. Luo, W.J. Lu, Y.-P. Sun, Z.-K. Liu, L.-Q. Chen, J. Robinson, Tuning Phase Transitions in 1T-TaS₂ via the Substrate, *Nano Letters* 17(6) (2017) 3471-3477.
- [102] S.-W. Wang, H. Medina, K.-B. Hong, C.-C. Wu, Y. Qu, A. Manikandan, T.-Y. Su, P.-T. Lee, Z.-Q. Huang, Z. Wang, F.-C. Chuang, H.-C. Kuo, Y.-L. Chueh, Thermally Strained Band Gap Engineering of Transition-Metal Dichalcogenide Bilayers with Enhanced Light-Matter Interaction toward Excellent Photodetectors, *ACS Nano* 11(9) (2017) 8768-8776.
- [103] S. Song, D.H. Keum, S. Cho, D. Perello, Y. Kim, Y.H. Lee, Room Temperature Semiconductor-Metal Transition of MoTe₂ Thin Films Engineered by Strain, *Nano Letters* 16(1) (2016) 188-193.
- [104] M. Calandra, Chemically exfoliated single-layer MoS_2 : Stability, lattice dynamics, and catalytic adsorption from first principles, *Physical Review B* 88(24) (2013) 245428.
- [105] W. Zhao, F. Ding, Energetics and kinetics of phase transition between a 2H and a 1T MoS₂ monolayer-a theoretical study, *Nanoscale* 9(6) (2017) 2301-2309.
- [106] J.H. Sung, H. Heo, S. Si, Y.H. Kim, H.R. Noh, K. Song, J. Kim, C.S. Lee, S.Y. Seo, D.H. Kim, H.K. Kim, H.W. Yeom, T.H. Kim, S.Y. Choi, J.S. Kim, M.H. Jo, Coplanar semiconductor-metal circuitry defined on few-layer MoTe₂ via polymorphic heteroepitaxy, *Nat Nanotechnol* 12(11) (2017) 1064-1070.
- [107] J. Xia, J. Wang, D. Chao, Z. Chen, Z. Liu, J.-L. Kuo, J. Yan, Z.X. Shen, Phase evolution of lithium intercalation dynamics in 2H-MoS₂, *Nanoscale* 9(22) (2017) 7533-7540.
- [108] L. Zhou, K. Xu, A. Zubair, X. Zhang, F. Ouyang, T. Palacios, M.S. Dresselhaus, Y. Li, J. Kong, Role of Molecular Sieves in the CVD Synthesis of Large-Area 2D MoTe₂, *Advanced Functional Materials* 27(3) (2017).
- [109] S. Wang, D. Zhang, B. Li, C. Zhang, Z. Du, H. Yin, X. Bi, S. Yang, Ultrastable In-Plane 1T-2H MoS₂ Heterostructures for Enhanced Hydrogen Evolution Reaction, *Advanced Energy Materials* 8(25) (2018) 1801345.
- [110] N. Zhao, L. Wang, Z. Zhang, Y. Li, Activating the MoS₂ Basal Planes for Electrocatalytic Hydrogen Evolution by 2H/1T' Structural Interfaces, *ACS Applied Materials & Interfaces* 11(45) (2019) 42014-42020.
- [111] K.A. Duerloo, Y. Li, E.J. Reed, Structural phase transitions in two-dimensional Mo- and W-dichalcogenide monolayers, *Nat Commun* 5 (2014) 4214.
- [112] K.A. Duerloo, E.J. Reed, Structural Phase Transitions by Design in Monolayer Alloys, *ACS Nano* 10(1) (2016) 289-97.

- [113] J.C. McGlynn, T. Dankwort, L. Kienle, N.A.G. Bandeira, J.P. Fraser, E.K. Gibson, I. Cascallana-Matías, K. Kamarás, M.D. Symes, H.N. Miras, A.Y. Ganin, The rapid electrochemical activation of MoTe₂ for the hydrogen evolution reaction, *Nature Communications* 10(1) (2019) 4916.
- [114] Y. Lee, N. Ling, D. Kim, M. Zhao, Y.A. Eshete, E. Kim, S. Cho, H. Yang, Heterophase boundary for active hydrogen evolution in MoTe₂, *Advanced Functional Materials* 32(10) (2022) 2105675.
- [115] Y. Chen, P. Ou, X. Bie, J. Song, Basal plane activation in monolayer MoTe₂ for the hydrogen evolution reaction via phase boundaries, *Journal of Materials Chemistry A* 8(37) (2020) 19522-19532.
- [116] J. Mann, Q. Ma, P.M. Odenthal, M. Isarraraz, D. Le, E. Preciado, D. Barroso, K. Yamaguchi, G. von Son Palacio, A. Nguyen, T. Tran, M. Wurch, A. Nguyen, V. Klee, S. Bobek, D. Sun, T.F. Heinz, T.S. Rahman, R. Kawakami, L. Bartels, 2-dimensional transition metal dichalcogenides with tunable direct band gaps: MoS₂(1-x)Se₂x monolayers, *Adv Mater* 26(9) (2014) 1399-404.
- [117] Z. Hemmat, J. Cavin, A. Ahmadiparidari, A. Ruckel, S. Rastegar, S.N. Misal, L. Majidi, K. Kumar, S. Wang, J. Guo, R. Dawood, F. Lagunas, P. Parajuli, A.T. Ngo, L.A. Curtiss, S.B. Cho, J. Cabana, R.F. Klie, R. Mishra, A. Salehi-Khojin, Quasi-Binary Transition Metal Dichalcogenide Alloys: Thermodynamic Stability Prediction, Scalable Synthesis, and Application, *Advanced Materials* 32(26) (2020) 1907041.
- [118] Y. Gong, Z. Liu, A.R. Lupini, G. Shi, J. Lin, S. Najmaei, Z. Lin, A.L. Elías, A. Berkdemir, G. You, H. Terrones, M. Terrones, R. Vajtai, S.T. Pantelides, S.J. Pennycook, J. Lou, W. Zhou, P.M. Ajayan, Band Gap Engineering and Layer-by-Layer Mapping of Selenium-Doped Molybdenum Disulfide, *Nano Letters* 14(2) (2014) 442-449.
- [119] J.-G. Song, G.H. Ryu, S.J. Lee, S. Sim, C.W. Lee, T. Choi, H. Jung, Y. Kim, Z. Lee, J.-M. Myoung, C. Dussarrat, C. Lansalot-Matras, J. Park, H. Choi, H. Kim, Controllable synthesis of molybdenum tungsten disulfide alloy for vertically composition-controlled multilayer, *Nature Communications* 6 (2015) 7817.
- [120] Two-dimensional semiconductor alloys: Monolayer Mo_{1-x}W_xSe₂.
- [121] Q. Fu, L. Yang, W. Wang, A. Han, J. Huang, P. Du, Z. Fan, J. Zhang, B. Xiang, Synthesis and enhanced electrochemical catalytic performance of monolayer WS₂(1-x)Se₂x with a tunable band gap, *Advanced Materials* 27(32) (2015) 4732-4738.
- [122] B. Li, L. Huang, M. Zhong, N. Huo, Y. Li, S. Yang, C. Fan, J. Yang, W. Hu, Z. Wei, J. Li, Synthesis and Transport Properties of Large-Scale Alloy Co_{0.16}Mo_{0.84}S₂ Bilayer Nanosheets, *ACS Nano* 9(2) (2015) 1257-1262.
- [123] O.B. Aslan, I.M. Datye, M.J. Mleczko, K. Sze Cheung, S. Krylyuk, A. Bruma, I. Kalish, A.V. Davydov, E. Pop, T.F. Heinz, Probing the Optical Properties and Strain-Tuning of Ultrathin Mo_{1-x}W_xTe₂, *Nano Letters* 18(4) (2018) 2485-2491.
- [124] Anisotropic thermal transport in van der Waals layered alloys WSe₂(1-x)Te₂x, *Applied Physics Letters* 112(24) (2018) 241901.
- [125] Q. Gong, L. Cheng, C. Liu, M. Zhang, Q. Feng, H. Ye, M. Zeng, L. Xie, Z. Liu, Y. Li, Ultrathin MoS₂(1-x)Se₂x Alloy Nanoflakes For Electrocatalytic Hydrogen Evolution Reaction, *ACS Catalysis* 5(4) (2015) 2213-2219.
- [126] Y. Nakayasu, Y. Yasui, R. Taniki, K. Oizumi, H. Kobayashi, N. Nagamura, T. Tomai, I. Honma, One-Pot Rapid Synthesis of Mo(S,Se)₂ Nanosheets on Graphene for Highly Efficient Hydrogen Evolution, *ACS Sustainable Chemistry & Engineering* (2018).

- [127] Y. Lei, S. Pakhira, K. Fujisawa, X. Wang, O.O. Iyiola, N. Perea López, A. Laura Elías, L. Pulickal Rajukumar, C. Zhou, B. Kabius, N. Alem, M. Endo, R. Lv, J.L. Mendoza-Cortes, M. Terrones, Low-temperature Synthesis of Heterostructures of Transition Metal Dichalcogenide Alloys ($\text{W}_x\text{Mo}_{1-x}\text{S}_2$) and Graphene with Superior Catalytic Performance for Hydrogen Evolution, *ACS Nano* 11(5) (2017) 5103-5112.
- [128] Y. Gao, Y. Liu, Z. Liu, Controllable growth of two-dimensional materials on noble metal substrates, *Iscience* 24(12) (2021) 103432.
- [129] J. Shi, D. Ma, G.-F. Han, Y. Zhang, Q. Ji, T. Gao, J. Sun, X. Song, C. Li, Y. Zhang, X.-Y. Lang, Y. Zhang, Z. Liu, Controllable Growth and Transfer of Monolayer MoS_2 on Au Foils and Its Potential Application in Hydrogen Evolution Reaction, *ACS Nano* 8(10) (2014) 10196-10204.
- [130] Y. Wu, L. Wang, H. Li, Q. Dong, S. Liu, Strain of 2D materials via substrate engineering, *Chinese Chemical Letters* 33(1) (2022) 153-162.
- [131] J. Chaste, A. Missaoui, S. Huang, H. Henck, Z. Ben Aziza, L. Ferlazzo, C. Naylor, A. Balan, A.T.C. Johnson, Jr., R. Braive, A. Ouerghi, Intrinsic Properties of Suspended MoS_2 on SiO_2/Si Pillar Arrays for Nanomechanics and Optics, *ACS Nano* 12(4) (2018) 3235-3242.
- [132] B. Hammer, J.K. Nørskov, Theoretical surface science and catalysis—calculations and concepts, *Advances in catalysis* 45 (2000) 71-129.
- [133] A. Allain, J. Kang, K. Banerjee, A. Kis, Electrical contacts to two-dimensional semiconductors, *Nature Materials* 14(12) (2015) 1195-1205.
- [134] J. Kang, W. Liu, D. Sarkar, D. Jena, K. Banerjee, Computational Study of Metal Contacts to Monolayer Transition-Metal Dichalcogenide Semiconductors, *Physical Review X* 4(3) (2014) 031005.
- [135] I. Popov, G. Seifert, D. Tománek, Designing Electrical Contacts to MoS_2 Monolayers: A Computational Study, *Physical Review Letters* 108(15) (2012) 156802.

Chapter 3 : Methodology

3.1 Introduction

As an increasingly important subfield of materials science, computational materials science has played a crucial role in discovering new materials and unveiling their properties. Thanks to the advance of high-performance computers and new theories, various materials simulation methods have been developed to guide the material design process. For example, the first-principles calculation describes the electronic structures and all relevant physical properties of materials based on quantum mechanics; molecular dynamics simulate the motion of atoms and molecules by solving Newton's equations of motion; Monte Carlo simulation solves various material problems, such as atomic migration, based on statistical mechanics; and finite element method provides solutions to complex engineering problems (e.g. heat transfer) by dividing the system into small parts and solving differential equations [1]. These simulation methods are designed to treat materials at different length scales ranging from electronic to macroscale.

Among various simulation methods, the first-principles calculation is of great significance because it can accurately describe the atomic structure without the input of any fitting parameters from the experimental data, holding immense promise for material bottom-up design. However, accurate predictions from *ab initio* methods inevitably lead to high computational complexity. For complex material systems like alloys, serious computations on all possible configurations are non-trivial. This challenge can be successfully addressed by the applications of cluster expansion, an effective tool to estimate configuration-dependent properties, or machine learning, a method from artificial intelligence that uses data to make predictions [2, 3]. Combing one of those methods with

first-principles calculations, high accuracy of material property predictions could be achieved at a reasonable computational cost [4, 5].

Since this thesis aims at understanding the structural, electronic and chemical properties of materials at an atomic level, density-functional theory based first-principles calculations were employed. In addition, to address the computational complexity of alloy modelling, cluster expansion method was employed to calculate the formation enthalpies of alloys, and machine learning method was applied to predict the stabilities and adsorption properties of alloys. This chapter will review the theoretical background of calculation methods used in this thesis.

3.2 First-principles methods

First-principles method is based solely on quantum mechanics without using any empirical parameters. It treats electrons and nuclei as basic particles and describes the interactions between them in mathematical forms. With the accurate description of the interaction between electrons and nuclei provided, given only the atomic numbers of the constituent atoms, the energy and structure of a material system can be obtained, and all material properties related to the electronic structure of a system can be derived.

One of the most crucial parts of quantum mechanics is the accurate description of the interaction between particles. The first attempt of quantum description of an atom can be traced to the Bohr model proposed in 1913 [6, 7]. After that, in 1926, the Schrödinger equation was established to describe the behaviors of small particles in terms of energy in mathematical forms [8]. The Schrödinger equation takes into account the wave nature of electrons and can be expressed as the following:

$$H\Psi(\vec{r}, \vec{R}) = E\Psi(\vec{r}, \vec{R}) \quad (3.2)$$

Here, H , Ψ and E denotes the Hamiltonian operator, wave function and the total energy of the system, respectively. \vec{r} and \vec{R} refer to the coordinates of the electron and nucleus.

The Hamiltonian operator H is an energy operator generally including the kinetic and potential energies of the system. The kinetic energies come from the motions of electrons and nuclei, and the potential energies come from three different Coulomb interactions: nucleus-electron, electron-electron, and nucleus-nucleus interaction. According to the Born-Oppenheimer approximation, since nuclei are much heavier than electrons, the coordinates of the nuclei in a system are considered to be fixed, making the separation of the wave functions of nuclei and electrons in a system possible [9]. As a result, The Hamiltonian operator H can be written as:

$$H = E_i^{kin} + U_{li} + U_{ij} \quad (3.2)$$

The first term on the right side is the kinetic energy of electrons, which can be expressed in the atomic unit as:

$$E_i^{kin} = -\frac{1}{2} \sum_i^n \nabla_i^2 \quad (3.3)$$

where ∇^2 is the Laplacian operator and n is the number of electrons in the system. The second term calculates the Coulomb interaction between nuclei and electrons given by:

$$U_{li} = - \sum_l^N \sum_i^n \frac{Z_l}{|\vec{r}_{li}|} \quad (3.4)$$

where n , N and Z_l are the number of electrons and nuclei, and the charge of the nuclei. The minus sign before double sums in the equation indicates that the interaction between particles is attraction.

The final term U_{ij} is the Coulomb interaction between electrons written as:

$$U_{ij} = \frac{1}{2} \sum_{i \neq j}^n \frac{1}{|\vec{r}_{ij}|} \quad (3.5)$$

It is noted that a factor of $\frac{1}{2}$ is used for double-counting correction. In theory, the total energy of the system can be directly obtained by solving the Schrödinger equation (Equation 3.1). However, due to the many-body problem, the computations for systems consisting of a large number of electrons are still out of reach. The complexity of calculations largely comes from the Coulomb interaction between electrons. To solve the Schrödinger equation for large systems numerically, further approximations are necessary.

In 1928, Hartree introduced the self-consistent field method, known as the Hartree method, to calculate approximate wave functions and energies for n -electron systems [10]. The Hartree method assumes that each electron in the system is independent, and their interactions can be approximated with mean-field approaches. With this assumption, the n -electron wave functions of the system can be described by the product of single-electron wave functions:

$$\Psi = \psi_1\psi_2\psi_3 \cdots \psi_n \quad (3.6)$$

However, the Hartree method oversimplifies the interactions between electrons. It does not consider the antisymmetry principle and the exchange and correlation energies coming from the n -electron interactions. The Hartree method is further improved by Fock in 1930 by using a Slater determinant to fulfill the antisymmetric property of the wave functions [11]:

$$\Psi(\vec{r}_1, \vec{r}_2, \dots, \vec{r}_n) = \frac{1}{\sqrt{n!}} \begin{vmatrix} \psi_1(\vec{r}_1) & \psi_2(\vec{r}_1) & \cdots & \psi_n(\vec{r}_1) \\ \psi_1(\vec{r}_2) & \psi_2(\vec{r}_2) & \cdots & \psi_n(\vec{r}_2) \\ \vdots & \vdots & \ddots & \vdots \\ \psi_1(\vec{r}_n) & \psi_2(\vec{r}_n) & \cdots & \psi_n(\vec{r}_n) \end{vmatrix} \quad (3.7)$$

where $1/\sqrt{n!}$ is the normalization factor for the system containing n electrons. The wave equation including the wave function written in Slater determinant form is now given by (in the atomic unit):

$$\left(-\frac{1}{2}\nabla^2 + U_{ext}(\vec{r}) + U_{ij}(\vec{r}) \right) \Psi(\vec{r}) = E\Psi(\vec{r}) \quad (3.8)$$

Here, $U_{ext}(\vec{r})$ denotes the interaction between nuclei and electrons. Equation 3.8 is called the Hartree-Fock equation.

The Hartree-Fock (HF) method brings the accuracy of Hartree energy to a higher level by considering the antisymmetry principle and electronic exchange effect. However, it neglects the electronic correlation energy, which can lead to unavoidable deviations from experimental results. Several post-Hartree-Fock methods have been proposed to include the electronic correlation to the wave functions, such as Møller-Plesset perturbation theory (MP) and Configuration interaction (CI) [12, 13]. Besides, alternative methods to HF have been developed to include the correlation energies and reduce computational cost, such as density functional theory, which will be discussed in detail in the following Section 3.3.

3.3 Density functional theory

Although the HF method partially eases the calculations of wave equations, its application is still limited to small systems with only dozens of atoms, hindering their use in condensed-matter physics and computational chemistry. Fortunately, reduced computations can be achieved by alternative methods such as the famous density functional theory (DFT). In the mid-1960s, Hohenberg and Kohn proposed two fundamental theorems (HK theorems) which laid the foundation of DFT, followed by the further development of DFT by Kohn and Sham (KS DFT) [14, 15]. The first HK theorem states that the ground-state energy from the Schrödinger equation can be uniquely determined by a functional of the electron density. By using the electron density with only three spatial coordinates, this theorem changes a $3n$ -dimensional equation to a three-dimensional one. The second HK theorem demonstrates an important property of the functional that can be used to solve the Schrödinger equation. It proves that the ground-state electron density

should minimize the energy of the overall functional [16]. Thus, true electron density and the corresponding energy of the system can be obtained by varying the electron density until the system energy is minimized. On the basis of the two HK theorems, KS DFT further treats electrons as non-interacting particles moving in an effective potential including external potential and Coulomb interaction between electrons. Based on this assumption, the electron density for an n -electron system can be written as a sum over a set of individual electron wave functions:

$$n(\vec{r}) = 2 \sum_i \psi_i^*(\vec{r})\psi_i(\vec{r}) \quad (3.9)$$

Here, the factor of 2 indicates that an individual electron wave function can be occupied by 2 electrons with different spins based on the Pauli exclusion principle. Besides, the Kohn-Sham equations can be written as:

$$\left(-\frac{1}{2}\nabla^2 + U_{ext}(\vec{r}) + U_H(\vec{r}) + U_{XC}(\vec{r}) \right) \psi_i(\vec{r}) = \varepsilon_i \psi_i(\vec{r}) \quad (3.10)$$

The first two terms on the left-hand side of are the kinetic energy of each electron and the Coulomb interaction between each electron and the collection of atomic nuclei. The third term is the Hartree potential describing the Coulomb interaction between one electron and the total electron density from all electrons in the system, which is written as:

$$U_H(\vec{r}) = \int \frac{n(\vec{r}')}{|\vec{r} - \vec{r}'|} d\vec{r}' \quad (3.11)$$

It is noted that each electron contributes to the total electron density of the system, so the interaction between each electron and the total electron density inevitably leads to an unphysical self-interaction. This self-interaction is corrected by $U_{XC}(\vec{r})$, which is the exchange-correlation potential defined as:

$$U_{XC}(\vec{r}) = \frac{\delta E_{XC}(\vec{r})}{\delta n(\vec{r})} \quad (3.12)$$

It is seen that a definition of $E_{XC}(\vec{r})$ is required to accurately compute exchange-correlation energy. However, the true form of $E_{XC}(\vec{r})$ term is not known in the DFT scheme.

To completely define the Kohn-Sham equations, approximations to the exchange-correlation functional are required. The simplest approximation is the local-density approximation (LDA) derived from the homogeneous electron gas model [16]. The general form of LDA for the exchange-correlation energy is given by:

$$E_{XC}^{LDA} = \int n(\vec{r})\epsilon_{XC}(\vec{r}) d\vec{r} \quad (3.12)$$

where ϵ_{XC} is the exchange-correlation energy per electron of a homogeneous electron gas of electron density $n(\vec{r})$. Although LDAs are extensively used in DFT calculations for semiconductor materials, the predictions are not always accurate since real material systems are not homogeneous. Another approximation method, the generalized gradient approximation (GGA) was then developed to approximate the exchange-correlation potential more accurately [17, 18]. The GGA approximation contains not only the electron density but also its gradient at a given point, and therefore in principle it can generate more accurate results compared to the LDA. Typical GGAs used in materials science are the Perdew-Wang functional (PW91) and the Perdew-Burke-Ernzerhof functional (PBE) [17, 19, 20]. In spite of these improvements, GGAs and LDAs are notorious for underestimating the band gaps of semiconductors. Advanced functionals like meta-GGA, PBE0, meta-GGA and HSE can give higher accuracy, but employing those functionals also significantly increases the computational cost. In addition, empirical parameters are introduced in these advanced functionals, making the calculations lose their first-principles origin [1]. The approximation of exchange-correlation potential also causes the poor treatment of intermolecular interactions in the system. Additional corrections are thus required if van der Waals forces are considered in the calculations.

Further approximations to DFT calculations for solids involve pseudopotentials which fix the core electrons and only allow valence electrons to move, periodic boundary conditions for approximating infinite system with unit cells, and plane wave basis sets to decompose Kohn-Sham wave functions along with using cut-off energies to truncate the plane-wave expansion [21-23]. Those methods further accelerate the calculations while remains the accuracy of the results.

In this study, DFT calculations were performed using a commercial code called Vienna ab initio simulation package (VASP) [23, 24]. The interactions of electrons with ion cores were represented by the projector-augmented wave (PAW) method [22], and the exchange-correlation functional was approximated by generalized gradient approximation (GGA) of Perdew-Burke-Ernzerhof (PBE) [17, 20]. It is noted that since PBE can underestimate the band gaps of semiconductors, the hybrid Heyd-Scuseria-Ernzerhof (HSE06) functional was implemented to obtain more accurate results for the electronic properties [25]. Additionally, in the calculations of adsorption properties, the DFT-D3 method was employed to take into account the effect of van der Waals (vdW) interactions [26, 27].

3.4 Cluster expansion method

DFT can be used to accurately calculate the ground-state properties of various materials, but it is still too slow to calculate complex systems such as disorder structures. For the case of alloy discovery, enumerations of all possible alloy configurations are often required to find the ground-state configurations and obtain desired properties. However, due to the limited computation time, traditional DFT studies only search for the lowest total energy among dozens of candidate configurations, leading to large probabilities of missing true ground-state

configurations. This problem can be partially addressed by combining DFT calculations with cluster expansions (CE).

Cluster expansion method is widely used in materials science to calculate the ground state energies of alloys and understand alloy thermodynamics [2, 4, 28, 29]. Similar to the Ising models for magnetic materials where the magnetic moment at each site is described by a spin variable (1 for spin up and -1 for spin down), in cluster expansions for alloys each metal site in lattice is assigned an occupation variable σ_i . For example, as illustrated in Fig. 3.1, for a binary alloy AB, σ_i equal to +1 indicates that this site in lattice space is occupied by atom A, and σ_i equal to -1 indicates that this site is present by atom B. A cluster expansion Hamiltonian can be constructed to describe the system in terms of σ_i [30, 31]:

$$\Delta H(\vec{\sigma}) = \sum_{\alpha} m_{\alpha} J_{\alpha} \xi_{\alpha}(\vec{\sigma}) \quad (3.13)$$

where α denotes a cluster, which can be singles, pairs, triplets, quadruples, etc. m_{α} is the number of symmetry-equivalent clusters of α , and J_{α} is the effective cluster interaction (ECI) parameter describing the energy contribution associated with cluster α . The summation runs over all possible symmetry-inequivalent clusters. ξ_{α} is the cluster correlation function given by:

$$\xi_{\alpha}(\vec{\sigma}) = \left\langle \prod_{i \in \alpha'} \sigma_i \right\rangle \quad (3.14)$$

where the angle bracket representing the average of the spin product of all symmetry-equivalent clusters α' of α .

The next step is the determination of ECIs by fitting the training data usually generated from DFT. The fitting process is guaranteed by machine learning approaches such as cross-validation and active learning to reach a given level of accuracy [32]. The fitted ECIs can then be

used to predict the formation energies of any alloy configurations quickly by just calculating the ξ_α .

In this thesis, CE method was employed using the Alloy-Theoretic Automated Toolkit (ATAT) code to fit the formation enthalpies of 2D alloys [30]. Unique ordered alloy structures were automatically generated by ATAT code and relaxed by DFT calculations. The formation enthalpies of those ordered structures were calculated using the following equation:

$$\Delta H(\vec{\sigma}) = E_{tot}(A_{1-x}B_x; \vec{\sigma}) - (1-x)E_{tot}(A) - xE_{tot}(B) \quad (3.15)$$

where x is the concentration of the alloy, and E_{tot} is the total energies obtained from DFT. The performance of the CE fitting was evaluated by cross-validation score with values of around 0.1 meV.

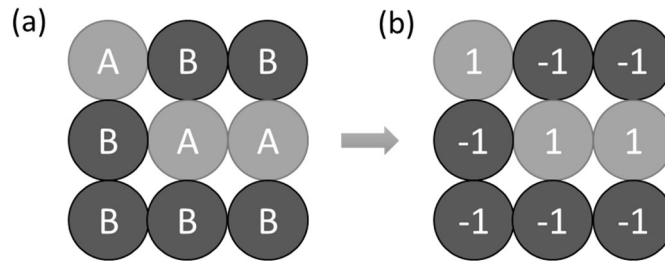


Fig. 3.1 Schematic of the alloy AB in a two-dimensional lattice space. Each site in the alloy can be represented by either (a) an atom type, or (b) an occupation variable (+1 for atom A and -1 for atom B).

3.5 Machine learning

The advance in artificial intelligence has enhanced the role of computers in science and is transforming materials science [3, 33]. The amount of data has experienced explosive growth over the past two decades in the field of materials science. With the help of machine learning algorithms, the information of those data can be extracted to explain experimental or theoretical results, and

thus accelerates the material discovery process. Machine learning has widespread applications in materials science, which is illustrated in Fig. 3.2.

In general, machine learnings are methods that use data to construct statistical models to make predictions. The basic steps of constructing a machine learning model involve data collection, data representation and model selection. The first step, data collection, is the most critical step since errors in data can mislead the following prediction process. Data used for machine learning can be obtained from experimental or theoretical results, and a number of materials online databases have emerged to assist researchers in the material informatics field, such as the Materials Project, Open Quantum Materials Database (OQMD) and Inorganic Crystal Structure Database (ICSD) [34-36]. It is worth noting that there are also several databases specific for 2D materials like 2DMatPedia, Computational 2D Materials Database (C2DB) and Materials Cloud two-dimensional crystals database (MC2D) [37-39]. However, compared to 3D materials databases, databases for 2D materials are still limited in size. Besides, after collecting the data, redundancy or abnormal values in data should further be removed to guarantee efficient ML models.

The representation of input data in suitable forms can increase the accuracy of an algorithm mapping its input data to the output data. A successful data representation should capture all the relevant information that can fully describe the data, but finding appropriate descriptors for data representation is a challenging task, which has been actively studied for several years [3]. Descriptors can contain simple information like atomic numbers, boiling points and electronegativities. They can also involve complex transformations, and some examples are Coulomb matrix featurization, the smooth overlap of atomic positions, and Fourier series of atomic radial distribution functions [40-43]. Additionally, built-in featurization has been developed for some deep learning methods [44].

After datasets have been collected and represented appropriately, it is necessary to select suitable machine learning models. Generally, machine learning algorithms can be divided into four main categories, i.e., supervised learning, unsupervised learning, semi-supervised learning and reinforcement learning. Several commonly used machine learning algorithms are naive Bayes classifiers, k-nearest-neighbour methods, decision trees, artificial neural networks and deep neural networks [45-48]. The selected model should then be optimized and tested to ensure the accuracy of the predictions.

Additionally, the development of automated machine learning (AutoML) further accelerates the applications of machine learning in various fields. AutoML can automate the data collection, data representation and model selection process, providing more accurate results than hand-coded algorithms [49].

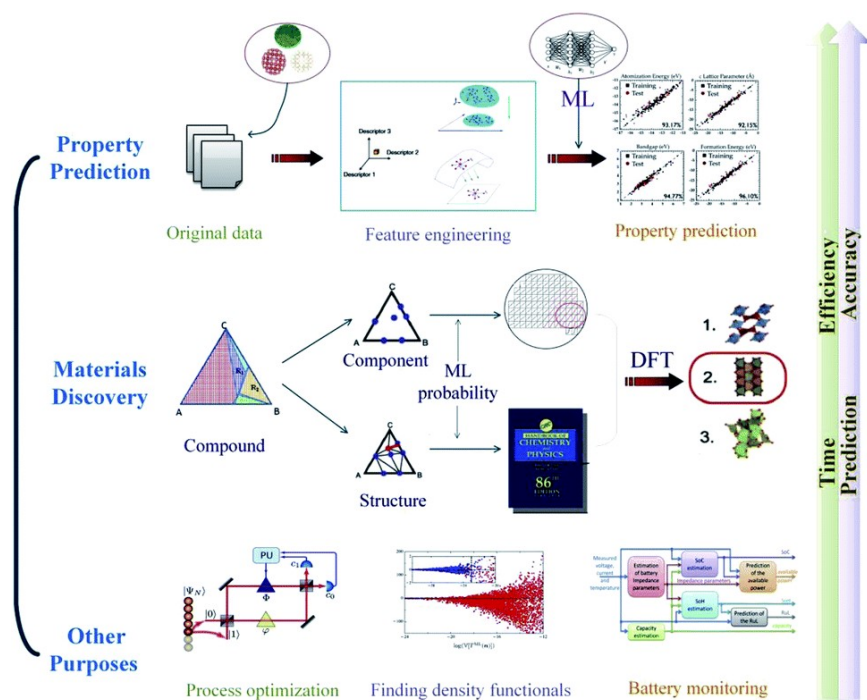


Fig. 3.2 Applications of machine learning methods in materials science [50].

3.6 References

- [1] J.G. Lee, Computational materials science: an introduction, Crc Press 2016.
- [2] J.M. Sanchez, F. Ducastelle, D. Gratias, Generalized cluster description of multicomponent systems, *Physica A: Statistical Mechanics and its Applications* 128(1) (1984) 334-350.
- [3] K.T. Butler, D.W. Davies, H. Cartwright, O. Isayev, A. Walsh, Machine learning for molecular and materials science, *Nature* 559(7715) (2018) 547-555.
- [4] J.-H. Yang, B.I. Yakobson, Unusual Negative Formation Enthalpies and Atomic Ordering in Isovalent Alloys of Transition Metal Dichalcogenide Monolayers, *Chemistry of Materials* 30(5) (2018) 1547-1555.
- [5] K. Tran, Z.W. Ulissi, Active learning across intermetallics to guide discovery of electrocatalysts for CO₂ reduction and H₂ evolution, *Nature Catalysis* 1(9) (2018) 696-703.
- [6] W.H.E. Schwarz, 100th Anniversary of Bohr's Model of the Atom, *Angewandte Chemie International Edition* 52(47) (2013) 12228-12238.
- [7] W. Thiel, Computational Catalysis—Past, Present, and Future, *Angewandte Chemie International Edition* 53(33) (2014) 8605-8613.
- [8] E. Schrödinger, Quantisierung als Eigenwertproblem, *Annalen der Physik* 384(4) (1926) 361-376.
- [9] M. Born, R. Oppenheimer, Zur Quantentheorie der Molekeln, *Annalen der Physik* 389(20) (1927) 457-484.
- [10] D.R. Hartree, The Wave Mechanics of an Atom with a Non-Coulomb Central Field. Part I. Theory and Methods, *Mathematical Proceedings of the Cambridge Philosophical Society* 24(1) (1928) 89-110.
- [11] V. Fock, „Selfconsistent field“ mit Austausch für Natrium, *Zeitschrift für Physik* 62(11) (1930) 795-805.
- [12] C. Møller, M.S. Plesset, Note on an Approximation Treatment for Many-Electron Systems, *Physical Review* 46(7) (1934) 618-622.
- [13] C. David Sherrill, H.F. Schaefer, The Configuration Interaction Method: Advances in Highly Correlated Approaches, in: P.-O. Löwdin, J.R. Sabin, M.C. Zerner, E. Brändas (Eds.), *Advances in Quantum Chemistry*, Academic Press 1999, pp. 143-269.
- [14] P. Hohenberg, W. Kohn, Inhomogeneous Electron Gas, *Physical Review* 136(3B) (1964) B864-B871.
- [15] W. Kohn, L.J. Sham, Self-Consistent Equations Including Exchange and Correlation Effects, *Physical Review* 140(4A) (1965) A1133-A1138.
- [16] D.S. Sholl, J.A. Steckel, *Density functional theory: a practical introduction*, John Wiley & Sons 2011.
- [17] J.P. Perdew, J.A. Chevary, S.H. Vosko, K.A. Jackson, M.R. Pederson, D.J. Singh, C. Fiolhais, Atoms, molecules, solids, and surfaces: Applications of the generalized gradient approximation for exchange and correlation, *Physical Review B* 46(11) (1992) 6671-6687.
- [18] D.C. Langreth, M.J. Mehl, Beyond the local-density approximation in calculations of ground-state electronic properties, *Physical Review B* 28(4) (1983) 1809-1834.
- [19] K. Burke, J.P. Perdew, Y. Wang, Derivation of a generalized gradient approximation: The PW91 density functional, *Electronic density functional theory*, Springer 1998, pp. 81-111.
- [20] J.P. Perdew, K. Burke, M. Ernzerhof, Generalized Gradient Approximation Made Simple, *Physical Review Letters* 77(18) (1996) 3865-3868.

- [21] P. Schwerdtfeger, The Pseudopotential Approximation in Electronic Structure Theory, *ChemPhysChem* 12(17) (2011) 3143-3155.
- [22] P.E. Blöchl, Projector augmented-wave method, *Physical Review B* 50(24) (1994) 17953-17979.
- [23] G. Kresse, J. Furthmüller, Efficient iterative schemes for ab initio total-energy calculations using a plane-wave basis set, *Physical Review B* 54(16) (1996) 11169-11186.
- [24] G. Kresse, D. Joubert, From ultrasoft pseudopotentials to the projector augmented-wave method, *Physical Review B* 59(3) (1999) 1758-1775.
- [25] A.V. Krugau, O.A. Vydrov, A.F. Izmaylov, G.E. Scuseria, Influence of the exchange screening parameter on the performance of screened hybrid functionals, *The Journal of chemical physics* 125(22) (2006) 224106.
- [26] S. Grimme, J. Antony, S. Ehrlich, H. Krieg, A consistent and accurate ab initio parametrization of density functional dispersion correction (DFT-D) for the 94 elements H-Pu, *The Journal of Chemical Physics* 132(15) (2010) 154104.
- [27] S. Grimme, S. Ehrlich, L. Goerigk, Effect of the damping function in dispersion corrected density functional theory, *Journal of Computational Chemistry* 32(7) (2011) 1456-1465.
- [28] L.G. Ferreira, S.-H. Wei, A. Zunger, First-principles calculation of alloy phase diagrams: The renormalized-interaction approach, *Physical Review B* 40(5) (1989) 3197-3231.
- [29] L. Cao, C. Li, T. Mueller, The Use of Cluster Expansions To Predict the Structures and Properties of Surfaces and Nanostructured Materials, *Journal of Chemical Information and Modeling* 58(12) (2018) 2401-2413.
- [30] A. Van De Walle, M. Asta, G. Ceder, The alloy theoretic automated toolkit: A user guide, *Calphad* 26(4) (2002) 539-553.
- [31] J. Kang, S. Tongay, J. Li, J. Wu, Monolayer semiconducting transition metal dichalcogenide alloys: Stability and band bowing, *Journal of Applied Physics* 113(14) (2013) 143703.
- [32] A. van de Walle, G. Ceder, Automating first-principles phase diagram calculations, *Journal of Phase Equilibria* 23(4) (2002) 348.
- [33] G.L.W. Hart, T. Mueller, C. Toher, S. Curtarolo, Machine learning for alloys, *Nature Reviews Materials* 6(8) (2021) 730-755.
- [34] A. Jain, S.P. Ong, G. Hautier, W. Chen, W.D. Richards, S. Dacek, S. Cholia, D. Gunter, D. Skinner, G. Ceder, Commentary: The Materials Project: A materials genome approach to accelerating materials innovation, *APL materials* 1(1) (2013) 011002.
- [35] J.E. Saal, S. Kirklin, M. Aykol, B. Meredig, C. Wolverton, Materials design and discovery with high-throughput density functional theory: the open quantum materials database (OQMD), *Jom* 65(11) (2013) 1501-1509.
- [36] D. Zagorac, H. Müller, S. Ruehl, J. Zagorac, S. Rehme, Recent developments in the Inorganic Crystal Structure Database: theoretical crystal structure data and related features, *Journal of applied crystallography* 52(5) (2019) 918-925.
- [37] J. Zhou, L. Shen, M.D. Costa, K.A. Persson, S.P. Ong, P. Huck, Y. Lu, X. Ma, Y. Chen, H. Tang, Y.P. Feng, 2DMatPedia, an open computational database of two-dimensional materials from top-down and bottom-up approaches, *Scientific Data* 6(1) (2019) 86.
- [38] M. Gjerding, A. Taghizadeh, A. Rasmussen, S. Ali, F. Bertoldo, T. Deilmann, U. Holguin, N. Knøsgaard, M. Kruse, S. Manti, Recent progress of the computational 2D materials database (C2DB), *arXiv preprint arXiv:2102.03029* (2021).
- [39] N. Mounet, M. Gibertini, P. Schwaller, D. Campi, A. Merkys, A. Marrazzo, T. Sohler, I.E. Castelli, A. Cepellotti, G. Pizzi, N. Marzari, Two-dimensional materials from high-throughput

- computational exfoliation of experimentally known compounds, *Nat Nanotechnol* 13(3) (2018) 246-252.
- [40] D.C. Elton, Z. Boukouvalas, M.S. Butrico, M.D. Fuge, P.W. Chung, Applying machine learning techniques to predict the properties of energetic materials, *Scientific Reports* 8(1) (2018) 9059.
- [41] M. Rupp, A. Tkatchenko, K.-R. Müller, O.A. Von Lilienfeld, Fast and accurate modeling of molecular atomization energies with machine learning, *Physical review letters* 108(5) (2012) 058301.
- [42] A.P. Bartók, R. Kondor, G. Csányi, On representing chemical environments, *Physical Review B* 87(18) (2013) 184115.
- [43] O.A. Von Lilienfeld, R. Ramakrishnan, M. Rupp, A. Knoll, Fourier series of atomic radial distribution functions: A molecular fingerprint for machine learning models of quantum chemical properties, *International Journal of Quantum Chemistry* 115(16) (2015) 1084-1093.
- [44] Y. Bengio, A. Courville, P. Vincent, Representation learning: A review and new perspectives, *IEEE transactions on pattern analysis and machine intelligence* 35(8) (2013) 1798-1828.
- [45] D.J. Hand, K. Yu, Idiot's Bayes—not so stupid after all?, *International statistical review* 69(3) (2001) 385-398.
- [46] G. Shakhnarovich, Nearest-neighbor methods in learning and vision, Massachusetts Institute2005.
- [47] J. Schmidhuber, Deep learning in neural networks: An overview, *Neural networks* 61 (2015) 85-117.
- [48] S.B. Kotsiantis, Decision trees: a recent overview, *Artificial Intelligence Review* 39(4) (2013) 261-283.
- [49] T.T. Le, W. Fu, J.H. Moore, Scaling tree-based automated machine learning to biomedical big data with a feature set selector, *Bioinformatics* 36(1) (2019) 250-256.
- [50] J. Cai, X. Chu, K. Xu, H. Li, J. Wei, Machine learning-driven new material discovery, *Nanoscale Advances* 2(8) (2020) 3115-3130.

Chapter 4 : Basal Plane Activation in Monolayer MoTe₂ for Hydrogen Evolution Reaction via Phase Boundaries

Defect engineering involves the introduction of point defects, grain boundaries, and phase boundaries to the materials structures for modifying their chemical environments, and it has been demonstrated as an effective method to enhance the HER performance of 2D TMDCs. Among various defects, phase boundaries in 2D TMDCs are rarely explored and their role in catalyzing HER is unclear. Using first-principles calculations, the first manuscript systematically studied the structural stabilities and HER activities of 2H/1T' phase boundaries in one representative 2D TMDC, 2D MoTe₂. It was demonstrated that phase boundaries can provide a viable pathway to activate the basal plane of 2D MoTe₂. Catalytic active sites for the HER were identified at the stable phase boundaries, and the underlying HER mechanisms associated with the phase boundaries were clarified.

- This chapter has been published in *Journal of Materials Chemistry A*, appeared as: Yiqing Chen, Pengfei Ou, Xiaohan Bie, and Jun Song. **Basal plane activation in monolayer MoTe₂ for the hydrogen evolution reaction via phase boundaries.** *Journal of Materials Chemistry A*, **2020**, 8, 19522-19532.

DOI: 10.1039/D0TA06165D

4.1 Abstract

Two-dimensional transition metal dichalcogenides (2D TMDCs) have attracted tremendous interest as one prominent material group promising inexpensive electrocatalysts for hydrogen evolution reaction (HER). In the present study, using monolayer MoTe₂ as a representative, we demonstrated that phase boundaries can provide a viable pathway to activate the basal plane of 2D TMDCs for enhanced HER performance. Comprehensive first-principles calculations have been performed to examine the energetics and structural stabilities of possible 2H/1T' phase boundary configurations. Three categories of sites, Te, Mo and hollow sites, have been identified in energetically stable phase boundaries, as potential catalytic centers for HER, all indicating enhanced HER activity than the pristine basal lattice. In particular, the hollow sites, a new group of sites induced by phase boundaries, show great promise by exhibiting a Gibbs free energy (ΔG_H) near the thermoneutral value for hydrogen adsorption, comparable to that of Pt. The mechanisms underlying hydrogen adsorption at phase boundaries were then revealed, shown to be attributed to the unique local hydrogen adsorption geometries and electronic structures at phase boundaries. Our study clarifies the important mechanistic aspects underlying hydrogen activation at phase boundaries, providing valuable theoretical insights towards designing new class of high-performance HER electrocatalysts based on 2D TMDCs.

4.2 Introduction

Electrochemical water splitting is of particular importance to the production of hydrogen, crucial for the global goal towards clean energy economy and sustainability [1]. One core challenge in research efforts on water splitting is to identify efficient catalysts to facilitate evolution of H₂, i.e. hydrogen-evolution reaction (HER). Currently, platinum (Pt) and Pt-based

materials are regarded as the *de facto* standard catalysts for HER, but suffer high cost and material scarcity, which hinder their large-scale utilization [2, 3]. Therefore, there have been great efforts for alternative, non-Pt catalysts with low cost and high performance [4]. Among various potential non-Pt catalyst candidates, monolayer transition-metal dichalcogenides (TMDCs) are found to be effective towards HER [5-8]. For instance, theoretical and experimental studies have suggested that monolayer MoS₂ can catalyze HER at a moderate overpotential of 0.1-0.2 V with Gibbs free energy of adsorption close to zero (<0.1 eV) at its edge sites [9].

However, for monolayer TMDCs, the active sites for HER are limited to the edge sites while the basal plane is inert, rendering large surface area catalytically useless [10, 11]. Such limitation has motivated a great quest aiming to activate the basal plane of TMDCs [12, 13]. One popular method resulted from the quest is the introduction of (point) defects in TMDCs, which has been shown to lead to significant enhancement in HER activity [10, 13-16]. Yet, with the introduction of defects come the abundant dangling bonds at defect sites, which may poison the HER reaction and cause structural instabilities [17]. A few other studies have suggested the approach of transforming TMDCs from the semiconducting 2H phase to metallic 1T(or 1T') phase. This 2H→1T(1T') phase transformation is shown to provide numerous active sites in the basal plane and at the same time improves the electrical conductivity of TMDCs [18-20]. However, the 1T(1T') phase of most TMDCs is metastable and can easily revert back to the 2H phase [21]. More recently, Zhu et al. demonstrated from their experimental study that the basal plane of monolayer MoS₂ can be activated by introducing phase boundaries [17]. This facile route can provide a high density of active sites while retaining the structural stability by 2H-1T phase integration [22]. It hints promising new avenues towards basal plane activation of TMDCs without deteriorating the structural stability.

Phase boundaries in TMDCs can be controllably induced via several methods, e.g., thermal treatment [23-25], particle irradiation [26], and strain engineering [27-29]. Meanwhile, it is worth noting that, for group-VI TMDCs, 1T' phase is energetically more favourable than 1T phase. Therefore it is reasonable to expect that, compared to 2H/1T phase boundaries, 2H/1T' phase boundaries would be thermodynamically more preferable, and be more are more likely to meets the requirement for structural stability and large-scale synthesis. Among the big family of monolayer TMDCs, MoTe₂ is an appealing candidate for achieving 2H/1T' phase boundaries [30-32] because of small energy difference between the 2H and 1T' phases [31]. Therefore thermodynamically it is expected that the phase boundaries in MoTe₂ are relatively easy to form, and indeed they have already been successfully synthesized by chemical vapor deposition (CVD) [33] and heteroepitaxy [30]. In addition, several studies on the Schottky metal-semiconductor junction have reported improved catalytic activity by local charge redistribution. As a result, the respective semiconducting and metallic natures of 2H and 1T' MoTe₂ together might synergistically lead to enhancement in HER at the boundary region [34-36]. Previous studies have also shown that MoTe₂ phase boundaries exhibit excellent electrical properties [33, 37, 38], an important factor that influences the overall catalytic activity towards HER [39]. It was reported that the atomically coherent contact within 2H/1T' MoTe₂ and the contact between 1T' MoTe₂ and current collector (e.g. Au electrodes) exhibited low Schottky barrier height and thus low contact resistance[30, 35]. The high conductivity of MoTe₂ and neglectable contact resistance at the boundaries contribute to a fast electron transfer speed [39-41] and holds promise for the engineering of high-performance electrocatalysts in the future.

However, in contrast to the numerous studies on isolated defects and edges in TMDCs with respect to HER, research work on phase boundaries has been rather scarce, except for some recent

studies examining specific phase boundaries in MoS₂ to show the existence of active sites on S atoms for hydrogen adsorption to potentially enhance HER activity [17, 42]. Consequently, knowledge regarding HER at phase boundaries in TMDCs remains largely absent, necessitating dedicated studies. Aiming at such need, here in this paper, we perform systematic density functional theory (DFT) calculations to investigate HER activities at phase boundaries in MoTe₂ as a representative TMDC system. Possible 2H/1T' phase boundaries are constructed to examine their structural stabilities. Various candidate adsorption sites, namely Te, Mo and hollow sites, are explored on the stable configurations. Our calculations show that all adsorption sites at MoTe₂ phase boundaries are activated, with the hollow sites as the most active sites for HER and exhibiting outstanding HER activity comparable to that of Pt. Besides, we propose mechanisms to understand such activation at the phase boundaries. Hydrogen adsorptions at the Te sites are interpreted and predicted by Fermi-abundance (D_F) model while the adsorption at Mo and hollow sites are qualitatively understood by analyzing the local charge distribution and density of states. The HER activity at the phase boundary was shown to be strongly dependent on the local hydrogen adsorption geometry and electronic structures.

4.3 Methods and models

Monolayer MoTe₂ has three polymorphs, semiconducting 2H phase, and metallic 1T and 1T' phases. Figs. 4.1(a) and 4.1(b) show the trigonal prismatic 2H phase consisting of 1×1 unit cells, and the distorted octahedral 1T' phase with zigzag chains consisting of 2×1 supercells. It is worth to note that the 1T phase of MoTe₂ is metastable and would readily transform into the 1T' phase, and therefore is not discussed in our study. On base of 2H and the 1T' phases, a series of 2H/1T' phase boundaries are constructed (see Supporting Information for details). In describing the phase boundaries, the name convention used in the study of Zhao et al. [43] is used but modified

accordingly to fit our 2H/1T' case. A phase boundary is thus named using the form of $D_M(-A - B)|S$, where D represents the direction of a MoTe_2 phase boundary, being zigzag (ZZ) or armchair (AC), with its subscript M denoting the type of the atoms (Te or Mo) shared by two phases at the boundary, and S indicates whether the phase boundary is rich in Te ($S = +$) or deficient in Te ($S = -$). A and B represent the types of edge configurations for 2H and 1T' nanoribbons respectively at the phase boundary. There are four edge configurations, i.e., α , β , C and T for a phase boundary along the ZZ direction (See Fig. 4.1(a)-(b)). On the other hand, since all phase boundaries along the AC direction have the same edge configurations, the form thus simplifies to become $AC_M|S$ only.

Fig. 4.1(c) shows configurations of those stable phase boundary structures after geometry relaxation. Fig. 4.1(d) further illustrates a couple of sample relaxed structures of ZZ and AC phase boundaries in both top and side views. It is worth noting that for ZZ phase boundaries, the D_{3h} symmetry of 2H MoS_2 inevitably leads to different edge structures at both ends of a 2H MoS_2 nanosheet. Thus, periodicity along the ZZ direction would mandate two different phase boundaries (details see Supporting Information), which however would make accurate evaluation of the phase boundary formation energy difficult. To address such challenge, for ZZ phase boundaries, we construct a nanoribbon-like structure instead of a fully periodic sheet, as suggested in the study of Zhou et al. [44], containing one phase boundary in the middle while one 2H edge and one 1T' edge at each end. The dimension of the vacuum space along the non-periodic direction is set to be larger than 20\AA to ensure no image interaction. Meanwhile benchmark calculations have been performed to ensure that the separation between the nanoribbon edges is sufficiently large to avoid any artificial effect arising from edge-edge or edge-boundary interactions (see Supporting Information

for details). On the other hand, for AC phase boundaries, periodicity along the AC direction can be satisfied, and thus a periodic sheet rather than nanoribbon is adopted as the model structure.

All DFT calculations were performed employing the VIENNA ab initio simulation package (VASP) [45, 46] using the projector-augmented wave method [47]. The exchange-correlation functional was described by generalized gradient approximation (GGA) parametrized by Perdew, Burke, and Ernzerhof [48, 49]. For electronic structure calculations, we also performed additional benchmark using other exchange-correlation functionals, e.g., HSE06 [50], and confirmed that the results were not much affected by the usage of different functionals (details see Section 4.7.2 in Supporting Information). A kinetic cutoff energy of 550 eV was set for the plane-wave basis functions. All structures were relaxed until the atomic forces are less than 0.01 eV/Å and total energies were converged to 10^{-5} eV. Given that hydrogen adsorption and HER characteristics would be affected by hydrogen coverage, we considered different hydrogen coverages, ranging from 25% to 100%. Nonetheless, for simplicity and clarity of presentation, below the results presented mostly correspond to a hydrogen coverage of 50%. Additionally, in the calculations of hydrogen adsorption, the effect of van der Waals (vdW) interactions was included using DFT-D3 method [51, 52].

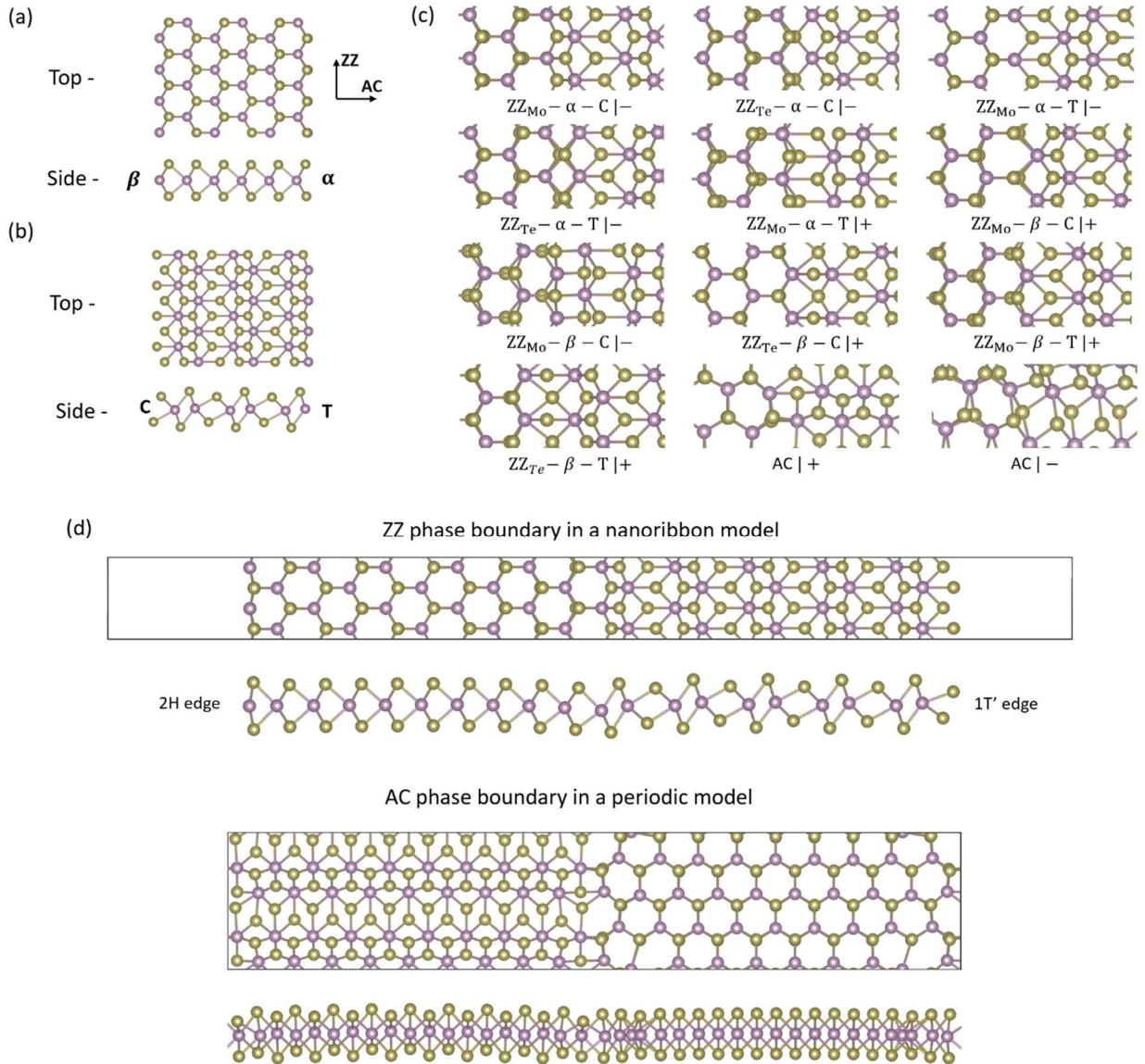


Fig. 4.1 The top and side views of pristine (a) 2H and (b) 1T' MoTe₂, where Mo atoms are shown in purple and Te atoms are shown in brown, with the black arrows indicating the AC and ZZ directions of MoTe₂ lattice. Two types of 2H edges (i.e., α and β) and 1T' edges (i.e., C and T) are indicated on the side views. (c) The relaxed configurations of the twelve 2H/1T' phase boundaries examined, named following the convention suggested by Zhao et al. [43]. (d) The top and side views of a representative ZZ phase boundary, $ZZ_{Mo}-\alpha-C|-$ embedded in a nanoribbon model with 2H and 1T' edges at each side, and an AC phase boundary $AC|+$ embedded in a periodic sheet model.

4.4 Results and discussion

4.4.1 Formation energies of MoTe₂ phase boundaries

Before evaluating hydrogen adsorption and HER at MoTe₂ phase boundaries, we first investigate the formation energies of phase boundaries. For a ZZ phase boundary, its formation energy E_f can be determined from the total energy of the structure E_T as the following [32]:

$$E_T = N_{Mo}\mu_{Mo} + N_{Te}\mu_{Te} + L(\sigma_H + \sigma_{T'} + E_f) \quad (4.3)$$

where N_{Mo} and N_{Te} are the numbers of Mo and Te atoms in the phase boundary respectively, L is the phase boundary length, σ_H and $\sigma_{T'}$ are the formation energies of 2H and 1T' edges per unit length, which can be obtained from separate calculations (details see Section 4.7.3 in Supporting Information), and μ_{Mo} and μ_{Te} are the chemical potentials of Mo and Te respectively. To maintain thermodynamic equilibrium, the allowable range of μ_{Te} and μ_{Mo} are constraint by the following condition:

$$\mu_{MoTe_2} = \mu_{Mo} + 2\mu_{Te} \quad (4.4)$$

where μ_{MoTe_2} represents the average weighted chemical potential of 2H and 1T' phases. μ_{Te} varies depending on the chemical environment, assuming higher and lower values under Te-rich and Mo-rich conditions, respectively. The upper and lower limits of μ_{Te} can be regarded as being defined by the chemical potentials of alpha Te and body-centered cubic Mo respectively, thus ranging from -3.54 eV to -3.14 eV. The details of formation energy calculation can be found in Supporting Information.

For AC phase boundaries, periodic structures are constructed (cf. Fig. 4.1(d)), and the total energy of the structure can be written as:

$$E_T = N_{Mo}\mu_{Mo} + N_{Te}\mu_{Te} + 2E_fL \quad (4.5)$$

From Eqs. (4.1) and (4.3), the formation energy E_f can then be determined. The E_f values of various phase boundaries as functions of μ_{Te} are shown in Fig. 4.2. The lowest energy phase boundary is found to be $ZZ_{Mo} - \alpha - C| -$ boundary under Mo-rich conditions ($-3.54 \text{ eV} < \mu_{Te} < -3.27 \text{ eV}$), while it becomes the $ZZ_{Mo} - \beta - T| +$ boundary when the environment becomes Te-rich ($-3.27 \text{ eV} \leq \mu_{Te} < -3.14 \text{ eV}$). These results are in agreement with the recent studies on ZZ phase boundaries of MoTe_2 [32]. Further analyses reveal that the formation energy of a phase boundary is strongly correlated with the local bond distortion. For instance, $ZZ_{Te} - \beta - C| +$ boundary, the one with the highest formation energy, exhibits the most significant Mo-Te bond elongation/shrinkage at the boundary (details see Section 4.7.4 in Supporting Information). This large bond length variation induces significant mechanical stress/strain, leading to increase in the formation energy. In comparison, the bond distortion in low formation energy boundaries, e.g., $ZZ_{Mo} - \beta - C| -$ boundary, is much moderate (see Fig. 4.10). It is also worthy to note from Fig. 4.2 that phase boundaries rich in Te ($S = +$) and deficient in Te ($S = -$) show opposite dependence on μ_{Te} , i.e., E_f respectively increasing and decreasing monotonically as μ_{Te} increases. Such opposite dependence is directly related to the sign of N_{Te} value, which is positive and negative for phase boundaries rich in Te ($S = +$) and deficient in Te ($S = -$) respectively.

With lower formation energy indicative of better stability and easier formation, consequently below we only consider the two low-energy boundaries, i.e., $ZZ_{Mo} - \alpha - C| -$ and $ZZ_{Mo} - \beta - T| +$ for our investigation on HER activities. Further to the energetic evaluation, we have also performed *ab-initio* molecular dynamics (AIMD) simulations for $ZZ_{Mo} - \alpha - C| -$ and $ZZ_{Mo} - \beta - T| +$ boundaries to confirm their thermal stability at room temperature (details please see Section 4.7.5 in Supporting Information).

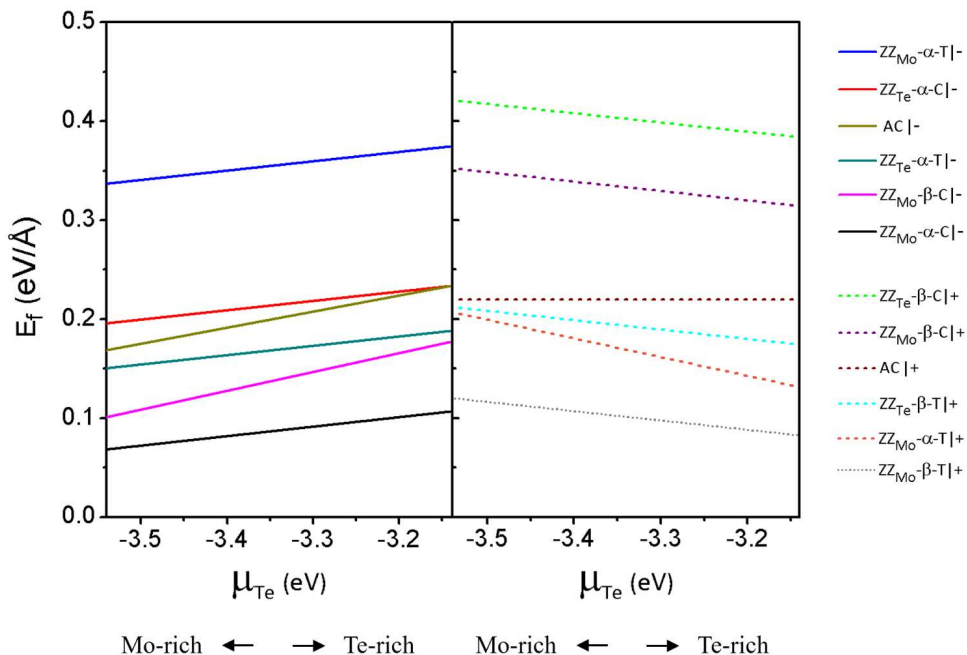


Fig. 4.2 Formation energies of the phase boundaries as functions of the chemical potential of Te, μ_{Te} .

4.4.2 Hydrogen adsorption at MoTe₂ phase boundaries

To investigate HER at the two phase boundaries of $ZZ_{Mo} - \alpha - C| -$ and $ZZ_{Mo} - \beta - T| +$, we first identify the possible hydrogen adsorption sites at the boundary. Those sites are illustrated in Fig. 4.3(a) and (c). As seen from the figure, we note that at the vicinity of the phase boundary hydrogen may adsorb at the hollow site (the triangle site surrounded by three adjacent Mo atoms in the middle of the three-layered structures, details see Section 4.7.6 in Supporting Information), or immediately above Mo or Te atoms. It should be noted that in addition to those sites mentioned above, we have also considered possible hydrogen adsorption at the bridge site (site between two Te atoms). However, our results show that the interaction between hydrogen and the bridge site is rather weak, rendering it not a stable adsorption site for hydrogen, as a result of which a hydrogen atom initially placed at the bridge site will move to its immediate neighboring

Mo or Te site. Therefore, below we only consider the stable adsorption sites, namely Te, Mo, and hollow sites. For simplicity in describing those adsorption sites, below we refer to the hollow site as HL, while the sites immediately above Mo or Te atoms as X_n where $X = \text{Mo or Te}$ and n is an integer indicating the n^{th} site associated with X atom. In comparison to those sites at phase boundaries, their corresponding counterparts in pristine 2H and 1T' lattices of MoTe_2 are also identified (illustrated in Fig. 4.13, see Supporting Information) and examined as the respective reference sites.

One of the first steps of HER is hydrogen adsorption (i.e., the Volmer step) at the electrode surface. Generally, to achieve good catalytic performance, the binding between hydrogen and the electrode surface should be neither too strong nor too weak. In accordance, it is desirable for hydrogen adsorption have a Gibbs free energy ΔG_H close to the thermoneutral value near zero. The Gibbs free energy ΔG_H can be calculated as follows [53]:

$$\Delta G_H = \Delta E_H + \Delta E_{ZPE} - T\Delta S_H \quad (6.4)$$

where ΔE_H is the adsorption energy of the n^{th} H atom and is defined as:

$$\Delta E_H = E_{\text{MoTe}_2+n\text{H}} - E_{\text{MoTe}_2+(n-1)\text{H}} - \frac{1}{2}E_{\text{H}_2} \quad (4.7)$$

where $E_{\text{MoTe}_2+n\text{H}}$ is the total energy of MoTe_2 phase boundary with adsorbed hydrogen atoms, $E_{\text{MoTe}_2+(n-1)\text{H}}$ is the total energy of MoTe_2 phase boundary without adding a hydrogen atom, and E_{H_2} is the energy of a gas phase hydrogen molecule. ΔE_{ZPE} is the difference in zero-point energy of hydrogen in the adsorbed state and the gas phase. Our benchmark calculations have confirmed that vibrational frequencies do not differ notably for different hydrogen coverages and structures, and that there is little variation in ΔE_{ZPE} . Consequently ΔE_{ZPE} is simply taken to be a constant

value (i.e., 0.02 eV). ΔS_H is the entropy term approximated as half of entropy of the gas phase H_2 as $\Delta S_H \approx \frac{1}{2} S_{H_2}$ [54]. T is the temperature, taken to be the room temperature ($T = 298 K$) in our study. Under ambient conditions, the term $T\Delta S_H$ approximately assumes a value of 0.2 eV and thus Eq. (4.4) becomes:

$$\Delta G_H = \Delta E_H + 0.22 \text{ eV} \quad (4.8)$$

The Gibbs free energies of hydrogen adsorption at various sites in the boundary regions of $ZZ_{Mo} - \alpha - C| -$ and $ZZ_{Mo} - \beta - T| +$ respectively were examined. These values are presented in Fig. 4.3(b) and (d), in comparison with corresponding energies at the respective counterpart sites on pristine 2H or 1T' $MoTe_2$. As mentioned earlier in Section 4.2, the results correspond to a hydrogen coverage of 50%. It should be noted that Mo atoms connecting the 2H and 1T' phases of $MoTe_2$ at the boundary have two corresponding sites from pristine 2H and 1T' $MoTe_2$ respectively, in which case only the site of lower ΔG_H is considered for comparison. It is apparent from Fig. 4.3 that phase boundaries render ΔG_H lower and closer to zero compared to pristine 2H or 1T' $MoTe_2$, indicative of improved HER activity at the phase boundary. Moreover, examining the difference in adsorption energy (between a site at the phase boundary and its reference site in the pristine 2H or 1T' lattice), we note that the difference is more significant for sites on the 2H phase side. One salient observation from Fig. 4.3 is that hollow sites at phase boundaries exhibit near-zero ΔG_H values, in sharp contrast to their counterparts in the pristine $MoTe_2$. In particular, ΔG_H of the hollow site in $ZZ_{Mo} - \alpha - C| -$ shows a negative value close to zero ($\Delta G_H = -0.10 \text{ eV}$), exhibiting strong adsorption of hydrogen, which is comparable to that of Pt ($\Delta G_H = -0.09 \text{ eV}$) [14]. These results suggest that hollow sites at phase boundaries may promise drastic boost to the HER activity. It is also important to recognize that that HER is a multistep electrochemical process. In this regard, we have also examined the subsequent steps beyond the

Volmer step, and confirmed the Volmer step to be the determining step for the overall HER performance (details see Section 4.7.8 in Supporting Information).

Further calculations have also been performed to examine the generality of our results above. In particular, nearly identical hydrogen adsorption behaviors (e.g., ΔG_H) at different sites were also found for few-layer MoTe₂ nanosheets (details see Section 4.7.9 in Supporting Information). Furthermore, we also confirmed that similar phase boundary induced HER enhancement exists in other TMDC systems, thus likely a generic phenomenon (details see Section 4.7.10 in Supporting Information).

To further evaluate the implication of the phase boundary to HER performance, a volcano curve is plotted as shown in Fig. 4.3(e). In the plot, the theoretical exchange current density i_0 is calculated based on the Gibbs free energy ΔG_H . Adsorption sites with a negative ΔG_H are located around the left leg of the volcano, and the i_0 at pH 0 can be calculated by the following expression:

$$i_0 = -ek_0 \frac{1}{1 + \exp(-\Delta G_H/k_B T)} \quad (4.9)$$

where k_0 is the rate constant with a value of $200 \text{ s}^{-1} \text{ site}^{-1}$ fitted to give a reasonable overall magnitude of the rate, and k_B is the Boltzmann constant. For the other case where adsorption sites are located around the right leg of the volcano (ΔG_H is positive), the i_0 is given by:

$$i_0 = -ek_0 \frac{1}{1 + \exp(-\Delta G_H/k_B T)} \exp(-\Delta G_H/k_B T) \quad (4.10)$$

Adsorption sites with ΔG_H close to zero are located at the peak of the volcano curve, indicating the highest exchange current density and the optimal HER performance. We find that two hollow sites are located very close to the peak of the volcano curve with a very high exchange current density, suggesting them as the potential sites to offer best performance at the boundaries. Meanwhile, the

influence of hydrogen coverage on ΔG_H is illustrated in Fig. 4.3(f). As seen in the figure, with the sites HL1, Mo2 and Te1 as representatives, we see that ΔG_H as a function of hydrogen coverage, exhibits a similar trend for different adsorption sites with the hollow sites always remaining to be the ones with the smallest $|\Delta G_H|$ values. As the hydrogen coverage increases, ΔG_H first increases till a coverage $\sim 70\%$, followed by a slight decrease with further increase in the coverage. In particular, for the HL1 site shown in Fig. 4.3(f), one can see that the free energy close to zero occurs around 50%-60% hydrogen coverage, indicative of an optimal coverage for HER. Increasing hydrogen coverage beyond this range would increase $\Delta G_H (>0)$ for all sites, thus expected to lower the HER activity. On the other hand, decreasing hydrogen coverage below this range, though negatively impacting the hollow sites, renders the ΔG_H values of other sites closer to zero. Therefore, Fig. 4.3(f) also suggests more effective HER performance with hydrogen adsorption below 60% coverage.

Overall, our calculations above confirmed that phase boundaries in MoTe_2 can provide active sites with significantly better hydrogen adsorption characteristics, thus potentially contributing to boosting the overall HER performance of MoTe_2 .

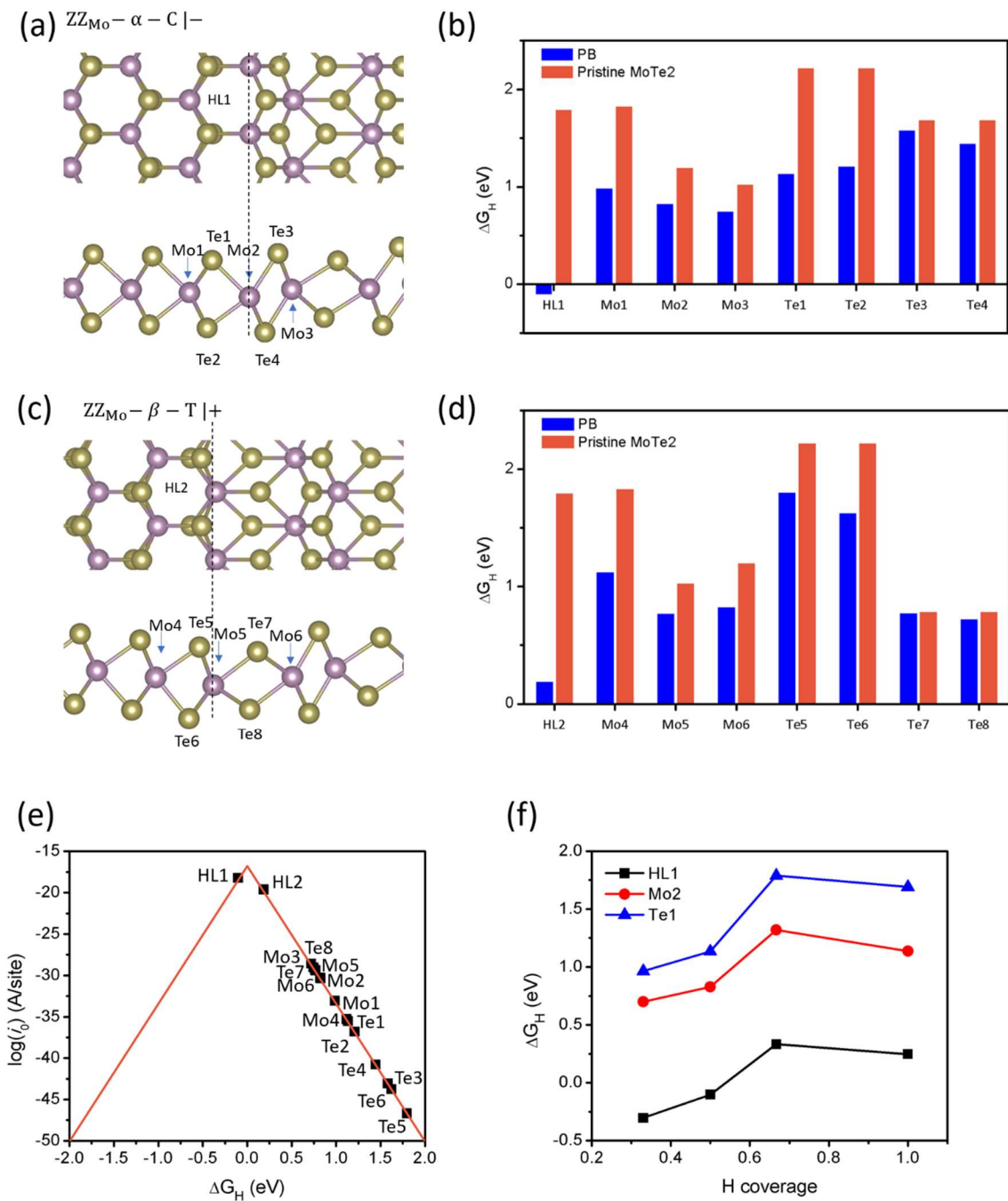


Fig. 4.3 (a), (c) Adsorption sites of $ZZ_{Mo-\alpha-C|-}$ and $ZZ_{Mo-\beta-T|+}$ phase boundaries respectively. Adsorption sites are labeled as Hollow (HL), Mo, and Te categories, respectively. (b), (d) ΔG_H values of $ZZ_{Mo-\alpha-C|-}$ and $ZZ_{Mo-\beta-T|+}$ phase boundaries, compared with the respective adsorption energies on pristine MoTe₂ at the representative hydrogen coverage of 50%. For Mo2 or Mo5 site, there exist two corresponding sites, in either pristine 2H or 1T' MoTe₂ lattice, and we only presented the pristine lattice site of lower ΔG_H here for comparison. (e) Volcano plot between the theoretical exchange current density i_0 and Gibbs free energy ΔG_H . (f) ΔG_H as a function of hydrogen coverage for three sites, HL1, Mo2 and Te1.

4.4.3 Relation of hydrogen adsorption to electronic properties

The key characteristics of a catalyst are fundamentally prescribed by their electronic structures. In this regard, we have performed comprehensive analysis of the electronic structures of those phase boundaries containing MoTe₂ systems to further understand the interaction between hydrogen and the various adsorption sites at the phase boundary. Generally, not every electronic state in the band contributes equally to the bonding between hydrogen and adsorption site. Huang et al. revealed that the closer an electronic state is to the Fermi level (E_F), the greater its contribution to the bonding [55]. Examining the density of states (DOS), we analyzed the states associated with different adsorption sites, with reference to the Fermi level. Some sample analysis is shown in Fig. 4.4(a), where the two Te adsorption sites, Te1 and Te5 (cf. Fig. 4.3), are compared (DOS of other Te sites are also examined, see Fig. 4.17 in Supporting Information). As noted from the figure, the Te1 site has more occupied states near the E_F compared to Te5, thus expected to have stronger hydrogen adsorption. This prediction based on the electronic analysis agrees well with the ΔG_H results, i.e., $\Delta G_{H-Te1} = 1.13 \text{ eV} < \Delta G_{H-Te5} = 1.80 \text{ eV}$ (cf. Fig. 4.3 above).

To further quantitatively understand the relation between ΔG_H and the electronic structure, we note that, according to the Fermi-abundance (D_F) model [15, 55, 56], the band structures of adsorption sites can be described by the following descriptor:

$$D_F = \frac{\int_{-\infty}^{E_F} E D(E) f_T'(E - E_F) dE}{\int_{-\infty}^{E_F} D(E) f_T'(E - E_F) dE} \quad (4.9)$$

where $D(E)$ is the density of states, and $-f_T'(E - E_F)$ is the derivative of the Fermi-Dirac distribution function $f_T(E - E_F) = \{\exp[(E - E_F)/k_B T] + 1\}^{-1}$, used as an effective weight factor $w(E)$ to evaluate the contribution of every electronic state to the surface reaction. The

spreading of the $w(E)$ is sensitive to the magnitude of $k_B T$, where k_B is the Boltzmann's constant and T is not the actual temperature but a parametric temperature [15, 55], and thus $k_B T$ serves as an adjustable parameter to tune the weight factor. As suggested by previous studies [15, 55], when $k_B T$ assumes a value of 0.4 eV, optimal correlation can be achieved between D_F and the surface bonding and reactivity, and in particular, ΔG_H of hydrogen adsorption would exhibit a linear trend with the D_F of the catalyst.

Guided by the above model, we then analyzed the relationship between HER activities of various sites at phase boundaries with their corresponding electronic structures. We started by examining the group of Te sites at $ZZ_{Mo} - \alpha - C| -$ and $ZZ_{Mo} - \beta - T| +$ boundaries. Fig. 4.4(b) plots the D_F values of various Te sites versus corresponding ΔG_H values. An apparent linear relation between D_F and ΔG_H can be observed, with a larger D_F indicating stronger H-Te bonding. This suggests that D_F serve as a good metric to quantify the HER activity of Te sites at MoTe_2 phase boundaries. The Fermi-abundance model is also expected to apply to a broad class of other adsorption sites in both phase boundaries and pristine lattices, where hydrogen predominately interacts with a single host atom at the adsorption site (see below for further discussion) [15, 56].

However, despite the success of the Fermi-abundance model in describing the Te sites, it fails to yield good representation of the HER activity for other sites, i.e., the Mo and hollow sites, at MoTe_2 phase boundaries, as demonstrated in Fig. 4.18 (details see Section 4.7.12 in Supporting Information). This indicates clear limitation of the Fermi-abundance model. To understand such limitation, we took a closer look at those Mo and hollow sites at phase boundaries. For insights into how hydrogen interacts with atoms at different sites, we examined the charge distribution contour associated with hydrogen adsorption, based on the spatial charge density difference $\Delta\rho(\mathbf{r})$:

$$\Delta\rho(\mathbf{r}) = \rho_{PB-H}(\mathbf{r}) - \rho_{PB}(\mathbf{r}) - \rho_H(\mathbf{r}) \quad (4.10)$$

where $\rho_{PB-H}(\mathbf{r})$ and $\rho_{PB}(\mathbf{r})$ are the space charge densities of the phase boundaries with and without hydrogen adsorption, at location \mathbf{r} . $\rho_H(\mathbf{r})$ is the electron charge density of an hydrogen atom at the same position in a reference pristine supercell. The obtained charge distribution contours of phase boundaries with H adsorbed on Te1, Mo1 and HL1 sites are shown in Fig. 4.5(a)-(c) as representatives of three types of adsorption sites (See Figs 4.19 and 4.20 in Supporting Information for the charge distributions of other adsorption configurations). The yellow and cyan colors in the contour signal gain and loss of charges respectively, indicative of the overlap of various orbitals from different atoms. For adsorption at the Te1 site, we see from Fig. 4.5(a) that hydrogen mostly interacts with the Te atom alone, showing a clear charge gain to hydrogen from Te, whereas the interactions between hydrogen and other atoms are negligible. Now examining the Mo1 site, we see from Fig. 4.5(b) that hydrogen not only interacts with the Mo atom, but also with the surrounding Te atoms. Apart from a charge transfer from Mo and H atom, there is an apparent loss of charges from neighbor Te atoms to H atom. The difference in local atomic interactions at Te1 and Mo1 sites are also well reflected in the DOS plots. As seen from Fig. 4.5(d), one can see that for the Te1 site, only the states of Te atom diminish significantly upon hydrogen adsorption. The 5s and 5p states of the Te atom hybrid with 1s state of hydrogen to result in the energy splitting and the formation of new bonding states. In comparison, for the Mo1 site, decrease in the states of both Mo and Te atoms near the Fermi level can be observed. The hybridization of 1s state of hydrogen with 5s and 5p bonding states of Te atom and 4d bonding states of Mo atom results in the formation of new bonding states. Therefore, with multiple orbitals from different atoms taken part in the interaction between the H atom and the catalyst, the Fermi-abundance model is no longer suitable to describe HER activity for Mo sites. Nonetheless, despite quantitative

assessment of the activation at Mo sites being not possible, qualitative evaluation based on the DOS plots is possible. As shown in Fig. 4.21 (see Supporting Information), Mo sites in phase boundaries have more occupied states near the E_F compared to their counterparts in the pristine lattice, and thus expected to have stronger hydrogen adsorption.

Regarding the HL site, it resembles the Mo1 site in the fact that hydrogen adsorption also involves multiple atoms. As shown in Fig. 4.5(c), hydrogen adsorbed at the HL site is not sitting on top of an individual atom but in close vicinity with three adjacent Mo atoms along the x-y plane, showing a clear charge gain to hydrogen from these Mo atoms. Similar to what described above for the Mo1 site, hydrogen adsorption at the HL site may also be understood by examining the Mo atoms hydrogen interacts with. Fig. 4.5(d) shows the DOS plots of Mo and Te atoms after hydrogen adsorption at the HL1 site. We can see that the 4d states of the Mo atom hybridize with the 1s state of hydrogen, resulting in the formation of new bonding states, while the DOS of the Te atom remains nearly unchanged with no new bonding states formed post adsorption. Thus, the interaction between multiple Mo atoms and H atom occurs and causes the failure of the Fermi-abundance model to describe HER activity at the HL sites. However, the activations at HL sites can still be evaluated based on the DOS plots of Mo atoms (See Fig. 4.21 in Supporting Information).

The above analysis of electronic structures provides us with critical insights for assessing hydrogen adsorption. However, there remains a puzzle why only HL sites exhibit optimal adsorption performance (with near zero ΔG_H , cf. Fig. 4.3). Fig. 4.6 shows the projected density of states (pDOS) of 4d orbitals of the Mo atom (i.e., the Mo1 atom) shared by the Mo1 and HL1 sites, for hydrogen adsorption at the Mo1 and HL1 sites respectively. One can see that 4d states yield a high peak near the Fermi level (prior to hydrogen adsorption), indicating its great contribution to

the bonding. Specifically, these orbitals are dxy and $dx^2 - y^2$ orbitals. In order to form a strong bonding upon hydrogen adsorption, it is preferable to have an overlap between the $1s$ orbital of hydrogen and dxy or $dx^2 - y^2$ orbital of the Mo atom, while overlapping between $1s$ of hydrogen and other d orbitals (e.g. dz^2) of Mo is less desirable and would render the Mo-H bond weaker.

Upon hydrogen adsorption, we see from Fig. 4.5(b) that, for adsorption at the Mo1 site, the distribution of electronic charge shows an orbital character of dz^2 , indicating a interaction between Mo dz^2 and hydrogen $1s$. Also, from the pDOS plot in Fig. 4.6, we can see that the new $4d$ bonding state post hydrogen adsorption at the Mo1 site mainly originates from the dz^2 states. In contrast, for hydrogen adsorption at the HL1 site, it mainly interacts with the d orbitals of three adjacent Mo atoms parallel with the xy plane, i.e. dxy or $dx^2 - y^2$ orbitals (cf. Fig. 4.5(c)), with the distribution of electronic charge of Mo atoms showing apparent $dx^2 - y^2$ and dxy characters. In accordance, as seen from the pDOS plot in Fig. 4.6, $dx^2 - y^2$ orbital contributes most to the formation of $4d$ bonding states for the case of the HL1 site (for another Mo atom neighboring the HL1 site, dxy orbital contributes most to the formation of $4d$ bonding states, see Fig. 4.22 in Supporting Information). These bonding correspond to the strong hydrogen adsorption, hence optimal hydrogen adsorption at HL sites.

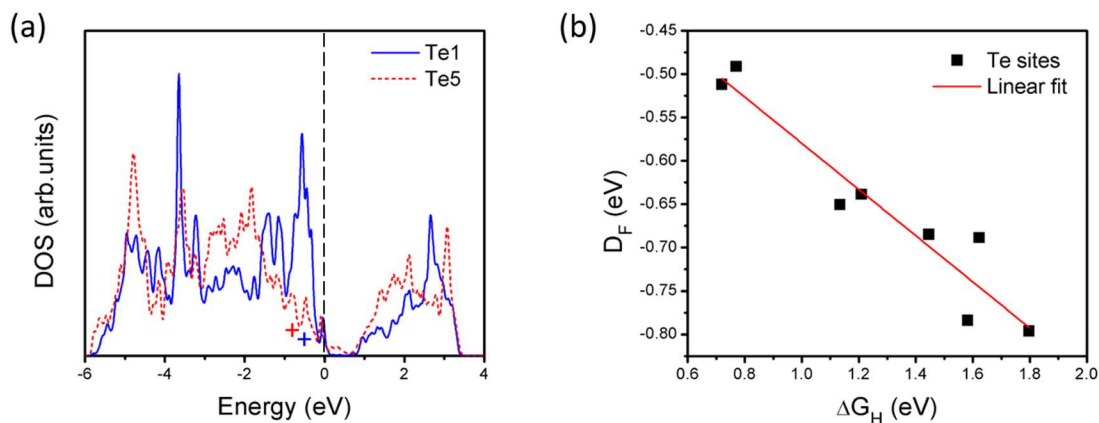


Fig. 4.4 (a) DOS of two representative Te atoms for H adsorption sites. The symbol “+” labels the position of Fermi-abundance center (D_F). (b) Relationship between D_F values and ΔG_H for Te atoms.

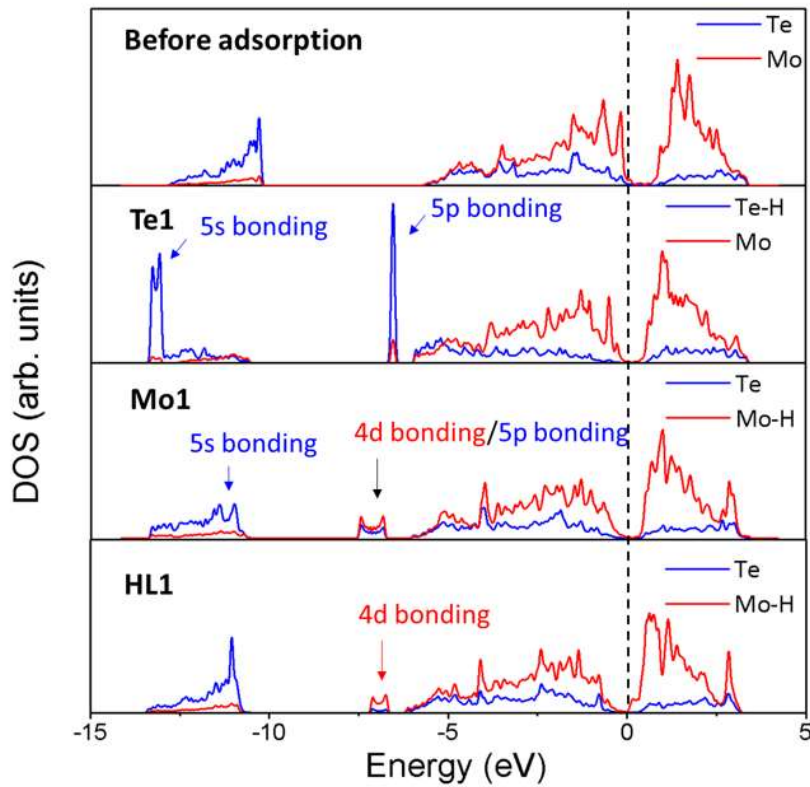
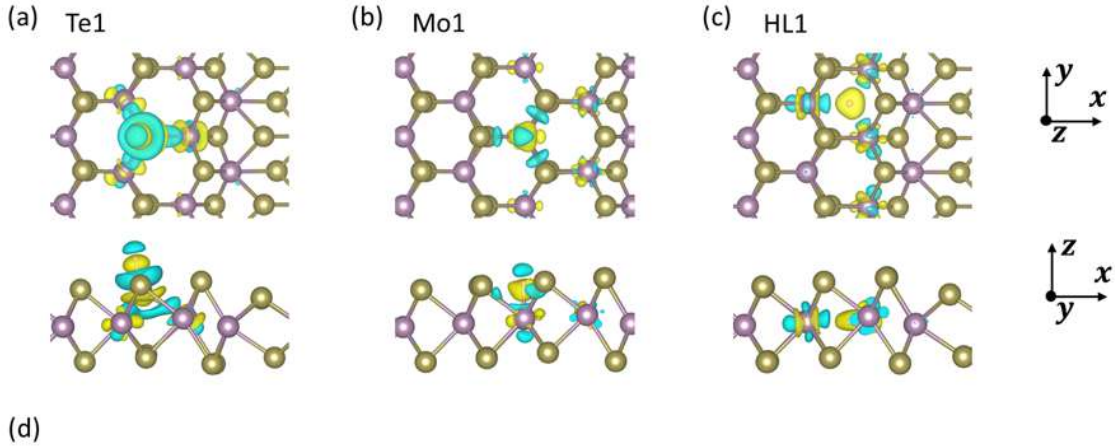


Fig. 4.5 Charge distribution contour plots for hydrogen adsorption sites (a) Te1, (b) Mo1 and (c) HL1 sites at the MoTe₂ phase boundary. The yellow and cyan surfaces correspond to gain and loss of charge respectively, with isosurface of $0.003e/\text{\AA}^3$. (d) DOS plots for Te and Mo atoms respectively (top panel) before hydrogen adsorption, (second panel) after hydrogen adsorption on

Te1 site, (third panel) after hydrogen adsorption at the Mo1 site, and (bottom panel) after hydrogen adsorption at the HL1 site.

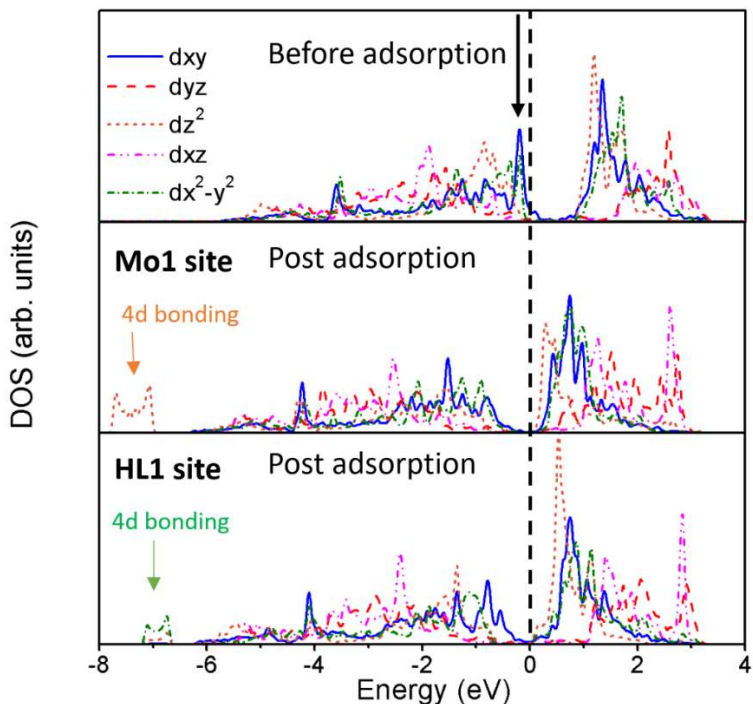


Fig. 4.6 Projected DOS (pDOS) plots for the d orbitals of the Mo1 atom along the MoTe₂ phase boundary, (top panel) before adsorption, after adsorption on Mo1 site, and after adsorption on HL1 site. Black arrow indicates the reinforcing states of dx_y and $dx^2 - y^2$ orbitals near the Fermi level.

4.5 Conclusion

In summary, comprehensive first-principles calculations have been performed to investigate HER activities at phase boundaries in TMDC, using MoTe₂ as a representative. Possible 2H/1T' phase boundaries have been constructed, with their structural stability and formation energies examined to identify stable configurations. Three categories of sites, namely Te, Mo and hollow sites, in energetically stable phase boundaries were identified as potential catalytic centers for HER. All those sites were demonstrated to activate hydrogen adsorption by reducing the magnitude of the Gibbs free energy ΔG_H , promising to enhance HER activity. In

particular, the hollow sites were found to exhibit ΔG_H near the thermoneutral value, comparable to that of Pt at moderate hydrogen coverages. The mechanisms underlying such activation at phase boundaries were then revealed, and found to be attributed to the unique local hydrogen adsorption geometries and electronic structures at phase boundaries. Specifically, for the Te sites where hydrogen interacts almost solely with the host atom (i.e., Te), the catalytic activity is well understood and predicted by the Fermi-abundance model. The Fermi-abundance model and similar interpretation are also expected to apply to a broad class of other adsorption sites in both phase boundaries and pristine lattices, where hydrogen predominately interacts with a single host atom at the adsorption site. However, the Fermi-abundance model breaks down for the Mo and hollow sites where hydrogen adsorption assumes a more complex geometry and involves multiple atoms, though qualitative assessment can still be made by analyzing the local charge distribution and density of states. In addition, we elucidated that the optimal hydrogen adsorption performance at hollow sites originates from the fact that the phase boundary modifies the d_{xy} and $d_{x^2-y^2}$ orbitals of Mo atoms, thus giving rise to much stronger binding with hydrogen.

Our study demonstrates a viable pathway to activate the basal plane of 2D TMDCs for HER through phase boundary engineering and clarifies the important mechanistic aspects underlying hydrogen activation at phase boundaries, providing valuable theoretical insights towards designing new class of high-performance HER electrocatalysts based on 2D TMDCs.

4.6 Acknowledgements

This research is supported by the Natural Sciences and Engineering Research Council of Canada (NSERC) Discovery Grant (grant #: NSERC RGPIN-2017-05187), and the McGill

Engineering Doctoral Award (MEDA). The authors would also like to acknowledge the Compute Canada and Calcul Québec for providing computing resources.

4.7 Supporting information

4.7.1 Benchmark studies on nanoribbon models

As stated in the manuscript, we have performed benchmark calculations to ensure that our results are not affected by edge-edge or edge-boundary interactions. We evaluated the formation energies (E_f) of phase boundaries and the Gibbs free energy of adsorption ΔG_H as functions of the number (n) of unit cells in each phase. Fig. 4.7 shows some sample results from our benchmark calculations for the phase boundary $ZZ_{Mo} - \beta - T|+$. As seen from Fig. 4.7, the simulation cell should have no less than 8 unit cells between the edge and boundary to avoid artificial effects. In our calculations, we used $n = 10$.

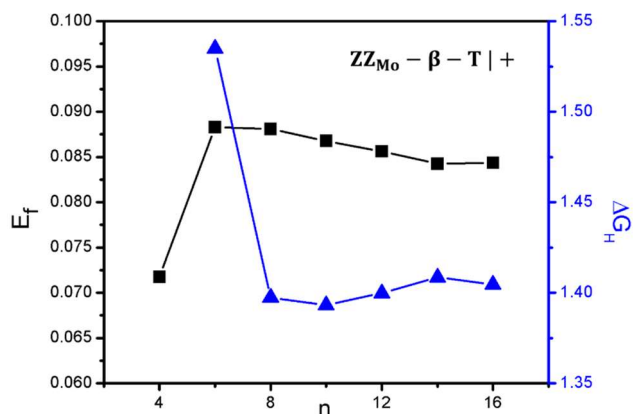


Fig. 4.7 Benchmark studies of the possible effect, induced by edge-edge and edge-boundary interactions, on the formation energy E_f of the phase boundary $ZZ_{Mo} - \beta - T|+$ and the Gibbs free energy of adsorption ΔG_H as functions of the number (n) of unit cells in each phase. E_f was calculated under Te-rich condition ($\mu_{Te} = -3.14$ eV), and the hydrogen coverage in benchmark studies was set as 1.

4.7.2 The effect of exchange-correlation functional on the electronic structure calculations

Fig. 4.8 below shows the total DOS of pristine 2H and 1T' MoTe₂, obtained from calculations using generalized gradient approximation (GGA-PBE) [48] and hybrid exchange-correlation functional (HSE06) [50]. We can see from the figure that for 2H or 1T' MoTe₂, the DOS plots from GGA-PBE and HSE06 are quite similar, which indicates that our conclusion will not change even if the calculations are done based on other functionals.

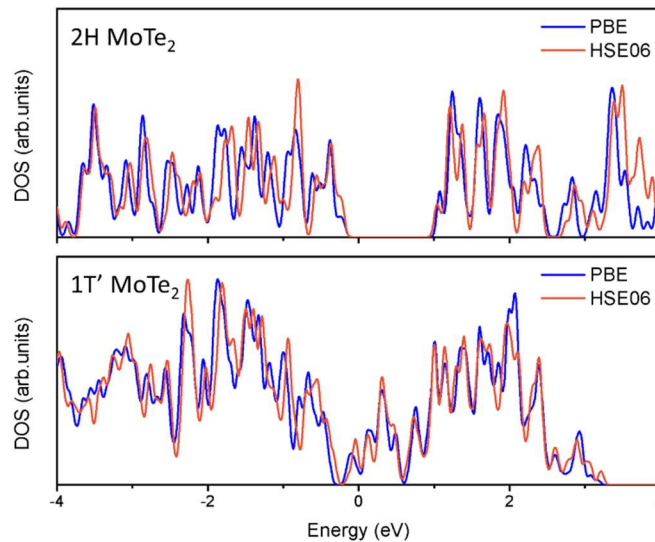


Fig. 4.8 Total density of states (DOS) of pristine 2H MoTe₂ and pristine 1T' MoTe₂, obtained from calculations using GGA-PBE [48] (red) and HSE06 [50] (blue) functionals.

4.7.3 Details of formation energy calculations of zigzag phase boundaries

Nanoribbon-like structures have been employed in other studies to explore the stabilities of zigzag phase boundaries for TMDCs [32, 44]. In the present study, we adopt this method to calculate the formation energies of zigzag phase boundaries in MoTe₂. The total energy of a phase boundary structure, E_T , can be obtained as follows:

$$E_T = N_{Mo}\mu_{Mo} + N_{Te}\mu_{Te} + L(\sigma_H + \sigma_{T'} + E_f) \quad (4.11)$$

where the parameters N_{Mo} , N_{Te} , L and E_T are readily obtained from DFT calculations, and μ_{Te} has a range of $[-3.54, -3.14]$ eV. In order to calculate the formation energy E_f , we need to determine the two parameters, σ_H and $\sigma_{T'}$. Here, we construct a 2H MoTe₂ nanoribbon and a 1T' MoTe₂ nanoribbon, as shown in Fig. 4.9(a)-(b). 2H MoTe₂ nanoribbon consists of two edges, i.e. β and α , and its total energy E_H can be expressed as:

$$\sigma_{H\alpha} + \sigma_{H\beta} = \frac{E_H - N_{Mo}\mu_{Mo} - N_{Te}\mu_{Te}}{L} \quad (4.12)$$

Since β and α are inseparable in the simulation cell, a series of triangle quantum dots are further used to calculate the edge β , as shown in Fig. 4.9(c). Then we could have the relationship between the total energy $E_{tri}(n)$ and quantum dot n as:

$$f(n) = E_{tri}(n) - \frac{n(n+1)}{2}\mu_{MoTe_2} = (2\mu_{Te} + 3\sigma_{H\beta})n + 3E_{cor} + 2\mu_{Te} \quad (4.13)$$

where E_{cor} is the energy of three corners of the quantum dot. As shown in Fig. 4.9(d), by fitting the plot of $f(n)$, the edge energy $\sigma_{H\beta}$ can be obtained from the slope. Then the edge energy $\sigma_{H\alpha}$ can be calculated from Eq. (4.12).

For 1T' MoTe₂ nanoribbon, same edges can be constructed at both ends of the phase boundary structures in a simulation cell. Therefore, its total energy $E_{T'}$ can be expressed as:

$$\sigma_{T'} = \frac{E_{T'} - N_{Mo}\mu_{Mo} - N_{Te}\mu_{Te}}{2L} \quad (4.14)$$

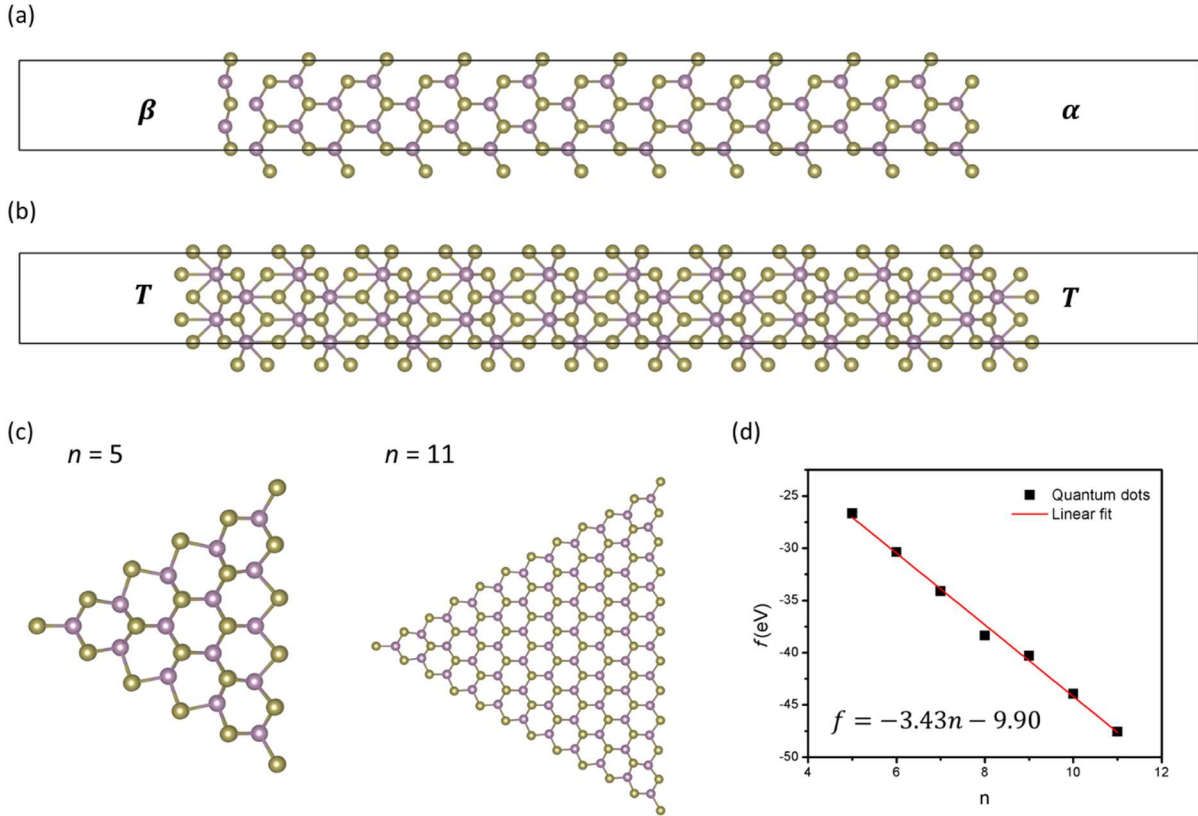


Fig. 4.9 (a), (b) Simulation cells of 2H MoTe₂ nanoribbon and 1T' MoTe₂ nanoribbon respectively. (c) Top views of quantum dot n , using $n = 5$ and $n = 11$ as representatives. (d) Linear fitting of $f(n)$ (see Eq. (4.13)) as a function of n .

4.7.4 Local bond variation at the phase boundary

The formation energy of a phase boundary is strongly correlated with the local bond distortion at the boundary. The bond distortion for each phase boundary is evaluated by comparing the Mo-Te bond lengths at the phase boundary with those in the pristine MoTe₂. As shown in Fig. 4.10(b), from $ZZ_{Mo} - \beta - C| +$, $ZZ_{Mo} - \beta - C| +$ to $ZZ_{Te} - \beta - C| +$ boundary, the formation energy increases with the increased variation in Mo-Te bond lengths.

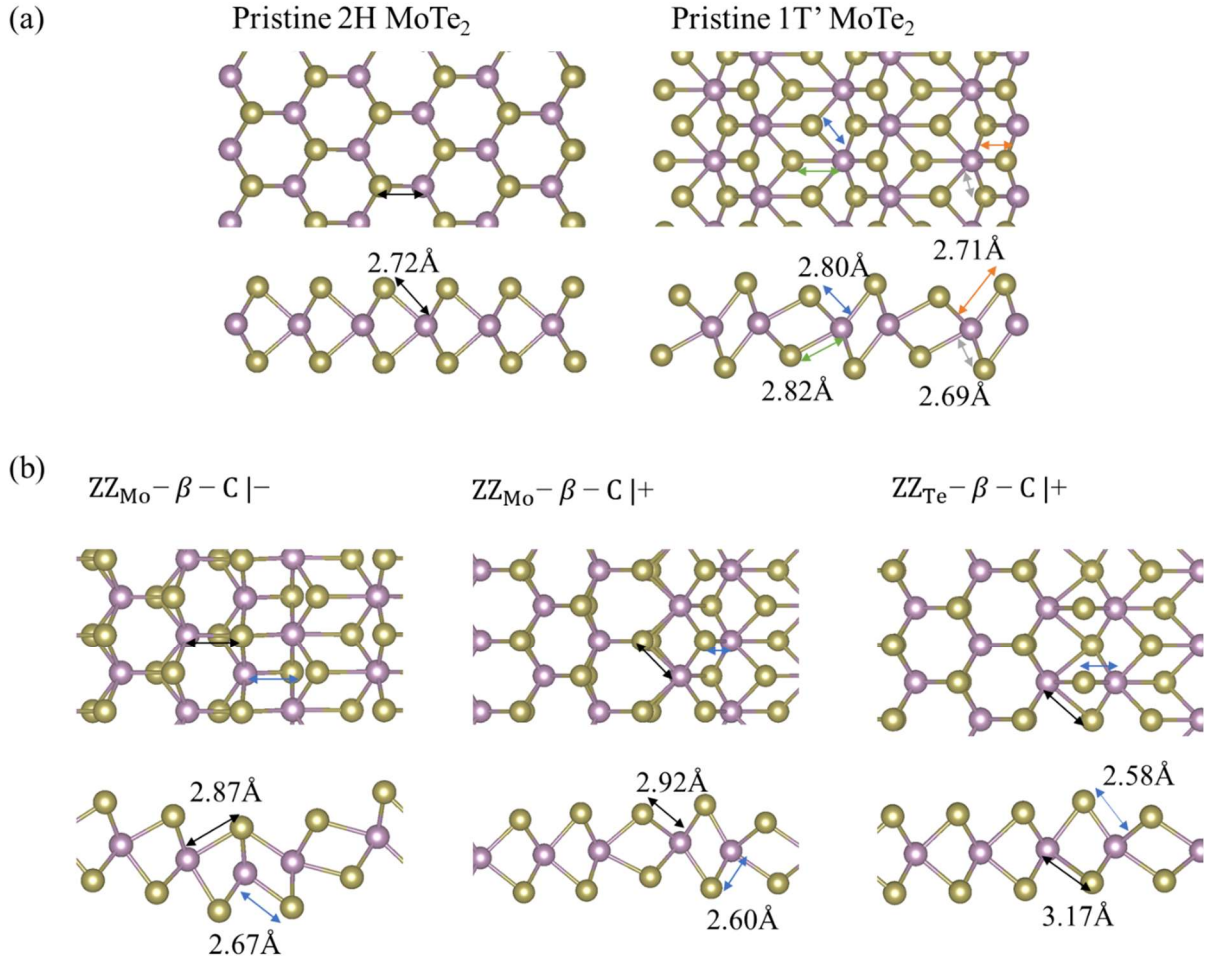


Fig. 4.10 (a) Top and side views of pristine 2H and 1T' MoTe₂, where the black arrow indicates the Mo-Te bond length of pristine 2H MoTe₂, while blue, green, orange and yellow arrows indicate various Mo-Te bonds length of pristine 1T' MoTe₂. (b) Top and side views of representative ZZ phase boundaries. For each phase boundary configuration, black and blue arrows indicate the longest and shortest Mo-Te bonds at the phase boundary, respectively.

4.7.5 Thermal stability of phase boundaries at room temperature

To examine the thermal stability of the phase boundaries, we have performed a series of finite-temperature ab-initio molecular dynamics (AIMD) simulations in which phase boundaries were equilibrated at 300K (with isothermal-isobaric (NPT) ensemble with a 1.0 fs time step). In general we found that the system reaches equilibrium after 500fs. Fig. 4.11 below shows some benchmark results for the two low-energy boundaries, i.e., $ZZ_{Mo} - \alpha - C | -$ and $ZZ_{Mo} - \beta -$

$T|+$. As seen in Fig. 4.11(b), the structures of these two boundaries remain stable at 300K, except for lattice vibration due to thermal fluctuation (as compared to the configurations at 0K, c.f., Fig. 4.1(c)). Additional benchmark AIMD simulations have also been performed at higher temperature of 600K, at which the boundaries are also found to remain stable.

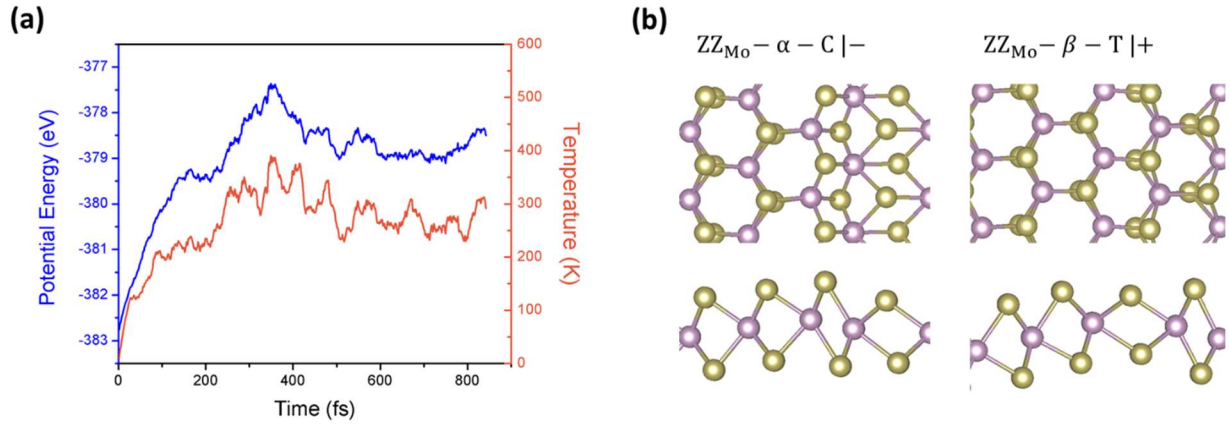


Fig. 4.11 (a) The potential energy (blue curve, left vertical axis) and temperature (red curve, right vertical axis) of $MoTe_2$ boundaries with simulation time. (b) Snapshots of configurations of $ZZ_{Mo} - \alpha - C |-$ and $ZZ_{Mo} - \beta - T |+$ boundaries at room temperature (300K).

4.7.6 Hydrogen adsorption at HL sites

The hydrogen adsorption configurations at HL sites for phase boundaries and pristine structures are shown in Fig. 4.12. In the case of phase boundaries, hydrogen is adsorbed in the middle of the three-atom-thick monolayer surrounded by three Mo atoms. In contrast, for the pristine $MoTe_2$, the hydrogen atom tends to be adsorbed on Te atoms on the surface rather than the Mo atoms in the middle layer. To investigate the degree of activation of Mo atoms by the formation of phase boundaries, we manually put the hydrogen directly into the middle of the hollow site for the case of pristine $MoTe_2$, so that it will not be adsorbed on the Te atom from the top layer. The adsorption site is denoted as Pristine HL. As shown in Table 4.1, in comparison with the results for other HL sites, $\Delta G_{H-Pristine HL}$ shows a value of 0.74 eV, much larger than the

values for the hollow sites in the phase boundary region. Therefore, the activation of Mo atoms after the formation of phase boundaries leads to the adsorption into the HL sites.

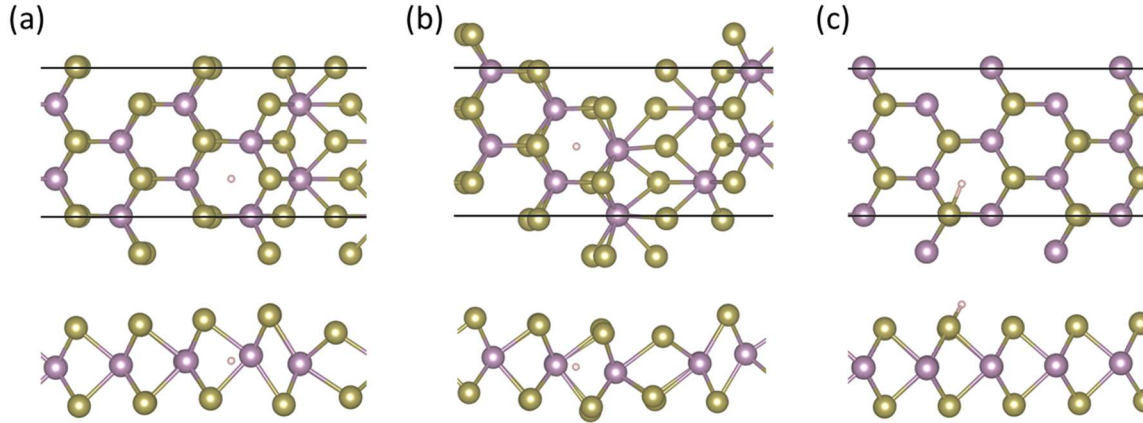


Fig. 4.12 (a), (b), (c) The hydrogen adsorption configurations for HL1, HL2 and the pristine MoTe₂.

Table 4.1 ΔG_H values for different hollow sites.

| Site | ΔG_H (eV) |
|-------------|-------------------|
| HL1 | -0.10 |
| HL2 | 0.19 |
| Pristine | 1.79 |
| Pristine HL | 0.74 |

4.7.7 Adsorption sites of pristine 2H and 1T' MoTe₂

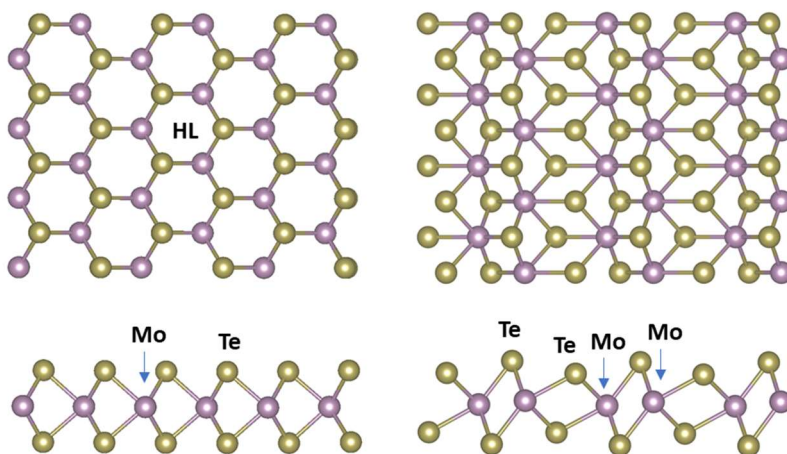


Fig. 4.13 Adsorption sites of pristine 2H and 1T' MoTe₂. Adsorption sites are categorized into hollow (HL), Mo, and Te sites respectively, and labelled accordingly.

4.7.8 Free energy diagrams for the hydrogen evolution at the phase boundaries

The HER is a multistep electrochemical process. What we have calculated in the manuscript is the first step, i.e. Volmer step, where the first hydrogen is adsorbed onto a MoTe₂ catalyst, describing by $H^+ + e^- + * \rightarrow H^*$. The second step is the release of H₂ molecules, which is achieved by either the Heyrovsky ($H^* + H^+ + e^- \rightarrow H_2 + *$) or Tafel ($2H^* \rightarrow H_2 + 2*$) reaction. To determine the HER pathway on MoTe₂ phase boundaries, we calculated the free energy diagrams of Volmer-Heyrovsky reactions and Volmer-Tafel reactions using HL1, Mo2, and Te1 sites as representatives for each category of sites. As shown in Fig. 4.14(a), the active sites for Volmer reaction will keep catalytic activity for the Heyrovsky reaction. Thus, the Volmer reaction is the determining step for HER following Volmer-Heyrovsky reactions. In contrast, as shown in Fig. 4.14(b), The ΔG_H values of the Tafel reaction for all three adsorption sites are greater than the corresponding values for the Volmer reaction. Therefore, the calculated free energy diagrams indicate that Volmer-Heyrovsky reaction is the preferred pathway for HER, with the Volmer step

being the critical step. Consequently, the ΔG_H of the Volmer step can be used to evaluate the overall HER activity of the MoTe₂ boundary.

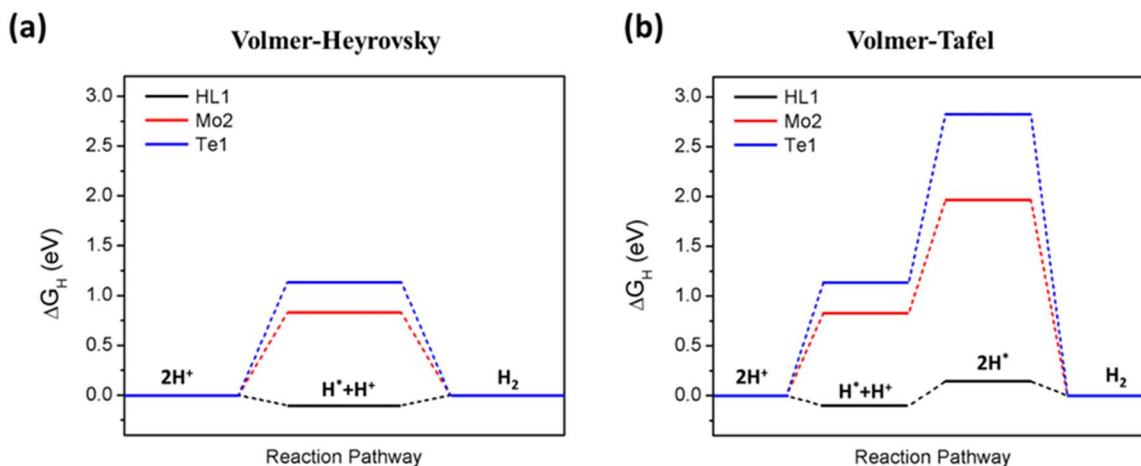


Fig. 4.14 Free energy diagram of the HER following (a) the Volmer-Heyrovsky pathway and (b) the Volmer-Tafel pathway at HL1, Mo2, and Te1 sites along the MoTe₂ phase boundaries.

4.7.9 HER performance of few-layer MoTe₂ nanosheets

We have performed additional calculations to investigate the HER performance of few-layer MoTe₂ nanosheets. Fig. 4.15 presented the results on a double-layered MoTe₂ nanosheet containing phase boundaries, in comparison with the monolayer case. We can see that the ΔG_H values of different adsorption sites, i.e., HL, Mo, and Te sites in single- and double-layered MoTe₂ nanosheets are nearly identical (under the same H coverage, i.e., 100%), indicative of the catalytic activity in HER not altered by layer numbers. Three-layer MoTe₂ nanosheet model has also been constructed with benchmark calculations performed, which also confirmed no change in ΔG_H values at different adsorption sites.

The ignorable influence of layer number is likely attributed to the weak interlayer interaction (which is VdW in nature). Therefore, though our focus is on monolayer TMDCs, we believe the main conclusions would also apply to few-layer TMDC nanosheets.

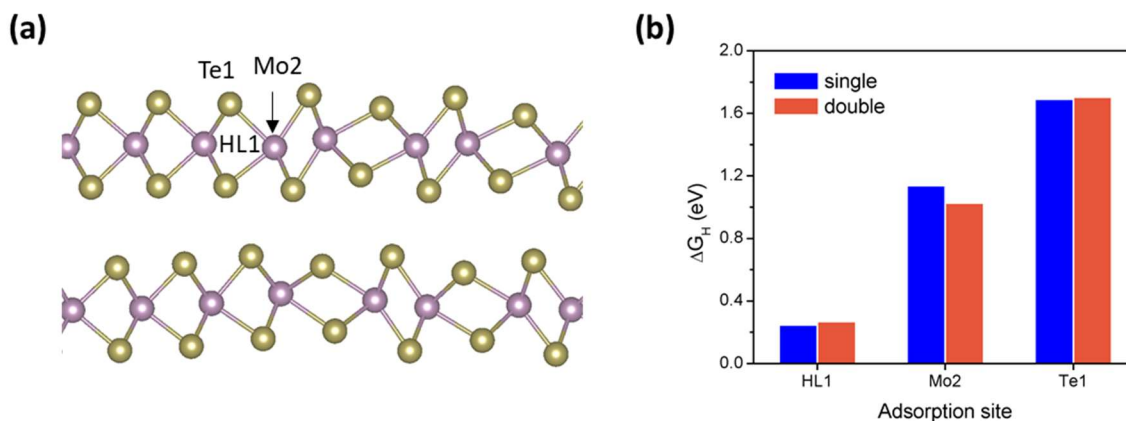


Fig. 4.15 (a) Side view of a double-layered MoTe₂ nanosheet containing phase boundaries in each layer, where Mo atoms are colored purple and Te atoms are colored brown. The three adsorption sites, selected as representatives and labeled as HL1, Mo2, and Te1, are indicated in the figure. (b) ΔG_H values at those sites in single-layered and double-layered MoTe₂.

4.7.10 HER performance of other TMDC phase boundaries

We constructed MoSe₂ and WTe₂ phase boundaries, and selected three representative adsorption sites at the phase boundary (as well as their corresponding counterparts) to examine the HER activity (see Fig. 4.16(a)). As shown in Fig. 4.16(b), X1, HL1 and M1 sites at the basal plane of three pristine TMDCs exhibit similar high ΔG_H values, indicating inertness from pristine TMDC basal planes. On the other hand, the three sites, X1, HL1 and M1 at the phase boundary exhibit much lower ΔG_H values. This demonstrated that phase boundaries have similar enhancement effects to these TMDCs in terms of the HER activity. Therefore, the route of basal plane activation by phase boundaries is expected to work for different TMDCs.

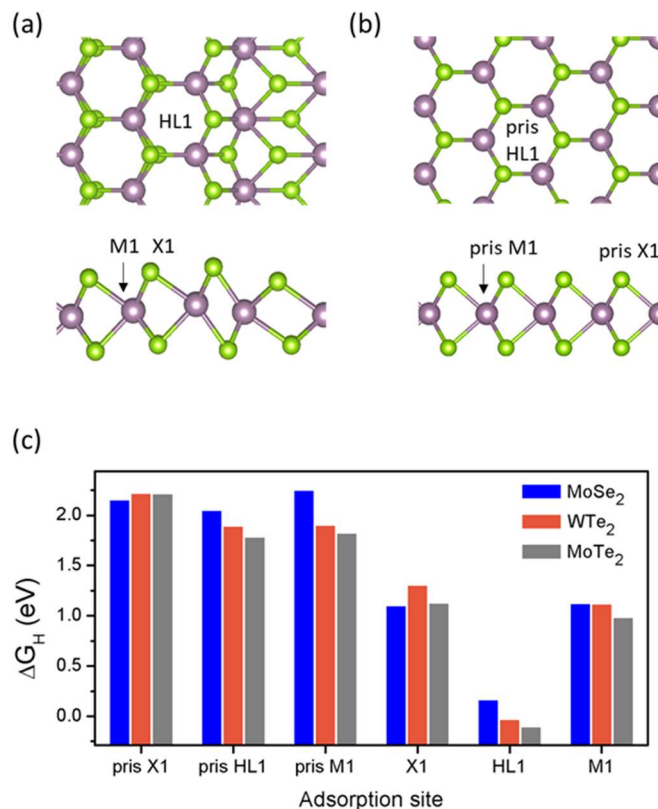


Fig. 4.16 (a) Representative adsorption sites in the TMDC phase boundary, labeled as HL1, M1 (metal site), and X1 (chalcogen site) respectively, as well as (b) their corresponding counterparts in the pristine TMDC basal plane, labeled as pris HL1, pris M1 (metal site), and pris X1 (chalcogen site) respectively. (c) ΔG_H values of X1, HL, M1 sites at MoSe₂, WTe₂, MoTe₂ phase boundaries, and at their corresponding counterparts in pristine TMDC basal planes.

4.7.11 DOS of different Te sites in phase boundaries

Fig. 4.17 shows the DOS plots for different Te sites in phase boundaries.

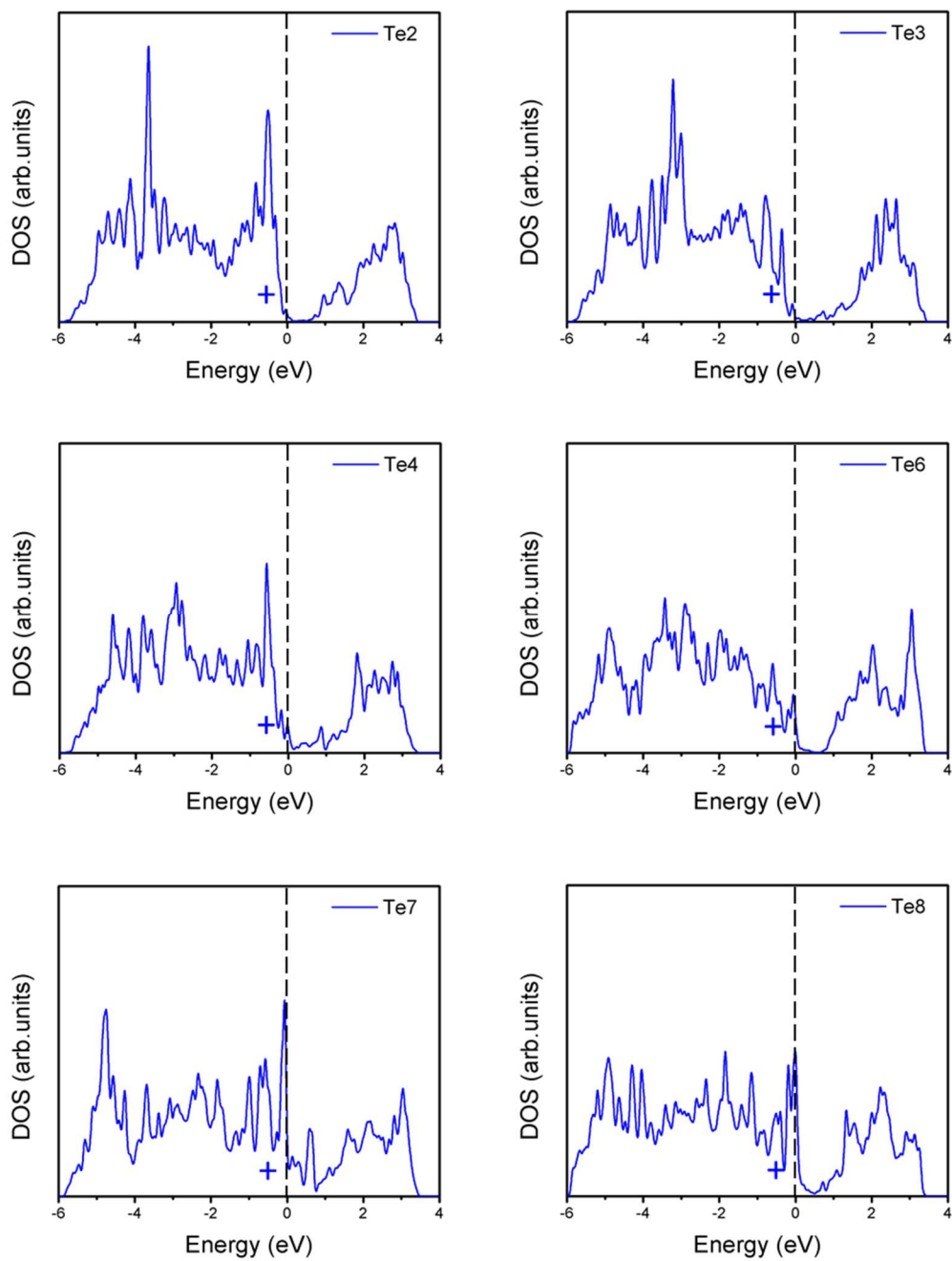


Fig. 4.17 Corresponding DOS plots of different Te sites (locations and configurations of those sites, please see Fig. 4.3(a) and (c)). The symbol “+” labels the position of Fermi-abundance center (D_F).

4.7.12 The Fermi-abundance model for Mo sites

The calculated D_F of various Mo sites as a function of ΔG_H is shown in Fig. 4.18(a), which apparently does not show a linear trend. Therefore, the Fermi-abundance model fails to describe the HER activity of Mo atoms. As described in the main text, this is because hydrogen adsorption at a Mo site involves hydrogen interacting with more than just the Mo atom, while the Fermi-abundance model is essentially limited to describing the relationship between a hydrogen atom and a single adsorption site. Similarly the model breaks down for the case of the HL sites, where hydrogen atom forms bonding with three Mo atoms.

We also plotted the d-band center values [57] of Mo sites at the phase boundary as functions of ΔG_H . We can see that the d-band center values do not display any clear trend with respect to ΔG_H , indicating that d-band center theory being not applicable.

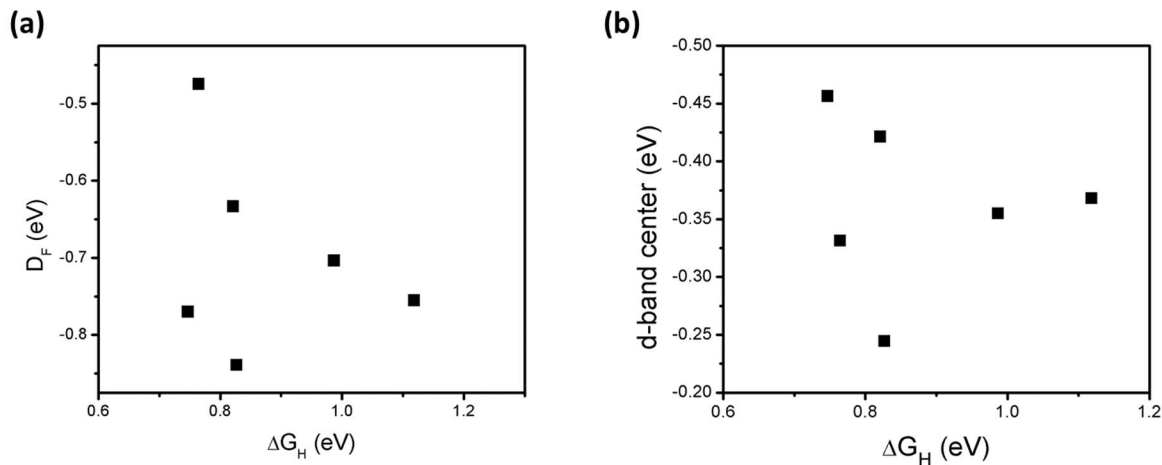


Fig. 4.18 Calculated (a) D_F and (b) d-band center of various Mo sites versus the corresponding ΔG_H values.

4.7.13 Charge distribution at various adsorption sites along phase boundaries

Fig. 4.19 and Fig. 4.20 show the charge distribution at various sites in MoTe_2 phase boundaries.

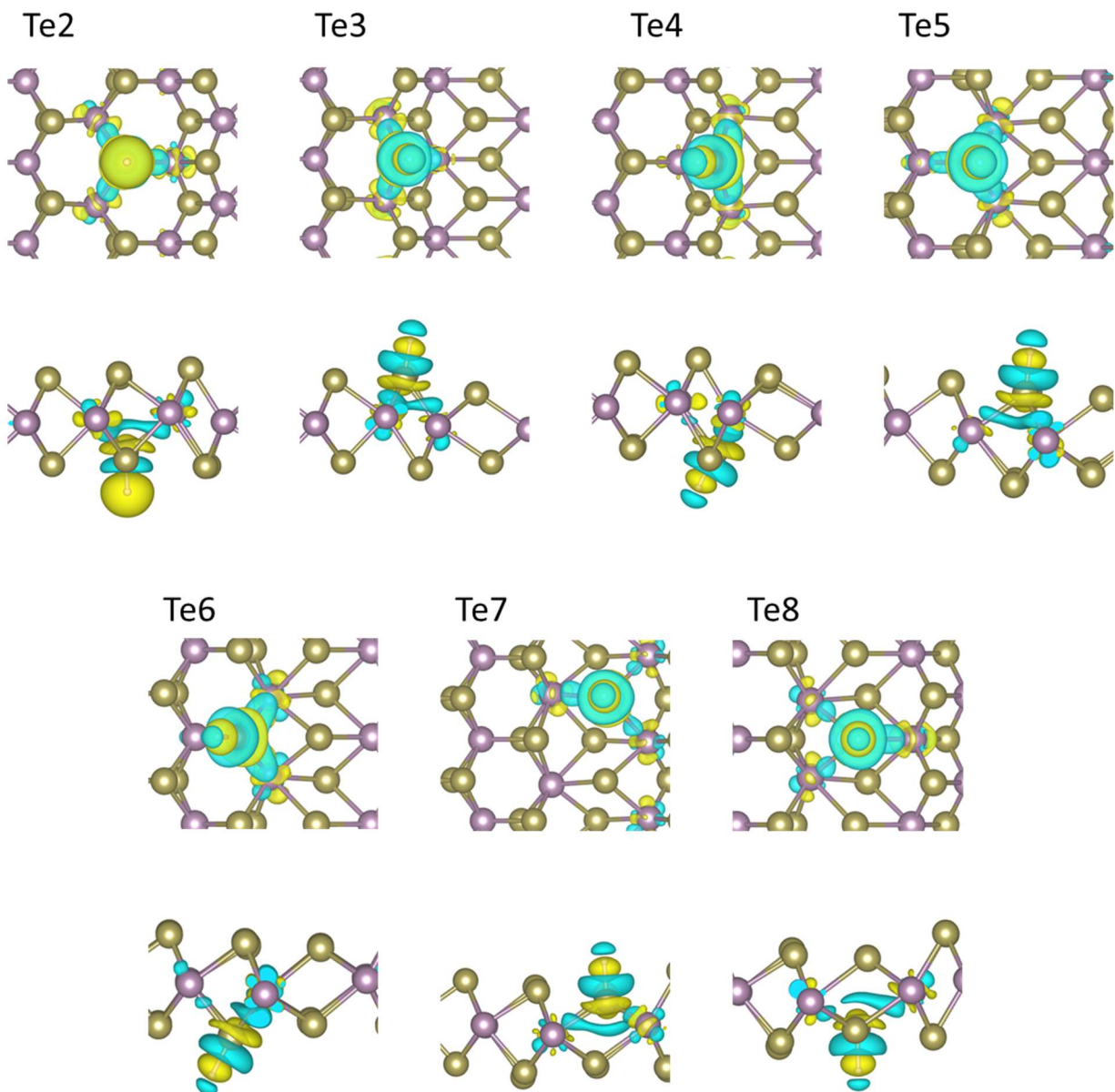


Fig. 4.19 Charge distribution at various Te sites in MoTe_2 phase boundaries.

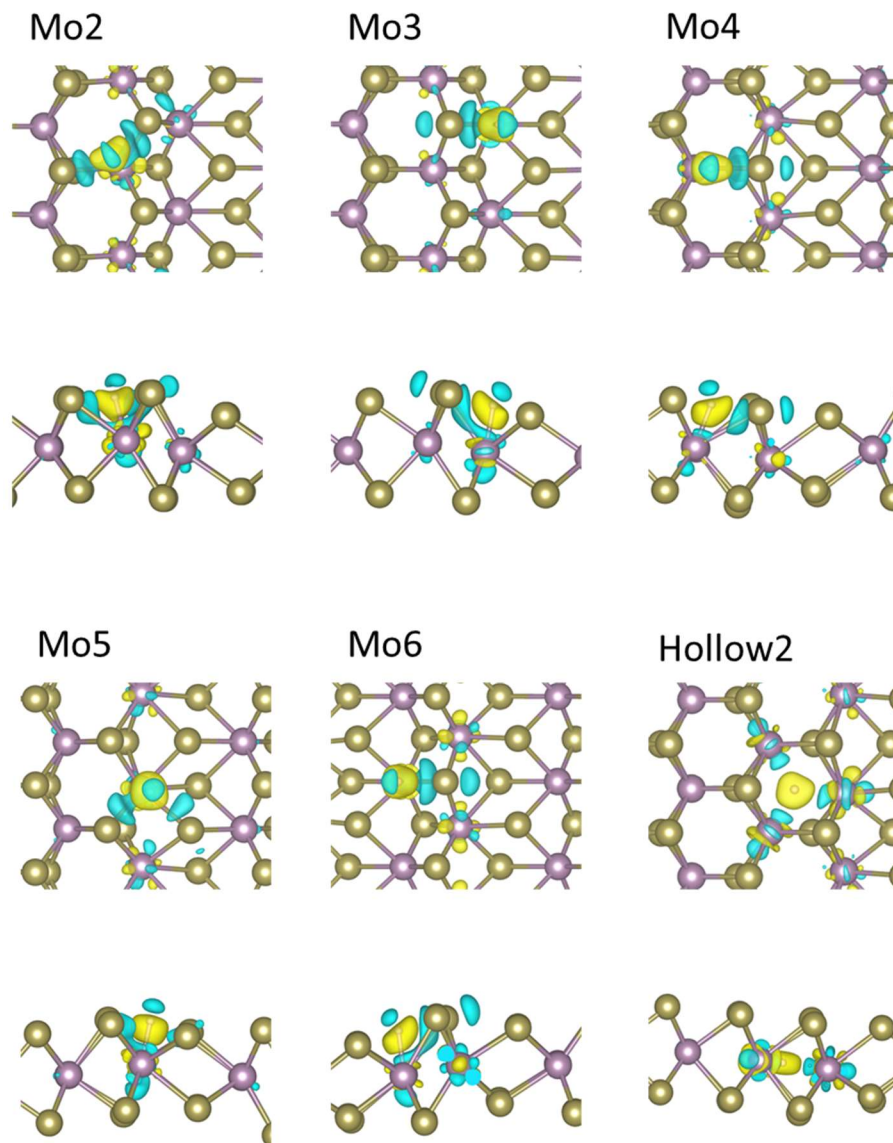


Fig. 4.20 Charge distribution at Mo and HL sites in MoTe₂ phase boundaries.

4.7.14 DOS plots of various Mo sites

Fig. 4.21 shows the DOS of Mo sites in phase boundaries in comparison with the Mo site in pristine MoTe_2 sites.

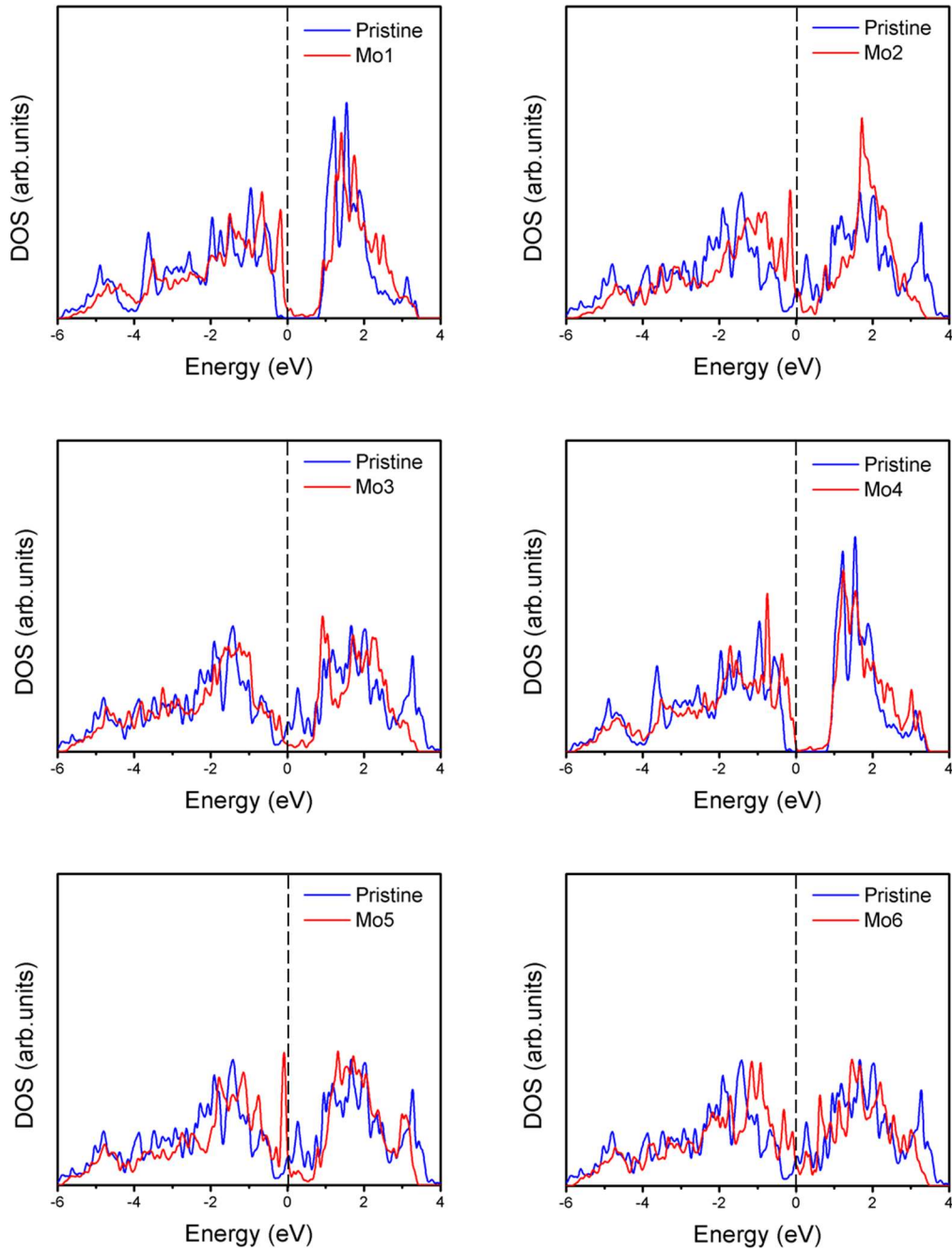


Fig. 4.21 DOS of Mo sites in phase boundaries in comparison with the Mo site in pristine MoTe_2 sites (locations and configurations of those sites, please see Fig. 4.3(a), (c) and Fig. 4.10).

4.7.15 Projected DOS for d orbitals of Mo2 atoms

Fig. 4.22 shows the projected DOS plot for the d orbitals of the Mo2 atom along the MoTe₂ phase boundary.

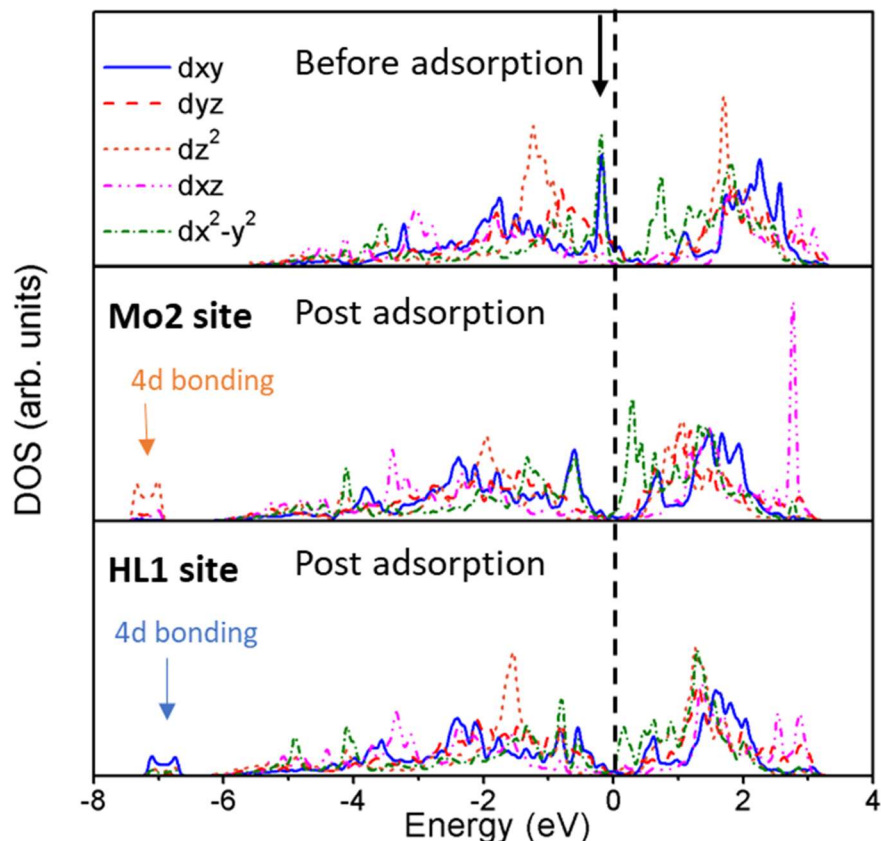


Fig. 4.22 Projected DOS (pDOS) plot for the d orbitals of the Mo₂ atom along the MoTe₂ phase boundary, (top panel) before adsorption, after adsorption on Mo₂ site, and after adsorption on HL1 site. Black arrow indicates the reinforcing states of d_{xy} and $d_{x^2 - y^2}$ orbitals near the Fermi level.

4.8 References

- [1] J.A. Turner, Sustainable Hydrogen Production, *Science* 305(5686) (2004) 972-974.
- [2] S. Trasatti, Work function, electronegativity, and electrochemical behaviour of metals: III. Electrolytic hydrogen evolution in acid solutions, *Journal of Electroanalytical Chemistry and Interfacial Electrochemistry* 39(1) (1972) 163-184.
- [3] N. Cheng, S. Stambula, D. Wang, M.N. Banis, J. Liu, A. Riese, B. Xiao, R. Li, T.K. Sham, L.M. Liu, G.A. Botton, X. Sun, Platinum single-atom and cluster catalysis of the hydrogen evolution reaction, *Nat Commun* 7 (2016) 13638.

- [4] Y. Jiao, Y. Zheng, M. Jaroniec, S.Z. Qiao, Design of electrocatalysts for oxygen- and hydrogen-involving energy conversion reactions, *Chem Soc Rev* 44(8) (2015) 2060-86.
- [5] A.B. Laursen, S. Kegnaes, S. Dahl, I. Chorkendorff, Molybdenum sulfides—efficient and viable materials for electro- and photoelectrocatalytic hydrogen evolution, *Energy & Environmental Science* 5(2) (2012) 5577-5591.
- [6] T.F. Jaramillo, K.P. Jørgensen, J. Bonde, J.H. Nielsen, S. Horch, I. Chorkendorff, Identification of active edge sites for electrochemical H₂ evolution from MoS₂ nanocatalysts, *science* 317(5834) (2007) 100-102.
- [7] B. Hinnemann, P.G. Moses, J. Bonde, K.P. Jørgensen, J.H. Nielsen, S. Horch, I. Chorkendorff, J.K. Nørskov, Biomimetic hydrogen evolution: MoS₂ nanoparticles as catalyst for hydrogen evolution, *Journal of the American Chemical Society* 127(15) (2005) 5308-5309.
- [8] Y.R. An, X.L. Fan, Z.F. Luo, W.M. Lau, Nanopolygons of Monolayer MS₂: Best Morphology and Size for HER Catalysis, *Nano Lett* 17(1) (2017) 368-376.
- [9] B. Hinnemann, P.G. Moses, J. Bonde, K.P. Jørgensen, J.H. Nielsen, S. Horch, I. Chorkendorff, J.K. Nørskov, Biomimetic Hydrogen Evolution: MoS₂ Nanoparticles as Catalyst for Hydrogen Evolution, *Journal of the American Chemical Society* 127(15) (2005) 5308-5309.
- [10] Y. Chen, K. Yang, B. Jiang, J. Li, M. Zeng, L. Fu, Emerging two-dimensional nanomaterials for electrochemical hydrogen evolution, *Journal of Materials Chemistry A* 5(18) (2017) 8187-8208.
- [11] C.R. Zhu, D. Gao, J. Ding, D. Chao, J. Wang, TMD-based highly efficient electrocatalysts developed by combined computational and experimental approaches, *Chem Soc Rev* 47(12) (2018) 4332-4356.
- [12] M. Liu, M.S. Hybertsen, Q. Wu, A Physical Model for Understanding the Activation of MoS₂ Basal-Plane Sulfur Atoms for the Hydrogen Evolution Reaction, *Angewandte Chemie International Edition*.
- [13] C. Wang, H. Lu, K. Tang, Z. Mao, Q. Li, X. Wang, C. Yan, Atom removal on the basal plane of layered MoS₂ leading to extraordinarily enhanced electrocatalytic performance, *Electrochimica Acta* 336 (2020) 135740.
- [14] Y. Ouyang, C. Ling, Q. Chen, Z. Wang, L. Shi, J. Wang, Activating Inert Basal Planes of MoS₂ for Hydrogen Evolution Reaction through the Formation of Different Intrinsic Defects, *Chemistry of Materials* 28(12) (2016) 4390-4396.
- [15] H. Shu, D. Zhou, F. Li, D. Cao, X. Chen, Defect Engineering in MoSe₂ for the Hydrogen Evolution Reaction: From Point Defects to Edges, *ACS Appl Mater Interfaces* 9(49) (2017) 42688-42698.
- [16] C. Tsai, K. Chan, F. Abild-Pedersen, J.K. Nørskov, Active edge sites in MoSe₂ and WSe₂ catalysts for the hydrogen evolution reaction: a density functional study, *Phys Chem Chem Phys* 16(26) (2014) 13156-64.
- [17] J. Zhu, Z.C. Wang, H. Dai, Q. Wang, R. Yang, H. Yu, M. Liao, J. Zhang, W. Chen, Z. Wei, N. Li, L. Du, D. Shi, W. Wang, L. Zhang, Y. Jiang, G. Zhang, Boundary activated hydrogen evolution reaction on monolayer MoS₂, *Nat Commun* 10(1) (2019) 1348.
- [18] D. Voiry, M. Salehi, R. Silva, T. Fujita, M. Chen, T. Asefa, V.B. Shenoy, G. Eda, M. Chhowalla, Conducting MoS(2) nanosheets as catalysts for hydrogen evolution reaction, *Nano Lett* 13(12) (2013) 6222-7.
- [19] M.A. Lukowski, A.S. Daniel, F. Meng, A. Forticaux, L. Li, S. Jin, Enhanced hydrogen evolution catalysis from chemically exfoliated metallic MoS₂ nanosheets, *J Am Chem Soc* 135(28) (2013) 10274-7.

- [20] Q. Tang, D.-e. Jiang, Mechanism of Hydrogen Evolution Reaction on 1T-MoS₂ from First Principles, *ACS Catalysis* 6(8) (2016) 4953-4961.
- [21] M. Calandra, Chemically exfoliated single-layer MoS₂: Stability, lattice dynamics, and catalytic adsorption from first principles, *Physical Review B* 88(24) (2013) 245428.
- [22] D. Wang, X. Zhang, S. Bao, Z. Zhang, H. Fei, Z. Wu, Phase engineering of a multiphase 1T/2H MoS₂ catalyst for highly efficient hydrogen evolution, *Journal of Materials Chemistry A* 5(6) (2017) 2681-2688.
- [23] S. Kim, J.H. Kim, D. Kim, G. Hwang, J. Baik, H. Yang, S. Cho, Post-patterning of an electronic homojunction in atomically thin monoclinic MoTe₂, *2D Materials* 4(2) (2017) 024004.
- [24] Y. Yu, G.-H. Nam, Q. He, X.-J. Wu, K. Zhang, Z. Yang, J. Chen, Q. Ma, M. Zhao, Z. Liu, High phase-purity 1T'-MoS₂ and 1T'-MoSe₂-layered crystals, *Nature chemistry* 10(6) (2018) 638-643.
- [25] L. Li, Z. Qin, L. Ries, S. Hong, T. Michel, J. Yang, C. Salameh, M. Bechelany, P. Miele, D. Kaplan, M. Chhowalla, D. Voiry, Role of Sulfur Vacancies and Undercoordinated Mo Regions in MoS₂ Nanosheets toward the Evolution of Hydrogen, *ACS Nano* 13(6) (2019) 6824-6834.
- [26] P. Valerius, S. Kretschmer, B.V. Senkovskiy, S. Wu, J. Hall, A. Herman, N. Ehlen, M. Ghorbani-Asl, A. Grueneis, A.V. Krashenninikov, Reversible crystalline-to-amorphous phase transformation in monolayer MoS₂ under grazing ion irradiation, *2D Materials* 7(2) (2020) 025005.
- [27] R. Zhao, Y. Wang, D. Deng, X. Luo, W.J. Lu, Y.-P. Sun, Z.-K. Liu, L.-Q. Chen, J. Robinson, Tuning Phase Transitions in 1T-TaS₂ via the Substrate, *Nano Letters* 17(6) (2017) 3471-3477.
- [28] S.-W. Wang, H. Medina, K.-B. Hong, C.-C. Wu, Y. Qu, A. Manikandan, T.-Y. Su, P.-T. Lee, Z.-Q. Huang, Z. Wang, F.-C. Chuang, H.-C. Kuo, Y.-L. Chueh, Thermally Strained Band Gap Engineering of Transition-Metal Dichalcogenide Bilayers with Enhanced Light-Matter Interaction toward Excellent Photodetectors, *ACS Nano* 11(9) (2017) 8768-8776.
- [29] S. Song, D.H. Keum, S. Cho, D. Perello, Y. Kim, Y.H. Lee, Room Temperature Semiconductor-Metal Transition of MoTe₂ Thin Films Engineered by Strain, *Nano Letters* 16(1) (2016) 188-193.
- [30] J.H. Sung, H. Heo, S. Si, Y.H. Kim, H.R. Noh, K. Song, J. Kim, C.S. Lee, S.Y. Seo, D.H. Kim, H.K. Kim, H.W. Yeom, T.H. Kim, S.Y. Choi, J.S. Kim, M.H. Jo, Coplanar semiconductor-metal circuitry defined on few-layer MoTe₂ via polymorphic heteroepitaxy, *Nat Nanotechnol* 12(11) (2017) 1064-1070.
- [31] K.A. Duerloo, E.J. Reed, Structural Phase Transitions by Design in Monolayer Alloys, *ACS Nano* 10(1) (2016) 289-97.
- [32] A. Li, J. Pan, X. Dai, F. Ouyang, Electrical contacts of coplanar 2H/1T' MoTe₂ monolayer, *Journal of Applied Physics* 125(7) (2019).
- [33] L. Zhou, K. Xu, A. Zubair, X. Zhang, F. Ouyang, T. Palacios, M.S. Dresselhaus, Y. Li, J. Kong, Role of Molecular Sieves in the CVD Synthesis of Large-Area 2D MoTe₂, *Advanced Functional Materials* 27(3) (2017).
- [34] X. Ji, K. Wang, Y. Zhang, H. Sun, Y. Zhang, T. Ma, Z. Ma, P. Hu, Y. Qiu, MoC based Mott-Schottky electrocatalyst for boosting the hydrogen evolution reaction performance, *Sustainable Energy & Fuels* 4(1) (2020) 407-416.
- [35] D. Qi, Q. Wang, C. Han, J. Jiang, Y. Zheng, W. Chen, W. Zhang, A.T.S. Wee, Reducing the Schottky barrier between few-layer MoTe₂ and gold, *2D Materials* 4(4) (2017) 045016.
- [36] Z. Zhuang, Y. Li, Z. Li, F. Lv, Z. Lang, K. Zhao, L. Zhou, L. Moskaleva, S. Guo, L. Mai, MoB/g-C₃N₄ interface materials as a Schottky catalyst to boost hydrogen evolution, *Angewandte Chemie* 130(2) (2018) 505-509.

- [37] W. Luo, M. Zhu, G. Peng, X. Zheng, F. Miao, S. Bai, X.-A. Zhang, S. Qin, Carrier Modulation of Ambipolar Few-Layer MoTe₂ Transistors by MgO Surface Charge Transfer Doping, *Advanced Functional Materials* 28(15) (2018) 1704539.
- [38] Y.Q. Bie, G. Grosso, M. Heuck, M.M. Furchi, Y. Cao, J. Zheng, D. Bunandar, E. Navarro-Moratalla, L. Zhou, D.K. Efetov, T. Taniguchi, K. Watanabe, J. Kong, D. Englund, P. Jarillo-Herrero, A MoTe₂-based light-emitting diode and photodetector for silicon photonic integrated circuits, *Nat Nanotechnol* 12(12) (2017) 1124-1129.
- [39] Y. Zhou, J.L. Silva, J.M. Woods, J.V. Pondick, Q. Feng, Z. Liang, W. Liu, L. Lin, B. Deng, B. Brena, F. Xia, H. Peng, Z. Liu, H. Wang, C.M. Araujo, J.J. Cha, Revealing the Contribution of Individual Factors to Hydrogen Evolution Reaction Catalytic Activity, *Adv Mater* 30(18) (2018) e1706076.
- [40] D.H. Keum, S. Cho, J.H. Kim, D.-H. Choe, H.-J. Sung, M. Kan, H. Kang, J.-Y. Hwang, S.W. Kim, H. Yang, K.J. Chang, Y.H. Lee, Bandgap opening in few-layered monoclinic MoTe₂, *Nature Physics* 11 (2015) 482.
- [41] Y. Yin, J. Han, Y. Zhang, X. Zhang, P. Xu, Q. Yuan, L. Samad, X. Wang, Y. Wang, Z. Zhang, P. Zhang, X. Cao, B. Song, S. Jin, Contributions of Phase, Sulfur Vacancies, and Edges to the Hydrogen Evolution Reaction Catalytic Activity of Porous Molybdenum Disulfide Nanosheets, *J Am Chem Soc* 138(25) (2016) 7965-72.
- [42] N. Zhao, L. Wang, Z. Zhang, Y. Li, Activating the MoS₂ Basal Planes for Electrocatalytic Hydrogen Evolution by 2H/1T' Structural Interfaces, *ACS Appl Mater Interfaces* 11(45) (2019) 42014-42020.
- [43] W. Zhao, F. Ding, Energetics and kinetics of phase transition between a 2H and a 1T MoS₂ monolayer-a theoretical study, *Nanoscale* 9(6) (2017) 2301-2309.
- [44] S. Zhou, J. Han, J. Sun, D.J. Srolovitz, MoS₂ edges and heterophase interfaces: energy, structure and phase engineering, *2D Materials* 4(2) (2017).
- [45] G. Kresse, D. Joubert, From ultrasoft pseudopotentials to the projector augmented-wave method, *Physical Review B* 59(3) (1999) 1758-1775.
- [46] G. Kresse, J. Furthmüller, Efficient iterative schemes for ab initio total-energy calculations using a plane-wave basis set, *Physical Review B* 54(16) (1996) 11169-11186.
- [47] P.E. Blöchl, Projector augmented-wave method, *Physical Review B* 50(24) (1994) 17953-17979.
- [48] J.P. Perdew, K. Burke, M. Ernzerhof, Generalized Gradient Approximation Made Simple, *Physical Review Letters* 77(18) (1996) 3865-3868.
- [49] J.P. Perdew, J.A. Chevary, S.H. Vosko, K.A. Jackson, M.R. Pederson, D.J. Singh, C. Fiolhais, Atoms, molecules, solids, and surfaces: Applications of the generalized gradient approximation for exchange and correlation, *Physical Review B* 46(11) (1992) 6671-6687.
- [50] J. Heyd, G.E. Scuseria, M. Ernzerhof, Hybrid Functionals Based on A Screened Coulomb Potential, *J. Chem. Phys.* 118 (2003) 8207.
- [51] S. Grimme, J. Antony, S. Ehrlich, H. Krieg, A consistent and accurate ab initio parametrization of density functional dispersion correction (DFT-D) for the 94 elements H-Pu, *The Journal of Chemical Physics* 132(15) (2010) 154104.
- [52] S. Grimme, S. Ehrlich, L. Goerigk, Effect of the damping function in dispersion corrected density functional theory, *Journal of Computational Chemistry* 32(7) (2011) 1456-1465.
- [53] J.K. Nørskov, T. Bligaard, A. Logadottir, J.R. Kitchin, J.G. Chen, S. Pandelov, U. Stimming, Trends in the Exchange Current for Hydrogen Evolution, *Journal of The Electrochemical Society* 152(3) (2005) J23-J26.

- [54] C. Tsai, F. Abild-Pedersen, J.K. Nørskov, Tuning the MoS₂ Edge-Site Activity for Hydrogen Evolution via Support Interactions, *Nano Letters* 14(3) (2014) 1381-1387.
- [55] B. Huang, L. Xiao, J. Lu, L. Zhuang, Spatially Resolved Quantification of the Surface Reactivity of Solid Catalysts, *Angewandte Chemie International Edition* 55(21) (2016) 6239-6243.
- [56] Y. Zhang, X. Chen, Y. Huang, C. Zhang, F. Li, H. Shu, The Role of Intrinsic Defects in Electrocatalytic Activity of Monolayer VS₂ Basal Planes for the Hydrogen Evolution Reaction, *The Journal of Physical Chemistry C* 121(3) (2017) 1530-1536.
- [57] M. Mavrikakis, B. Hammer, J.K. Nørskov, Effect of Strain on the Reactivity of Metal Surfaces, *Physical Review Letters* 81(13) (1998) 2819-2822.

Chapter 5 : Basal Plane Activation of Two-Dimensional Transition Metal Dichalcogenides via Alloying for Hydrogen Evolution Reaction: First-Principles Calculations and Machine Learning Prediction

The results from Chapter 4 demonstrated the capability of phase boundaries for activating the basal plane of 2D TMDCs for hydrogen evolution reaction. In addition to phase boundaries, alloying has also shown great potential in tuning the electronic and chemical properties of 2D TMDCs. Recently, monolayer and few-layer TMDC alloys have been achieved in experiments for catalyzing HER, exhibiting high HER activities outperforming that of their pristine counterparts. These experimental results also brought us to the question of catalytically active sites in those alloys. While the edges of 2D TMDC alloys are activated for HER confirmed by DFT calculations, whether the basal plane of 2D TMDCs can be activated by alloying remains unknown. Therefore, to understand the basal plane activation of 2D TMDCs via alloying, Chapter 5 computationally explored a series of 2D cation-mixed TMDC alloys of various compositions. A machine learning workflow was constructed to accurately predict the HER activities and thermodynamic stabilities of 2D TMDC alloys. From machine learning predictions it was found that alloying exhibits substantial effect in activating the basal plane. The mechanism underlying this alloying-induced basal plane activation was also analyzed.

- This chapter is to be submitted, appeared as: [Yiqing Chen](#), Pengfei Ou, Ying Zhao, and Jun Song. **Basal plane activation of two-dimensional transition metal dichalcogenides**

via alloying for hydrogen evolution reaction: first-principles calculations and machine learning prediction.

5.1 Abstract

Two-dimensional transition metal dichalcogenides (2D TMDCs) show promises as potential inexpensive electrocatalysts for hydrogen evolution reaction (HER). However, their performance is bottlenecked by the inertness of the basal plane. The present study demonstrates alloying as a viable route to address such limitation. A machine learning workflow based on density functional theory (DFT) calculations has been established to predict the HER activity and stability for a series of 2D cation-mixed TMDC alloys of various compositions. The results showed that alloying exhibits substantial effect in reducing the Gibbs free energy of hydrogen adsorption (ΔG_{H}) on the basal plane, able to render optimal ΔG_{H} for HER for certain TMDC alloys. The stability prediction of those TMDC alloys further showed their potential to be synthesized in experiments. The mechanism underlying this alloying induced basal plane activation originates from the electronic effect, in particular the *p*-band shifting, resulted from the chemical composition variation. The findings are expected to serve as a critical step for rational design and exploration of TMDC alloy based catalytic systems.

5.2 Introduction

Hydrogen is the cleanest fuel and considered as an ideal energy carrier for future energy systems [1]. The scalable H₂ production through water splitting requires efficient catalysts for hydrogen evolution reaction (HER) [2]. Conventionally, platinum group metals are regarded as the most active catalysts for HER; nevertheless, the high cost and material scarcity hinder their

large-scale application [3, 4]. As a result, developing alternative, non-Pt catalysts with low cost and high performance is of great importance [5].

Of many different candidates, two-dimensional transition metal dichalcogenides (2D TMDCs) have received substantive attention [6-8]. For example, MoS₂, WS₂, and WSe₂ have been intensively studied by both experimental [9] and computational methods [10] as potential HER electrocatalysts. However, the HER performance of these 2D TMDCs is still limited by the low density and poor reactivity of active sites. Consequently, there have great efforts attempting to overcome such limitation. One route towards further enhancement in catalytical activity of 2D TMDCs is through structural modification [11-13]. As an example, by exposing a high fraction of edge sites, 2D MoS₂ can catalyze HER at a moderate overpotential of 0.1-0.2 V with Gibbs free energy of adsorption close to zero (<0.1 eV) [14]. Another popular method is the introduction of defects in TMDCs. By introducing sulphur vacancies and strain, the HER performance of MoS₂ has been greatly improved, yielding the optimal ΔG_H close to 0 eV [15].

In addition to structural modification, it was also reported that substantial enhancement of HER activity can be achieved through composition modification, that is, via tailoring the chemical composition of 2D TMDCs by alloying at the metal or chalcogen sites [16-20]. For example, substituting a high concentration of W to Mo in MoS₂ is known to promote the electrocatalytic performance of MoS₂ [21]. Many 2D TMDCs have a structure analogous to that of graphite, where transition metal atoms are sandwiched between chalcogen atoms in a configuration of triangular prism [22]. The similar geometry of various 2D TMDCs enables the fabrication of ternary cation-mixed alloys [17, 19, 23-25]. These studies suggest alloying in 2D TMDC catalysts as a promising means for tuning reactivity and producing new active sites for HER. Unlike most of previous theoretical and experimental studies on HER of 2D TMDCs where the performance enhancement

was achieved via exposed edge sites or localized defect sites, alloying involves activation of the basal plane. The 2D nature of TMDCs makes the basal plane activation particularly attractive as it can provide high density of active sites on the tendentially exposed surface while retaining the structural integrity [12]. However, to-date basal plane activation of 2D TMDC alloys in the context of HER has not been systematically explored. Thus it is crucial to develop fundamental understanding in this aspect to guide the rational design of 2D TMDC alloys for highly active electrocatalysts for the HER.

With the help of theoretical surface science developed over the last decades, the density functional theory (DFT) method has become an accurate and efficient computational approach towards the investigation of adsorption and reaction processes on material surfaces [26]. Nonetheless, computational exploration of 2D TMDC alloys with multiple transition metal and/or chalcogen constituents by DFT is non-trivial. The complexity of 2D TMDC alloys arising from the multitudinous variations in chemical composition and combinations of various metals necessitates several orders of magnitude more calculations than what's needed for pristine single transition metal 2D TMDC structures. This renders it a formidable challenge to model 2D TMDC alloys using the traditional brute-force computational approach. Recently, it has been demonstrated that such challenge may be partially addressed by the application of machine learning (ML) techniques [27-32]. ML techniques can greatly reduce the computation need compared to the traditional approach, particularly for alloy or other complex material systems, promising a solution to bypass the computational bottleneck for *in-silico* materials design and exploration. They have found great success in predicting material properties, such as adsorption energies, *d*-band centers, bandgaps, vibrational free energies and melting temperatures, among others [33-39]. With

adequate input data collected and the ML framework properly devised, the trained ML models have demonstrated high accuracy at reasonable computational cost [33, 40, 41].

In this work, first-principles density functional theory (DFT) calculations combining machine learning models were employed to study the basal plane activation of cation-mixed 2D TMDC alloys for HER. Based on the DFT results, an ML workflow was developed and shown to successfully predict the Gibbs free energy of hydrogen adsorption (ΔG_H) on basal planes as well as the stability of 2D TMDC alloys. The significant effect of alloying in reducing ΔG_H has been demonstrated, and the stability of those alloys has been provided. The alloy formation process and possible factors leading to such reduction were investigated to reveal the underlying mechanism. Our findings were then summarized and their implications to the TMDC alloy based catalysts were discussed.

5.3 Results

5.3.1 Machine learning (ML) workflow

A typical monolayer TMDC contains metals in group IV (Ti, Zr, Hf), V (V, Nb, Ta) and VI (Cr, Mo, W) and chalcogens (S, Se) [42]. In this study, we first explored HER activity of the basal plane of a series of 2H-MX₂ alloys (M = Cr, Mo, W, V, Nb, Ta, Ti, Zr, Hf; X = S, Se). The template of hydrogen adsorption configuration was constructed by putting one hydrogen atom on top of the chalcogen site, as shown in Fig. 5.1(a). After enumeration at each transition metal site, we obtained 8496 unique adsorption configurations of cation-mixed ternary alloys based on 72 alloy combinations across 18 TMDC pristine structures. Aiming at solving the complexity of these calculations, a ML workflow was developed to predict the hydrogen adsorption energies of TMDC alloys, as shown in Fig. 5.1(b). Starting out, DFT calculations were performed on more than 1140

adsorption configurations. For each alloy, at least two configuration was randomly selected per concentration to ensure that the data set can represent the properties of TMDC alloys in the whole concentration range.

The normalized distribution of the DFT-calculated Gibbs free energy (ΔG_H) values of hydrogen adsorption is plotted in Fig. 5.2(a), from which some initial understanding of the HER performance of TMDC alloys can be obtained, elaborated in the follows. Generally, to achieve good catalytic performance towards HER, it is desirable for hydrogen adsorption to exhibit ΔG_H close to the thermoneutral value near zero. As seen from Fig. 5.2(a), there are a good portion of sites offered by TMDC alloys that exhibit ΔG_H values close to the optimal $\Delta G_H = 0$ eV. Here we select the range of $|\Delta G_H| \leq 0.1$ eV to represent the close vicinity of $\Delta G_H = 0$ eV, as the ideal region for effective HER. Demonstrated by the DFT results in Fig. 5.2(a), there are notable proportion of sites falling into this ΔG_H range. Meanwhile, we can see that these sites are predominantly from the transition metal disulfide alloys (MS_2), rather than the transition metal diselenide alloys (MSe_2). This indicates better potential for HER from MS_2 than MSe_2 . It is also interesting to note from Fig. 5.2(a) that the shape of ΔG_H distribution of MS_2 is similar to that of MSe_2 . This similarity suggests that alloying may induce similar effect for the HER activity of MS_2 and MSe_2 .

We then assigned feature vector to each TMDC alloy to represent the alloy structure numerically, thus relating the physical and chemical properties to the corresponding structures and using these data we collected to train the ML model. Based on previous material informatics literature [35, 37, 43, 44], three of the most relevant properties for predicting ΔG_H of TMDCs were selected, i.e., the atomic number (Z), the Pauling electronegativity (χ), and the Gibbs free energy of hydrogen adsorption on pristine MX_2 (ΔG_{H-MX_2}). Here, Z represents the atom type and account

for the steric effect, and χ accounts for the electronic affinity effect and its value was obtained from the Mendeleev database [45]. $\Delta G_{\text{H-MX}_2}$ serves as the benchmark reference and was used to estimate the variation in the Gibbs free energy. The $\Delta G_{\text{H-MX}_2}$ of 18 pristine TMDCs were calculated by DFT (see Table S1 in Supporting Information). Transition metal sites in the supercell were numbered and each site was described by these three properties. In addition, to account for the effect of the chalcogen atoms, Z and χ of S or Se were appended at the end of the feature vector. Since our supercell has 9 transition metal sites and each transition metal has 3 descriptors, a 29-dimension (27 for transition metals and 2 for chalcogen atoms) vector was created to represent each TMDC alloy (See details in Supporting information).

We created our ML model using gradient boosting regression, as selected by the automated ML package, TPOT [46]. Details of the ML model construction can be found in the Methods section. All the available DFT data were used to train the ML model. The whole data set was randomly split as training and testing sets according to a 7:3 ratio. The distribution of the data in training and testing set are presented in Fig. 5.8 in Supporting Information. To ensure that we have sufficient data for good prediction, learning curves of our ML model is also presented (See Fig. 5.10 in Supporting information). The accuracy of our model prediction is illustrated in the prediction performance plot Fig. 5.2(b), where the error in prediction is indicated by the deviation from the $X = Y$ line. We can see that the training set of our model is well fitted, and the test set shows slightly larger deviations than the training set, but still small. As demonstrated, our model successfully predicts ΔG_{H} values of HER on TMDC alloys, with a mean absolute error of 0.11 eV for the test set.

Additionally, to discover whether the abovementioned alloy configurations are synthesizable, we further investigated the thermodynamic stability of those 2D TMDC alloys using

the ML workflow, similar to that of ΔG_H prediction. However, unlike the ΔG_H prediction workflow which used a regression model to predict continuous valued output, we used a classification pipeline suggested by TPOT to determine whether the alloy configuration is stable or not (See details in the Methods section). The criteria of a stable 2D TMDC alloy is the critical temperature for complete miscibility $T_{CM} < 1000$ K. Fig. 5.2(c) plots the distribution of the stability of MS_2 and MSe_2 alloys based on the DFT-calculated data, showing that 49.2% of the MS_2 alloys and 52.7% of the MSe_2 alloys are regarded as stable. We then did the feature vector assignment to each TMDC alloy, similar to the ΔG_H prediction process, except that we switched one material property, i.e., ΔG_{H-MX_2} , to the total energy of pristine MX_2 (E_{MX_2}) (See Supporting Information for details) considering the physical properties of our target. During ML training, again, the whole data set was randomly split as training and testing sets according to a 7:3 ratio, with data distribution plots presented in Fig. 5.9 in Supporting Information. The learning curves of the ML model shows that we have enough data to reach desirable accuracy of the stability prediction (See Supporting Information for details). From the prediction performance plot presented in Fig. 5.2(d) we can see that our model successfully predicts the stability of TMDC alloys, with an accuracy of 89.3% for the testing set.

Therefore, it can be anticipated that the trained ML model can accurately predict ΔG_H and the stability of other adsorption configurations with the feature vector of the configuration assigned and fed into the ML model, thus providing a useful predictive tool for screening TMDC-based catalysts.

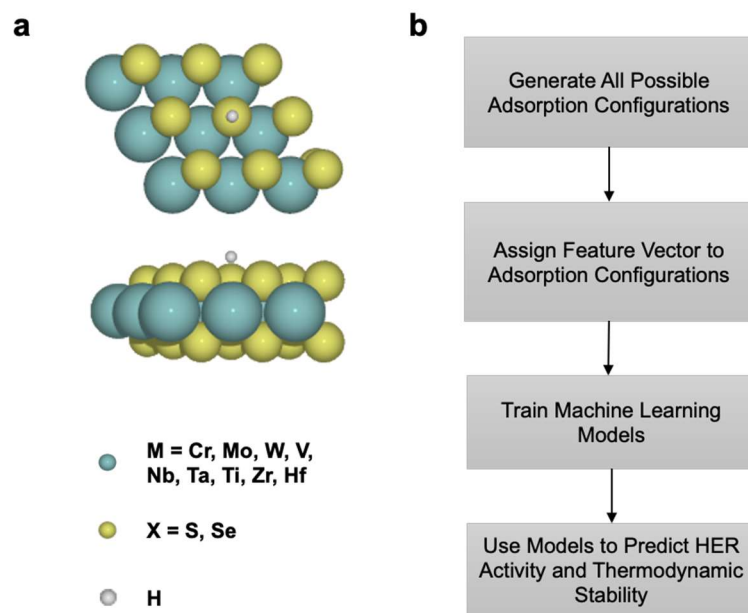


Fig. 5.1 (a) Template adsorption configuration of hydrogen on a 2D TMDC sheet, where transition metal (M=Cr, Mo, W, V, Nb, Ta, Ti, Zr or Hf) and chalcogen atoms (X = S, Se) are indicated by cyan and yellow spheres, while the hydrogen atom is shown in white. (b) Workflow for predicting ΔG_H and stability via machine learning.

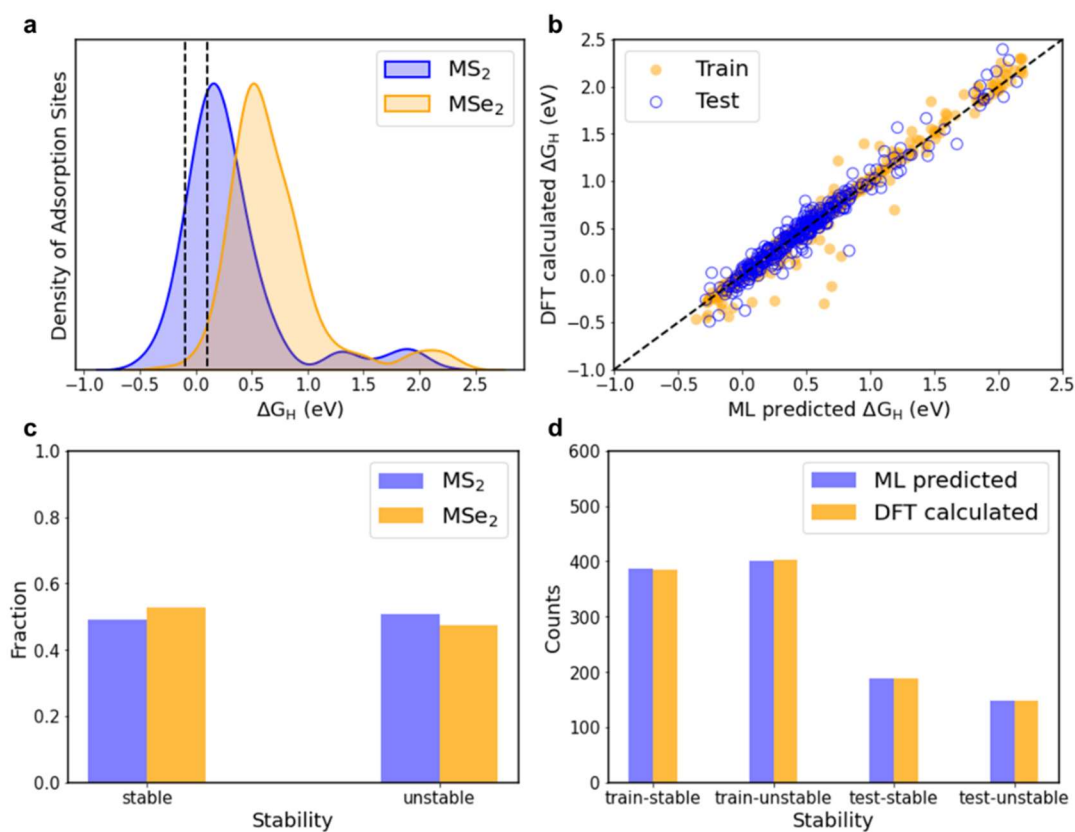


Fig. 5.2 (a) The normalized distribution of the DFT-calculated ΔG_H for hydrogen adsorption on MS_2 and MSe_2 respectively. Dashed lines indicate the 0.1 eV range around the optimal ΔG_H value of 0 eV. (b) Prediction performance of the training set and the test set for ΔG_H prediction. (c) The fraction of the DFT-calculated stable and unstable alloys for MS_2 and MSe_2 respectively. (d) Prediction performance of the training set and the test set for stability prediction.

5.3.2 Predictions of electrocatalytic activity of TMDC alloys

The HER activities of various TMDC alloys have been predicted by the ML framework (See Fig. 5.3 and Supporting Information). Among these TMDC alloys, only a small fraction has been investigated in experiments [17, 47, 48], notably the $Mo_{(1-x)}W_xS_2$ and $Mo_{(1-x)}W_xSe_2$ groups. Experimentally, these two groups of TMDC alloys have been shown to be active for HER at the edge sites, while it was believed that the basal planes of $Mo_{(1-x)}W_xS_2$ and $Mo_{(1-x)}W_xSe_2$ stay inert [17, 19, 23-25]. As shown in Fig. 5.3(a)-(b), all adsorption sites at basal planes of $Mo_{(1-x)}W_xS_2$ and $Mo_{(1-x)}W_xSe_2$ alloys have ΔG_H values much higher than the ideal range for HER (i.e., $|\Delta G_H| \leq 0.1$ eV) and can be regarded as inert, in good agreement with the experimental findings. Nonetheless, despite the overall basal inertness of $Mo_{(1-x)}W_xS_2$ and $Mo_{(1-x)}W_xSe_2$, we can see obvious lower ΔG_H for some alloy configurations compared to those of the corresponding pristine TMDCs. This illustrates apparent effect of alloying in reducing ΔG_H below what's expected from the simply interpolation of the ΔG_H of their pristine structures.

Moving to other TMDC alloy groups, similar effect of alloying induced reduction in ΔG_H can also be observed, which to the best of our knowledge, have not yet been studied previously in experiments. Representative plots are shown in Fig. 5.3(c)-(h). Some of the MS_2 alloys, such as $Mo_{(1-x)}V_xS_2$, $W_{(1-x)}Hf_xS_2$ and $Ti_{(1-x)}Zr_xS_2$, have ΔG_H lies in the ideal region for HER over a wide range of concentration, outperforming their pristine structures in electrocatalytic activities (See Supporting Information for other TMDC alloys). For example, as the ΔG_H vs. concentration plot

shown in Fig. 5.3(c), $\text{Mo}_{(1-x)}\text{V}_x\text{S}_2$ with the vanadium concentration in the range of 0.4-0.8 can yield ΔG_{H} close to zero. Particularly worth noting (see Fig. 5.3(c)) is that the introduction of a small fraction (e.g., 11%) of V atoms into MoS_2 can render a significant drop in ΔG_{H} , showing similar effect in enhancing the HER performance at the basal plane as the single-atom catalysis [49]. Meanwhile, the MSe_2 alloys are showing quite similar behaviors as their MS_2 counterparts but exhibiting relatively higher ΔG_{H} values, rendering less favorable results for HER in most cases. In addition, we can also note from the results that in general the effect of alloying tends to be more significant for a TMDC alloy when the difference of ΔG_{H} values of its corresponding pristine TMDCs is more pronounced (see, e.g., Fig. 5.3(e) where MoS_2 and VS_2 respectively have ΔG_{H} values of 2.00 eV and 0.27 eV), possibly because of more significant charge redistribution between atoms in those alloys as elaborated later.

We also compare the electrocatalytic performance of various TMDC alloys by calculating their respective fractions of enumerated adsorption sites that have optimal ΔG_{H} values ($|\Delta G_{\text{H}}| \leq 0.1$ eV) over the whole concentration range, with the mapping presented in Fig. 5.4(a) and Fig. 5.18(a) for MS_2 and MSe_2 alloys, respectively. By comparing two active site mappings, we can see that the sites of optimal ΔG_{H} values are predominantly from MS_2 alloys, while HER active sites on MSe_2 alloys are negligible. This observation agrees well with the DFT calculated results in Fig. 5.2(a). Therefore, we can narrow down our exploration for HER catalysts to only MS_2 alloys. Also noted from Fig. 5.4(a) is that MS_2 alloys with metal atoms exclusively from group-VI elements provide no effective adsorption sites, thus predicted to be undesirable toward HER. For cases involving elements from group-IV and/or group-V, some MS_2 alloys show promising performance towards HER. As seen in Fig. 5.4(a), a number of alloys exhibit high fraction of effective adsorption sites, with the fraction value close to or beyond 50%. Examining these alloys

in details, we note that some high fraction values, e.g., those of $\text{Hf}_{(1-x)}\text{Nb}_x\text{S}_2$ (71%) and $\text{Ti}_{(1-x)}\text{V}_x\text{S}_2$ (69%), may be attributed to their base metal disulfides, i.e., NbS_2 and TiS_2 , being active towards HER. Nonetheless, there are also cases among those where their base metal disulfides are inactive, e.g., $\text{Zr}_{(1-x)}\text{V}_x\text{S}_2$ (62%) and $\text{Zr}_{(1-x)}\text{Ta}_x\text{S}_2$ (47%). It is also interesting to note that the benefit of alloying in enhancing HER activity in general is most significant when there are mixtures of metal elements from different groups.

We further screened the MS_2 alloys by considering their stability, with the fractions of stable active sites for each MS_2 alloy presented in Fig. 5.4(b). We can see that around half of the active adsorption sites have been filtered, with the number of active adsorption sites on MS_2 dropping significantly from originally 1133 to only 448. This observation agrees well with the DFT-calculated results presented in Fig. 5.2(c). Although from Fig. 5.4(a) we have learned that MS_2 alloys with metal atoms from different groups result in enhanced HER activities, those alloys may suffer from low stability probably due to the large lattice mismatch between their base metal disulfides. For the extreme cases, i.e., alloying between elements from group-IV and group-VI, almost all MS_2 alloys are found to be unstable, leading to nearly no effective adsorption sites in this region as shown by the mapping from Fig. 5.4(b). Combining the effects of both basal plane activation and stability, in general, alloying between metal elements from group-IV and group-V is found to be most effective towards HER. In addition, in order to guide the synthesis of MS_2 alloys, the fractions of stable active sites for each MS_2 alloy at different concentrations are provided (See Fig. 5.19 in Supporting Information).

Previous studies on TMDCs mostly focus on alloying within group-VI elements while other cation-mixed alloys have been largely neglected. The results we presented here suggest

clearly indicates the necessity of expanding the exploration into other element groups in the design and development of TMDC alloys towards HER.

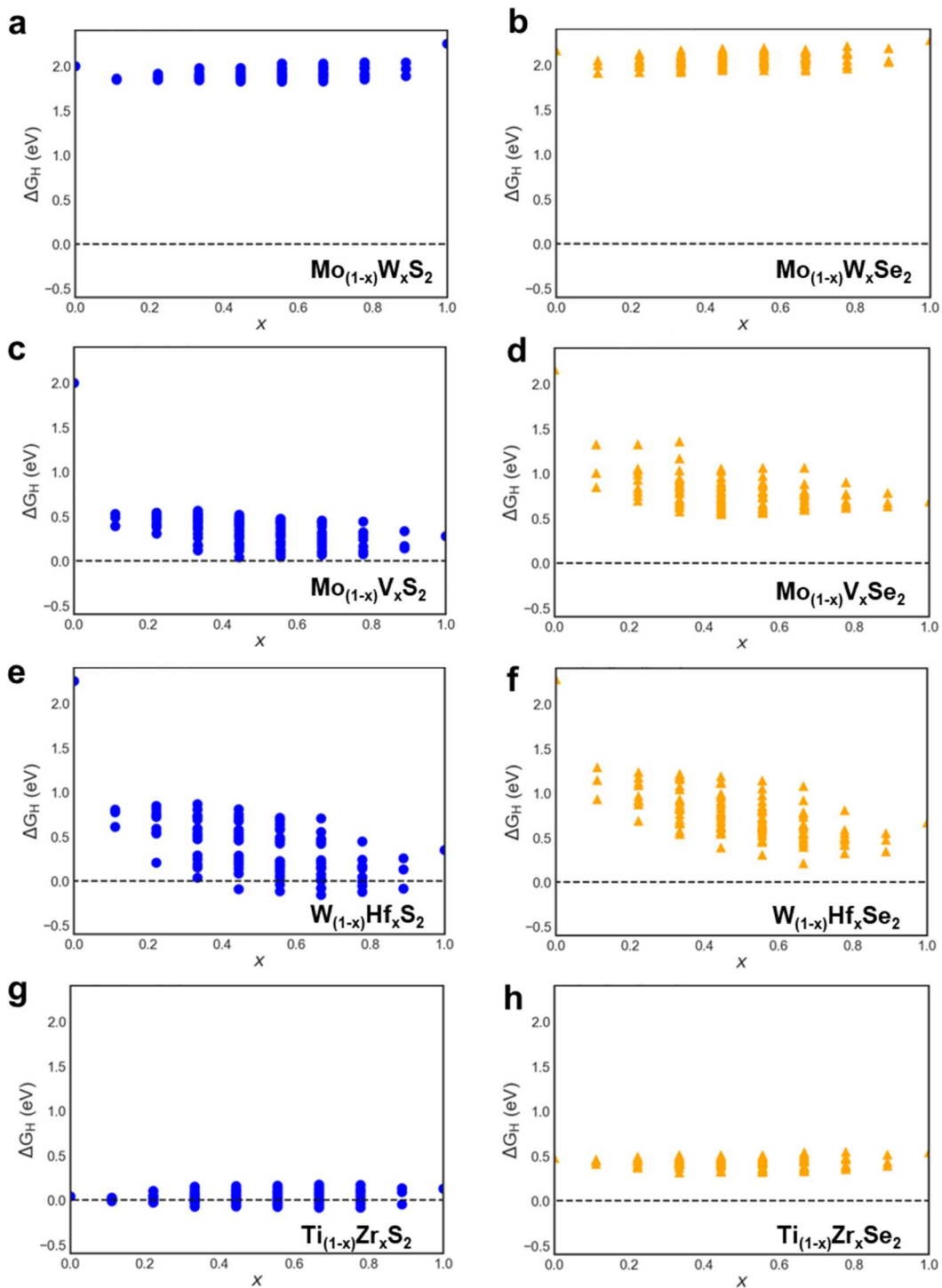


Fig. 5.3 (a)-(h) Machine learning predictions for ΔG_H of 8 representative TMDC ternary alloys at different concentrations. Black dash lines indicate the optimal ΔG_H to achieve best HER performance.

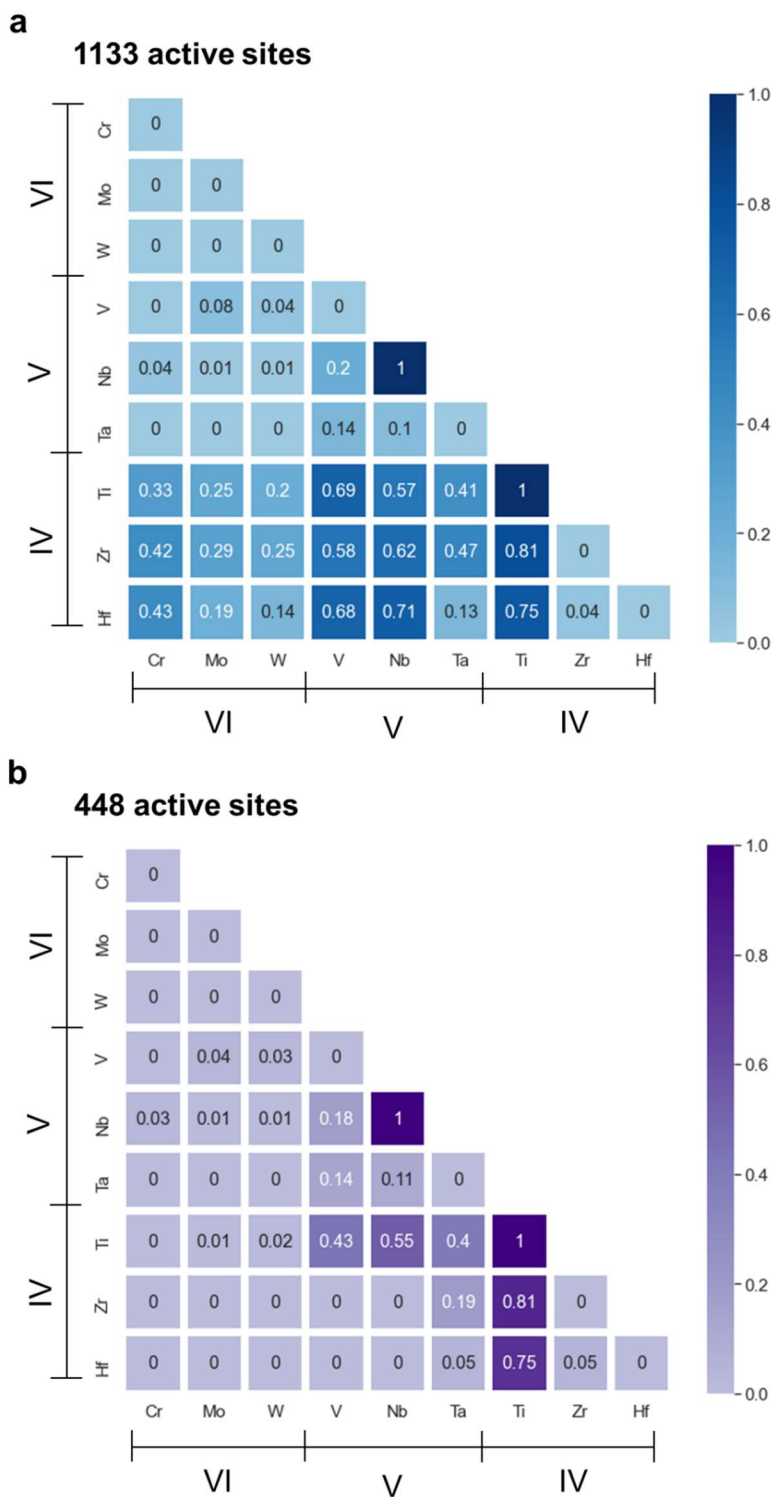


Fig. 5.4 HER activity heatmaps for MS₂ alloys showing (a) the fraction of adsorption sites of ΔG_H within the optimal range of (-0.1,0.1) eV for each alloy, and (b) the fraction of adsorption sites that are both stable and have optimal ΔG_H for each MS₂ alloy. The number indicates the fraction value an alloy exhibits, which is also reflected by the color.

5.3.3 The origin of alloying in enhancing HER activity

The results in Fig. 5.3 and Fig. 5.4 have clearly demonstrated the promising role of alloying in enhancing HER activity. To better utilize the information for rational TMDC alloy design towards HER, it is important to understand the underlying mechanism. As suggested by previous studies [50, 51], the influence of alloying on surface adsorption properties may be described by either electronic (or ligand) and/or geometrical (or ensemble) effect. Since hydrogen always adsorbs on the chalcogen atom (S or Se) of nearly identical geometrical fashion, effectively there is no geometrical effect in our study (see Fig. 5.16 in Supporting information). Therefore, it is expected that the influence of alloying on TMDCs would be dominated by the electronic effect resulted from the variation in chemical composition.

The electronic effect can be analyzed by examining the intrinsic electronic structures. In particular, we found that variation in chemical composition in TMDC alloys can significantly modify the *p* states of chalcogen atoms. One good metric to quantify such modification in the *p* state is the *p*-band center (denoted as ϵ_p in the follows) of the chalcogen atom (see details in the Methods section). The band centers, e.g., *d*-band and *p*-band centers, have also been used by previous studies [13, 52] in describing characteristics of electronic structures. In Fig. 5.5(a), we plotted the ΔG_H values of 140 randomly selected TMDC alloys versus their corresponding ϵ_p values. Overall we can see a good linear correlation between ΔG_H and ϵ_p , for both the MS₂ and MSe₂ alloy groups, despite some outliers. Those outlier data points can be partially attributed to

the fact of the p bands of chalcogen atoms being broad and somewhat lack of structure [53], which consequently can cause variation in ε_p . Nevertheless, the overall trends observed in Fig. 5.5(a) confirm that the electronic effect is related to the electronic structure of the adsorption (chalcogen) site, and a chalcogen site with a higher (lower) p -band center exhibits stronger (weaker) affinity to hydrogen. Meanwhile, we see that the linear fitting of the $\Delta G_{\text{H}}-\varepsilon_p$ data yields similar slopes for both MS_2 and MSe_2 alloy groups. Since the slope is indicative of the strength of the electronic effect [53], this suggests that alloying result in similar degree of electronic effect for both MS_2 and MSe_2 , consistent with our previous observations in Fig. 5.2(a). In accordance with the results shown in Fig. 5.5(a), we then proceeded to examine how alloying modifies the p -band center. Fig. 5.5(b) plots the ε_p of the adsorption sites with the best (lowest) ΔG_{H} at each concentration for two representatives, i.e., $\text{Mo}_{(1-x)}\text{V}_x\text{S}_2$ and $\text{W}_{(1-x)}\text{V}_x\text{Se}_2$ (See ε_p vs. x plots for all adsorption sites in $\text{Mo}_{(1-x)}\text{V}_x\text{S}_2$ and $\text{W}_{(1-x)}\text{V}_x\text{Se}_2$ in Fig. 5.20 in Supporting Information). Clearly alloying can significant increase ε_p from that of the pristine base metal disulfide/diselenide. The increased ε_p indicates the shifting of p bands to the Fermi energy, which stabilizes hydrogen adsorption and therefore leads to the enhanced HER activity of alloys.

As suggested by previous studies [54-56], more in-depth understanding of the effect of alloying on ε_p , can be obtained by analyzing the changes in the properties of TMDC alloys during their formation processes. In particular, the formation process can be decomposed into three steps, namely (i) volume deformation (VD), where the corresponding pristine TMDC was compressed or expanded from its equilibrium lattice constant to the alloy lattice constant, (ii) charge exchange (CEX), where mixture of atoms takes place and introduced into the unrelaxed alloy lattice constructed in step (i), and subsequently (iii) structural relaxation (SR) where the alloy lattice obtained in step (ii) was fully relaxed. The composition-weighted average of ε_p was calculated (see

Methods section for details) at each step for different TMDC alloys. The evolution of ε_p for four representative alloys was shown in Fig. 5.6(a). We note that the changes in ε_p in the VD and SR steps are negligible in some cases, e.g., $W_{0.22}V_{0.78}S_2$, but can be significant in other cases, e.g., $W_{0.22}V_{0.78}Se_2$. However, an interesting observation from the ε_p evolution results is that in the cases where the changes in ε_p in the VD and SR steps are significant, the changes in the two steps are always in the opposite directions and thus cancel each other, e.g., the case of $W_{0.22}V_{0.78}Se_2$. As a result, the CEX step effectively becomes the critical step responsible for the overall change in ε_p .

With a more focused analysis on the CEX step, we found that the change in ε_p during this step is strongly correlated with the charge transfer around the adsorption site. In particular, depending on the charge transfer direction, negative or positive change in ε_p is expected. Such correlation is elaborated below using $W_{0.22}V_{0.78}S_2$ and $W_{0.78}V_{0.22}S_2$ systems as examples, where the Bader [57] charge transfer analysis and charge density difference mapping (see Fig. 5.6(b)) were performed. In the case of $W_{0.22}V_{0.78}S_2$, on average each V atom has a charge accumulation of about 0.02e while each W atom shows a charge depletion of about 0.06e. The electron depletion and accumulation around W and V atoms respectively are also clearly revealed in the charge density difference map shown in Fig. 5.6(b), indicative of the electron transfer from W to V. The electron gain at V shifts its *d*-band center away from the Fermi level to lead to weaker interaction between V and S atoms [50, 58], which in return shifts the *p*-band center of S atom towards the Fermi level and therefore strengthen the H-S bond [59]. That is, charge gain at a transition metal would lead to an increased ε_p for the nearby chalcogen atoms. For instance, if we consider the case of hydrogen adsorption on the chalcogen atom surrounded by three V atoms, as shown in Fig. 5.6(b), the chalcogen atom undergoes substantial increase in ε_p (i.e., $\Delta\varepsilon_p = 0.38$ eV). Similar charge transfer and redistribution behaviors are also observed for the $W_{0.78}V_{0.22}S_2$ system, where each V

atom and W atom on average show charge gain and depletion of 0.040e and 0.021e respectively. If we examine the case of hydrogen adsorption on the chalcogen atom surrounded by three W atoms, the chalcogen atom exhibits a decrease in ε_p (i.e., $\Delta\varepsilon_p = -0.19$ eV) due to charge depletion from the surrounding W atoms. Since in $W_{0.22}V_{0.78}S_2$ and $W_{0.78}V_{0.22}S_2$, the hydrogen adsorbed chalcogen is more likely to be surrounded by V (with charge gain) and W (with charge depletion) respectively, the composition-weighted average of ε_p is expected to increase and decrease during the CEX step respectively, in agreement with the trends shown in Fig. 5.6(a).

From the above, we see that charge transfer is a critical factor affecting HER activity. Consequently, it also plays a large role in prescribing the local chemical ordering of adsorption sites yielding optimal HER activities. Taking $W_{(1-x)}V_xS_2$ as an example, since local charge transfer occurs from W to V, it can thus be hypothesized that hydrogen adsorption would prefer a chalcogen site with more V presence in its surrounding to achieve a charge accumulation center for maximized ε_p enhancement, and thus lower ΔG_H . Fig. 5.7 shows several representatives of the adsorption configurations offering the lowest ΔG_H at different compositions, alongside with the corresponding ΔG_H values as the composition x varies, obtained from DFT calculations, which corresponds quite well with our hypothesis.

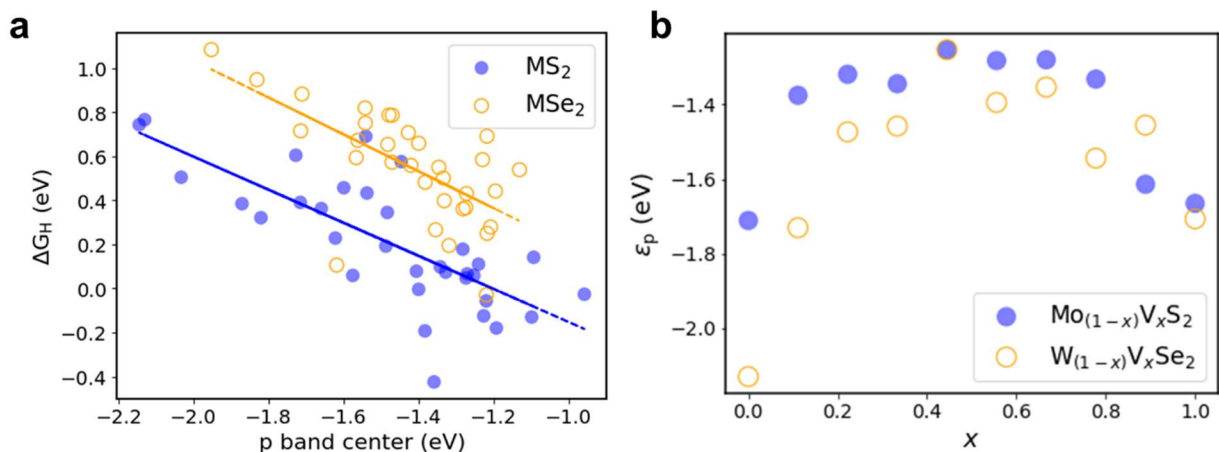


Fig. 5.5 (a) Relationship between ε_p values and ΔG_H for MS_2 and MSe_2 . (b) ε_p of the adsorption sites in $Mo_{(1-x)}V_xS_2$ and $W_{(1-x)}V_xSe_2$ alloys with the best (lowest) ΔG_H as a function of the composition (i.e., atomic fraction of V).

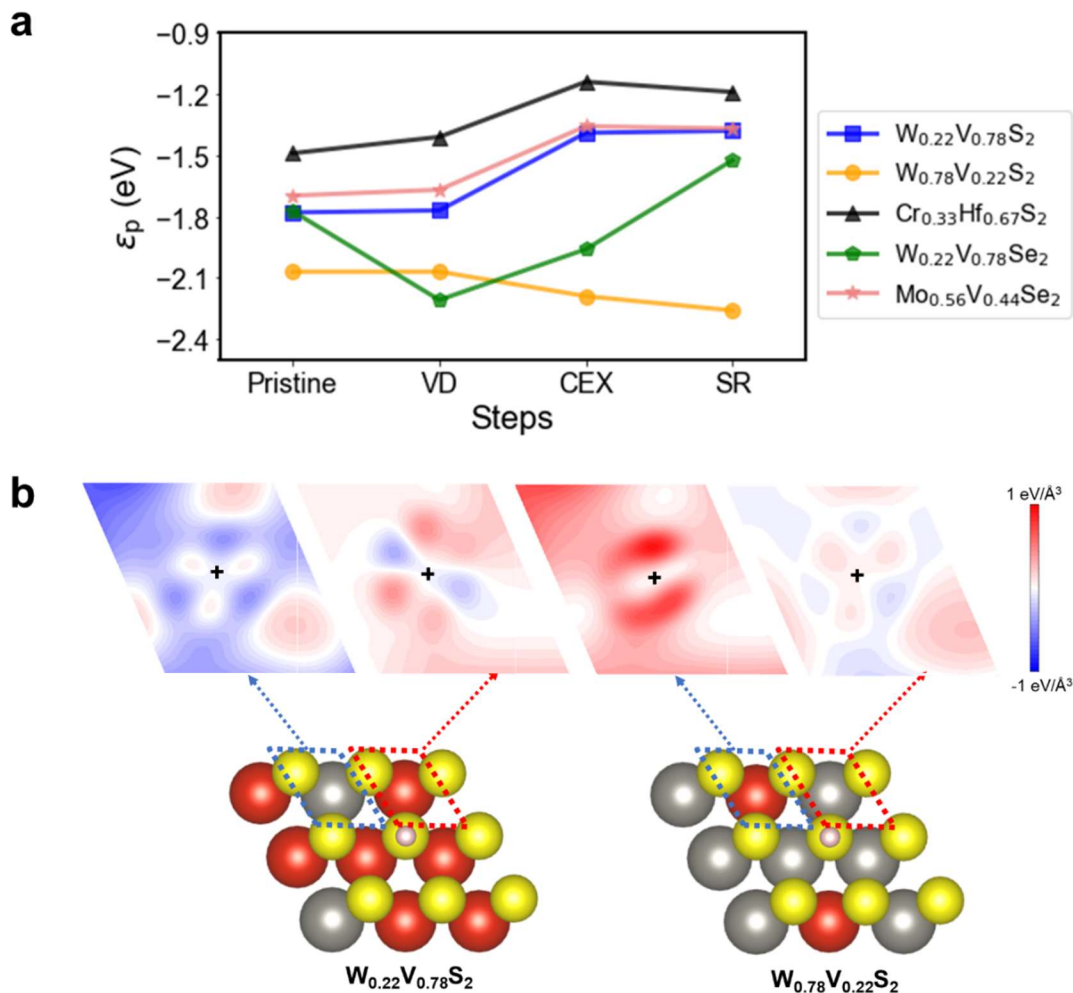


Fig. 5.6 (a) The evolution of composition-weighted average of ε_p at the VD, CEX, and SR steps. (b) Representative hydrogen adsorption configurations on $W_{0.22}V_{0.78}S_2$ and $W_{0.78}V_{0.22}S_2$ alloys, with related charge density difference maps of metal atoms at the vicinity of the adsorption site. Atoms are colored according to the follows: V (red), W (grey), S (yellow), and hydrogen (pink). The black cross symbol in charge density difference maps indicate the center of the metal atom (W or V).

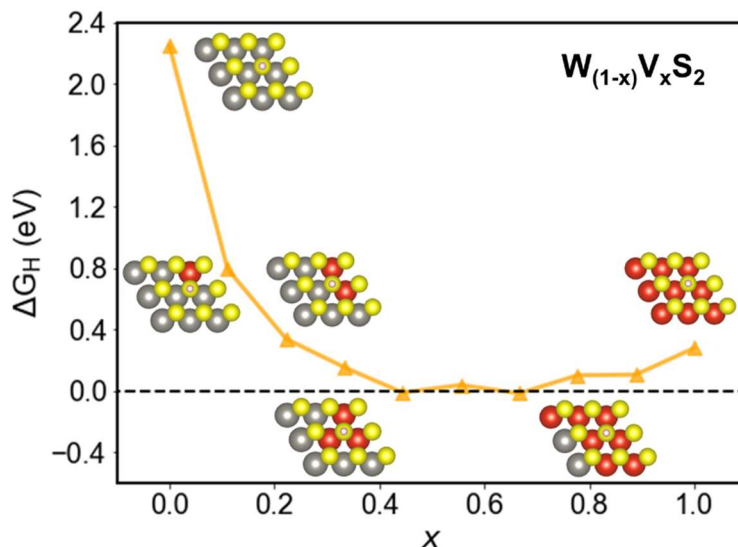


Fig. 5.7 Lowest ΔG_H values for hydrogen adsorption on $W_{(1-x)}V_xS_2$ as the composition (x) varies. The insets illustrate sample adsorption configurations yielding the lowest ΔG_H . V, W, S and hydrogen atoms are shown in red, grey, yellow, and pink respectively.

5.4 Conclusions

In summary, first-principles calculations in conjunction with machine learning were performed to investigate the basal plane activation of 2D TMDCs via alloying for hydrogen evolution reaction. The ML workflow was created based on more than 1140 DFT calculations, and feature vectors were then assigned accounting for the physical and chemical properties of both transition metals and chalcogen atoms. The Gibbs free energy of hydrogen adsorption ΔG_H and the stability of a series of 2D cation-mixed TMDC alloys of various compositions were shown to be accurately predicted by the ML model. Our results demonstrated that alloying leads to substantial reduction in ΔG_H with respect to the pristine TMDCs, and for a number of TMDC alloys, it can render ΔG_H in the ideal range for HER. Moreover, half of the active TMDC alloys were found to be stable, further indicating alloying as a viable route for basal plane activation. The alloying effect was also found to be mostly dependent on the transition metals, not much affected by the chalcogen atom type. Such alloying induced activation was then revealed to mainly

originate from the electronic effect resulted from the chemical composition variation. In particular, the electronic effect comes from *p*-band center shifting of the adsorption sites, attributed to the alloying produced local charge exchange. The present study provides essential mechanistic insights for a new route towards basal plane activation of 2D TMDCs for enhanced electrocatalytic performance. The insights coupled with the ML model, will enable machine-derived suggestions, a critical step for the complete roadmap of rational design and exploration of 2D TMDC alloy catalysts for HER.

5.5 Methods

5.5.1 Enumeration of hydrogen adsorption configurations

The ternary cation-mixed TMDC alloy system used in this study contains 9 MX₂ units (i.e., 3 × 3 supercell) with the hydrogen atom adsorbed on top of a certain chalcogen site. With the hydrogen atom fixed, Atomic Simulation Environment (ASE) [60, 61] was then used to generate all symmetrically inequivalent adsorption configurations by enumerating each transition metal site in the supercell. In total, 8496 alloy configurations were generated from 72 cation-mixed alloys based on 18 MX₂ pristine structures (M = Cr, Mo, W, V, Nb, Ta, Ti, Zr, Hf, X = S, Se). For each type of cation-mixed alloy, to avoid strain on the structures, pristine structure (i.e. MX₂) with the larger unit cell size was chosen as the template for enumeration.

5.5.2 Density-functional theory (DFT) calculations

After enumeration, a set of more than 580 adsorption configurations were partial randomly selected to perform DFT calculations. On top of the random selection, it is also ensured that at least one configuration per concentration per alloy was selected to make sure the data can correspond to various TMDC alloys in the whole concentration range. First-principles DFT

calculations were then performed on those adsorption configurations selected. All calculations were carried out employing the VIENNA ab initio simulation package (VASP) [62, 63] using the projector-augmented wave method [64]. The exchange-correlation functional was described by generalized gradient approximation (GGA) parametrized by Perdew, Burke, and Ernzerhof [65, 66]. A kinetic cutoff energy of 500 eV was set for the plane-wave basis functions, and the k -points for the Brillouin-zone integration are sampled on a mesh grid of $4 \times 4 \times 1$ and $12 \times 12 \times 1$ for geometry optimization and electronic structure calculation. All structures were relaxed until the atomic forces are less than 0.02 eV/Å and total energies were converged to 10^{-5} eV. To avoid interactions between repeated images along the layer direction within the periodic boundary condition, a vacuum with 20 Å thickness was introduced to the supercell. The effect of van der Waals (vdW) interactions was considered using the DFT-D3 method [67, 68].

The activity trend of catalyst towards HER can be described by the Gibbs free energy of hydrogen adsorption on the surface. According to the Sabatier principle, it is desirable for hydrogen adsorption to have a Gibbs free energy of hydrogen adsorption close to the thermoneutral value near zero [69]. The Gibbs free energy of hydrogen adsorption, denoted as ΔG_H in the follows, can be calculated as:

$$\Delta G_H = \Delta E_H + \Delta E_{ZPE} - T\Delta S_H \quad (5.1)$$

where ΔE_H is the hydrogen adsorption energy, defined as:

$$\Delta E_H = E_{\text{alloy-H}} - E_{\text{alloy}} - \frac{1}{2}E_{H_2} \quad (5.2)$$

where $E_{\text{alloy-H}}$ is the total energy of hydrogen-adsorbed alloy structure, E_{alloy} is the total energy of alloy structure without hydrogen atom, and E_{H_2} denotes the energy of an isolated hydrogen gas molecule. ΔE_{ZPE} is the difference in zero-point energy of hydrogen in the adsorbed state and the

gas phase. ΔS_H is the entropy term approximated as half of entropy of the gas phase H_2 as $\Delta S_H \approx \frac{1}{2} S_{H_2}$ [70]. T is the room temperature of 298.15K.

To ensure the predicted 2D TMDC alloys are synthesizable, the stability of these alloys was evaluated by their miscibility, i.e., their ability to avoid phase segregation, at certain temperature. The miscibility of an alloy at temperature T with concentration x can be evaluated by its free energy of mixing $G_{\text{mix}}(x, T)$, which is defined as:

$$G_{\text{mix}}(x, T) = \Delta H(x) - T\Delta S(x) \quad (5.3)$$

where $\Delta H(x)$ is the formation enthalpy, which can be calculated from DFT. $\Delta S(x)$ is the entropy and was estimated by mean-field approximation [54, 71]:

$$\Delta S(x) = -k_B [x \ln x + (1 - x) \ln(1 - x)] \quad (5.4)$$

Here, k_B is the Boltzmann constant. Negative and positive $G_{\text{mix}}(x, T)$ correspond to miscible and immiscible alloys, respectively. Since the entropy $\Delta S(x)$ is always positive, $G_{\text{mix}}(x, T)$ can be lowered by increasing the temperature T until complete miscibility in alloys is achieved. We here used the critical temperature for complete miscibility (T_{CM}) of alloys to determine the stability of 2D TMDC alloys. Since we should consider the complete miscibility of alloys under experimentally achievable temperatures, we set $T_{\text{CM}} < 1000$ K as the criteria for stable alloys, while alloys with $T_{\text{CM}} \geq 1000$ K are regarded as unstable alloys. It is noted that when calculating T_{CM} for some of the 2D TMDC alloys, such as $\text{Mo}_{(1-x)}\text{W}_x\text{S}_2$, due to the limitation of calculations, their T_{CM} can exhibit negative values because those alloys are already stable at 0 K. But these unphysical values do not affect the results because they can also be categorized into stable alloys.

Analyses of the electronic structures of the alloys were performed. We examined the density of states (DOS) associated with the adsorption sites to understand the interaction between

hydrogen and the adsorption site on the alloy configurations. According to the widely employed d -band center model of Hammer and Nørskov [72], the ΔG_H of hydrogen adsorption can be analyzed using the d -band center (ε_d) of the catalyst. Also, previous study demonstrates that the p -band center of chalcogen atoms in TMDCs can be used as descriptor for ΔG_H [13, 52]. In our case, since H interacts directly with the chalcogen atoms, a p -band center should be considered and is calculated as the following:

$$\varepsilon_p = \frac{\int_{-\infty}^{+\infty} E D_p(E) dE}{\int_{-\infty}^{+\infty} D_p(E) dE} \quad (5.5)$$

where E is the energy level and $D_p(E)$ is the p states in catalysts.

To analyze the changes in ε_p during formation process of TMDC alloys, we decomposed the formation process into three steps (VD, CEX and SR) and the composition-weighted average of ε_p for alloy $M1_{(1-x)}M2_xX_2$ at each step is calculated as the following:

$$\varepsilon_i = (1 - x)\varepsilon_{i,M1X_2} + x\varepsilon_{i,M2X_2} \quad (5.6)$$

where x, i are the concentration of alloy and i representing step VD, CEX or SR. $\varepsilon_{i,M1X_2}$ and $\varepsilon_{i,M2X_2}$ are the ε_p of two base lattices at step i .

5.5.3 Construction of machine learning (ML) model

The selection of the ML model is a key process to achieve the high efficiency of the predictions. In this study, we used an automated machine learning package, TPOT [46], to evaluate the performance of different machine-learning algorithms and to find the best modeling pipeline for the dataset. The generation size and population size for running TPOT were set as 5 and 20, respectively. 5-fold cross-validation was used when evaluating pipelines. We used regression to predict the ΔG_H of 2D TMDC alloys, while classification was chosen for the prediction of their

stabilities. For ΔG_H prediction, as recommended by TPOT, we chose the pipeline using gradient boosting regression as implemented in the Scikit-learn Python library [73]. For stability prediction, the pipeline suggested by TPOT contains three estimators, i.e., stacking estimator, recursive feature elimination, and random forest classifier [46]. Detailed information of the ML models can be found in code provided in this work. The code used to perform this work is available at https://github.com/YiqingChen524/2D_TMDC_alloys.

5.6 Acknowledgements

This research is supported by the Natural Sciences and Engineering Research Council of Canada (NSERC) Discovery Grant (grant #: NSERC RGPIN-2017-05187), and the McGill Engineering Doctoral Award (MEDA). The authors would also like to acknowledge the Compute Canada and Calcul Québec for providing computing resources.

5.7 Supporting Information

5.7.1 Data distribution

To train the ML models, data sets for both ΔG_H and stability prediction were randomly split as training and testing sets according to a 7:3 ratio. For ΔG_H prediction model, as shown in Fig. 5.8(a), ΔG_H distributions of the training and testing set have similar shapes, with data distributed in the range of (-0.5, 2.5) eV. Fig. 5.9(a) shows the distribution of data for stability prediction. Similarly, it is found that stability data are evenly distributed in both the training and testing set. The good distribution of data for both ΔG_H and stability prediction ensure the accuracy of the ML training process.

We also evaluated the distribution of alloy types for data sets from ΔG_H and stability prediction, as shown in Fig. 5.8(b) and Fig. 5.9(b). The distribution plots suggest that the data we used for training ML are evenly distributed in different alloy types and can appropriately represent all 2D TMDC alloys.

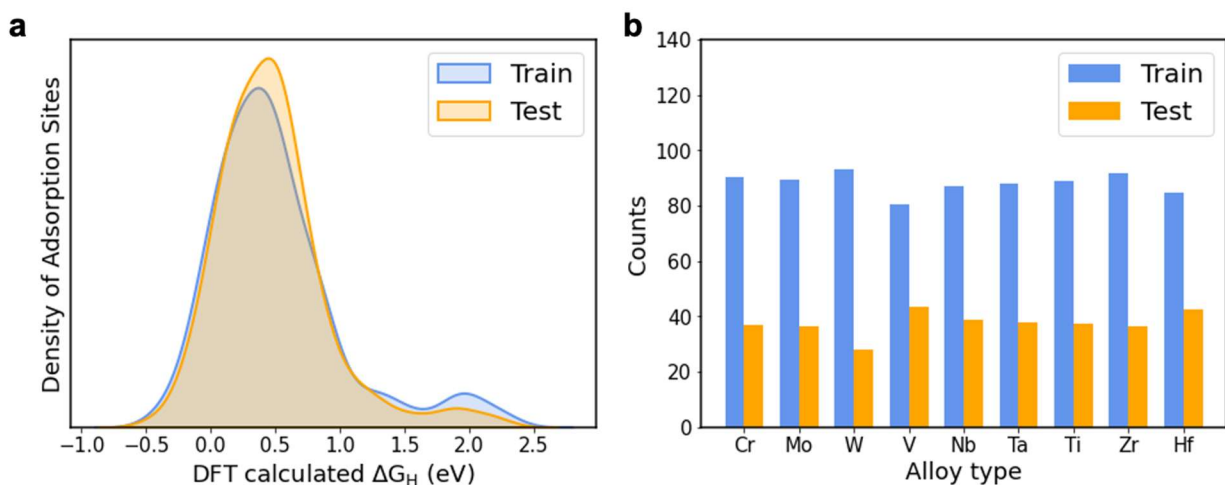


Fig. 5.8 (a) The normalized distribution of the DFT-calculated ΔG_H for the training and testing set, respectively. (b) The distribution of alloy types for the training and testing set for ΔG_H prediction.

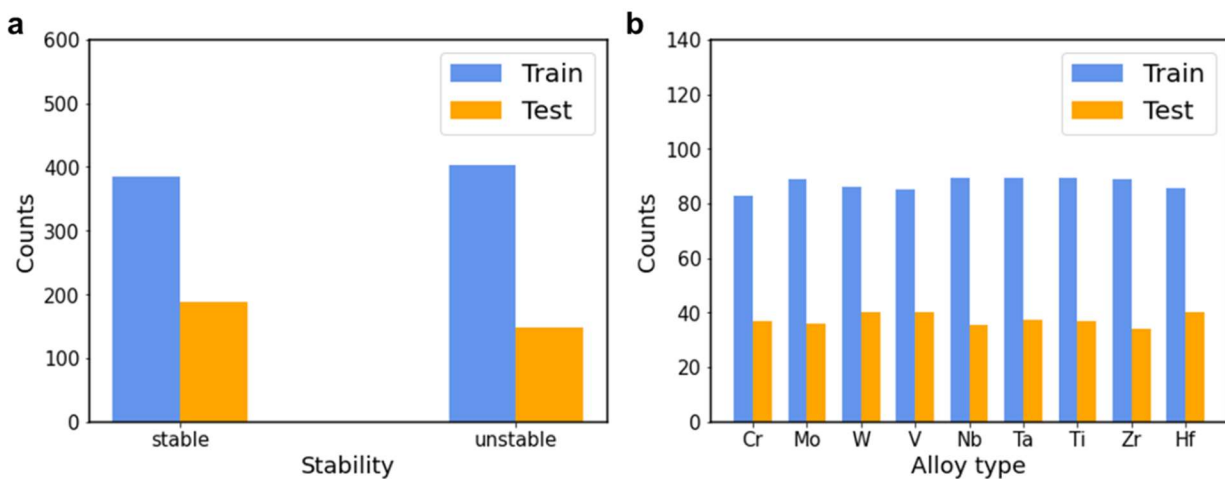


Fig. 5.9 (a) The distribution of stability of alloys for the training and testing set. (b) The distribution of alloy types for the training and testing set for stability prediction.

5.7.2 Performance of ML model

To evaluate the performance of our ML models, in this study, we used mean absolute error (MAE) and root-mean-square error (RMSE) to measure the errors of regression model, and accuracy and F1-score to measure the errors of classification model.

MAE is defined as the sum of absolute values divided by the number of the data:

$$\text{MAE} = \frac{1}{N} \sum_{i=1}^N |y - y_i| \quad (5.7)$$

where N , y and y_i represent the number of data, observed value and predicted value.

RMSE is the standard deviation of the predicted errors calculated as:

$$\text{RMSE} = \left[\frac{1}{N} \sum_{i=1}^N (y - y_i)^2 \right]^{1/2} \quad (5.8)$$

Accuracy is the fraction of correct predictions:

$$\text{Accuracy} = \frac{\text{Number of correct predictions}}{\text{Total number of predictions}} \quad (5.9)$$

And F1-score is defined as the harmonic mean of precision and recall:

$$\text{F1} = \frac{2 * \text{precision} * \text{recall}}{\text{precision} + \text{recall}} \quad (5.10)$$

where precision is the number of the true positives over the number of predicted positives, and recall is the number of true positives over the number of actual positives.

In this work, we used regression to predict ΔG_H and classification to predict the stability of the 2D TMDC alloys. 10-fold cross-validation was used when evaluating the ML models. The corresponding learning curves of these two models are presented in Fig. 5.10, which show the

magnitude of the modeling error as the size of training data varies. The convergence of the training and validation scores indicate that we have enough data used for training.

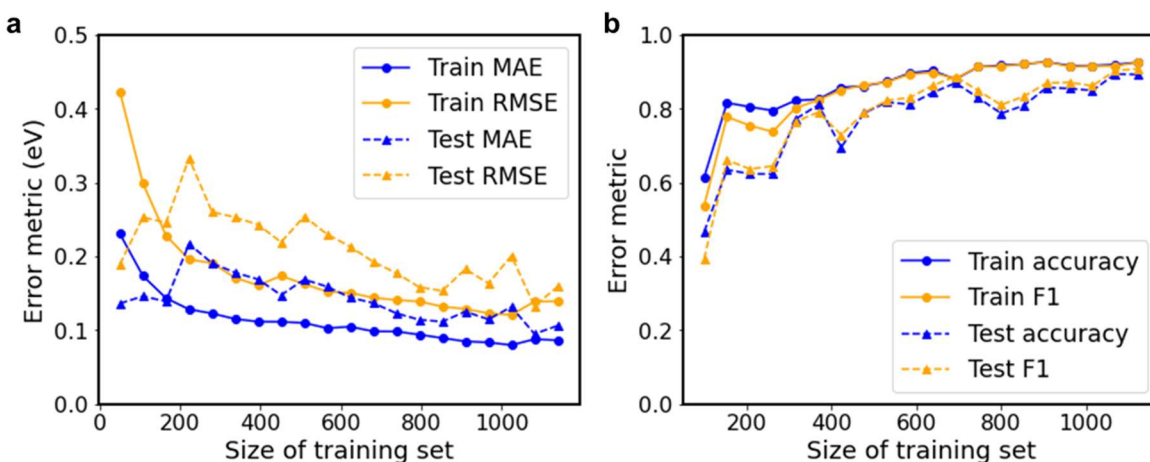


Fig. 5.10 Error metrics vs. size of training set or testing set for the prediction of (a) ΔG_H and (b) stability of 2D TMDC alloys.

5.7.3 Gibbs free energies of hydrogen adsorption on pristine MX_2

The table below shows the calculated Gibbs free energy of hydrogen adsorption on 18 pristine 2D TMDCs.

Table 5.1 Gibbs free energies of hydrogen adsorption on pristine MX_2

| MS_2 | $\Delta G_{\text{H-MS}_2}$ (eV) | MSe_2 | $\Delta G_{\text{H-MSe}_2}$ (eV) |
|----------------|---------------------------------|-----------------|----------------------------------|
| CrS_2 | 1.367 | CrSe_2 | 1.392 |
| MoS_2 | 1.997 | MoSe_2 | 2.160 |
| WS_2 | 2.249 | WSe_2 | 2.278 |
| VS_2 | 0.277 | VSe_2 | 0.688 |
| NbS_2 | -0.009 | NbSe_2 | 0.363 |
| TaS_2 | 0.168 | TaSe_2 | 0.461 |
| TiS_2 | 0.040 | TiSe_2 | 0.478 |
| ZrS_2 | 0.126 | ZrSe_2 | 0.540 |
| HfS_2 | 0.347 | HfSe_2 | 0.671 |

5.7.4 Feature vector assignment

Fig. 5.11 illustrates how feature vector is assigned to each unique alloy structure. Here, we use $\text{Mo}_{0.89}\text{W}_{0.11}\text{S}_2$ as a representative. Transition metal sites in the supercell are numbered and each site is described in order by the following three properties: the atomic number of the element (Z), the Pauling electronegativity of the element (χ), and the Gibbs free energy of hydrogen adsorption of pristine MX_2 ($\Delta G_{\text{H-MX}_2}$) for ΔG_{H} prediction or total energy of pristine MX_2 (E_{MX_2}) for stability prediction. After describing all transition metal sites, Z and χ of chalcogen atom are appended at the end of the feature vector. A 29-dimension vector is created and can represent each alloy configuration in our study.

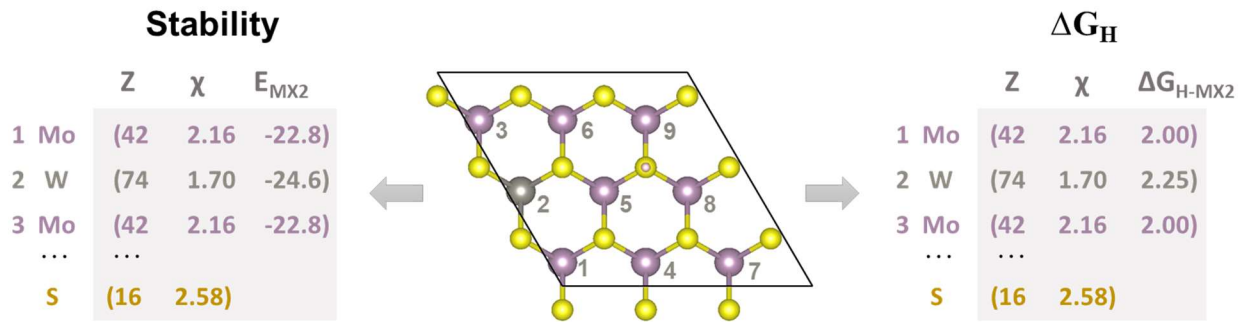


Fig. 5.11 Illustration of feature vector assignment. Alloy structures are reduced to numerical representations.

5.7.5 Electrocatalytic Activity of 72 TMDC Alloys

Fig. 5.12-17 show the machine learning predicted ΔG_H values for various TMDC ternary alloys at different concentrations.

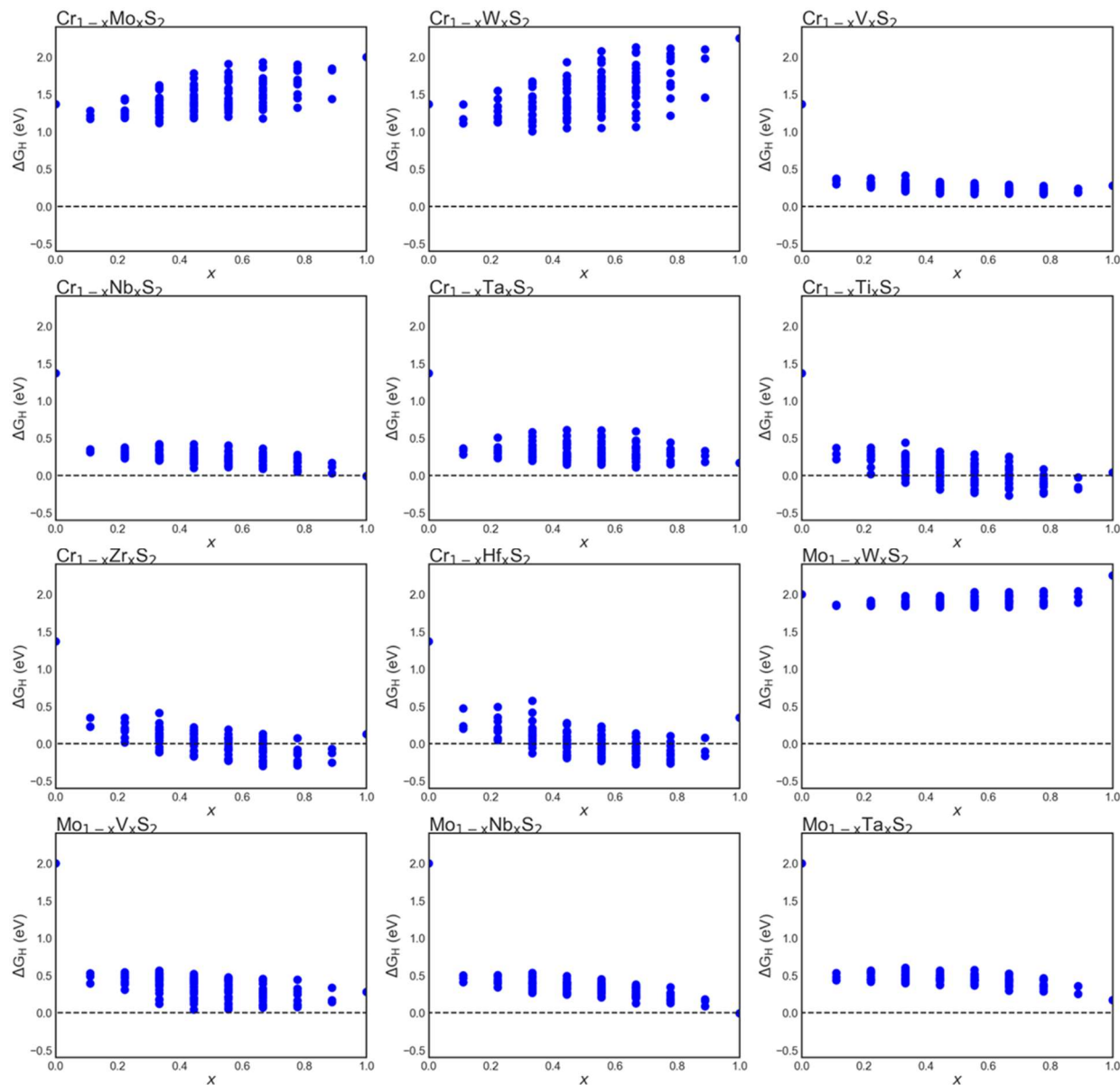


Fig. 5.12 Machine learning predicted ΔG_H values of TMDC ternary alloys at different concentrations. Black dash lines indicate the optimal ΔG_H desirable for HER.

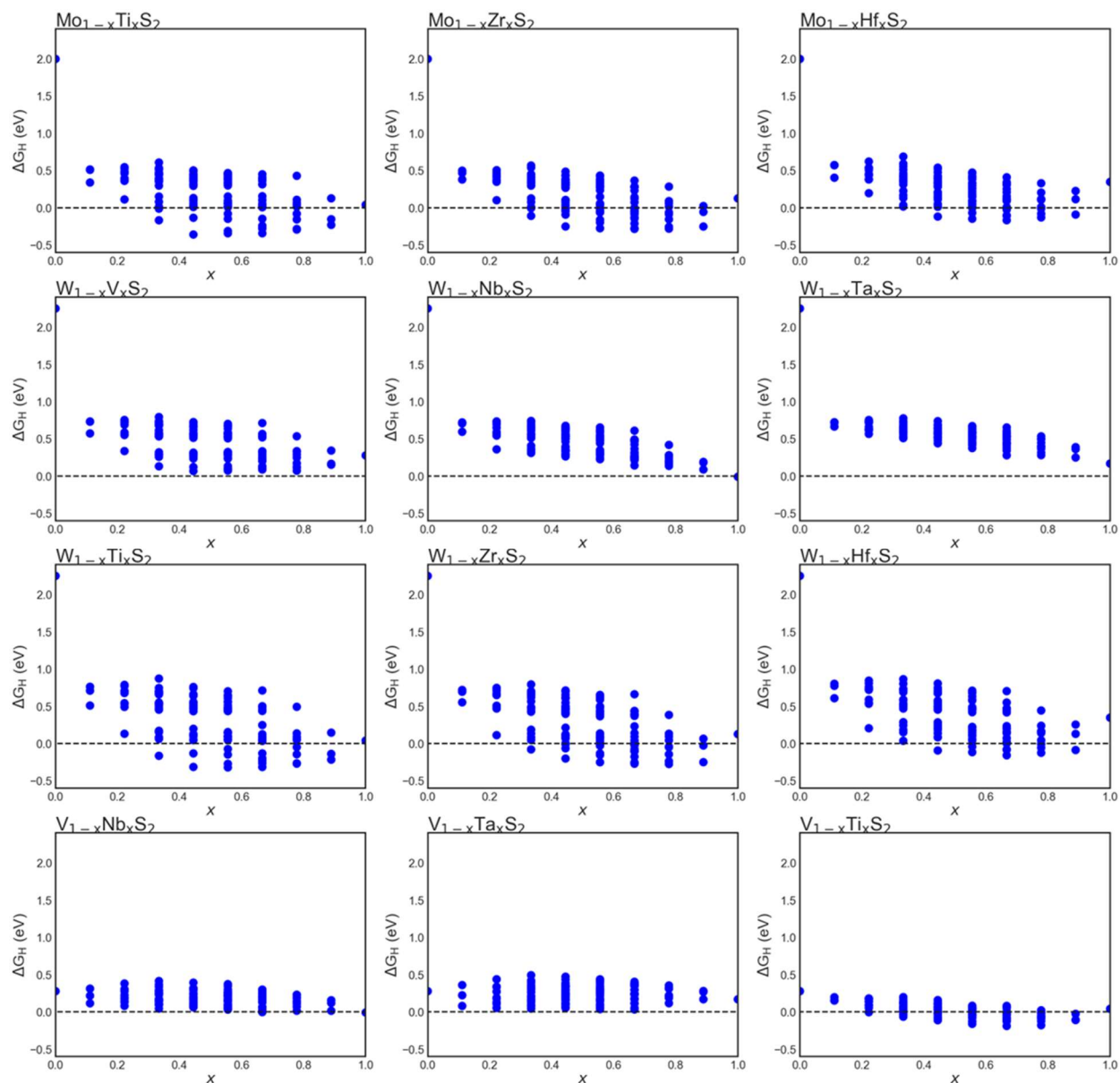


Fig. 5.13 Machine learning predicted ΔG_H values of TMDC ternary alloys at different concentrations. Black dash lines indicate the optimal ΔG_H desirable for HER.

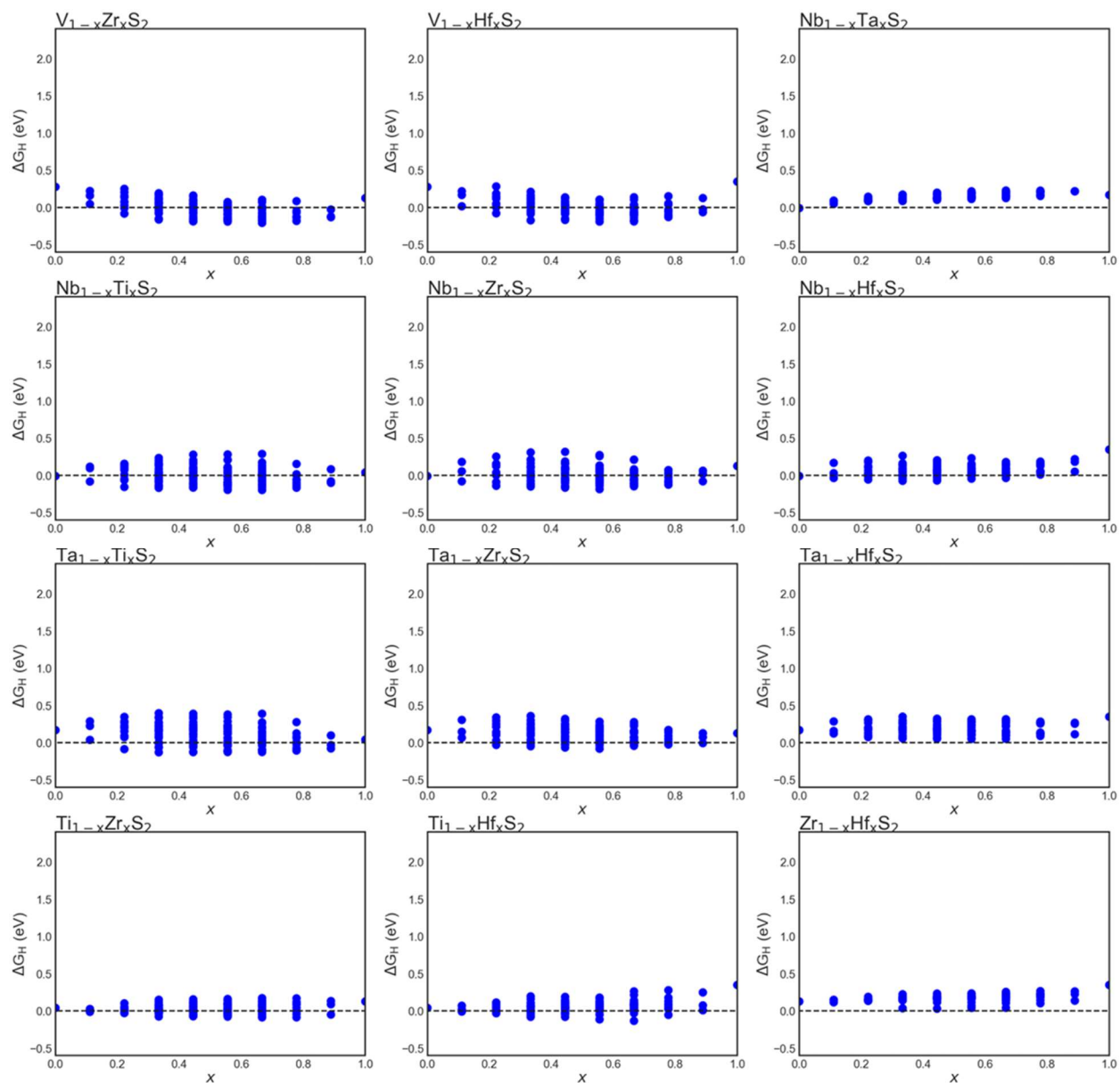


Fig. 5.14 Machine learning predicted ΔG_H values of TMDC ternary alloys at different concentrations. Black dash lines indicate the optimal ΔG_H desirable for HER.

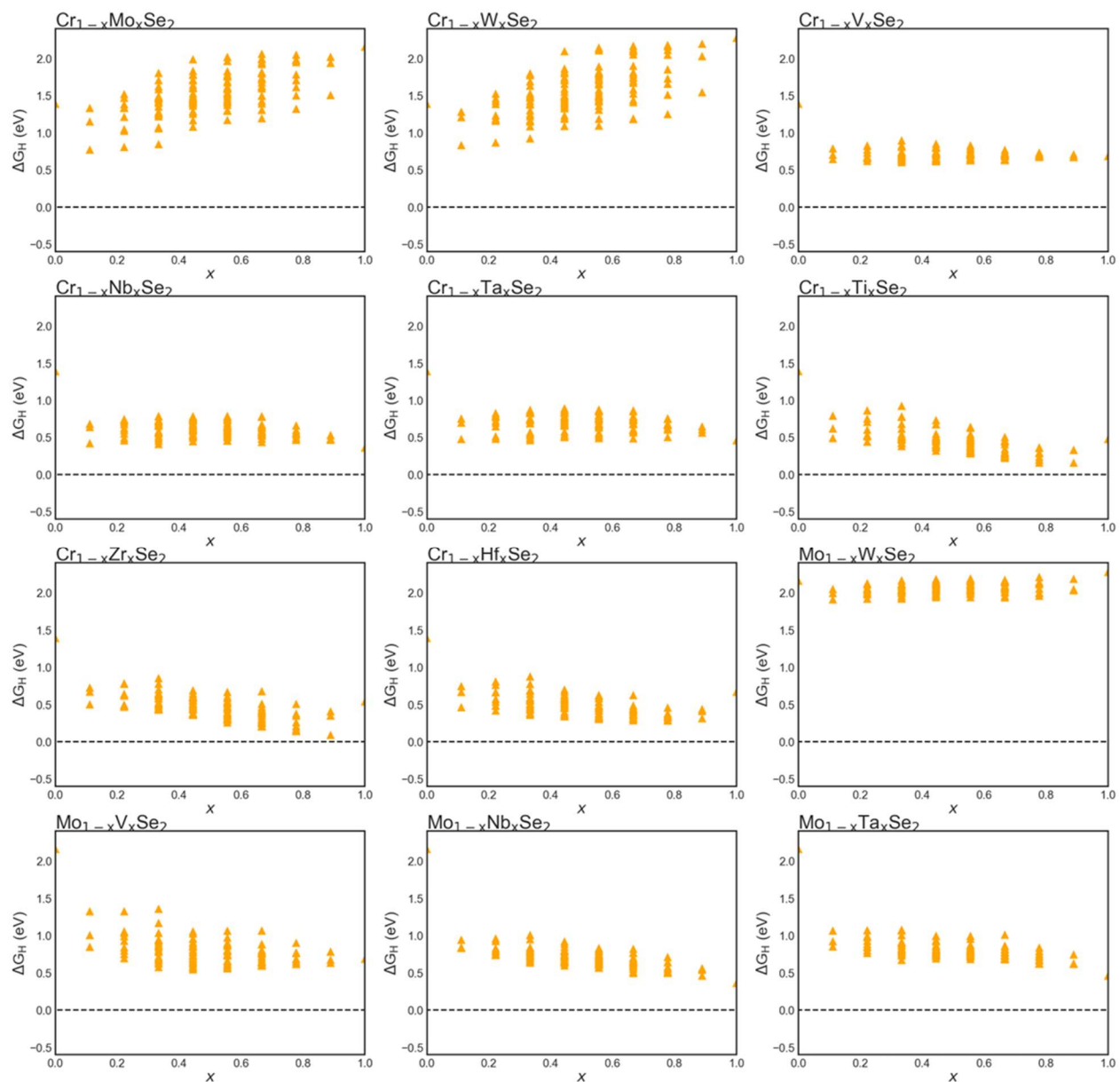


Fig. 5.15 Machine learning predicted ΔG_H values of TMDC ternary alloys at different concentrations. Black dash lines indicate the optimal ΔG_H desirable for HER.

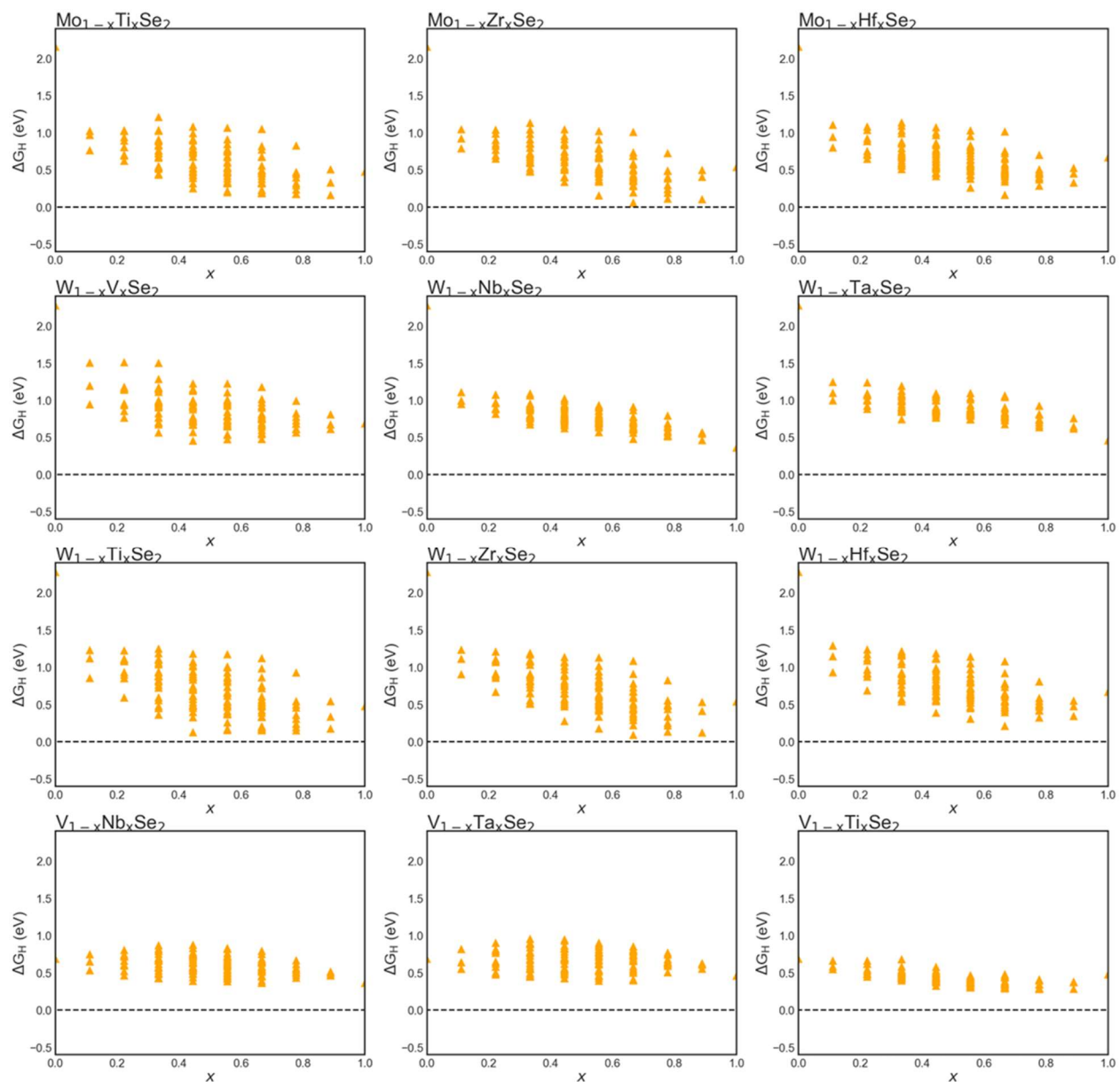


Fig. 5.16 Machine learning predicted ΔG_H values of TMDC ternary alloys at different concentrations. Black dash lines indicate the optimal ΔG_H desirable for HER.

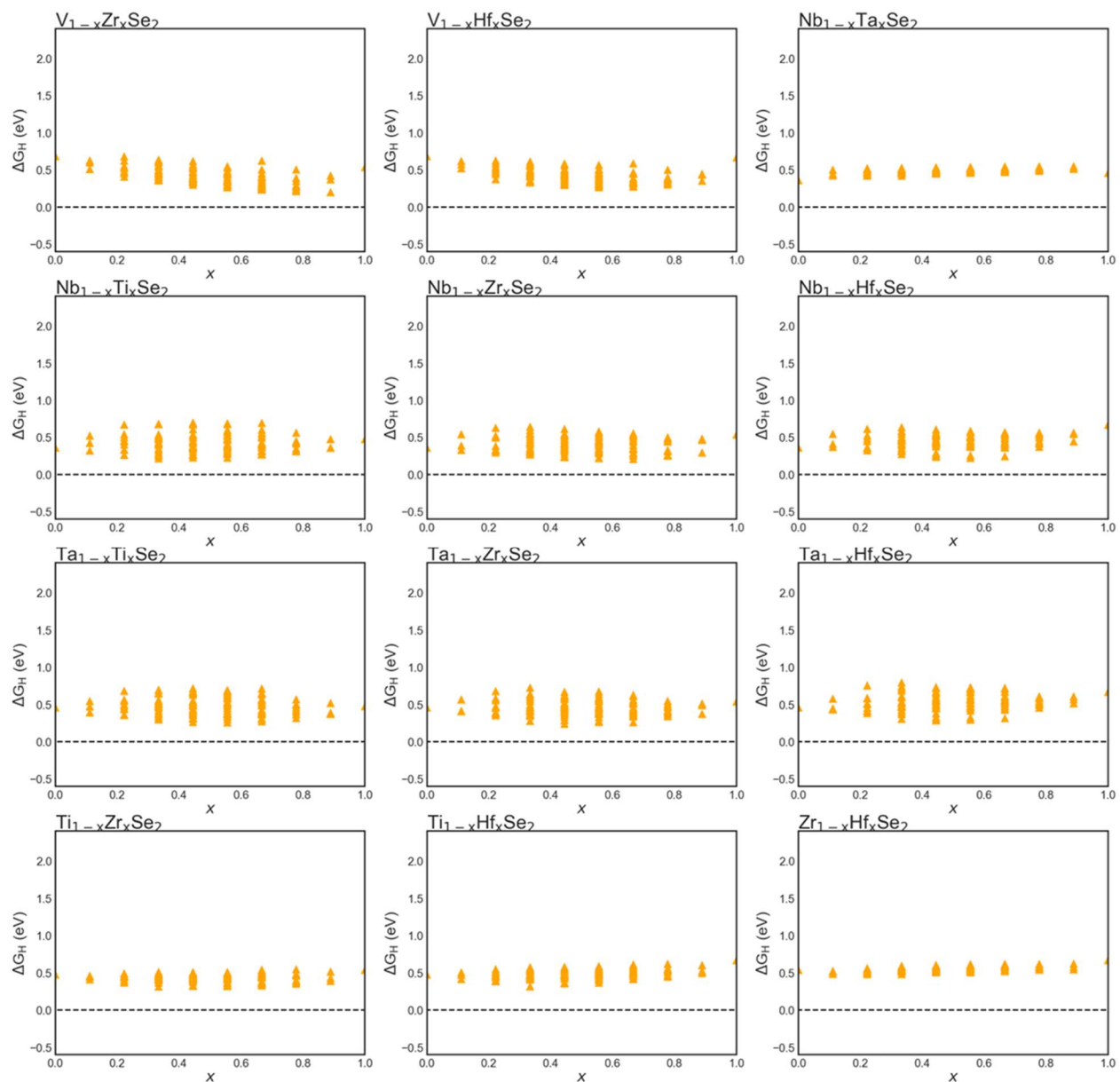


Fig. 5.17 Machine learning predicted ΔG_H values of TMDC ternary alloys at different concentrations. Black dash lines indicate the optimal ΔG_H desirable for HER.

5.7.6 HER activity mapping for MSe₂

Fig. 5.18 presents the fraction of effective adsorption sites with or without stability considerations for each 2D MSe₂ alloy.

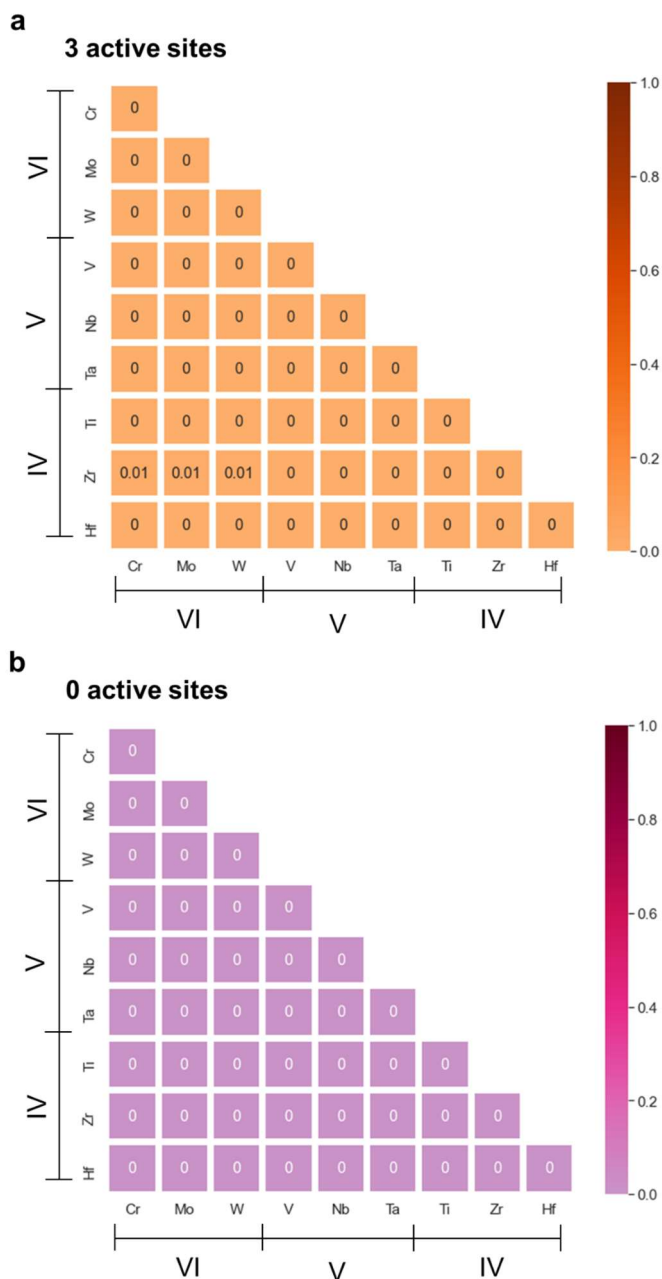


Fig. 5.18 HER activity heatmaps for MSe₂ alloys showing (a) the fraction of adsorption sites of ΔG_H within the optimal range of (-0.1,0.1) eV for each alloy, and (b) the fraction of adsorption sites that are stable and have optimal ΔG_H for each MSe₂ alloy. The number indicates the fraction value an alloy exhibits, which is also reflected by the color.

5.7.7. HER activity mapping for MS₂ at different concentrations

Fig. 5.19 shows the fraction of stable effective adsorption sites for each MS₂ alloy at different concentrations.

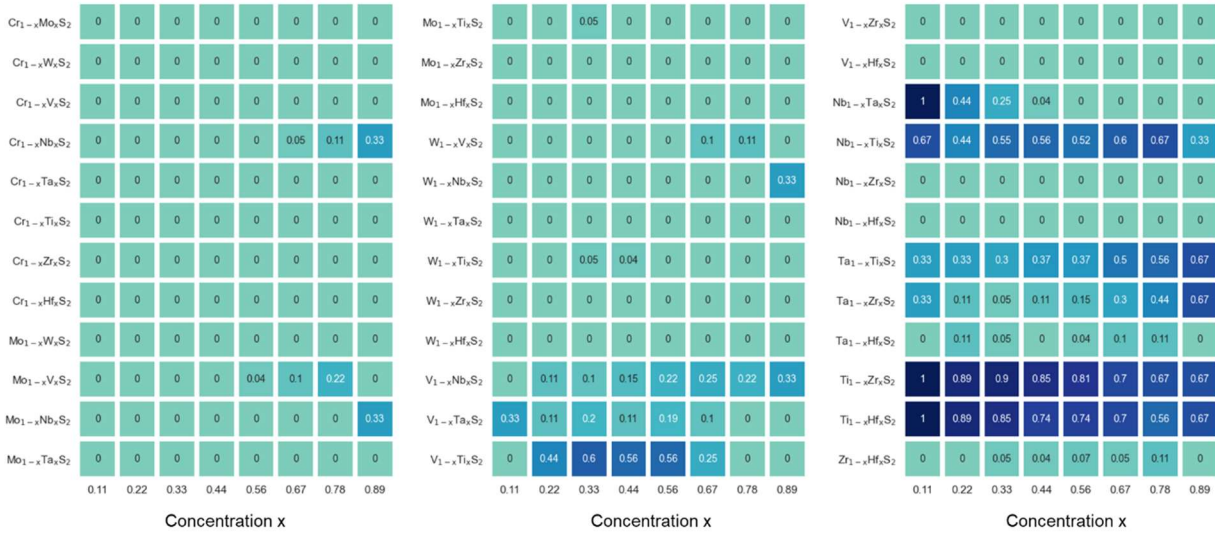


Fig. 5.19 HER activity heatmap for MS₂ alloys showing the fraction of adsorption sites that are stable and have optimal ΔG_H for each alloy at different concentrations. The number indicates the fraction value an alloy exhibits, which is also reflected by the color.

5.7.8 p-band center ϵ_p vs. concentration x of TMDC alloys

Fig. 5.20 shows p-band center versus concentration plots considering all adsorption sites in Mo_(1-x)V_xS₂ and W_(1-x)V_xSe₂.

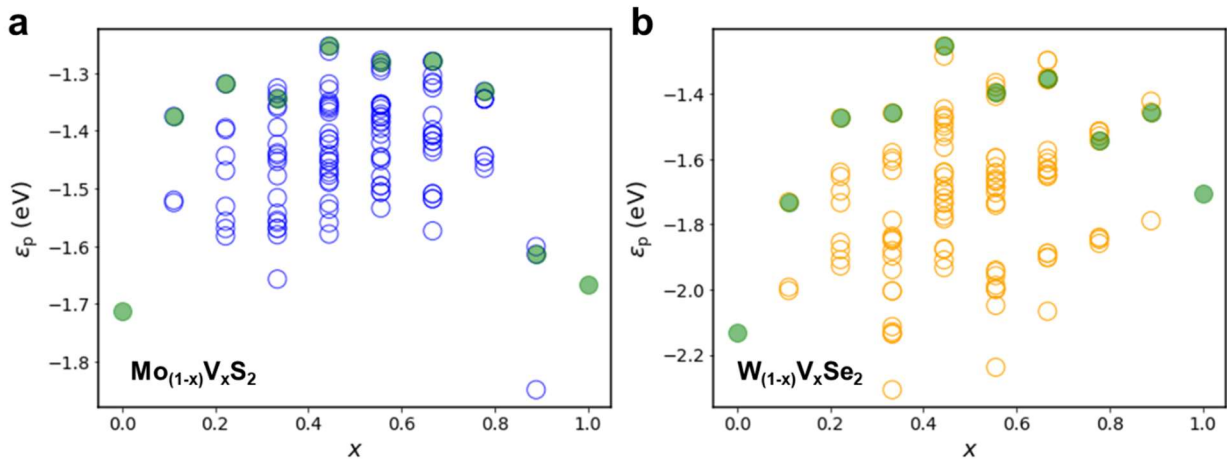


Fig. 5.20 p-band center ε_p vs. concentration x plots for all adsorption sites in (a) $\text{Mo}_{(1-x)}\text{V}_x\text{S}_2$ and (b) $\text{W}_{(1-x)}\text{V}_x\text{Se}_2$. Green solid points here highlight the adsorption sites with the best (lowest) ΔG_{H} at each concentration.

5.7.9 Example adsorption configurations

Fig. 5.21 shows hydrogen adsorption configurations on six representative TMDC alloys. It is found that hydrogen remains adsorption at top of the chalcogen atoms after structural relaxation for all cases.

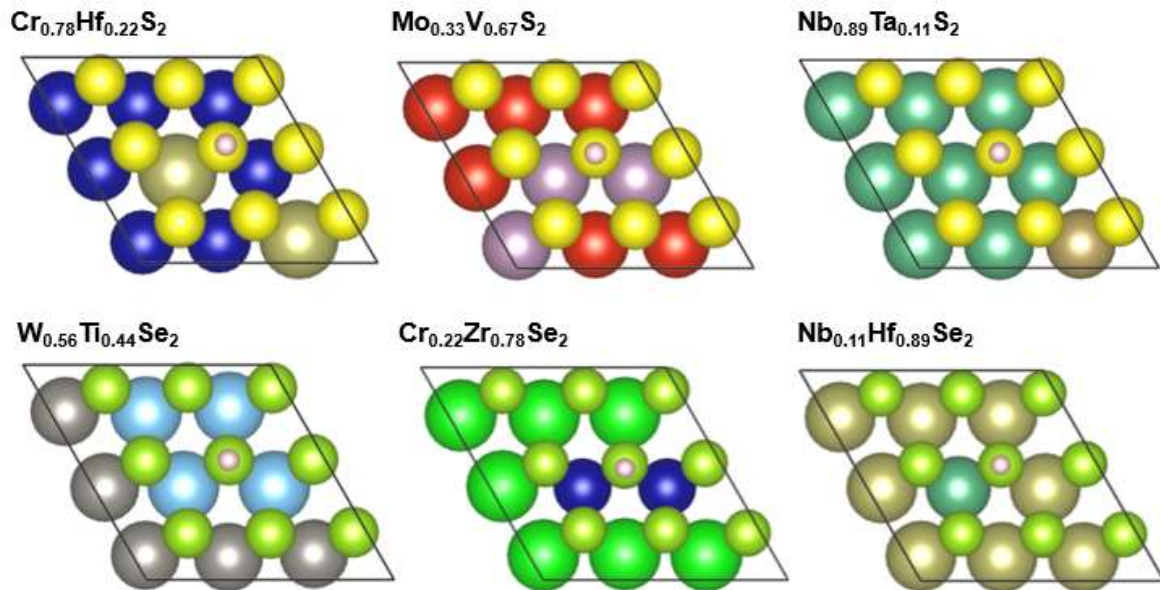


Fig. 5.21 Example hydrogen adsorption configurations on six representative TMDC alloys, where S atoms, Se atoms and H atoms are colored yellow, green, and pink respectively.

5.8 References

- [1] M.S. Dresselhaus, I.L. Thomas, Alternative energy technologies, *Nature* 414(6861) (2001) 332-337.
- [2] Z.W. Seh, J. Kibsgaard, C.F. Dickens, I. Chorkendorff, J.K. Nørskov, T.F. Jaramillo, Combining theory and experiment in electrocatalysis: Insights into materials design, *Science* 355(6321) (2017) eaad4998.
- [3] S. Trasatti, Work function, electronegativity, and electrochemical behaviour of metals: III. Electrolytic hydrogen evolution in acid solutions, *Journal of Electroanalytical Chemistry and Interfacial Electrochemistry* 39(1) (1972) 163-184.

- [4] N. Cheng, S. Stambula, D. Wang, M.N. Banis, J. Liu, A. Riese, B. Xiao, R. Li, T.K. Sham, L.M. Liu, G.A. Botton, X. Sun, Platinum single-atom and cluster catalysis of the hydrogen evolution reaction, *Nat Commun* 7 (2016) 13638.
- [5] Y. Jiao, Y. Zheng, M. Jaroniec, S.Z. Qiao, Design of electrocatalysts for oxygen- and hydrogen-involving energy conversion reactions, *Chem Soc Rev* 44(8) (2015) 2060-86.
- [6] Y. Chen, K. Yang, B. Jiang, J. Li, M. Zeng, L. Fu, Emerging two-dimensional nanomaterials for electrochemical hydrogen evolution, *Journal of Materials Chemistry A* 5(18) (2017) 8187-8208.
- [7] S. Jayabal, G. Saranya, J. Wu, Y. Liu, D. Geng, X. Meng, Understanding the high-electrocatalytic performance of two-dimensional MoS₂ nanosheets and their composite materials, *Journal of Materials Chemistry A* 5(47) (2017) 24540-24563.
- [8] X. Chia, M. Pumera, Layered transition metal dichalcogenide electrochemistry: journey across the periodic table, *Chem Soc Rev* 47(15) (2018) 5602-5613.
- [9] A. Ambrosi, Z. Sofer, M. Pumera, 2H → 1T phase transition and hydrogen evolution activity of MoS₂, MoSe₂, WS₂ and WSe₂ strongly depends on the MX₂ composition, *Chem Commun (Camb)* 51(40) (2015) 8450-3.
- [10] D.B. Putungan, S.H. Lin, J.L. Kuo, A first-principles examination of conducting monolayer 1T'-MX₂ (M = Mo, W; X = S, Se, Te): promising catalysts for hydrogen evolution reaction and its enhancement by strain, *Phys Chem Chem Phys* 17(33) (2015) 21702-8.
- [11] Y.R. An, X.L. Fan, Z.F. Luo, W.M. Lau, Nanopolygons of Monolayer MS₂: Best Morphology and Size for HER Catalysis, *Nano Lett* 17(1) (2017) 368-376.
- [12] J. Zhu, Z.C. Wang, H. Dai, Q. Wang, R. Yang, H. Yu, M. Liao, J. Zhang, W. Chen, Z. Wei, N. Li, L. Du, D. Shi, W. Wang, L. Zhang, Y. Jiang, G. Zhang, Boundary activated hydrogen evolution reaction on monolayer MoS₂, *Nat Commun* 10(1) (2019) 1348.
- [13] Y. Ouyang, C. Ling, Q. Chen, Z. Wang, L. Shi, J. Wang, Activating Inert Basal Planes of MoS₂ for Hydrogen Evolution Reaction through the Formation of Different Intrinsic Defects, *Chemistry of Materials* 28(12) (2016) 4390-4396.
- [14] B. Hinnemann, P.G. Moses, J. Bonde, K.P. Jørgensen, J.H. Nielsen, S. Horch, I. Chorkendorff, J.K. Nørskov, Biomimetic Hydrogen Evolution: MoS₂ Nanoparticles as Catalyst for Hydrogen Evolution, *Journal of the American Chemical Society* 127(15) (2005) 5308-5309.
- [15] H. Li, C. Tsai, A.L. Koh, L. Cai, A.W. Contryman, A.H. Fragapane, J. Zhao, H.S. Han, H.C. Manoharan, F. Abild-Pedersen, J.K. Nørskov, X. Zheng, Corrigendum: Activating and optimizing MoS₂ basal planes for hydrogen evolution through the formation of strained sulphur vacancies, *Nat Mater* 15(3) (2016) 364.
- [16] Y. Lei, S. Pakhira, K. Fujisawa, X. Wang, O.O. Iyiola, N. Perea Lopez, A. Laura Elias, L. Pulickal Rajukumar, C. Zhou, B. Kabius, N. Alem, M. Endo, R. Lv, J.L. Mendoza-Cortes, M. Terrones, Low-temperature Synthesis of Heterostructures of Transition Metal Dichalcogenide Alloys (W_xMo_{1-x}S₂) and Graphene with Superior Catalytic Performance for Hydrogen Evolution, *ACS Nano* 11(5) (2017) 5103-5112.
- [17] H. Wang, L. Ouyang, G. Zou, C. Sun, J. Hu, X. Xiao, L. Gao, Optimizing MoS₂ Edges by Alloying Isovalent W for Robust Hydrogen Evolution Activity, *ACS Catalysis* 8(10) (2018) 9529-9536.
- [18] S.M. Tan, M. Pumera, Composition-Graded MoWS_x Hybrids with Tailored Catalytic Activity by Bipolar Electrochemistry, *ACS Applied Materials & Interfaces* 9(48) (2017) 41955-41964.

- [19] M. Zhuang, L.-Y. Gan, M. Zou, Y. Dou, X. Ou, Z. Liu, Y. Ding, I.H. Abidi, A. Tyagi, M. Jalali, Engineering sub-100 nm Mo (1– x) W x Se 2 crystals for efficient hydrogen evolution catalysis, *Journal of Materials Chemistry A* 6(7) (2018) 2900-2907.
- [20] O.E. Meiron, V. Kuraganti, I. Hod, R. Bar-Ziv, M. Bar-Sadan, Improved catalytic activity of Mo 1– x W x Se 2 alloy nanoflowers promotes efficient hydrogen evolution reaction in both acidic and alkaline aqueous solutions, *Nanoscale* 9(37) (2017) 13998-14005.
- [21] J. Greeley, M. Mavrikakis, Alloy catalysts designed from first principles, *Nature Materials* 3(11) (2004) 810-815.
- [22] L.M. Xie, Two-dimensional transition metal dichalcogenide alloys: preparation, characterization and applications, *Nanoscale* 7(44) (2015) 18392-401.
- [23] Q. Gong, L. Cheng, C. Liu, M. Zhang, Q. Feng, H. Ye, M. Zeng, L. Xie, Z. Liu, Y. Li, Ultrathin MoS₂(1–x)Se_{2x} Alloy Nanoflakes For Electrocatalytic Hydrogen Evolution Reaction, *ACS Catalysis* 5(4) (2015) 2213-2219.
- [24] Q. Fu, L. Yang, W. Wang, A. Han, J. Huang, P. Du, Z. Fan, J. Zhang, B. Xiang, Synthesis and enhanced electrochemical catalytic performance of monolayer WS₂ (1–x) Se_{2x} with a tunable band gap, *Advanced Materials* 27(32) (2015) 4732-4738.
- [25] V. Kiran, D. Mukherjee, R.N. Jenjeti, S. Sampath, Active guests in the MoS₂/MoSe₂ host lattice: efficient hydrogen evolution using few-layer alloys of MoS(2(1-x))Se(2x), *Nanoscale* 6(21) (2014) 12856-63.
- [26] B. Hammer, J.K. Nørskov, Theoretical surface science and catalysis—calculations and concepts, *Advances in catalysis* 45 (2000) 71-129.
- [27] J. Schmidt, M.R.G. Marques, S. Botti, M.A.L. Marques, Recent advances and applications of machine learning in solid-state materials science, *npj Computational Materials* 5(1) (2019) 83.
- [28] K.T. Butler, D.W. Davies, H. Cartwright, O. Isayev, A. Walsh, Machine learning for molecular and materials science, *Nature* 559(7715) (2018) 547-555.
- [29] K. Omata, Screening of New Additives of Active-Carbon-Supported Heteropoly Acid Catalyst for Friedel–Crafts Reaction by Gaussian Process Regression, *Industrial & Engineering Chemistry Research* 50(19) (2011) 10948-10954.
- [30] A. Mannodi-Kanakkithodi, M.Y. Toriyama, F.G. Sen, M.J. Davis, R.F. Klie, M.K. Chan, Machine-learned impurity level prediction for semiconductors: the example of Cd-based chalcogenides, *npj Computational Materials* 6(1) (2020) 1-14.
- [31] C.T. Chen, G.X. Gu, Generative Deep Neural Networks for Inverse Materials Design Using Backpropagation and Active Learning, *Advanced Science* (2020) 1902607.
- [32] C. Wang, K. Aoyagi, P. Wisesa, T. Mueller, Lithium Ion Conduction in Cathode Coating Materials from On-the-Fly Machine Learning, *Chemistry of Materials* (2020).
- [33] T. Toyao, Z. Maeno, S. Takakusagi, T. Kamachi, I. Takigawa, K.-i. Shimizu, Machine Learning for Catalysis Informatics: Recent Applications and Prospects, *ACS Catalysis* 10(3) (2020) 2260-2297.
- [34] T. Toyao, K. Suzuki, S. Kikuchi, S. Takakusagi, K.-i. Shimizu, I. Takigawa, Toward effective utilization of methane: machine learning prediction of adsorption energies on metal alloys, *The Journal of Physical Chemistry C* 122(15) (2018) 8315-8326.
- [35] L. Bassman, P. Rajak, R.K. Kalia, A. Nakano, F. Sha, J. Sun, D.J. Singh, M. Aykol, P. Huck, K. Persson, P. Vashishta, Active learning for accelerated design of layered materials, *npj Computational Materials* 4(1) (2018) 74.

- [36] M.O.J. Jäger, E.V. Morooka, F. Federici Canova, L. Himanen, A.S. Foster, Machine learning hydrogen adsorption on nanoclusters through structural descriptors, *npj Computational Materials* 4(1) (2018) 37.
- [37] K. Tran, Z.W. Ulissi, Active learning across intermetallics to guide discovery of electrocatalysts for CO₂ reduction and H₂ evolution, *Nature Catalysis* 1(9) (2018) 696-703.
- [38] K.T. Schütt, H. Glawe, F. Brockherde, A. Sanna, K.-R. Müller, E.K. Gross, How to represent crystal structures for machine learning: Towards fast prediction of electronic properties, *Physical Review B* 89(20) (2014) 205118.
- [39] F. Legrain, J. Carrete, A. van Roekeghem, S. Curtarolo, N. Mingo, How chemical composition alone can predict vibrational free energies and entropies of solids, *Chemistry of Materials* 29(15) (2017) 6220-6227.
- [40] Z. Yang, W. Gao, Q. Jiang, A machine learning scheme for the catalytic activity of alloys with intrinsic descriptors, *Journal of Materials Chemistry A* 8(34) (2020) 17507-17515.
- [41] P. Schlexer Lamoureux, K.T. Winther, J.A. Garrido Torres, V. Streibel, M. Zhao, M. Bajdich, F. Abild-Pedersen, T. Bligaard, Machine Learning for Computational Heterogeneous Catalysis, *ChemCatChem* 11(16) (2019) 3581-3601.
- [42] M. Chhowalla, H.S. Shin, G. Eda, L.-J. Li, K.P. Loh, H. Zhang, The chemistry of two-dimensional layered transition metal dichalcogenide nanosheets, *Nature Chemistry* 5(4) (2013) 263-275.
- [43] Z. Li, S. Wang, W.S. Chin, L.E. Achenie, H. Xin, High-throughput screening of bimetallic catalysts enabled by machine learning, *Journal of Materials Chemistry A* 5(46) (2017) 24131-24138.
- [44] S.J. Davie, N. Di Pasquale, P.L. Popelier, Kriging atomic properties with a variable number of inputs, *The Journal of Chemical Physics* 145(10) (2016) 104104.
- [45] M. Lukasz, mendelev--A Python resource for properties of chemical elements, ions and isotopes, 2014.
- [46] R.S. Olson, N. Bartley, R.J. Urbanowicz, J.H. Moore, Evaluation of a Tree-based Pipeline Optimization Tool for Automating Data Science, *Proceedings of the Genetic and Evolutionary Computation Conference 2016*, Association for Computing Machinery, Denver, Colorado, USA, 2016, pp. 485-492.
- [47] Z. Hemmat, J. Cavin, A. Ahmadiparidari, A. Ruckel, S. Rastegar, S.N. Misal, L. Majidi, K. Kumar, S. Wang, J. Guo, R. Dawood, F. Lagunas, P. Parajuli, A.T. Ngo, L.A. Curtiss, S.B. Cho, J. Cabana, R.F. Klie, R. Mishra, A. Salehi-Khojin, Quasi-Binary Transition Metal Dichalcogenide Alloys: Thermodynamic Stability Prediction, Scalable Synthesis, and Application, *Advanced Materials* 32(26) (2020) 1907041.
- [48] X. Gan, R. Lv, X. Wang, Z. Zhang, K. Fujisawa, Y. Lei, Z.-H. Huang, M. Terrones, F. Kang, Pyrolytic carbon supported alloying metal dichalcogenides as free-standing electrodes for efficient hydrogen evolution, *Carbon* 132 (2018) 512-519.
- [49] H. Duan, C. Wang, G. Li, H. Tan, W. Hu, L. Cai, W. Liu, N. Li, Q. Ji, Y. Wang, Y. Lu, W. Yan, F. Hu, W. Zhang, Z. Sun, Z. Qi, L. Song, S. Wei, Single-Atom-Layer Catalysis in a MoS₂ Monolayer Activated by Long-Range Ferromagnetism for the Hydrogen Evolution Reaction: Beyond Single-Atom Catalysis, *Angewandte Chemie International Edition* 60(13) (2021) 7251-7258.
- [50] P. Liu, J.K. Nørskov, Ligand and ensemble effects in adsorption on alloy surfaces, *Physical Chemistry Chemical Physics* 3(17) (2001) 3814-3818.

- [51] A. Ramstad, F. Strisland, T. Ramsvik, A. Borg, CO adsorption on the Pt/Rh(100) surface studied by high-resolution photoemission, *Surface Science* 458(1) (2000) 135-146.
- [52] Y. Chen, P. Ou, X. Bie, J. Song, Basal plane activation in monolayer MoTe₂ for the hydrogen evolution reaction via phase boundaries, *Journal of Materials Chemistry A* 8(37) (2020) 19522-19532.
- [53] M. Mavrikakis, B. Hammer, J.K. Nørskov, Effect of Strain on the Reactivity of Metal Surfaces, *Physical Review Letters* 81(13) (1998) 2819-2822.
- [54] J. Kang, S. Tongay, J. Li, J. Wu, Monolayer semiconducting transition metal dichalcogenide alloys: Stability and band bowing, *Journal of Applied Physics* 113(14) (2013) 143703.
- [55] J.-H. Yang, B.I. Yakobson, Unusual Negative Formation Enthalpies and Atomic Ordering in Isovalent Alloys of Transition Metal Dichalcogenide Monolayers, *Chemistry of Materials* 30(5) (2018) 1547-1555.
- [56] L.G. Ferreira, S.-H. Wei, A. Zunger, First-principles calculation of alloy phase diagrams: The renormalized-interaction approach, *Physical Review B* 40(5) (1989) 3197-3231.
- [57] G. Henkelman, A. Arnaldsson, H. Jónsson, A fast and robust algorithm for Bader decomposition of charge density, *Computational Materials Science* 36(3) (2006) 354-360.
- [58] F. Gao, D.W. Goodman, Pd–Au bimetallic catalysts: understanding alloy effects from planar models and (supported) nanoparticles, *Chemical Society Reviews* 41(24) (2012) 8009-8020.
- [59] C. Tsai, K. Chan, J.K. Nørskov, F. Abild-Pedersen, Theoretical insights into the hydrogen evolution activity of layered transition metal dichalcogenides, *Surface Science* 640 (2015) 133-140.
- [60] A. Hjorth Larsen, J. Jørgen Mortensen, J. Blomqvist, I.E. Castelli, R. Christensen, M. Dulák, J. Friis, M.N. Groves, B. Hammer, C. Hargus, E.D. Hermes, P.C. Jennings, P. Bjerre Jensen, J. Kermode, J.R. Kitchin, E. Leonhard Kolsbjerg, J. Kubal, K. Kaasbjerg, S. Lysgaard, J. Bergmann Maronsson, T. Maxson, T. Olsen, L. Pastewka, A. Peterson, C. Rostgaard, J. Schiøtz, O. Schütt, M. Strange, K.S. Thygesen, T. Vegge, L. Vilhelmsen, M. Walter, Z. Zeng, K.W. Jacobsen, The atomic simulation environment—a Python library for working with atoms, *Journal of Physics: Condensed Matter* 29(27) (2017) 273002.
- [61] M. Ångqvist, W.A. Muñoz, J.M. Rahm, E. Fransson, C. Durniak, P. Rozyczko, T.H. Rod, P. Erhart, ICET – A Python Library for Constructing and Sampling Alloy Cluster Expansions, *Advanced Theory and Simulations* 2(7) (2019) 1900015.
- [62] G. Kresse, D. Joubert, From ultrasoft pseudopotentials to the projector augmented-wave method, *Physical Review B* 59(3) (1999) 1758-1775.
- [63] G. Kresse, J. Furthmüller, Efficient iterative schemes for ab initio total-energy calculations using a plane-wave basis set, *Physical Review B* 54(16) (1996) 11169-11186.
- [64] P.E. Blöchl, Projector augmented-wave method, *Physical Review B* 50(24) (1994) 17953-17979.
- [65] J.P. Perdew, K. Burke, M. Ernzerhof, Generalized Gradient Approximation Made Simple, *Physical Review Letters* 77(18) (1996) 3865-3868.
- [66] J.P. Perdew, J.A. Chevary, S.H. Vosko, K.A. Jackson, M.R. Pederson, D.J. Singh, C. Fiolhais, Atoms, molecules, solids, and surfaces: Applications of the generalized gradient approximation for exchange and correlation, *Physical Review B* 46(11) (1992) 6671-6687.
- [67] S. Grimme, J. Antony, S. Ehrlich, H. Krieg, A consistent and accurate ab initio parametrization of density functional dispersion correction (DFT-D) for the 94 elements H-Pu, *The Journal of Chemical Physics* 132(15) (2010) 154104.

- [68] S. Grimme, S. Ehrlich, L. Goerigk, Effect of the damping function in dispersion corrected density functional theory, *Journal of Computational Chemistry* 32(7) (2011) 1456-1465.
- [69] G. Rothenberg, *Catalysis: concepts and green applications*, John Wiley & Sons 2017.
- [70] C. Tsai, F. Abild-Pedersen, J.K. Nørskov, Tuning the MoS₂ Edge-Site Activity for Hydrogen Evolution via Support Interactions, *Nano Letters* 14(3) (2014) 1381-1387.
- [71] W.R.L. Lambrecht, B. Segall, Anomalous band-gap behavior and phase stability of c-BN--diamond alloys, *Physical Review B* 47(15) (1993) 9289-9296.
- [72] B. Hammer, J.K. Nørskov, Electronic factors determining the reactivity of metal surfaces, *Surface Science* 343(3) (1995) 211-220.
- [73] F. Pedregosa, G. Varoquaux, A. Gramfort, V. Michel, B. Thirion, O. Grisel, M. Blondel, P. Prettenhofer, R. Weiss, V. Dubourg, *Scikit-learn: Machine learning in Python*, the *Journal of machine Learning research* 12 (2011) 2825-2830.

Chapter 6 : Two-Dimensional III-Nitride Alloys: Electronic and Chemical Properties of Monolayer Ga_(1-x)Al_xN

Chapters 4 and 5 studied two modification strategies, i.e., introducing phase boundaries and alloying, for activating the basal plane of 2D TMDCs for hydrogen evolution reaction. Recently, a new class of 2D materials, 2D III-nitrides, has been successfully synthesized and demonstrated excellent electronic properties. To broaden the modification strategies to other 2D systems, Chapter 6 investigated the role of alloying in tuning the electronic and chemical properties of 2D III-nitrides using 2D Ga_(1-x)Al_xN alloys as representatives. Density functional theory calculations and cluster expansion method were employed to study the atomic arrangements and stability of 2D Ga_(1-x)Al_xN alloys. It was found that tunable band gaps and chemical properties of 2D Ga_(1-x)Al_xN random alloys can be achieved by varying the chemical compositions. The effect of strain on the electronic and catalytic properties of 2D Ga_(1-x)Al_xN was also investigated.

- This chapter is to be submitted, appeared as: Yiqing Chen, Pengfei Ou, Ying Zhao, and Jun Song. **Two-dimensional III-nitride alloys: Electronic and chemical properties of monolayer Ga_(1-x)Al_xN**

6.1 Abstract

Potential applications of III-nitrides have made their monolayer allotropes, i.e., two-dimensional (2D) III-nitrides, attracted much attention. Recently, alloying has been demonstrated as an effective method to control the properties of 2D materials. In this study, the stability, electronic and chemical properties of monolayer $\text{Ga}_{(1-x)}\text{Al}_x\text{N}$ alloys were investigated employing density functional theory (DFT) calculations and the cluster expansion (CE) method. The results show that 2D $\text{Ga}_{(1-x)}\text{Al}_x\text{N}$ alloys are thermodynamically stable and complete miscibility in the alloys can be achieved at ambient temperature (>85 K). By analyzing CE results, the atomic arrangement of 2D $\text{Ga}_{(1-x)}\text{Al}_x\text{N}$ was revealed, showing that Ga/Al atoms tend to mix with the Al/Ga atoms in their next nearest site. The band gaps of $\text{Ga}_{(1-x)}\text{Al}_x\text{N}$ random alloys can be tuned by varying the chemical composition, and the corresponding bowing parameter was calculated as -0.17 eV. Biaxial tensile strain was also found to change the band gap values of $\text{Ga}_{(1-x)}\text{Al}_x\text{N}$ random alloys ascribed to its modifications to the CBM positions. The chemical properties of $\text{Ga}_{(1-x)}\text{Al}_x\text{N}$ can also be significantly altered by strain, making them good candidates as photocatalysts for water splitting. The present study can play a crucial role in optimizing and designing 2D III-nitrides for next-generation electronics and photocatalysts.

6.2 Introduction

III-nitrides, including AlN, GaN and InN and their alloys, are promising semiconductors that possess tunable band gaps covering the spectral range from ultraviolet to infrared [1, 2]. The excellent properties of III-nitrides have made them ideal candidate materials for modern electronic and optoelectronic devices [2, 3]. Meanwhile, due to their unique surface properties, III-nitrides

exhibit great potential in photocatalysis and have recently gained importance in hydrogen evolution reaction, oxygen evolution reaction and carbon dioxide reduction [4-7].

The wide-ranging applications of III-nitrides have also brought their monolayer allotropes, i.e., two-dimensional (2D) III-nitrides, into the focus of research interest. 2D III-nitrides was first predicted using first-principles calculations [8], and then synthesized via graphene encapsulation [9]. 2D III-nitrides were found to have different forms, among which graphene-like planar GaN and AlN (2D hexagonal GaN and AlN) were extensively studied [10, 11]. Previous works demonstrated the stability of 2D hexagonal GaN and AlN from *ab initio* phonon calculations [12, 13]. Additionally, 2D hexagonal GaN and AlN were found to remain their stability under thermal excitations as confirmed by *ab initio* finite temperature molecular dynamics (MD) calculations performed under 1000 K [14]. Similar to bulk semiconductors, 2D III-nitrides have demonstrated desirable properties for a broad range of applications. For example, the band gap of 2D hexagonal GaN can be tailored by decorating with H or F adatoms, showing potential for optoelectronic devices [15]; 2D GaN/ Mg(OH)₂ heterostructure was predicted to have suitable band structures and adsorption abilities that promote water splitting [16].

However, the applications of 2D III-nitrides are bottlenecked by their low stability [8]. Since their bulk counterparts do not have layered structures like graphite, the fabrication of layered III-nitrides inevitably introduces unsaturated dangling bonds on the surface, which makes the synthesis difficult and thus hampers their large-scale applications. In addition, it is always desirable to extend and tune the physical and chemical properties of 2D III-nitrides. Historically, alloying as an effective strategy has been widely used in semiconductor science to achieve tunable band gaps for materials and enhance their thermodynamic stability [17, 18]. Recently, alloying in 2D materials have been realized and demonstrated continuously tunable electronic and optical

properties [19, 20]. 2D alloys like $\text{Mo}_{(1-x)}\text{W}_x\text{S}_2$ and $\text{Mo}_{(1-x)}\text{W}_x\text{Se}_2$ were found to exhibit negative formation energies, which indicate that alloying can successfully stabilize 2D structures [19]. Among III-nitrides, Kanli et al. investigated the dynamical stability and band gap bowing of 2D $\text{Ga}_{(1-x)}\text{Al}_x\text{N}$ ordered alloys [21]; Wines et al. demonstrated the electronic and thermoelectric properties of 2D $\text{B}_{(1-x)}\text{Al}_x\text{N}$, $\text{Al}_{(1-x)}\text{Ga}_x\text{N}$, and $\text{Ga}_{(1-x)}\text{In}_x\text{N}$ alloys [10]. However, despite those great prior efforts, several aspects of 2D III-nitride alloys remain not well understood, i.e., the atomic ordering of alloy structures and the band gap bowing effect for random alloys. In addition, the strain effect to the electronic properties and the chemical properties of 2D $\text{Ga}_{(1-x)}\text{Al}_x\text{N}$ have not been explored.

In light of the above limitations, the present study investigated the stability, electronic and chemical properties of monolayer $\text{Ga}_{(1-x)}\text{Al}_x\text{N}$ alloys employing density functional theory calculations and the cluster expansion method. The stability of 2D $\text{Ga}_{(1-x)}\text{Al}_x\text{N}$ alloys was examined and the atomic arrangement of alloys was revealed. We found that 2D $\text{Ga}_{(1-x)}\text{Al}_x\text{N}$ alloys are thermodynamically stable, and the complete miscibility in alloys can be achieved at ambient temperature. Using random alloy structures, the electronic properties of 2D $\text{Ga}_{(1-x)}\text{Al}_x\text{N}$ alloys were then investigated, with the band gap bowing parameter calculated as -0.17 eV. Biaxial tensile strain was then applied to study their effect to the band gap values and chemical properties of 2D $\text{Ga}_{(1-x)}\text{Al}_x\text{N}$ alloys, with continuously tunable properties observed by varying chemical composition. Our work may guide the future design of 2D $\text{Ga}_{(1-x)}\text{Al}_x\text{N}$ alloys in electronics and photocatalysis.

6.3 Computational methods

6.3.1 Cluster expansion

In the CE formalism [22, 23], each metal site in an alloy configuration is assigned an occupation variable σ_i , with σ_i being equal to +1 or -1, representing which species is present at this site (e.g., +1 for Ga, and -1 for Al). In this way, any alloy configuration can be well described by a vector $\vec{\sigma} = (\sigma_1, \sigma_2, \sigma_3, \dots)$ containing all the σ_i information of the lattice. As a result, the formation enthalpy of a particular alloy configuration is expressed as [24, 25]:

$$\Delta H(\vec{\sigma}) = \sum_{\alpha} m_{\alpha} J_{\alpha} \xi_{\alpha}(\vec{\sigma}) \quad (6.1)$$

where α denotes a cluster, including singles, pairs and triplets. m_{α} is the number of symmetry-equivalent clusters of α , and J_{α} is the effective cluster interaction (ECI) parameter, representing the energy contribution from cluster α . The summation is taken over all symmetry-nonequivalent clusters. ξ_{α} is the cluster correlation function defined as:

$$\xi_{\alpha}(\vec{\sigma}) = \left\langle \prod_{i \in \alpha'} \sigma_i \right\rangle \quad (6.2)$$

with the angle bracket representing the average of the spin product of all symmetry-equivalent clusters α' of α . The ECIs are determined by fitting a certain number of samples obtained from density functional theory (DFT) calculations, and the fitted ECIs can then be used to predict the formation enthalpies of any alloy configurations quickly by just calculating the ξ_{α} .

In this work, CE method was employed using the Alloy-Theoretic Automated Toolkit (ATAT) code to fit the formation enthalpies of $\text{Ga}_{(1-x)}\text{Al}_x\text{N}$ alloys [24]. The formation enthalpies of 70 ordered structures up to 22 atoms per cell were calculated from density functional theory

(DFT) calculations, and then were used to fit the ECI values. The performance of the CE fitting was evaluated by cross-validation score with values of around 0.1 meV. The fitted ECIs were then used to predict the formation enthalpies of more than 1000 $\text{Ga}_{(1-x)}\text{Al}_x\text{N}$ alloy configurations.

6.3.2 Special quasi-random structure (SQS) method

SQS method was applied to investigate the stability and electronic properties of totally disorder $\text{Ga}_{(1-x)}\text{Al}_x\text{N}$ alloys [26]. For a random alloy, the correlation function is defined as $(2x - 1)^k$, with x the concentration of alloy and k the number of metal sites in the cluster (e.g., $k = 2$ for pairs.) [26]. SQS method generates special structures that have correlation functions close to random alloys, then these SQS structures can be used to simulate the physical properties of random alloys. In this study, SQS structures were constructed in 6×6 supercells for $x = 1/6, 1/3, 1/2, 2/3,$ and $5/6$.

6.3.3 Free energy of random alloys

The free energy of random alloys $F(x, T)$ is temperature-dependent and can be analytically estimated using the following equation:

$$F(x, T) = \Delta H(x) - TS(x) \quad (6.3)$$

Here, $\Delta H(x)$ is the formation enthalpy obtained from DFT calculations and T is the temperature. $S(x)$ is the entropy and can be estimated by a mean-field approach, which is defined as [25, 27]:

$$S(x) = -k_B [x \ln x + (1 - x) \ln(1 - x)] \quad (6.4)$$

where k_B is the Boltzmann constant. Positive and negative free energies indicate immiscible and miscible alloys, and the miscibility of alloys is tunable by increasing the temperature. The above equations can be used to estimate the critical temperature for complete miscibility (T_{CM}) of random alloys.

6.3.4 DFT calculations

Spin-polarized DFT calculations [28] were performed employing the Vienna Ab Initio Simulation Package (VASP) [29, 30]. The interactions of electrons with ion cores were represented by the projector-augmented wave (PAW) method [31], and the exchange-correlation was described by the Perdew-Burke-Ernzerhof (PBE) functional [32, 33]. To obtain more accurate band gap values, the hybrid Heyd-Scuseria-Ernzerhof (HSE06) functional was implemented for the calculation of electronic properties [34]. A kinetic cutoff energy of 550 eV was set for the plane-wave basis functions. To avoid periodic image interactions, a vacuum layer of at least 15 Å was set along the layer direction for all the structures. All structures were relaxed until the residual forces were smaller than 0.02 eV/Å and the electronic energy converged to 10^{-5} eV. For alloys generated for CE fitting, the k-point density was 1000 K points per reciprocal atom; for SQS structures with larger supercells, a Γ -centered k-point mesh of $2 \times 2 \times 1$ was used. For the calculations of the adsorption, the effect of van der Waals (vdW) interactions was considered using the DFT-D3 method [35, 36].

6.4 Results and discussion

6.4.1 Configurations and stabilities of $\text{Ga}_{(1-x)}\text{Al}_x\text{N}$ alloys

We start from 2D GaN and AlN with graphene-like planar honeycomb structures. The optimized structures of 2D hexagonal GaN and AlN are presented in Fig. 6.1, with lattice constants calculated as 3.21Å and 3.13Å respectively, comparable to those reported in the previous theoretical studies [21, 37]. 68 unique 2D $\text{Ga}_{(1-x)}\text{Al}_x\text{N}$ alloy configurations in the whole concentration range were then generated based on the pristine structures and optimized using PBE functionals. It is found that after structural optimization, $\text{Ga}_{(1-x)}\text{Al}_x\text{N}$ alloys retain their original

hexagonal planar cell shape (See exemplified $\text{Ga}_{(1-x)}\text{Al}_x\text{N}$ in Fig. 6.7 in Supporting information). Due to such small lattice distortion in the structures, it is expected that the standard CE method can properly match the structures and accurately fit the formation enthalpies of $\text{Ga}_{(1-x)}\text{Al}_x\text{N}$ alloys [38].

Fig. 6.2(a) shows the CE simulated results for 2D $\text{Ga}_{(1-x)}\text{Al}_x\text{N}$ alloys. It is seen that the formation enthalpies ΔH for all alloy configurations are positive, which indicates that no $\text{Ga}_{(1-x)}\text{Al}_x\text{N}$ alloy structures can be stable at 0 K. We also constructed a series of SQS structures representing random alloys at concentrations of $x = 1/6, 1/3, 1/2, 2/3$ and $5/6$, with corresponding optimized configurations shown in Fig. 6.2(c) and calculated ΔH plotted in Fig. 6.2(a). As demonstrated, random alloys also have positive ΔH that lies within the range of CE predicted values. This implies that $\text{Ga}_{(1-x)}\text{Al}_x\text{N}$ random alloys are also unstable and have the tendency of segregation at 0 K. To understand the relationship between atomic arrangement and the ΔH , the fitted ECI parameters were analyzed and presented in Fig. 6.2(b). Here, only small clusters (pairs and triplets) are presented, as the contributions of larger clusters to the ΔH are negligible. For a cluster, positive/negative J_α indicates that the interaction between the same species at the metal sites is repulsive/attractive, and such an atomic arrangement will lead to a positive/negative energy contribution to the formation enthalpy. By analyzing ECIs, as shown in Fig. 6.2(b), we observed negative J_α values with highest magnitudes for the nearest pair and triplet, indicative of a tendency of clustering but not alloying for neighboring atoms. However, it can be seen that J_α for the next nearest pair is positive, and the magnitude is also comparably high. This makes the mixing of next nearest atoms possible. Therefore, if there exist stable $\text{Ga}_{(1-x)}\text{Al}_x\text{N}$ alloys, it is likely to observe clustering in alloys but only with a size of 2 or 3 atoms.

To further investigate the stability of $\text{Ga}_{(1-x)}\text{Al}_x\text{N}$ alloys, we calculated the phonon dispersion curves of $2 \times 2 \text{ Ga}_{0.5}\text{Al}_{0.5}\text{N}$, which is the alloy configuration predicted to have the highest

ΔH among all concentrations (See Fig. 6.8 in Supporting information). The phonon frequencies are found to be positive, indicating the stability of this alloy structure. Since 2×2 $\text{Ga}_{0.5}\text{Al}_{0.5}\text{N}$ has the highest ΔH and is found to be stable, we can safely assume that all other alloy configurations should be stable. Moreover, since the magnitude of the positive ΔH is very small (below 7 meV), it is anticipated that negative free energies of mixing for alloys can be easily achieved by considering the entropic contributions. We calculated the free energy of mixing for $\text{Ga}_{(1-x)}\text{Al}_x\text{N}$ random alloys. As depicted in Fig. 6.3, by increasing the temperature to room temperature (300 K), the free energies of random alloys continuously decrease from positive to negative. The critical temperature for complete miscibility is calculated as 85 K, at which temperature the free energies of random alloys in the whole concentration range start to become negative. Therefore, thermodynamically stable $\text{Ga}_{(1-x)}\text{Al}_x\text{N}$ alloys is experimentally achievable.

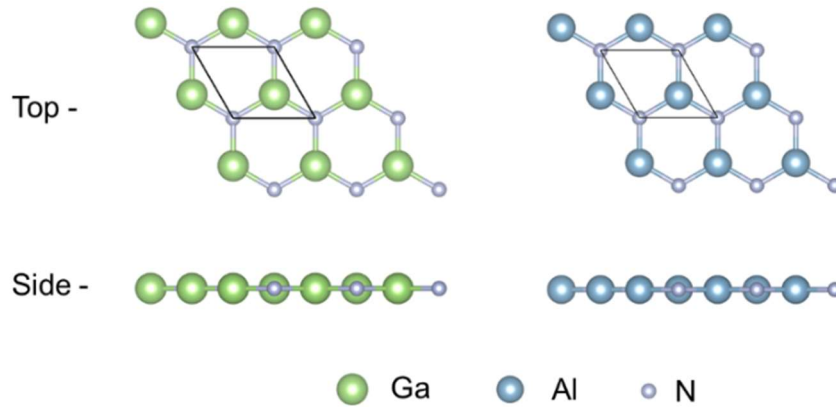


Fig. 6.1 The top and side views of monolayer III nitrides, where Ga, Al and N atoms are shown in green, blue and grey, respectively.

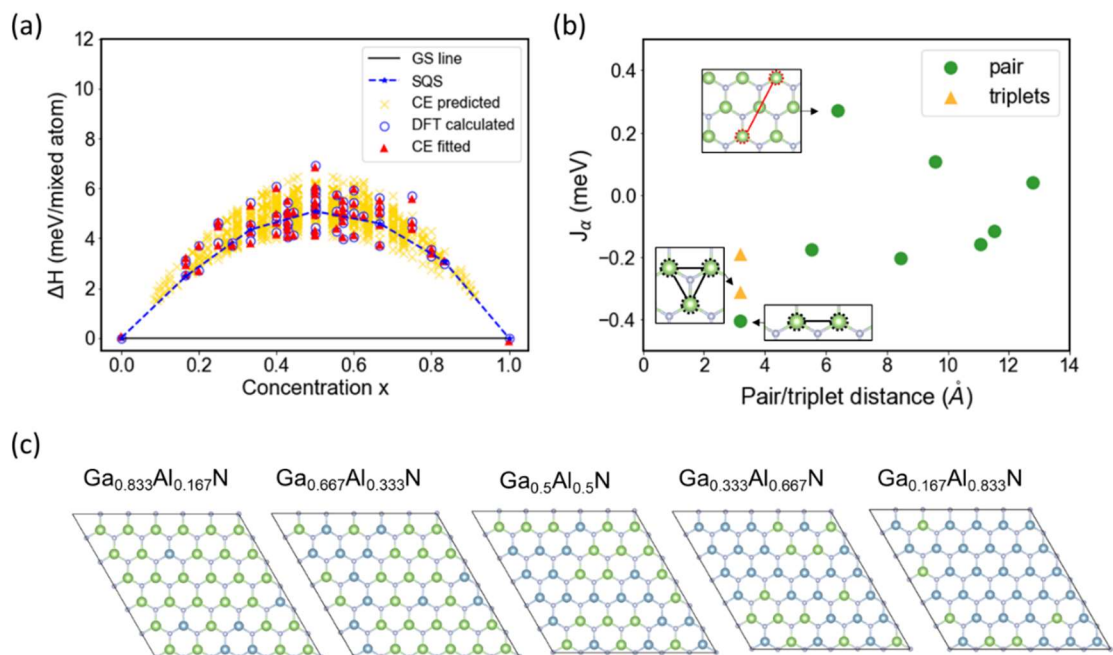


Fig. 6.2 (a) DFT calculated and cluster expansion fitted results for the formation enthalpies ΔH of $\text{Ga}_{(1-x)}\text{Al}_x\text{N}$ at different concentration. The ΔH values of ground structures are shown in black solid line, and ΔH values of random alloys generated using special quasi-random structure (SQS) method are shown in blue dash line. (b) effective cluster interaction (ECI) J_α for cluster figures, i.e., pairs and triplets, as a function of cluster diameter. (c) Atomic configurations of SQS structures at different concentration, where Ga, Al and N atoms are shown in green, blue and grey.

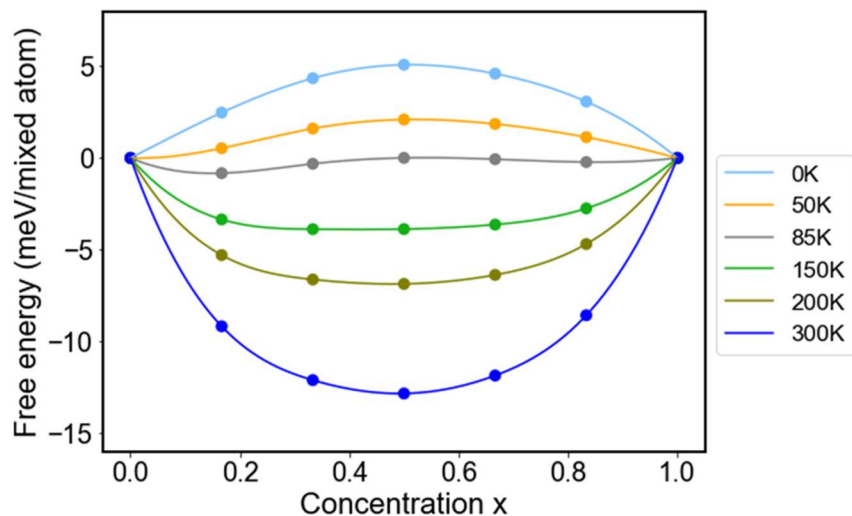


Fig. 6.3 Free energies of mixing for $\text{Ga}_{(1-x)}\text{Al}_x\text{N}$ random alloys vs. concentration x under different temperatures.

6.4.2 Electronic properties

As alloying is expected to change the electronic properties of 2D III-nitrides, we then investigated the evolution of the band gap with the composition x for $\text{Ga}_{(1-x)}\text{Al}_x\text{N}$ random alloys. For the calculations of band gap values, HSE06 functionals were used to obtain accurate results. The band gaps of pristine GaN and AlN are calculated as 3.44 and 4.04 eV respectively, in good agreement with previous works [11, 12]. Following Vegard's law [39], the lattice constant for alloys should vary linearly with the concentration x . We observed such linearity for $\text{Ga}_{(1-x)}\text{Al}_x\text{N}$ random alloys, as shown in Fig. 6.9, with the lattice constant decreasing linearly with increasing Al concentration. On the other hand, the dependence of band gap on concentration is often nonlinear and can be described using a quadratic rule:

$$E_g(x) = (1 - x)E_g(0) + xE_g(1) - bx(1 - x) \quad (6.5)$$

where b is the bowing parameter describing the deviation from the linearity. Fig. 6.4(a) shows that band gaps of random alloys increase nonlinearly with the increasing x . The variation of the band gap comes from the shifting of conduction band minimum (CBM), as shown in Fig. 6.4(b). By mixing Al into GaN, CBM continuously moves to higher energy levels, while the valence band maximum (VBM) remains nearly constant. The bowing parameter b is calculated as -0.17 eV. We noted that in the previous study, the bowing parameter for ordered 2D $\text{Ga}_{(1-x)}\text{Al}_x\text{N}$ alloys was calculated as -0.35 eV [21]. The difference in b values might originate from the different atomic arrangements of alloys. To demonstrate the accuracy of our calculations, 2x2 ordered alloy configurations used in the previous work were utilized to perform band gap calculations, with obtained $b = -0.33$ eV (See Fig. 6.10), comparable to that in the previous work. The results indicate that ordering effect on the electronic properties of 2D $\text{Ga}_{(1-x)}\text{Al}_x\text{N}$ cannot be neglected. As 2x2 ordered alloy structures consider only the most extreme cases of $\text{Ga}_{(1-x)}\text{Al}_x\text{N}$, random structures

used in this work are more likely to be consistent with the real alloys in experiments. Therefore, b obtained from random alloys are expected to be more accurate to calculate the band gaps of $\text{Ga}_{(1-x)}\text{Al}_x\text{N}$ alloys realized in experiments. Apart from the observed band bowing effect, the continuous changes of band gap values with concentrations also demonstrate that band gap tailoring of 2D III-nitrides is achievable via alloying.

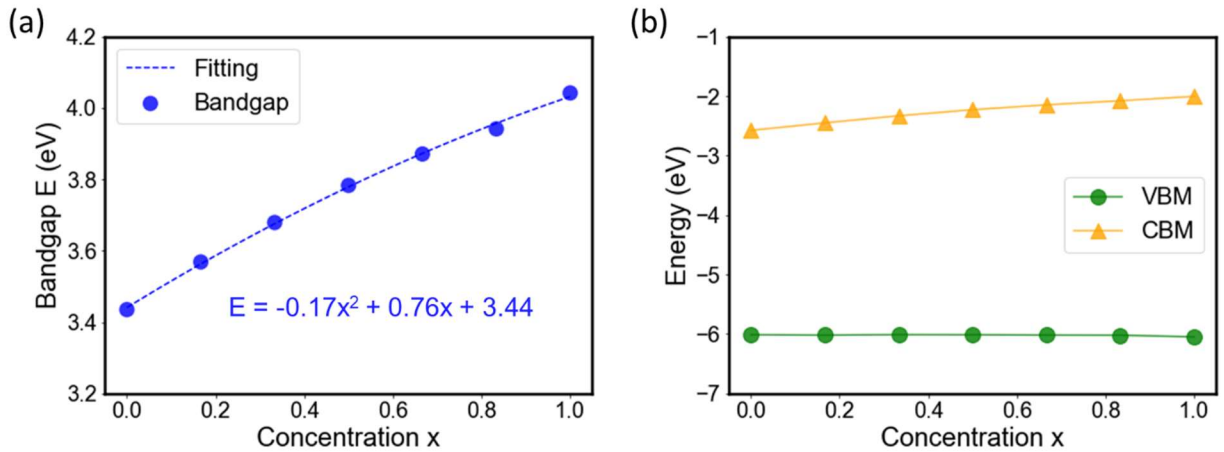


Fig. 6.4 (a) Band gap E of $\text{Ga}_{(1-x)}\text{Al}_x\text{N}$ random alloys as a function of concentration x . (b) The VBM and CBM positions of $\text{Ga}_{(1-x)}\text{Al}_x\text{N}$ random alloys as a function of concentration x .

6.4.3 Effect of strain

The electronic properties of 2D $\text{Ga}_{(1-x)}\text{Al}_x\text{N}$ under the tensile strain are further investigated, which is of importance for the tuning of physical and chemical properties. We used $\text{Ga}_{0.5}\text{Al}_{0.5}\text{N}$ random alloys as a representative of $\text{Ga}_{(1-x)}\text{Al}_x\text{N}$ alloys and studied the band gap variation under an applied biaxial in-plane tensile strain up to 8% for GaN, AlN and $\text{Ga}_{0.5}\text{Al}_{0.5}\text{N}$. It is noted that such high strains were proven to be affordable for 2D III-nitrides, as previous work observed an 8% strain in stable AlN nanosheets epitaxially grown on Ag(111) substrate [40]. As shown in Fig. 6.5(a), the change in band gap is more significant for GaN than AlN under the same strain. The band gaps decrease monotonically with increasing strains from 3.44 to 1.85 eV for GaN and from

4.04 to 3.12 eV for AlN. By contrast, the effect of strain on the band gaps of Ga_{0.5}Al_{0.5}N is moderate, with band gap values dropping from 3.78 to 2.51 eV until 8% strain. The VBM and CBM positions of GaN, AlN and Ga_{0.5}Al_{0.5}N under various strains are presented in Fig. 6.5(b). We can see that after applying strain, for all three structures, CBM positions gradually shift to lower energy levels, contributing to the decreasing band gap values, while the changes in VBM positions are negligible. These results indicate the possibilities of adjusting the electronic properties of 2D Ga_(1-x)Al_xN alloys by strain engineering, showing promise for potential novel optoelectronic applications.

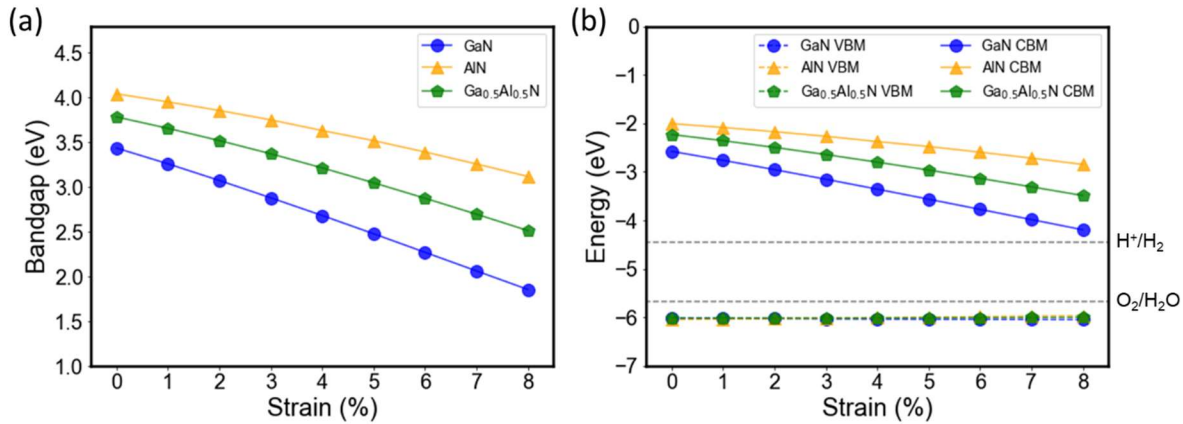


Fig. 6.5 (a) Band gap values of GaN, AlN and Ga_(1-x)Al_xN random alloy as a function of strain. (b) The VBM and CBM positions of GaN, AlN and Ga_(1-x)Al_xN random alloy as a function of strain. Black dash lines indicate the position of potentials of oxidation (O₂/H₂O) and reduction (H⁺/H₂) at pH 0 for water splitting.

6.4.4 Potential applications in photocatalysis

As wide band gap semiconductors, 2D III-nitrides are also potential photocatalysts with appropriate band edge positions for water splitting. To drive two half-reactions of water splitting, i.e., hydrogen evolution reaction (HER) and oxygen evolution reaction (OER), at pH 0, a suitable photocatalyst should have the energy of CBM more positive than -4.44 eV for reduction of H⁺ and the energy of VBM more negative than -5.67 eV for oxidation of H₂O [16]. As indicated in Fig.

6.5(b), GaN, AlN and Ga_{0.5}Al_{0.5}N have suitable band edge positions for water splitting under acidic conditions. Although the applied strains will narrow the band gaps and lower the CBM positions, the CBM positions of III-nitrides are still positive enough for water reduction even at 8% strain.

Finally, the chemical reactivity on 2D Ga_(1-x)Al_xN was explored, using 2D Ga_{0.5}Al_{0.5}N random alloy as a representative. We selected HER as an example reaction to study the tuning of the chemical reactivity on 2D Ga_(1-x)Al_xN. The HER activity on surfaces can be evaluated by the Gibbs free energy of hydrogen adsorption ΔG_H calculated as:

$$\Delta G_H = \Delta E_H + \Delta E_{ZPE} - T\Delta S_H \quad (6.6)$$

where ΔE_H , ΔZPE and ΔS are the calculated adsorption energy of hydrogen on a catalyst surface, the change in zero-point energy and entropy, respectively. T is the temperature set to room temperature (298.15 K). Generally, to achieve good HER performance, it is desirable to have a ΔG_H close to zero, which indicates that the binding between the hydrogen atom and the catalyst surface is neither too strong nor too weak. For hydrogen adsorption on GaN, AlN and Ga_{0.5}Al_{0.5}N, the adsorption configuration with the lowest adsorption energy is presented for each substrate, as shown in Fig. 6.6(a). It is found that the hydrogen adsorption configurations on all substrates are similar, with hydrogen atoms adsorbed on top of the N atoms. The calculated ΔG_H for hydrogen adsorption on GaN and AlN are 0.97 and 1.67 eV. As alloying continuously tunes the electronic structures, it is expected that the ΔG_H for Ga_{0.5}Al_{0.5}N should have a value between those for pristine GaN and AlN. The ΔG_H for Ga_{0.5}Al_{0.5}N is calculated as 1.16 eV as expected, closer to that for GaN because the H atom prefers to adsorb on the N atom surrounded by Ga atoms (See Fig. 6.6(a)).

Additionally, the modifications to the chemical reactivity of 2D III-nitride alloys can further be realized by strain. As depicted in Fig. 6.6(b), by applying biaxial in-plane tensile strain up to 8%, the ΔG_H for adsorption on 2D Ga_{0.5}Al_{0.5}N random alloy decreases from 1.16 eV to -0.25

eV, indicating a transition of adsorption strength from weak to strong. We note that the ΔG_H for the alloy is close to the thermoneutral value near zero at 7% strain, which demonstrates that optimal catalytic performance on 2D $\text{Ga}_{(1-x)}\text{Al}_x\text{N}$ can be achieved by strain engineering.

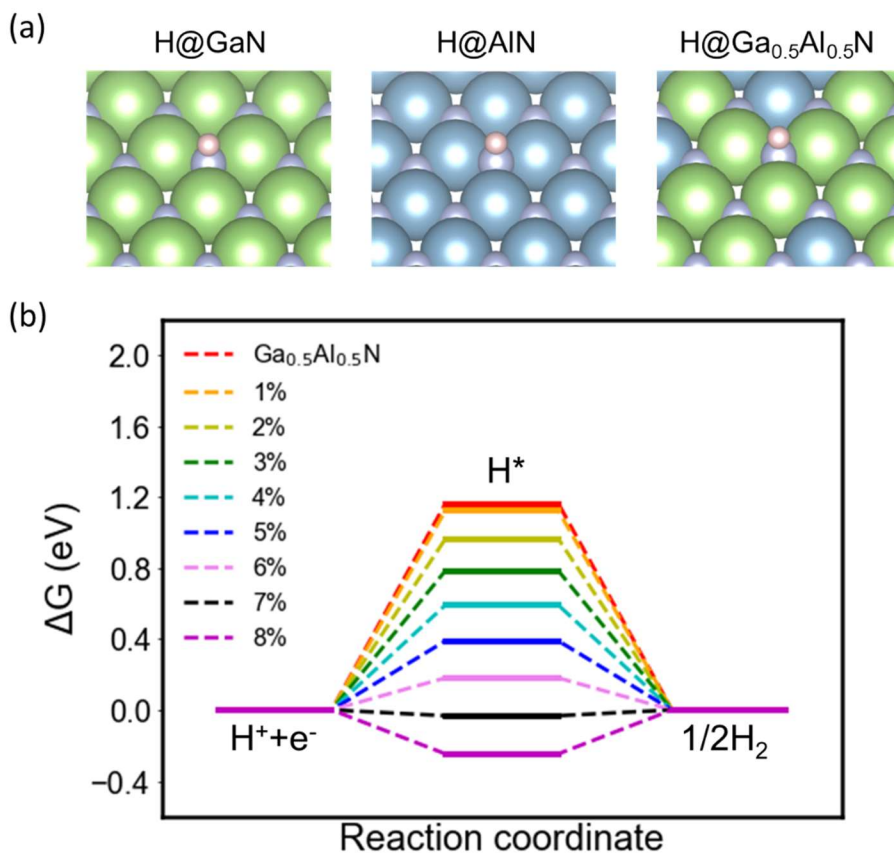


Fig. 6.6 (a) Atomic configurations of hydrogen adsorption on GaN, AlN and $\text{Ga}_{0.5}\text{Al}_{0.5}\text{N}$, where Ga, Al, N and H atoms are shown in green, blue, grey and pink. (b) Calculated ΔG_H for $\text{Ga}_{0.5}\text{Al}_{0.5}\text{N}$ random alloy under tensile strain.

6.5 Conclusion

In conclusion, density functional theory in conjunction with the cluster expansion method were performed on monolayer $\text{Ga}_{(1-x)}\text{Al}_x\text{N}$ alloys to investigate their stability, electronic and catalytic properties. Our results show that 2D $\text{Ga}_{(1-x)}\text{Al}_x\text{N}$ alloys are thermodynamically stable. Although positive formation enthalpies ΔH are observed for all alloy configurations, the calculated

free energies of alloy formation indicate the complete miscibility in the alloys achieved at only 85 K, far below the room temperature. By analyzing the fitted ECI parameters, the atomic arrangement of alloys was then revealed, showing that Ga/Al atoms tend to mix with the Al/Ga atoms in their next nearest site. On the front of electronic properties, by varying chemical compositions, the band gaps of $\text{Ga}_{(1-x)}\text{Al}_x\text{N}$ random alloys exhibit an apparent bowing effect with bowing parameter $b = -0.17$ eV, which comes from the variation of CBM positions with alloy concentrations. Besides, we found that biaxial tensile strain can further decrease the band gap values of random alloys significantly, due to its modifications to the CBM positions of alloys. Meanwhile, as potential photocatalysts, $\text{Ga}_{(1-x)}\text{Al}_x\text{N}$ random alloys are confirmed to have suitable band edge positions for water splitting over the entire range of concentration, even under high strains. Finally, on the front of chemical properties, by examining hydrogen adsorption on 2D $\text{Ga}_{0.5}\text{Al}_{0.5}\text{N}$ under biaxial strains, we found that $\text{Ga}_{0.5}\text{Al}_{0.5}\text{N}$ is an ideal catalyst for HER with Gibbs free energy of hydrogen adsorption ΔG_{H} close to zero at 7% strain. The present study might guide the future design of electronics and broaden the possible usage of 2D III-nitrides in photocatalysis.

6.6 Acknowledgements

This research is supported by the Natural Sciences and Engineering Research Council of Canada (NSERC) Discovery Grant (grant #: NSERC RGPIN-2017-05187), and the McGill Engineering Doctoral Award (MEDA). The authors would also like to acknowledge the Compute Canada and Calcul Québec for providing computing resources.

6.7 Supporting Information

6.7.1 Optimized geometries of various $\text{Ga}_{(1-x)}\text{Al}_x\text{N}$ alloys

Fig. 6.7 presents the optimized geometries of five representative $\text{Ga}_{(1-x)}\text{Al}_x\text{N}$ alloys automatically generated by ATAT code. It was observed that $\text{Ga}_{(1-x)}\text{Al}_x\text{N}$ alloys retain their original hexagonal planar cell shape after structural optimization.

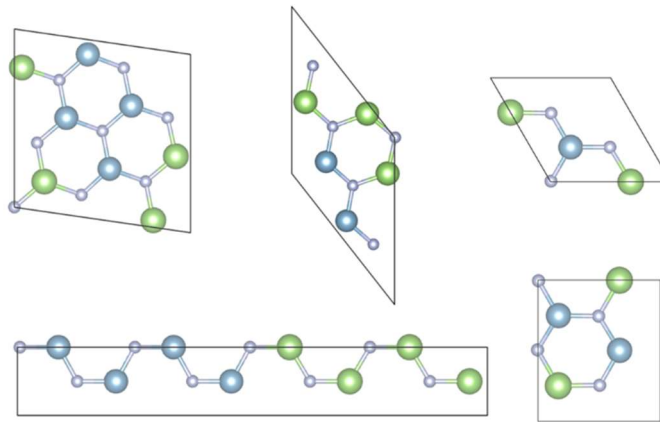


Fig. 6.7 Top views of optimized geometries of five representative $\text{Ga}_{(1-x)}\text{Al}_x\text{N}$ alloys generated by ATAT code. Ga, Al and N atoms are shown in green, blue and grey, respectively.

6.7.2 Phonon calculations of 2D GaN, AlN and $\text{Ga}_{0.5}\text{Al}_{0.5}\text{N}$

To investigate the stabilities of 2D $\text{Ga}_{0.5}\text{Al}_{0.5}\text{N}$ alloys, phonon dispersion calculations have been performed on 2×2 $\text{Ga}_{0.5}\text{Al}_{0.5}\text{N}$ alloy, which is predicted to have the highest formation enthalpies among all alloy configurations. Phonon dispersion curves for 2D GaN, AlN and 2×2 $\text{Ga}_{0.5}\text{Al}_{0.5}\text{N}$ are shown in Fig. 6.8. The phonon frequencies are found to be positive for all three structures, indicating the stability of these structures. Since other $\text{Ga}_{(1-x)}\text{Al}_x\text{N}$ alloys have lower formation enthalpies compared to that of 2×2 $\text{Ga}_{0.5}\text{Al}_{0.5}\text{N}$, it is expected that all $\text{Ga}_{(1-x)}\text{Al}_x\text{N}$ alloys should be stable.

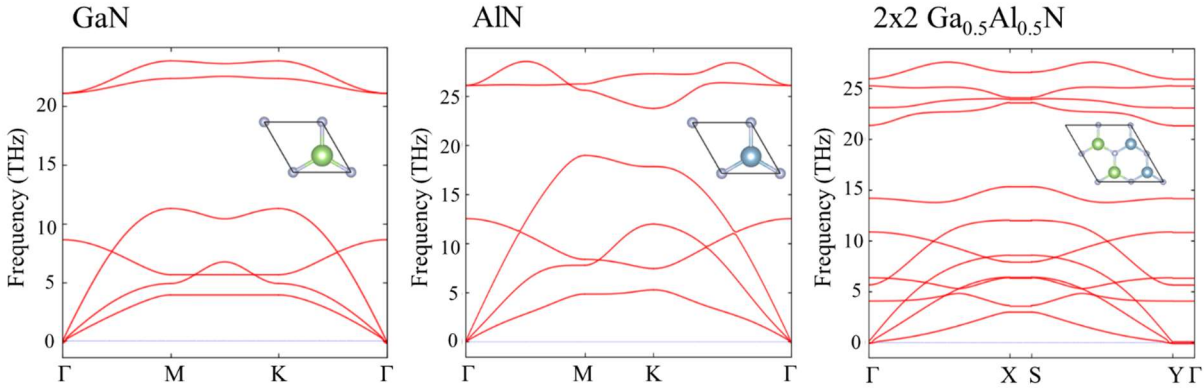


Fig. 6.8 Phonon dispersion curves for 2D GaN, AlN and 2x2 Ga_{0.5}Al_{0.5}N, respectively. Corresponding atomic structures are shown in each plot.

6.7.3 Vegard's law

As shown in Fig. 6.9, the lattice constant for Ga_(1-x)Al_xN random alloys varies linearly with the concentration, following Vegard's law.

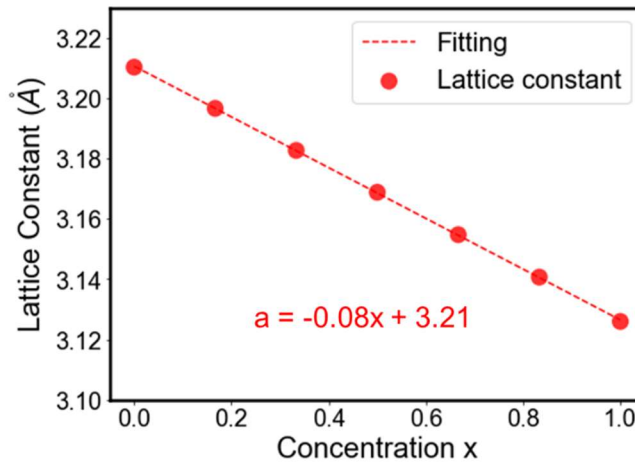


Fig. 6.9 Lattice constant a of Ga_(1-x)Al_xN random alloys as a function of concentration x .

6.7.4. Band gap variation using 2x2 Ga_(1-x)Al_xN ordered alloys

The band gaps of 2x2 ordered alloy configurations were calculated and shown in Fig. 6.10. The bowing parameter b was calculated as -0.33 eV, comparable to that in the literature [21].

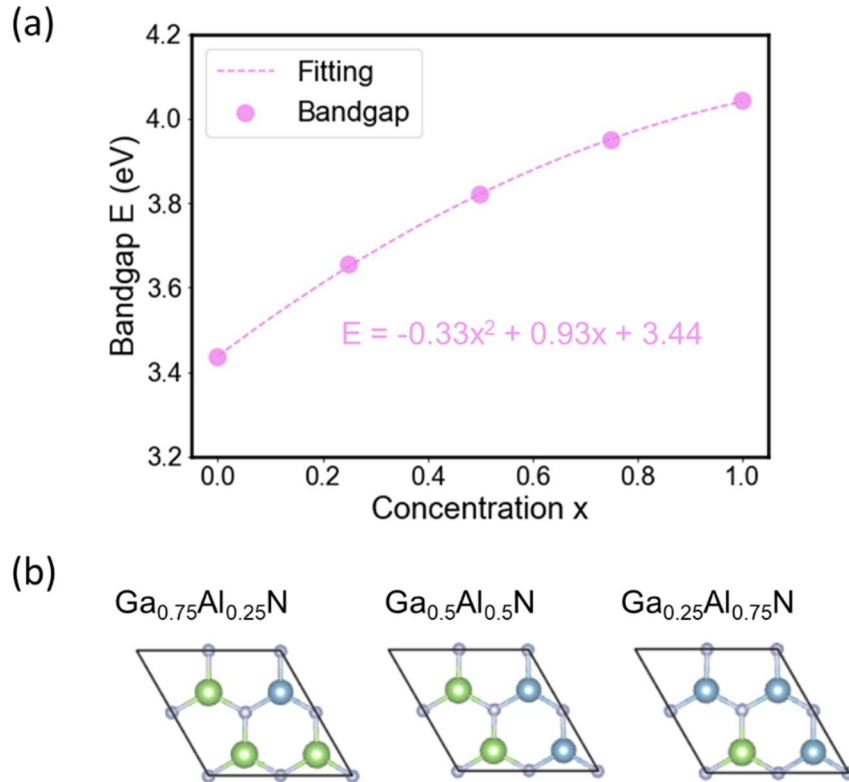


Fig. 6.10 (a) Band gap E of 2×2 $\text{Ga}_{(1-x)}\text{Al}_x\text{N}$ ordered alloys as a function of concentration x . (b) The top views of 2×2 $\text{Ga}_{(1-x)}\text{Al}_x\text{N}$ ordered alloys used for band gap calculations.

6.8 References

- [1] S. Mokkaḡati, C. Jagadish, III-V compound SC for optoelectronic devices, *Materials Today* 12(4) (2009) 22-32.
- [2] Z.C. Feng, III-nitride devices and nanoengineering, World Scientific 2008.
- [3] S. Nakamura, T. Mukai, M. Senoh, Candela-class high-brightness InGaN/AlGaN double-heterostructure blue-light-emitting diodes, *Applied Physics Letters* 64(13) (1994) 1687-1689.
- [4] A.V. Akimov, J.T. Muckerman, O.V. Prezhdo, Nonadiabatic Dynamics of Positive Charge during Photocatalytic Water Splitting on GaN(10-10) Surface: Charge Localization Governs Splitting Efficiency, *Journal of the American Chemical Society* 135(23) (2013) 8682-8691.
- [5] R.T. Rashid, Y. Chen, X. Liu, F.A. Chowdhury, M. Liu, J. Song, Z. Mi, B. Zhou, Tunable green syngas generation from CO_2 and H_2O with sunlight as the only energy input, *Proceedings of the National Academy of Sciences* 119(26) (2022) e2121174119.
- [6] M.G. Kibria, Z. Mi, Artificial photosynthesis using metal/nonmetal-nitride semiconductors: current status, prospects, and challenges, *Journal of Materials Chemistry A* 4(8) (2016) 2801-2820.
- [7] D. Wang, A. Pierre, M.G. Kibria, K. Cui, X. Han, K.H. Bevan, H. Guo, S. Paradis, A.-R. Hakima, Z. Mi, Wafer-Level Photocatalytic Water Splitting on GaN Nanowire Arrays Grown by Molecular Beam Epitaxy, *Nano Letters* 11(6) (2011) 2353-2357.

- [8] H.L. Zhuang, A.K. Singh, R.G. Hennig, Computational discovery of single-layer III-V materials, *Physical Review B* 87(16) (2013) 165415.
- [9] Z.Y. Al Balushi, K. Wang, R.K. Ghosh, R.A. Vilá, S.M. Eichfeld, J.D. Caldwell, X. Qin, Y.-C. Lin, P.A. DeSario, G. Stone, S. Subramanian, D.F. Paul, R.M. Wallace, S. Datta, Joan M. Redwing, J.A. Robinson, Two-dimensional gallium nitride realized via graphene encapsulation, *Nature Materials* 15(11) (2016) 1166-1171.
- [10] Z. Huang, T.-Y. Lü, H.-Q. Wang, S.-W. Yang, J.-C. Zheng, Electronic and thermoelectric properties of the group-III nitrides (BN, AlN and GaN) atomic sheets under biaxial strains, *Computational Materials Science* 130 (2017) 232-241.
- [11] D. Kecik, A. Onen, M. Konuk, E. Gürbüz, F. Ersan, S. Cahangirov, E. Aktürk, E. Durgun, S. Ciraci, Fundamentals, progress, and future directions of nitride-based semiconductors and their composites in two-dimensional limit: A first-principles perspective to recent synthesis, *Applied Physics Reviews* 5(1) (2018).
- [12] A. Onen, D. Kecik, E. Durgun, S. Ciraci, GaN: From three- to two-dimensional single-layer crystal and its multilayer van der Waals solids, *Physical Review B* 93(8) (2016) 085431.
- [13] C. Bacaksiz, H. Sahin, H.D. Ozaydin, S. Horzum, R.T. Senger, F.M. Peeters, Hexagonal AlN: Dimensional-crossover-driven band-gap transition, *Physical Review B* 91(8) (2015) 085430.
- [14] E. Gürbüz, S. Cahangirov, E. Durgun, S. Ciraci, Single layers and multilayers of GaN and AlN in square-octagon structure: Stability, electronic properties, and functionalization, *Physical Review B* 96(20) (2017) 205427.
- [15] Q. Chen, H. Hu, X. Chen, J. Wang, Tailoring band gap in GaN sheet by chemical modification and electric field: Ab initio calculations, *Applied Physics Letters* 98(5) (2011) 053102.
- [16] K. Ren, J. Yu, W. Tang, A two-dimensional vertical van der Waals heterostructure based on g-GaN and Mg(OH)₂ used as a promising photocatalyst for water splitting: A first-principles calculation, *Journal of Applied Physics* 126(6) (2019) 065701.
- [17] C. Schnohr, Compound semiconductor alloys: From atomic-scale structure to bandgap bowing, *Applied physics reviews* 2(3) (2015) 031304.
- [18] J.L. Martins, A. Zunger, Stability of Ordered Bulk and Epitaxial Semiconductor Alloys, *Physical Review Letters* 56(13) (1986) 1400-1403.
- [19] J.-H. Yang, B.I. Yakobson, Unusual Negative Formation Enthalpies and Atomic Ordering in Isovalent Alloys of Transition Metal Dichalcogenide Monolayers, *Chemistry of Materials* 30(5) (2018) 1547-1555.
- [20] S. Sandhya, K. Alex, H.J. A., K. Vidya, A. Amey, V. Robert, I.J. Carlos, Y.B. I., T.C. Sekhar, A.P. M., Quaternary 2D Transition Metal Dichalcogenides (TMDs) with Tunable Bandgap, *Advanced Materials* 29(35) (2017) 1702457.
- [21] M. Kanli, A. Onen, A. Mogulkoc, E. Durgun, Characterization of two-dimensional Ga_{1-x}Al_xN ordered alloys with varying chemical composition, *Computational Materials Science* 167 (2019) 13-18.
- [22] J.M. Sanchez, F. Ducastelle, D. Gratias, Generalized cluster description of multicomponent systems, *Physica A: Statistical Mechanics and its Applications* 128(1) (1984) 334-350.
- [23] L.G. Ferreira, S.-H. Wei, A. Zunger, First-principles calculation of alloy phase diagrams: The renormalized-interaction approach, *Physical Review B* 40(5) (1989) 3197-3231.
- [24] A. Van De Walle, M. Asta, G. Ceder, The alloy theoretic automated toolkit: A user guide, *Calphad* 26(4) (2002) 539-553.
- [25] J. Kang, S. Tongay, J. Li, J. Wu, Monolayer semiconducting transition metal dichalcogenide alloys: Stability and band bowing, *Journal of Applied Physics* 113(14) (2013) 143703.

- [26] A. Zunger, S.H. Wei, L.G. Ferreira, J.E. Bernard, Special quasirandom structures, *Physical Review Letters* 65(3) (1990) 353-356.
- [27] W.R.L. Lambrecht, B. Segall, Anomalous band-gap behavior and phase stability of c-BN--diamond alloys, *Physical Review B* 47(15) (1993) 9289-9296.
- [28] W. Kohn, L.J. Sham, Self-Consistent Equations Including Exchange and Correlation Effects, *Physical Review* 140(4A) (1965) A1133-A1138.
- [29] G. Kresse, D. Joubert, From ultrasoft pseudopotentials to the projector augmented-wave method, *Physical Review B* 59(3) (1999) 1758-1775.
- [30] G. Kresse, J. Furthmüller, Efficient iterative schemes for ab initio total-energy calculations using a plane-wave basis set, *Physical Review B* 54(16) (1996) 11169-11186.
- [31] P.E. Blöchl, Projector augmented-wave method, *Physical Review B* 50(24) (1994) 17953-17979.
- [32] J.P. Perdew, K. Burke, M. Ernzerhof, Generalized Gradient Approximation Made Simple, *Physical Review Letters* 77(18) (1996) 3865-3868.
- [33] J.P. Perdew, J.A. Chevary, S.H. Vosko, K.A. Jackson, M.R. Pederson, D.J. Singh, C. Fiolhais, Atoms, molecules, solids, and surfaces: Applications of the generalized gradient approximation for exchange and correlation, *Physical Review B* 46(11) (1992) 6671-6687.
- [34] A.V. Krukau, O.A. Vydrov, A.F. Izmaylov, G.E. Scuseria, Influence of the exchange screening parameter on the performance of screened hybrid functionals, *The Journal of chemical physics* 125(22) (2006) 224106.
- [35] S. Grimme, J. Antony, S. Ehrlich, H. Krieg, A consistent and accurate ab initio parametrization of density functional dispersion correction (DFT-D) for the 94 elements H-Pu, *The Journal of Chemical Physics* 132(15) (2010) 154104.
- [36] S. Grimme, S. Ehrlich, L. Goerigk, Effect of the damping function in dispersion corrected density functional theory, *Journal of Computational Chemistry* 32(7) (2011) 1456-1465.
- [37] D. Wines, F. Ersan, C. Ataca, Engineering the Electronic, Thermoelectric, and Excitonic Properties of Two-Dimensional Group-III Nitrides through Alloying for Optoelectronic Devices ($B_{1-x}Al_xN$, $Al_{1-x}Ga_xN$, and $Ga_{1-x}In_xN$), *ACS Applied Materials & Interfaces* 12(41) (2020) 46416-46428.
- [38] G. Ceder, A derivation of the Ising model for the computation of phase diagrams, *Computational Materials Science* 1(2) (1993) 144-150.
- [39] A.R. Denton, N.W. Ashcroft, Vegard's law, *Physical Review A* 43(6) (1991) 3161-3164.
- [40] P. Tsipas, S. Kassavetis, D. Tsoutsou, E. Xenogiannopoulou, E. Golias, S. Giamini, C. Grazianetti, D. Chiappe, A. Molle, M. Fanciulli, Evidence for graphite-like hexagonal AlN nanosheets epitaxially grown on single crystal Ag (111), *Applied Physics Letters* 103(25) (2013) 251605.

Chapter 7 : General Discussion

Due to the increasing global energy needs and rapidly dwindling reserves of fossil fuels, there is great demand for alternative energy sources. Among various energy sources, hydrogen is regarded as the cleanest fuel with the highest gravimetric energy density, showing great potential to replace fossil fuels [1, 2]. Hydrogen is not abundant in nature, but it can be produced from water splitting powered by renewable electricity. One challenge in water splitting is the lack of efficient and earth-abundant catalysts to facilitate the hydrogen evolution reaction, and thus there have been great efforts for developing HER catalysts with low cost and high performance [3, 4]. Recently, 2D materials like 2D TMDCs are found to be effective toward HER, and more importantly, their HER activities can be further tuned by various strategies, such as defect engineering, doping, strain engineering, alloying, etc. [5-9]. Aiming at improving the HER performance of 2D materials, Chapters 4-6 explored phase boundaries and alloys of 2D materials and investigated their capabilities for enhancing HER performance, providing mechanistic insights into engineering 2D materials for effective HER catalysts, and more generally, guiding the rational design of potential 2D materials-based catalytic systems. The major findings, current limitations, and future directions of this thesis are discussed below.

7.1 Strategies for activating the basal plane of 2D TMDCs for HER

2D TMDCs have attracted intense research attention as promising candidates for catalyzing HER due to their novel properties. The unique structures of 2D TMDCs allow abundant atomic combinations and rich phases, making their electronic and catalytic properties tunable. There have been a variety of strategies to improve the catalytic performance of 2D TMDCs [5-9]. Among them, phase boundary engineering and alloying show great potential since they can provide high

density of active sites on the surface while retaining structural integrity. However, their roles in 2D TMDCs for enhancing HER are unclear, necessitating dedicated studies. The present thesis systematically investigated these two strategies for activating the basal plane of 2D TMDCs and elucidated the corresponding HER mechanism in detail.

7.1.1 Phase boundary activated HER on 2D TMDCs

Group VI 2D TMDCs are the most widely studied 2D TMDCs. Among them, 2D MoTe₂ is the best candidate for achieving phase boundaries because of the small energy difference between 2H and 1T' phases [10]. While phase boundaries of 2D TMDCs have been utilized to enhance HER activities in the basal plane [11], the reason for such activation was unclear. More importantly, to our knowledge, although 2D MoTe₂ phase boundaries are easy to form, they have never been explored for catalyzing HER neither experimentally nor theoretically. Therefore, in Chapter 4, 2D MoTe₂ were used as a representative of 2D TMDCs to construct 2H/1T' phase boundaries for catalyzing HER. Three categories of catalytic sites, namely Te, Mo, and hollow sites, were identified at the phase boundary region. As expected, all catalytic sites indicate enhanced HER activity compared to that of the pristine basal lattice. In particular, the hollow sites at the phase boundary are activated most significantly and exhibit optimal HER activity. Such activation is in sharp contrast to that of other two types of sites, which show only slight ΔG_H decrease attributed to the variation in electronic structures. The reason behind this significant activation was then understood by comparing the hydrogen adsorption configurations at hollow sites for phase boundaries and pristine structures (Fig. 4.12). Interestingly, while the hydrogen atom tends to be surrounded by Te atoms on the surface for the pristine structure, for phase boundaries, hydrogen goes inside the structure and is adsorbed in the middle of the three-atom-thick monolayer surrounded by three Mo atoms. As a matter of fact, for pristine MoTe₂, Mo atoms

exhibit stronger hydrogen adsorption ability compared to that of Te atoms. However, these Mo atoms are covered by a layer of Te atoms, and they are not active enough to attract H atoms into the middle layer, which leads to hydrogen adsorption on Te atoms with much higher ΔG_H values. By contrast, by introducing phase boundaries, Mo atoms are activated with stronger adsorption ability, which facilitates the hydrogen adsorption at the hollow sites.

The hollow sites identified in this thesis can be regarded as a new group of adsorption sites in 2D MoTe_2 induced by phase boundaries. Moreover, as demonstrated in the benchmark studies in Section 4.7.10, the activation of transition metals by phase boundaries to create efficient hollow sites for hydrogen adsorption may also be extended to other 2D TMDCs. Fig. 7.1 further summarizes the hydrogen adsorption abilities of the hollow sites of a variety of 2D TMDCs, considering four kinds of transition metals and three kinds of chalcogen atoms. It is found that for 2D TMDC phase boundaries with the same transition metals, the ΔG_H of the hollow sites decrease monotonically with the atomic number of chalcogens. Particularly, the hollow site of WTe_2 phase boundary exhibits a ΔG_H close to thermoneutral value of zero, indicating the best HER activity. Meanwhile, the ΔG_H values of the hollow sites also depend on the choice of transition metals. Specifically, MoX_2 and WX_2 exhibits similar ΔG_H values for the hollow sites at the phase boundaries, probably due to the similar properties of Mo and W elements. The adsorption properties of the hollow sites at the CrX_2 phase boundaries are slighter different from that of MoX_2 and WX_2 , with relatively higher ΔG_H values. By contrast, for 2D TMDC containing transition metal from another group, namely VX_2 , G_H values for the hollow sites at the phase boundaries drop dramatically as pristine VX_2 are much more active for HER compared to other three 2D TMDCs. Therefore, it is expected that tunable HER activities can be achieved by varying chemical components of 2D TMDC phase boundaries. This interesting topic is not covered by the present

thesis, which deserves further investigation. Additionally, it is crucial to understand the mechanism behind the influence of different combinations of transition metals and chalcogens so as to guide the design of 2D TMDC phase boundaries for HER, which is also an interesting task worth pursuing.

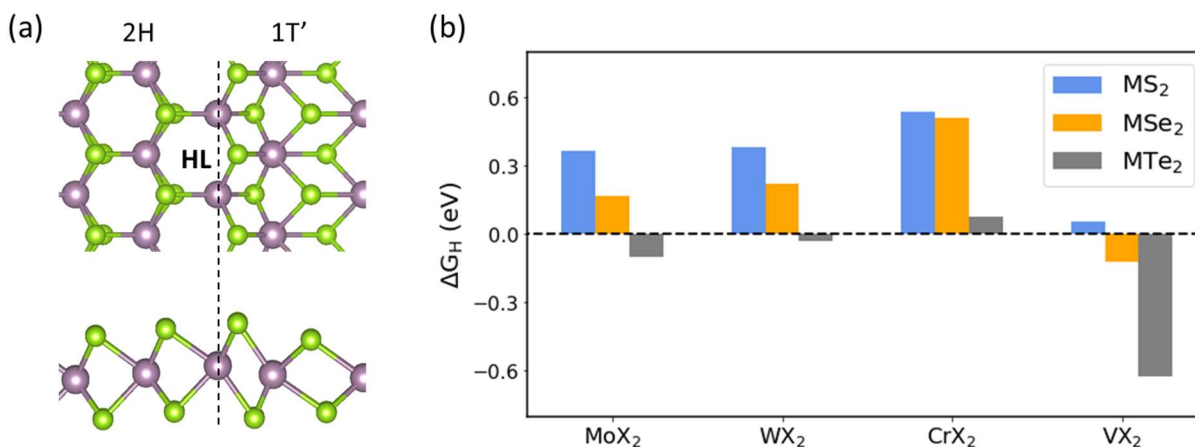


Fig. 7.1 (a) Top and side views of the hollow sites at the phase boundaries of 2D TMDCs, where transition metals ($M = Mo, W, Cr, \text{ and } V$) and chalcogens ($X = S, Se, \text{ and } Te$) are shown in purple and green. (b) ΔG_H of the hollow sites of various 2D TMDC phase boundaries.

While the present work focuses on monolayer $MoTe_2$, additional calculations have also been performed to have a glance on the HER performance of few-layer $MoTe_2$ phase boundaries (See Fig. 4.15). The results show that monolayer, double-layer, and three-layer $MoTe_2$ have nearly identical ΔG_H values at the phase boundary region. The ignorable influence of layer number is likely attributed to the weak van der Waals interaction between layers. Thus, the main conclusions of the present thesis would also be applicable to few-layer TMDC phase boundaries.

As previous reported for MoS_2 phase boundaries, the density of phase boundaries can affect the HER performance of 2D TMDCs as confirmed by the experiment [11]. However, the origin of enhanced HER performance by increased density of phase boundaries is unclear. This

enhancement could merely attribute to the increased number of active sites, or come from the increased HER activity of the catalytic sites induced by the adjacent phase boundaries. The present study does not consider the influence of phase boundary density on the HER activities, and thus further studies are needed to understand this boundary-boundary interactions in the basal plane of 2D TMDCs.

7.1.2 Alloying activated HER on 2D TMDCs

Recent experimental studies reported the fabrications of several 2D TMDC alloys, which exhibit enhanced HER activities with respect to the pristine structures [9, 12]. The catalytically active sites of these alloys were assumed to be mainly located on the edges, while the role of the basal plane of 2D TMDC alloys remains elusive. Therefore, a machine learning workflow was constructed to accurately the HER activities and thermodynamic stabilities of various 2D cation-mixed TMDC alloys, and for the first time, alloying was demonstrated as a viable route to activate the basal plane of 2D TMDCs.

To date, most of the experimental studies on 2D TMDC alloys in the context of HER focus on the predominant phase of most 2D TMDCs, namely the 2H phase, while research works on other phases (e.g., 1T and 1T') have been rather scarce. As a result, the present study only considered the 2H phase of 2D TMDC alloys. However, previous studies show that the basal plane of 1T' phase of group VI TMDCs is more active toward HER than that of the 2H phase [7], which makes 1T' TMDC alloys promising for basal plane activation and deserves further investigation. Before the exploration of 1T' TMDC alloys for HER, it is of great importance to investigate the stability of these alloys. We performed benchmark studies on the stabilities of 2H and 1T' TMDC alloys using $\text{Mo}_{(1-x)}\text{W}_x\text{Te}_2$ as an example. The stabilities of alloys were evaluated by the formation enthalpies ΔH , which were calculated using DFT calculations in conjunction with cluster

expansions, as illustrated in Fig. 7.2 (a) and (c). It is found that for both 2H and 1T' $\text{Mo}_{(1-x)}\text{W}_x\text{Te}_2$, there exist stable ground state structures with negative ΔH at 0 K, with 2H $\text{Mo}_{(1-x)}\text{W}_x\text{Te}_2$ ground state structures more stable than that of 1T' $\text{Mo}_{(1-x)}\text{W}_x\text{Te}_2$. Additionally, the ΔH of $\text{Mo}_{(1-x)}\text{W}_x\text{Te}_2$ random alloys were calculated. While 2H $\text{Mo}_{(1-x)}\text{W}_x\text{Te}_2$ random alloys show negative ΔH across the whole concentration range, 1T' $\text{Mo}_{(1-x)}\text{W}_x\text{Te}_2$ random alloys exhibit ΔH values slightly higher than zero for concentration $x = 0.333-0.667$, indicating the occurrence of the phase separation at 0 K at these concentrations. Nevertheless, the solubility in these alloys can be easily achieved by increasing the temperature. As pristine 1T' MoTe_2 and WTe_2 monolayers have been successfully fabricated and have shown high durability for HER [13, 14], it is expected that 1T' $\text{Mo}_{(1-x)}\text{W}_x\text{Te}_2$ alloys can be synthesized for further investigation of their catalytic performance.

In addition to cation-mixed alloys, anion-mixed TMDC alloys have also been realized experimentally for catalysis [9, 12], which are not explored in this thesis. While previous studies attribute the impressive HER performance of anion-mixed TMDC alloys to the chemically activated basal plane and the edges, further validations of the true adsorption sites by theoretical studies are not performed. Additionally, only the 2H phase of anion-mixed TMDC alloys has been investigated for HER, while the stability and HER activity of 1T' anion-mixed TMDC alloys remain unexplored. As the stability issue is important for alloy formation, we first investigated the stabilities of 1T' anion-mixed TMDC alloys using $\text{WSe}_{2(1-x)}\text{Te}_{2x}$ as an example and used its 2H counterpart for comparison. As shown in Fig. 7.2 (b), 2H $\text{WSe}_{2(1-x)}\text{Te}_{2x}$ show positive ΔH for all alloy configurations, indicative of instability at 0K, but complete miscibility in these alloys can be achieved at low temperatures since the magnitude of their ΔH is small. By contrast, as shown in Fig. 7.2 (d), 1T' $\text{WSe}_{2(1-x)}\text{Te}_{2x}$ alloys have negative ΔH , implying the formation of ordered alloys even at 0 K. Therefore, 1T' $\text{WSe}_{2(1-x)}\text{Te}_{2x}$ are more stable than that of 2H $\text{WSe}_{2(1-x)}\text{Te}_{2x}$, and it is

expected that 1T' $\text{WSe}_{2(1-x)}\text{Te}_{2x}$ alloys can be synthesized and deserve further investigation for applications as HER catalysts.

The stability issue arising from the alloy formation could be further addressed by fabricating high entropy alloys. High-entropy alloys are multicomponent compounds stabilized by high configurational entropy [15]. Previous studies reported 2D high-entropy TMDC alloys for electronic and catalytic applications [16, 17]. These multicomponent alloys allow high tunability of their electronic and chemical properties, and additional research efforts are required to explore their vast compositional spaces.

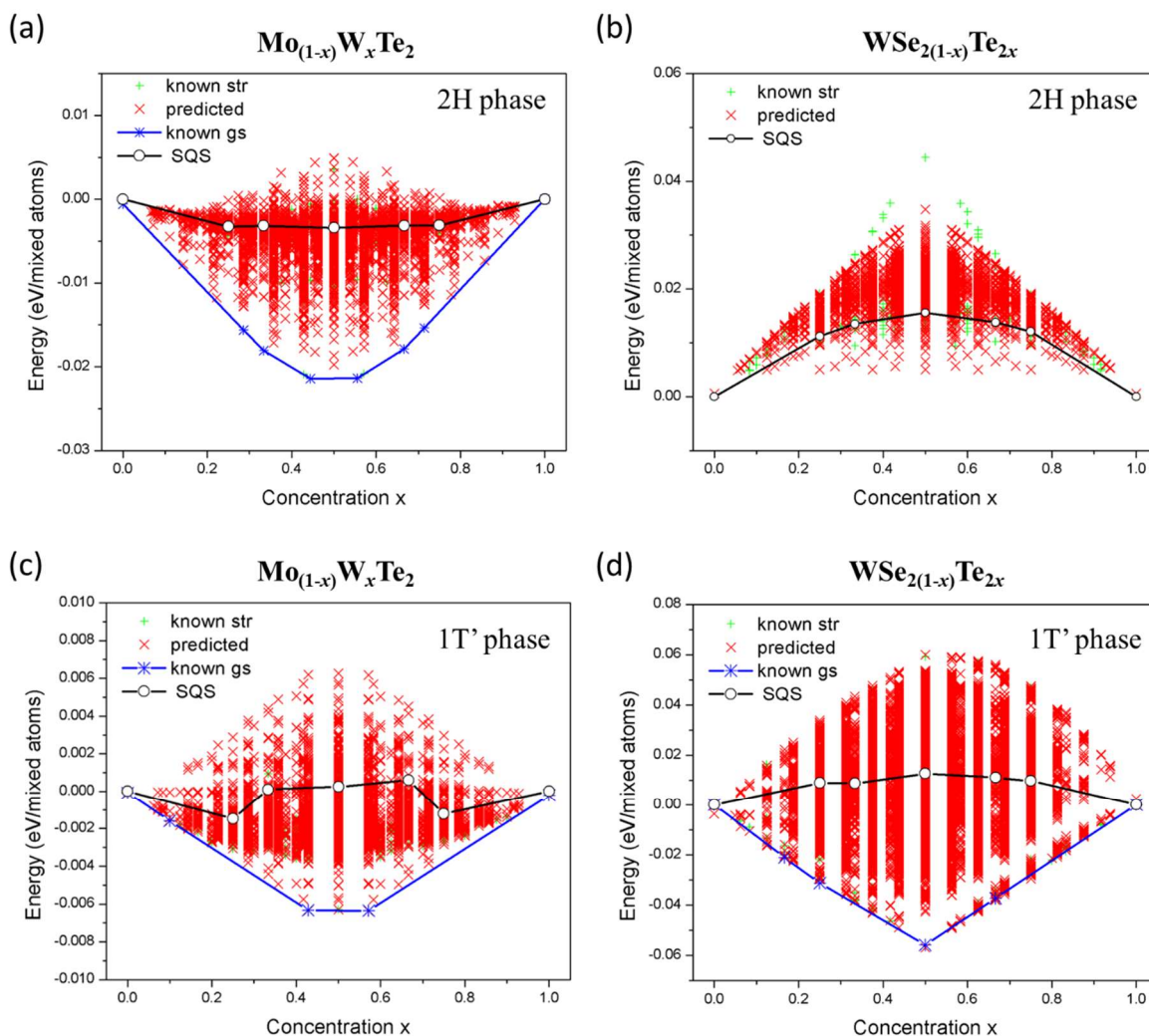


Fig. 7.2 DFT calculated and cluster expansion fitted results for the formation enthalpies ΔH of (a) $2H Mo_{(1-x)}W_xTe_2$, (b) $2H WSe_{2(1-x)}Te_{2x}$, (c) $1T' Mo_{(1-x)}W_xTe_2$, and (d) $1T' WSe_{2(1-x)}Te_{2x}$ at different concentration. The ΔH values of ground structures are shown in blue solid line, and ΔH values of random alloys generated using special quasi-random structure (SQS) method are shown in black dash line.

7.1.3 Phase boundaries in alloys for catalyzing HER

Chapters 4 and 5 have introduced two effective modification strategies, introducing phase boundaries and alloying, for enhancing the HER activities of 2D TMDCs. These two strategies can be combined to further tune the HER activities, as alloying was also found to trigger phase transition and thus create phase boundaries in 2D TMDCs [10]. 2D TMDCs such as $MoTe_2$ have 2H phases under ambient conditions, while the 1T' phase is found in WTe_2 in nature. As a result, phase transition from 2H to 1T' phase can be possibly achieved by varying the chemical composition of $Mo_{(1-x)}W_xTe_2$ and therefore create phase boundaries in alloys (See Fig. 7.3). These alloying-induced phase boundaries, while not investigated in this thesis, may possess novel properties and alter the catalytic properties of 2D TMDCs, which deserve further investigation.

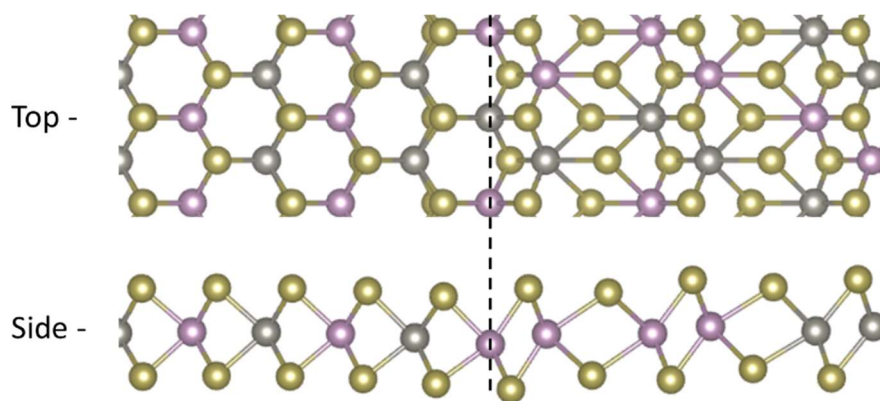


Fig. 7.3 Schematic of phase boundaries in 2D $Mo_{(1-x)}W_xTe_2$ alloys, where Mo, W and Te atoms are shown in purple, grey and brown. The black dash line indicates the phase boundary line.

7.2 Broadening alloying strategy to other 2D materials

This thesis systematically studied alloying as a tuning method for activating the basal plane of 2D TMDCs for enhanced HER performance. Besides, it would be interesting to understand whether alloying can be applied to other 2D systems and alter their electronic and catalytic properties. To this end, Chapter 6 has investigated the capability of alloying in tuning the electronic and catalytic properties of a group of emerging new 2D materials, namely 2D III-nitrides. It was found that complete miscibility in 2D $\text{Ga}_{(1-x)}\text{Al}_x\text{N}$ alloys can be achieved at very low temperatures. The band gaps and hydrogen adsorption abilities of 2D $\text{Ga}_{(1-x)}\text{Al}_x\text{N}$ random alloys can be tuned by varying the chemical compositions and the applied biaxial tensile strains, making 2D $\text{Ga}_{(1-x)}\text{Al}_x\text{N}$ potential candidates as photocatalysts for water splitting.

Unlike 2D TMDCs which have been extensively studied for a wide range of applications, the studies of 2D III-nitrides are still in their infancy due to the stability issue. This study serves as a starting point for using 2D III-nitride alloys for catalytic applications, but further experimental validations are necessary to prove their capabilities in this field. Additionally, Chapter 6 only provided benchmark studies on the HER activities of 2D III-nitrides, while the corresponding mechanism and reaction energetics were unraveled, which deserve further investigation.

Asides from alloying, another important modification strategy for improving HER activity, defect engineering, was not considered in 2D III-nitrides in this thesis. Defects in 2D III-nitrides may have the capability of altering the HER activity of 2D III-nitrides. However, they are rarely explored by experiments and require theoretical understanding. Therefore, additional efforts are required to investigate the influence of point defects, grain boundaries, and phase boundaries on the stability and chemical properties of 2D III-nitrides.

7.4 Descriptors for electronic structures of 2D catalysts

To better understand the interaction between hydrogen and adsorption sites, we also looked into the electronic structures of the adsorption sites at phase boundaries and alloys of 2D TMDCs. It is known that for transition metals, the characteristics of electronic structures are generally described by the d-band center, a universal descriptor developed by Norskov and coworkers to evaluate the electronic factors in the catalytic process [18]. Besides, the d-band center model can be further modified to a p-band center model so as to describe the chalcogen sites in 2D TMDC systems [19]. In the case of 2D TMDC alloys, as demonstrated in Fig. 5.5 (a) in Chapter 5, a good linear correlation can be observed between the p-band center and ΔG_{H} , despite some outliers. Those outliers could be partially attributed to the broad and structureless p bands compared to the narrow d bands [20]. Although approximate linear correlation can be established between the electronic structure and HER activity, those outlier data points should be treated cautiously and the theory to better describe the chalcogen sites in 2D TMDCs is worth pursuing.

Similarly, in Chapter 4, p-band center was applied to describe the characteristics of chalcogen sites at the phase boundaries of 2D MoTe₂. However, as shown in Fig. 7.4 (a), the p-band center values of Te atoms do not display a clear trend with respect to ΔG_{H} . We also plotted a modified version of p-band center, as developed by Ouyang et al. [19], with respect to ΔG_{H} (See Fig. 7.4 (b)), and this model also fails to capture the correlation between the electronic structure and HER activity. The failure of using the p-band center model to describe the electronic structures of 2D TMDC phase boundaries may come from the complex defect structures, which alter the chemical environment of adsorption sites. Generally, not every electronic state in the band contributes equally to the hydrogen bonding at the chalcogen site. To this end, we adopted the Fermi-abundance (D_{F}) model to replace the p-band center model [21]. This model considers the

fact that the closer the electronic state is to the Fermi level, the greater its contribution to the bonding. As plotted in Fig. 7.4 (c), a clear linear correlation between D_F and ΔG_H can be observed, indicating the successful application of Fermi-abundance model to quantify the HER activities of Te sites at phase boundaries.

It is worth noting that the D_F model cannot be used to describe the Mo and hollow sites at the MoTe_2 phase boundaries because hydrogen adsorption at these sites involves interaction with multiple orbitals from different atoms. This limitation of the D_F model was not addressed in this study and is worth further exploration.

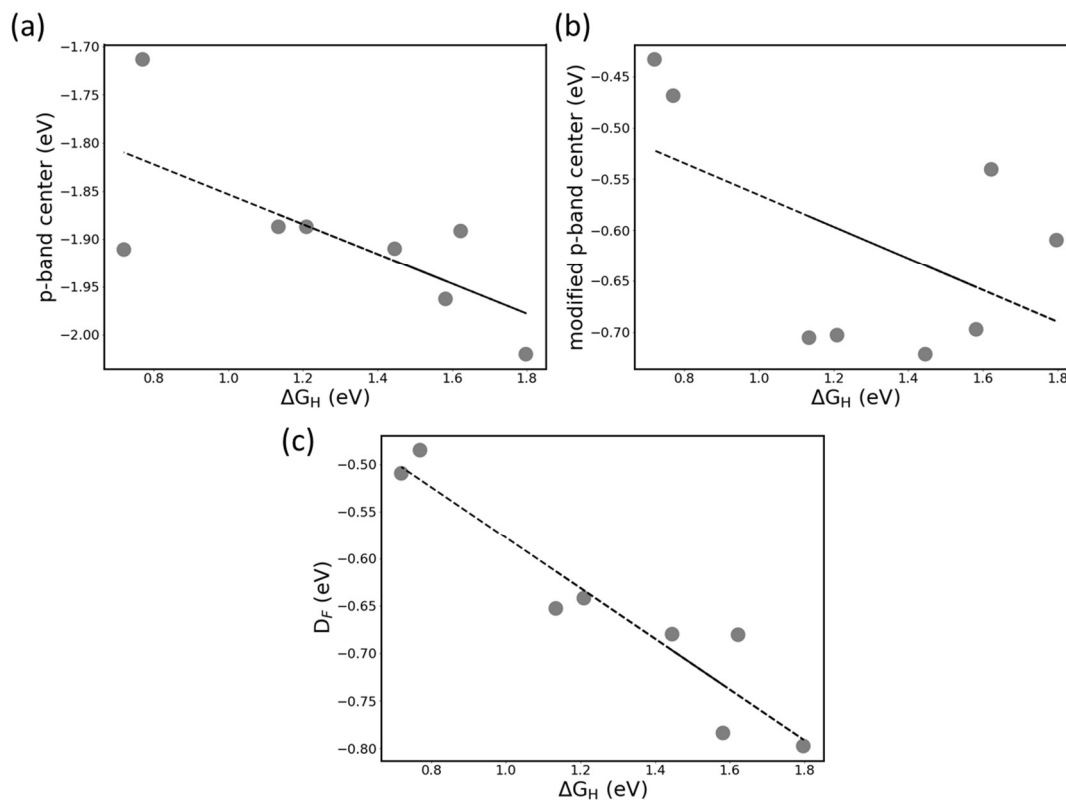


Fig. 7.4 Calculated (a) p-band center, (b) modified p-band center and (c) Fermi-abundance (D_F) values of various Te sites with respect to ΔG_H values.

7.5 References

- [1] M.S. Dresselhaus, I.L. Thomas, Alternative energy technologies, *Nature* 414(6861) (2001) 332-337.
- [2] X. Ren, H. Fan, C. Wang, J. Ma, H. Li, M. Zhang, S. Lei, W. Wang, Wind energy harvester based on coaxial rotatory freestanding triboelectric nanogenerators for self-powered water splitting, *Nano Energy* 50 (2018) 562-570.
- [3] Z.W. Seh, J. Kibsgaard, C.F. Dickens, I. Chorkendorff, J.K. Nørskov, T.F. Jaramillo, Combining theory and experiment in electrocatalysis: Insights into materials design, *Science* 355(6321) (2017) eaad4998.
- [4] Y. Jiao, Y. Zheng, M. Jaroniec, S.Z. Qiao, Design of electrocatalysts for oxygen- and hydrogen-involving energy conversion reactions, *Chem Soc Rev* 44(8) (2015) 2060-86.
- [5] H. Li, C. Tsai, A.L. Koh, L. Cai, A.W. Contryman, A.H. Fragapane, J. Zhao, H.S. Han, H.C. Manoharan, F. Abild-Pedersen, J.K. Nørskov, X. Zheng, Activating and optimizing MoS₂ basal planes for hydrogen evolution through the formation of strained sulphur vacancies, *Nature Materials* 15(1) (2016) 48-53.
- [6] X. Wang, L. Meng, B. Li, Y. Gong, Heteroatoms/molecules to tune the properties of 2D materials, *Materials Today* 47 (2021) 108-130.
- [7] D.B. Putungan, S.H. Lin, J.L. Kuo, A first-principles examination of conducting monolayer 1T'-MX₂ (M = Mo, W; X = S, Se, Te): promising catalysts for hydrogen evolution reaction and its enhancement by strain, *Phys Chem Chem Phys* 17(33) (2015) 21702-8.
- [8] J. Zhang, J. Wu, H. Guo, W. Chen, J. Yuan, U. Martinez, G. Gupta, A. Mohite, P.M. Ajayan, J. Lou, Unveiling Active Sites for the Hydrogen Evolution Reaction on Monolayer MoS₂, *Adv Mater* 29(42) (2017).
- [9] Q. Gong, L. Cheng, C. Liu, M. Zhang, Q. Feng, H. Ye, M. Zeng, L. Xie, Z. Liu, Y. Li, Ultrathin MoS₂(1-x)Se_{2x} Alloy Nanoflakes For Electrocatalytic Hydrogen Evolution Reaction, *ACS Catalysis* 5(4) (2015) 2213-2219.
- [10] K.A. Duerloo, E.J. Reed, Structural Phase Transitions by Design in Monolayer Alloys, *ACS Nano* 10(1) (2016) 289-97.
- [11] J. Zhu, Z.C. Wang, H. Dai, Q. Wang, R. Yang, H. Yu, M. Liao, J. Zhang, W. Chen, Z. Wei, N. Li, L. Du, D. Shi, W. Wang, L. Zhang, Y. Jiang, G. Zhang, Boundary activated hydrogen evolution reaction on monolayer MoS₂, *Nat Commun* 10(1) (2019) 1348.
- [12] Y. Nakayasu, Y. Yasui, R. Taniki, K. Oizumi, H. Kobayashi, N. Nagamura, T. Tomai, I. Honma, One-Pot Rapid Synthesis of Mo(S,Se)₂ Nanosheets on Graphene for Highly Efficient Hydrogen Evolution, *ACS Sustainable Chemistry & Engineering* (2018).
- [13] Y. Zhou, J.L. Silva, J.M. Woods, J.V. Pondick, Q. Feng, Z. Liang, W. Liu, L. Lin, B. Deng, B. Brena, F. Xia, H. Peng, Z. Liu, H. Wang, C.M. Araujo, J.J. Cha, Revealing the Contribution of Individual Factors to Hydrogen Evolution Reaction Catalytic Activity, *Adv Mater* 30(18) (2018) e1706076.
- [14] D. Lu, X. Ren, L. Ren, W. Xue, S. Liu, Y. Liu, Q. Chen, X. Qi, J. Zhong, Direct Vapor Deposition Growth of 1T' MoTe₂ on Carbon Cloth for Electrocatalytic Hydrogen Evolution, *ACS Applied Energy Materials* 3(4) (2020) 3212-3219.
- [15] M.-H. Tsai, J.-W. Yeh, High-Entropy Alloys: A Critical Review, *Materials Research Letters* 2(3) (2014) 107-123.

- [16] J. Cavin, A. Ahmadiparidari, L. Majidi, A.S. Thind, S.N. Misal, A. Prajapati, Z. Hemmat, S. Rastegar, A. Beukelman, M.R. Singh, K.A. Unocic, A. Salehi-Khojin, R. Mishra, 2D High-Entropy Transition Metal Dichalcogenides for Carbon Dioxide Electrocatalysis, *Adv Mater* (2021) e2100347.
- [17] S. Sandhya, K. Alex, H.J. A., K. Vidya, A. Amey, V. Robert, I.J. Carlos, Y.B. I., T.C. Sekhar, A.P. M., Quaternary 2D Transition Metal Dichalcogenides (TMDs) with Tunable Bandgap, *Advanced Materials* 29(35) (2017) 1702457.
- [18] J.K. Nørskov, F. Studt, F. Abild-Pedersen, T. Bligaard, *Fundamental concepts in heterogeneous catalysis*, John Wiley & Sons 2014.
- [19] Y. Ouyang, C. Ling, Q. Chen, Z. Wang, L. Shi, J. Wang, Activating Inert Basal Planes of MoS₂ for Hydrogen Evolution Reaction through the Formation of Different Intrinsic Defects, *Chemistry of Materials* 28(12) (2016) 4390-4396.
- [20] M. Mavrikakis, B. Hammer, J.K. Nørskov, Effect of Strain on the Reactivity of Metal Surfaces, *Physical Review Letters* 81(13) (1998) 2819-2822.
- [21] B. Huang, L. Xiao, J. Lu, L. Zhuang, Spatially Resolved Quantification of the Surface Reactivity of Solid Catalysts, *Angewandte Chemie International Edition* 55(21) (2016) 6239-6243.

Chapter 8 : Conclusions

8.1 Final conclusions

In this thesis, focusing on two important classes of 2D materials, namely 2D TMDCs and 2D III-nitrides, the properties of phase boundaries and alloys of 2D materials were systematically investigated, and their roles in catalyzing hydrogen evolution reaction were revealed. This thesis provides theoretical guidance for designing new classes of high-performance HER electrocatalysts and photocatalysts based on 2D materials. The main conclusions are summarized below.

1. The structural stabilities and HER activities of various 2H/1T' MoTe₂ phase boundaries were carefully examined using first-principles calculations. Potential catalytic centers in energetically stable phase boundaries were identified, which can be classified into three categories, namely Te, Mo, and hollow sites. All those sites exhibit enhanced HER activities compared to that of the pristine basal lattice, indicating that the basal plane of 2D MoTe₂ can be activated via phase boundaries. Particularly, the hollow sites were found to exhibit the highest HER activity, comparable to that of Pt-based catalysts.
2. The mechanisms of basal plane activation of 2D MoTe₂ for HER via phase boundaries were studied. The HER activities are found to be related to the unique local hydrogen adsorption geometries and electronic structures at phase boundaries. Specifically, the catalytic activities of Te sites were well understood and predicted by the Fermi-abundance model. Additionally, the optimal HER performance at the hollow sites comes from the modification of the d_{xy} and $d_{x^2-y^2}$ orbitals of Mo atoms by phase boundaries, thus giving rise to much stronger binding with hydrogen.

3. Based on DFT calculations, the HER activities and thermodynamic stabilities of more than 8400 2D cation-mixed TMDC alloy configurations were accurately predicted by a machine learning workflow, which accelerates the discovery process of candidate 2D TMDC alloys for catalytic applications.
4. The HER activities of various 2D TMDC alloys were studied. It was demonstrated that alloying leads to a substantial reduction in ΔG_H with respect to the pristine TMDCs. Moreover, a number of transition metal disulfide alloys show great potential for catalyzing HER, as some of their energetically stable active sites have ΔG_H in the ideal range. Meanwhile, it was found that alloying induced similar effects to the HER activities of transition metal sulfides and selenides.
5. The mechanism underlying the alloying-induced basal plane activation of 2D TMDCs was investigated in detail. The basal plane activation by alloying mainly originates from the electronic effect resulted from the chemical composition variation. Specifically, the local charge exchange produced by alloying results in the shifting of the p -band center of the adsorption sites, which changes the hydrogen adsorption ability.
6. The structural, electronic, and catalytic properties of 2D $\text{Ga}_{(1-x)}\text{Al}_x\text{N}$ alloys were investigated using density functional theory in conjunction with the cluster expansion method. Our results show that 2D $\text{Ga}_{(1-x)}\text{Al}_x\text{N}$ alloys are thermodynamically stable and complete miscibility in the alloys can be achieved below room temperature. Besides, the band gaps and ΔG_H of $\text{Ga}_{(1-x)}\text{Al}_x\text{N}$ random alloys can be tuned by varying chemical compositions. Furthermore, $\text{Ga}_{(1-x)}\text{Al}_x\text{N}$ random alloys are confirmed to have suitable band edge positions for water splitting over the entire range of concentration, showing great promise for photocatalysts.

7. The effect of biaxial tensile strain on the electronic and chemical properties of 2D $\text{Ga}_{(1-x)}\text{Al}_x\text{N}$ alloys was examined. We found that biaxial tensile strains can decrease the band gap values of random alloys significantly, due to their modifications to the CBM positions of alloys. Meanwhile, using 2D $\text{Ga}_{0.5}\text{Al}_{0.5}\text{N}$ as an example, hydrogen adsorption on 2D $\text{Ga}_{(1-x)}\text{Al}_x\text{N}$ alloy under strain was studied, with Gibbs free energy of hydrogen adsorption ΔG_{H} achieving optimal value at 7% strain.

8.2 Contribution to the original knowledge

The contribution to the original knowledge in this thesis is reflected in the following aspects:

1. Phase boundaries were theoretically predicted to provide catalytically active sites in monolayer MoTe_2 , demonstrating a new route to activate the basal plane of 2D MoTe_2 for HER.
2. The interaction between hydrogen and the various adsorption sites at the 2D TMDC phase boundary was clarified by analyzing the electronic structures of 2D MoTe_2 .
3. A machine learning workflow was constructed to accurately the HER activities and thermodynamic stabilities of various 2D cation-mixed TMDC alloys.
4. High-throughput screening on 2D TMDC alloys was performed for selecting candidate materials for catalyzing HER, providing machine-derived suggestions for catalyst design in experiments.
5. The mechanism underlying the alloying-induced basal plane activation of 2D TMDCs was first clarified, providing valuable theoretical insights into designing alloy catalysts based on 2D TMDCs.

6. The structural, electronic, and catalytic properties of 2D $\text{Ga}_{(1-x)}\text{Al}_x\text{N}$ alloys were examined, and 2D $\text{Ga}_{(1-x)}\text{Al}_x\text{N}$ alloys were predicted to be promising candidate materials for photocatalytic HER.
7. Strain effect on the hydrogen adsorption of 2D $\text{Ga}_{(1-x)}\text{Al}_x\text{N}$ alloys was investigated.

8.3 Future work

This thesis sheds some light on the rational design of high-performance HER catalysts based on 2D materials. However, there remain many unexplored areas in engineering and understanding 2D materials for improved catalytic performance. Some unresolved tasks that are worth pursuing in future research are listed below:

1. Band center theory plays an important role in describing electronic structures and understanding the activity trends of catalysts. However, band center models often break down for adsorption sites involving complex adsorption geometry and multiple atoms, which commonly exist in 2D materials. Moreover, while *d*-bands are utilized to well understand the interaction between adsorbates and transition metals, the adsorption abilities of chalcogen atoms in 2D TMDCs are strongly related to the *p*-bands. Compared to the *d*-bands, *p*-bands are usually broad and structureless, and thus they are not always sensitive to small chemical environment changes. Therefore, developing descriptors that better represent the electronic structures of 2D materials would be necessary for understanding the activity trends of 2D catalysts.
2. 2D TMDCs can exhibit different types of phases, namely trigonal prismatic (2H), octahedral (1T) and distorted (1T' and 1T'') phases, which exhibit strongly differing electronic and chemical properties. However, recent progress on 2D TMDC alloys for

catalysis mostly focuses on the 2H phase of 2D TMDCs, while the effect of alloying in other phases remains unexplored. Therefore, additional research efforts are required to understand how differing in phases would change the HER performance of 2D TMDC alloys and affect their electronic structures.

3. Besides from the activation of the basal plane for HER, alloying was also found to trigger phase transition in 2D TMDCs. The phase transition from 2H to 1T or 1T' phase achieved by varying the chemical composition could create phase boundaries in 2D TMDCs, and it is expected that these alloying-induced phase boundaries could alter the catalytic properties of 2D TMDCs, which deserves further investigations.
4. This thesis has investigated alloying as a possible route to tune the electronic and catalytic properties of 2D III-nitrides, while another important modification strategy, defect engineering was not explored in this class of materials. The influence of point defects, grain boundaries and phase boundaries on the adsorption properties of 2D III-nitrides needs to be understood.
5. Although alloying provides a viable way to enhance the HER performance of 2D materials, there is still one challenge that limits the application of 2D alloys, the synthesis of stable 2D alloys. The stability issue could be further addressed by fabricating 2D high entropy alloys. Besides, it is anticipated that these multicomponent alloys allow high tunability of their electronic and catalytic properties, making them promising materials for electrocatalytic and photocatalytic applications.